Deltares

IVM Institute for Environmental Studies

NIOO

waterbouwkundig LABORATORIUM

Validation and Application of Mud Model Scheldt Estuary

in the framework of LTV

dr ir T. van Kessel
ir J. Vanlede
dr M.A. Eleveld
dr D. van der Wal
B. De Maerschalck

1202021-000

Deltares

Title
Validation and Application of Mud Model Scheldt Estuary

Client	Project	Pages
MT-Kennis	1202021-000	131

Keywords
mud transport, 3D models, estuary models, Scheldt, remote-sensing

Summary
The present report describes work carried out during 2010 in the framework of the programme LTV Toegankelijkheid (Long Term Vision Scheldt Estuary – Accessibility). It consists of five parts: 1) Description of remote sensing activities and results regarding the water column; 2) Description of remote sensing activities and results regarding the supra- and intertidal bed; 3) Hydrodynamic simulation of 2006, based on improved and extended numerical grid; 4) Mud transport simulation of 2006, based on the new hydrodynamics and 5) Application of mud transport model to several cases. This work builds on and is a continuation of previous work (2006 – 2009).

References
KPP no. x

Version	Date	Author	Initials	Review	Initials	Approval	Initials
2.0	July 2011	T. van Kessel		J.C. Winterwerp		T. Schilperoort	
		J. Vanlede					
		M. Eleveld					
		D. van der Wal					
		B. De Maerschalck					

State
final

Contents

1 Introduction

The present report describes work carried out during 2010 in the framework of the programme LTV Toegankelijkheid (Long Term Vision Scheldt Estuary – Accessibility).

It consists of five parts:

1 Description of remote sensing activities and results regarding the water column;
2 Description of remote sensing activities and results regarding the supra- and intertidal bed;
3 Hydrodynamic simulation of 2006, based on improved and extended numerical grid;
4 Mud transport simulation of 2006, based on the new hydrodynamics;
5 Application of mud transport model to several cases.

This work builds on and is a continuation of previous work (2006 – 2009). A description thereof can be found in four reports (Van Kessel et al. 2006 – 2009), which are accessible via the Scheldt monitor (www.scheldemonitor.be).

The activities listed above are discussed in the following five chapters. Conclusions are drawn in the last chapter.

Activities 1 and 2 are a follow-up of 2008 remote sensing activities. The retrieval and processing algorithms have now been further improved and applied for the period 2006 – 2008. This applies to remote sensing of both water column and supra- or intertidal flats.

Activities 3 and 4 are a follow-up of 2009 model activities. The present activities deal with some improvement of the bathymetry, grid and hydrodynamic model on the one hand, and application hereof for a full year simulation for hydrodynamics and sediment transport. The selected year is 2006, which allows for a direct comparison with remote sensing data.

Finally, activity 5 deals with the impact assessment of Deurganckdok and freshwater discharge on sediment dynamics based on model results for the full year.

2 Remote sensing of the top of the water column

2.1 Introduction

Remote sensing may assist regular in situ monitoring and dynamic modelling of water quality parameters. In particular, it may provide information on the spatial heterogeneity of water quality parameters at the top of the water column. In estuaries, large-scale patterns of spatial variability include e.g. longitudinal gradients in tide and salinity that are amplified by the geometry. The temporal variation comprises semi-diurnal, neap-spring, seasonal and annual components.

Van der Wal et al. (2010) have shown that variation in mud content of the bed, and suspended particulate matter (SPM) in the water work on different time-scales: bottom sediment mainly shows seasonal changes, whereas SPM varies also on much shorter time-scales (such as semi-diurnal and neap-spring). This high variability should be kept in mind when evaluating the differences and similarities between in situ and remote sensing data sets (Eleveld et al., 2008). Characterisation of these variations is also important for management, e.g. when trying to assess the anthropogenic impact, such as increases in turbidity from dredge spoil dump, on the Westerschelde.

This chapter presents results from a study in which these topics were investigated with remote sensing data.

2.2 Materials and Methods

The availability of atmospherically corrected and geolocated (level-2, L2) reflectance measurements from the European Space Agency's Medium Resolution Imaging Spectrometer (MERIS) instrument has been providing new opportunities for monitoring of turbid coastal waters. These data sets have been used in an earlier project on mud transport in the Westerschelde estuary (Van Kessel et al., 2008; Van der Wal et al., 2010a). The current study covers a longer time period (years 2006 – 2008), which enabled selection of more (now 84) images with low cloud-coverage. See Appendix A.1 for a full overview of the collected remote sensing data.

To retrieve water quality parameters from MERIS reflectance, a spectral matching algorithm (HYDROPT) was used. HYDROPT compares the reflectances that were measured by MERIS with modelled reflectances as a function of e.g. total absorption and scattering (Van der Woerd and Pasterkamp, 2008; Van Kessel et al., 2008 section 2.1; Van der Wal et al., 2010a section 3.4). Main inputs for this algorithm consist of:

1 Satellite reflectance data from a selection of wavelengths (spectral bands).
2 The absorption and scattering properties of SPM, chlorophyll-*a* (CHL) and Coloured Dissolved Organic Matter (CDOM) for North Sea and Westerschelde waters.

The three following main methods were applied in the current study, and are elaborated in Sections 2.2.1 to 2.2.3.

1 Processing of the remote sensing reflectance data to optical water quality parameters with five different parameterisations of the hydro-optical algorithm, HYDROPT. Such a structured sensitivity study of HYDROPT had not yet been performed. It resulted in maps (snapshots) of SPM concentrations at the top of the water column. It also provided first estimates of CHL and CDOM concentrations in the Westerschelde.
2 Subsequent extraction of two water quality parameters (SPM and CHL) from each map, at the location of in situ measurement stations. The resulting time series were plotted and used for inter-comparison with field data (in situ measurements).
3 Finally, additional environmental data were analysed and composite SPM maps were created. Environmental variables (such as tide, wind, discharge or bathymetry) have an influence on SPM concentrations. They impose characteristic SPM response timescales and cause spatial differences. The maps of SPM concentrations were combined into map-composites. These composites were created for semi-diurnal, fortnightly, and seasonal timescales.

2.2.1 Processing with five different parameterisations

Five different parameterisations of the hydro-optical model were tested in the current study, because they could theoretically improve the retrieval of SPM, CHL and CDOM.

1 Original Seven band: First the same settings as in Van Kessel et al. (2008) were used
2 Seven band LUT (7BL): The range of the lookup table (LUT) for the spectral matching was expanded to accommodate for high total absorption and scattering
3 Seven band LUT high concentration (7BLC): The expanded LUT was used, and the initial concentrations were set to Westerschelde concentrations
4 Eight band corrected (8BC): MERIS band 8 (band centre at 681.25 nm) was added, and the absorption signal at this wavelength was corrected for a lab analysis error
5 Eight band no correction (8BNC)

All output maps of SPM, CHL, CDOM, their errors, and Kd at 560 nm were compared. The results from the five parameterisations were also compared as scatter-plots for three (station) locations (see also section 2.2).

Background for the five parameterisations:

1 Original Seven band: For consistency, first the same settings as in Van Kessel et al. (2008) were used: MERIS band 2:7 and 9; LUT16 and the North Sea and Westerschelde sIOP sets (Belgica2000 and Restwes99Oroma02mean).

2 Seven band LUT (7BL): The range of the lookup table (LUT) for the spectral matching was expanded to accommodate for high total absorption, a and scattering, b (LUT 102, Figure 2.1; see also Hommersom *et al.*, in press) to see if this solved the problem of zero values for CHL, and CDOM, at high SPM (Van Kessel et al., 2008).

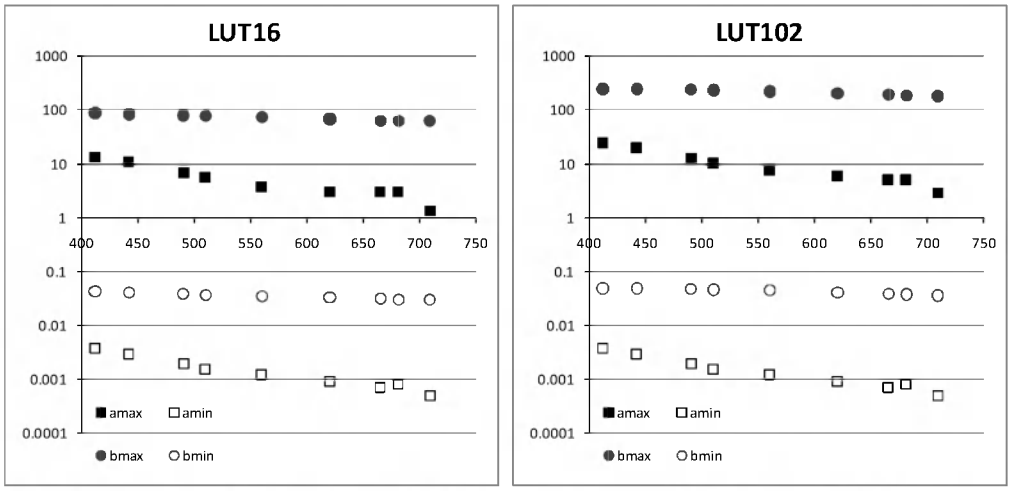

Figure 2.1 The absorption and scattering limits of the original and expanded optical mode.(X-axis wavelength (nm), y-axis a_{tot} and b_{tot} (m^{-1})).

3 Seven band LUT high concentration (7BLC): The expanded LUT was used, and the initial concentrations for the Westerschelde were changed from North Sea average to MWTL Westerschelde averages 6.5 mg m-3 CHL, 56.5 g m-3 SPM (both mean Waterbase MWTL 2006-2008), 1 CDOM (dimensionless, based on ResWes1999 and Oroma2002 data).

4 Eight band corrected (8BC) In the original setup (1), MERIS band 8 (band centre at 681.25 nm) was discarded. It was now added, because evidence increasingly seems to suggest that the contribution of fluorescence to the reflectance signal at 681.25 nm (bandwidth 7.5) is limited in case-2 waters. For the lower concentrations, water absorption limits the contribution of fluorescence to the reflectance to the surface (Babin et al., 1996). With increase in CHL, the chlorophyll fluorescence shifts towards higher wavelengths (>685 nm) (Gillerson et al., 2007).

5 Note, however, that in Restwes99Oroma02mean a CHL-a absorption peak occurs in a*SPM at 681 nm (Van Kessel et al., 2008, Fig 2.3), which seems to indicate a familiar problem with seston bleaching (Rijkeboer et al., 1998; Vos et al., 2003). This has now been corrected through fitting in a*SPM at 681 nm, and adding the residual to a*CHL681. It can be expected that this correction will lead to a minor improvement for both SPM and CHL. Even with this correction, the result might still lead to an underestimation of CHL concentration, because the underlying concentration normalisation in the bio-optical relations (cf. Eleveld et al., 2008) is influenced by SPM concentrations being higher than CHL concentrations (Van Kessel et al., 2008). Optimal correction requires reverting to the underlying datasets (cf. Van Kessel et al., 2007), which is beyond the scope of the current project.

6 Eight band no correction (8BNC).

2.2.2 Extraction of the water quality parameters and comparison with in situ data

In situ SPM data at the main in situ stations Vlissingen (VLI), Terneuzen (TER), Hansweert (HAN), Hoedekenskerke (HOE, limited data available) and Schaar van Ouden Doel (SCH) were obtained though Waterbase (www.waterbase.nl). At these locations, SPM remote sensing was also extracted from the SPM concentration maps. (Van der Wal et al. 2010a, Figure 1 provides a map of the locations of the monitoring stations.) Then, in situ measurements and remote sensing results were presented in time-series plots. Also the means per station were compared.

As a first test, time-series plots and means per stations were also calculated for two cases:

1 station 700, 2 km off Zeebrugge Harbour structures (and one station to the SW, NE and offshore), and
2 going upriver on the Zeeschelde (S15a near Doel – S22 near Antwerpen).

It was expected however, that the remote sensing products might be of somewhat lesser quality here, than in the Westerschelde estuary proper, because of differences in absorption and scattering characteristics, high SPM concentrations, and stray light from nearby vegetated land.

2.2.3 Creation of environmental SPM composites

The maps of the water quality parameters were reprojected to Dutch Rijksdriehoekscoordinaten (RD) and (for SPM) combined to composites. Note that every pixel giving a valid SPM value for water was used. Shallow areas are only sampled under high water conditions: their mean is based on a limited number of samples.

Tidal data were processed following van der Wal et al. (2010a). Classes were chosen with the objective to capture environmental conditions: comparing composites enables assessing variability in one component, whilst other variability is averaged out. This could facilitate assessment of the response of water quality parameters to influence of specific environmental factors or driving forces).

For semi-diurnal composites, four classes were created based on hours from HW Hansweert (HAN), a representative station located in the centre of the estuary (Table 2.1). These broad classes enable sampling of about 21 images per class, but also have a disadvantage: high currents near HAN occur at about 1 h before HW HAN, low currents at slack around 1 h after HW HAN (Koninklijke Marine – Dienst der Hydrografie, 2002). On the other hand, a minor lag in SPM response is to be expected but should occur within these (3 hours broad) classes.

Table 2.1 Classes of semi-diurnal composites

Tidal stage	Time (h) before (-) or after (+) HW HAN
LW	-6.1..-4.5, 4.5..+6.1
INcoming (flood)	-4.5..-1.5
HW	-1.5..+1.5
OUTgoing (ebb)	+1.5..+4.5

Table 2.2 shows the four classes that were chosen for the fortnightly cycle. Stronger currents occur at spring than at neap, because there is more water volume exchange. This would than result in higher surface SPM concentrations at spring than at neap.

Table 2.2 Spring tide fractions used to make neap-spring composites (Van der Wal et al., 2010a)

Tidal stage	Spring tide fraction
Neap	0 .. 0.25
Neap to mean	0.25 .. 0.5
Mean to spring	0.5 .. 0.75
Spring	0.75 .. 1

Finally, seasonal SPM composites (DJF, MAM, JJA, SON) were expected to capture wind forcing.

2.3 Results

The results presented below were derived from the methods described in the previous sections. These results are:

1 SPM and Chlorophyll-a concentrations from five different parameterisations (both maps and scatter-plots);
2 Time series of SPM; and
3 SPM composites.

2.3.1 SPM and CHL concentrations from five different parameterisations: maps and scatter-plots

The results presented here were derived from the method described in 2.1. The maps resulting from all five parameterisations (see 2.2.1) for three satellite images are presented in Appendix A.2. The maps resulting from the use of absorption and scattering characteristics for the North Sea are presented at the top of the page; those resulting from absorption and scattering characteristics for the Westerschelde at the bottom.

Visual comparison of the maps resulting from all five parameterisations for any one image (for example from 16-Oct-2006 in Appendix A.2) shows only minor differences. Between images (e.g between 16-Oct-2006, 20-Oct-2007, and 31-Mar-2008) there are major differences. This seems to confirm that driving processes and environmental conditions have an important impact on surface SPM concentrations. The results also illustrate that the retrieval of concentrations is quite robust, or insensitive to the changes in parameters.

For a detailed example of the latter: if the maps Seven band with adapted LUT (7BL) are compared with the other mapped test result in Appendix A.2 we see that the effects on SPM,

CHL and CDOM retrieval were minor. SPM concentrations in the outer estuary area are mostly between 5 and 30 g m^{-3}, as can be expected for this region (further supported in Section 2.3.2). However, note that CHL and CDOM also contain some values in the lowest class (indicated as purple). This class also comprises invalid (0 or -1) values. The expanded LUT did reduce the number of pixels in the lowest class (purple area) in the he K_{D560} maps (see Appendix A.2, 25-Mar-2007). Further inspection of the numeric results showed that there was indeed an increase in the number of valid values for K_{D560}.

To further increase the number of valid CHL and CDOM retrievals, the atmospheric correction of the MERIS L2 products should be improved. The atmospheric correction of MERIS L2 products for complex coastal waters is under current investigation (e.g. in the ESA COASTCOLOUR project).

Background on the effects of atmospheric correction on the retrieval of concentrations:
It appeared that invalid values in CDOM and CHL retrieval are caused by low reflectances in the shorter wavelengths of MERIS L2 data due to overcorrection by the atmosphere model, in combination with the high absorption by CHL, SPM and CDOM in the water. SPM retrieval benefits from additional scattering effects on reflectances.

Next, data from all images processed with Westerschelde sIOPs (and without taking quality flags into account) were used. The comparison of the SPM concentrations resulting from all five parameterisations was conducted at the location of three main stations VLI, HAN, and SCH (Figure 2.2 to Figure 2.7). When plotted against each other, SPM results from different parameterisations often end up on the 1:1 line. This confirms that the impact of theoretical improvements on the retrieval of concentrations is limited.

Based on these results it cannot be said that any of the parameterisations actually leads to better overall results. Therefore, it was decided to present results from the original Seven Band parameterisation of the algorithm, which has had been used in Van Kessel et al. (2008).

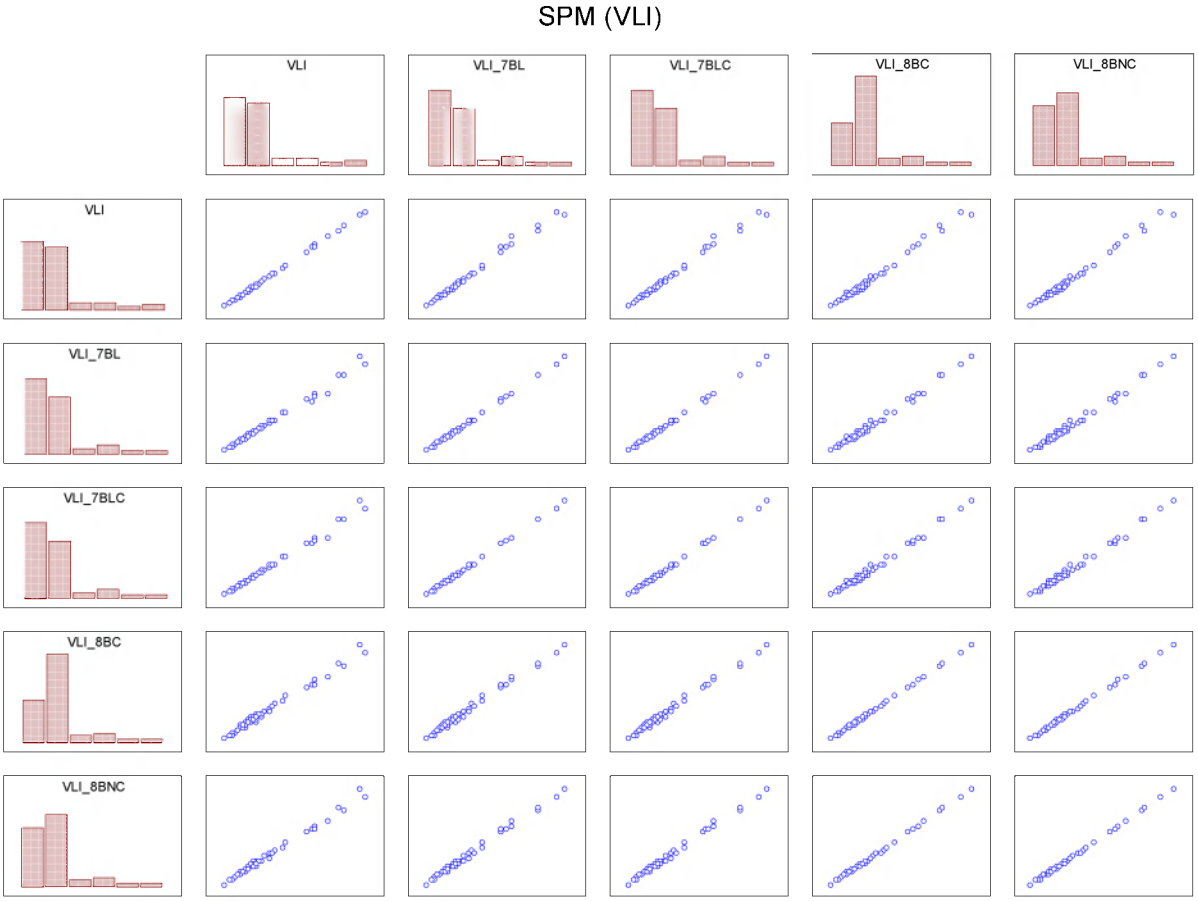

Figure 2.2 SPM concentrations from five parameterisations plotted against each other (from left to right and from top to bottom) for station Vlissingen (VLI). The five parameterisations are: Seven band, Seven band with adapted LUT (7BL), Seven band with adapted LUT and high initial concentrations(7BLC), Eight band corrected (8BC), and Eight band not corrected (8BNC). The plots are automatically scaled between highest and lowest values.

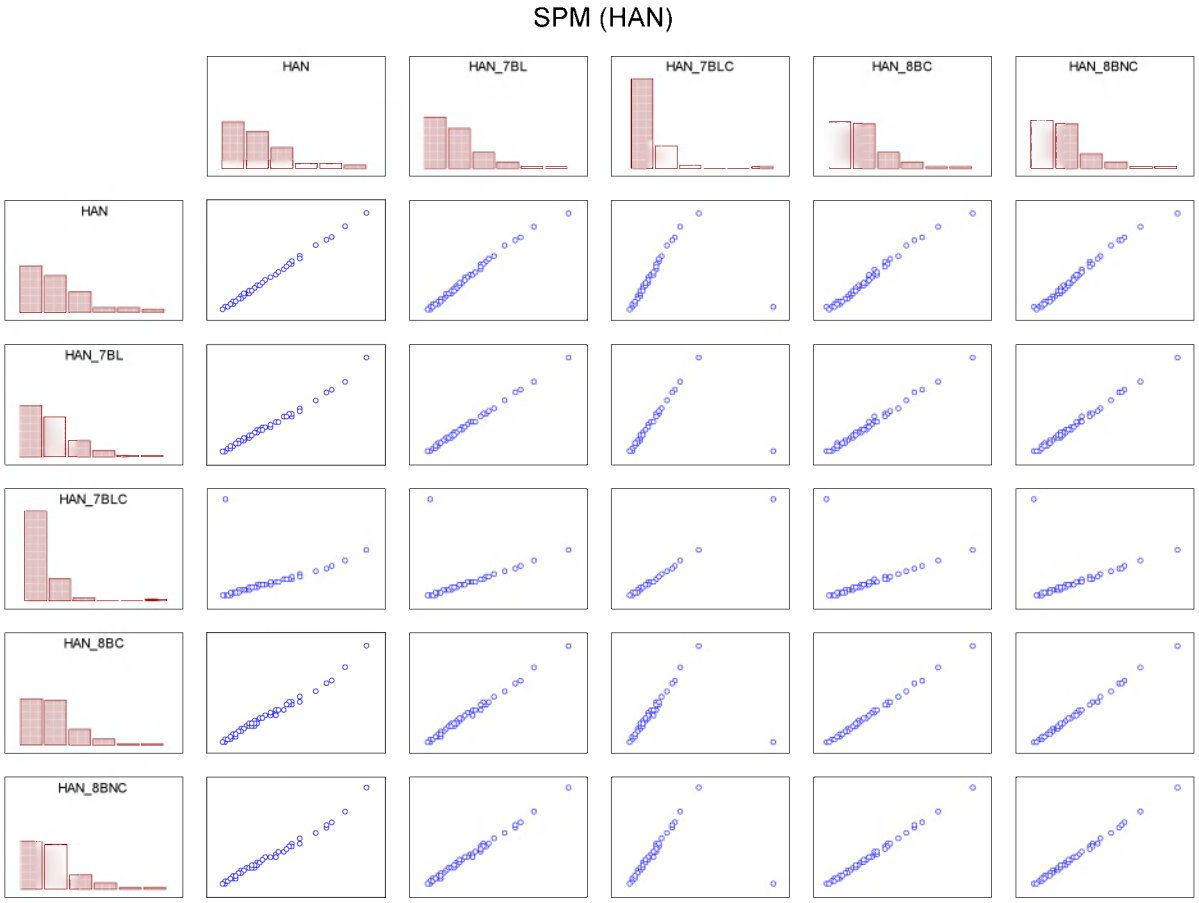

Figure 2.3 SPM concentrations from five parameterisations plotted against each other (from left to right and from top to bottom) for station Hansweert (HAN). Most values are actually close to the 1:1 line, but this is not always evident, because some scatter plots are distorted by a few outliers that influence the auto-scaling.

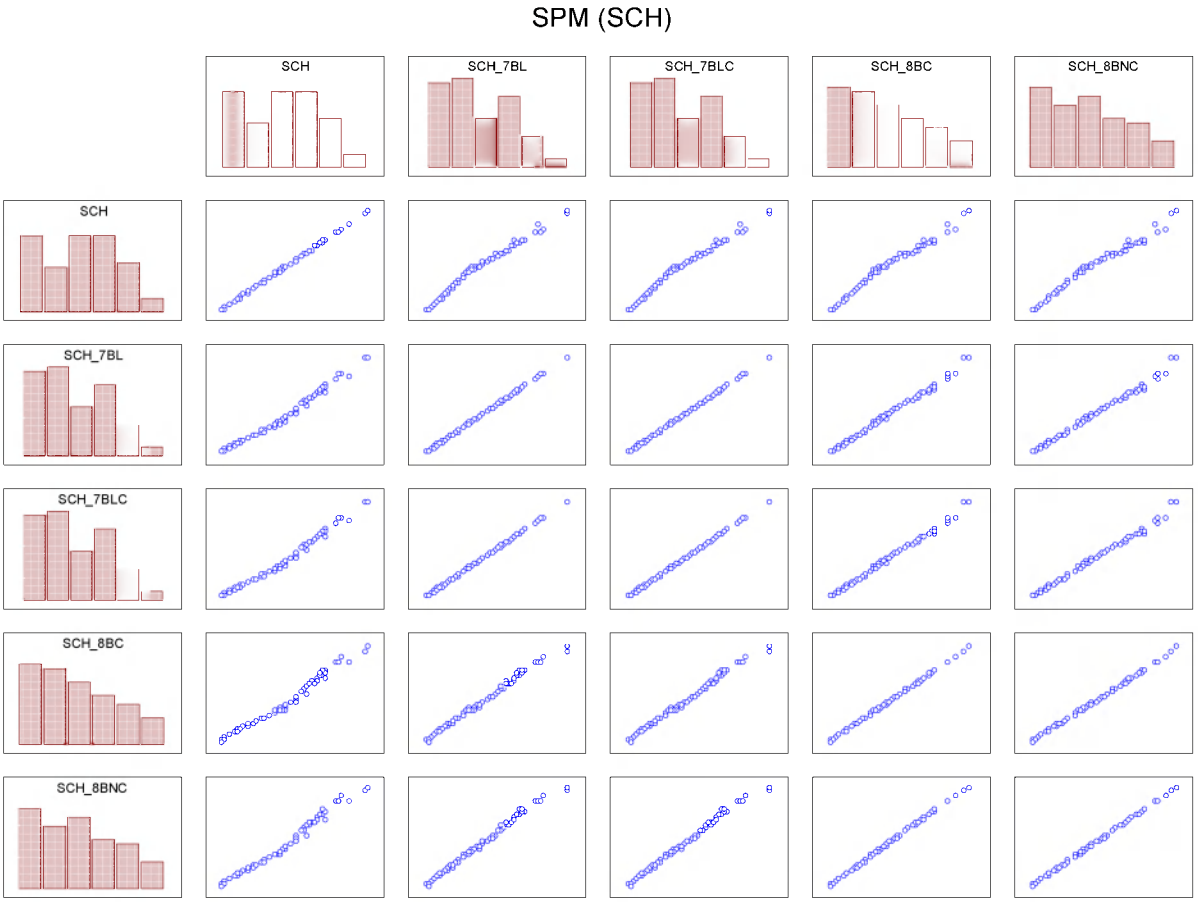

Figure 2.4 SPM concentrations from five parameterisations plotted against each other (from left to right and from top to bottom) for station Schaar van Ouden Doel (SCH).

Because some of the improvements (the inclusion of band 8) also aimed at preparing for better CHL demo products. CHL scatter-plots are also plotted.

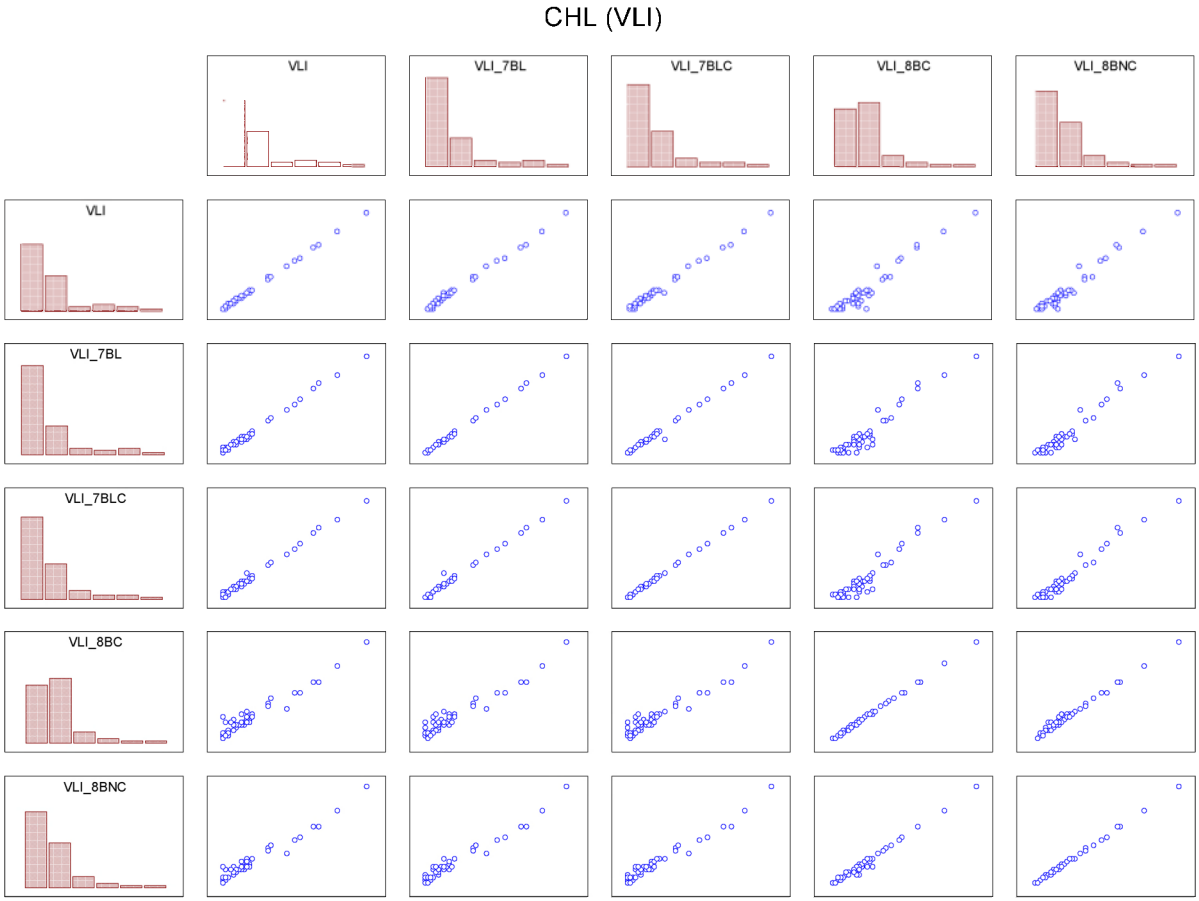

Figure 2.5 CHL concentrations from five parameterisations plotted against each other (from left to right and from top to bottom) other for station Vlissingen (VLI). The five parameterisations are: Seven band, Seven band with adapted LUT (7BL), Seven band with adapted LUT and high initial concentrations(7BLC), Eight band corrected (8BC), and Eight band not corrected (8BNC). Inclusion of the eighth band led to higher estimated concentrations in the lower CHL range, and lower concentrations in the higher range.

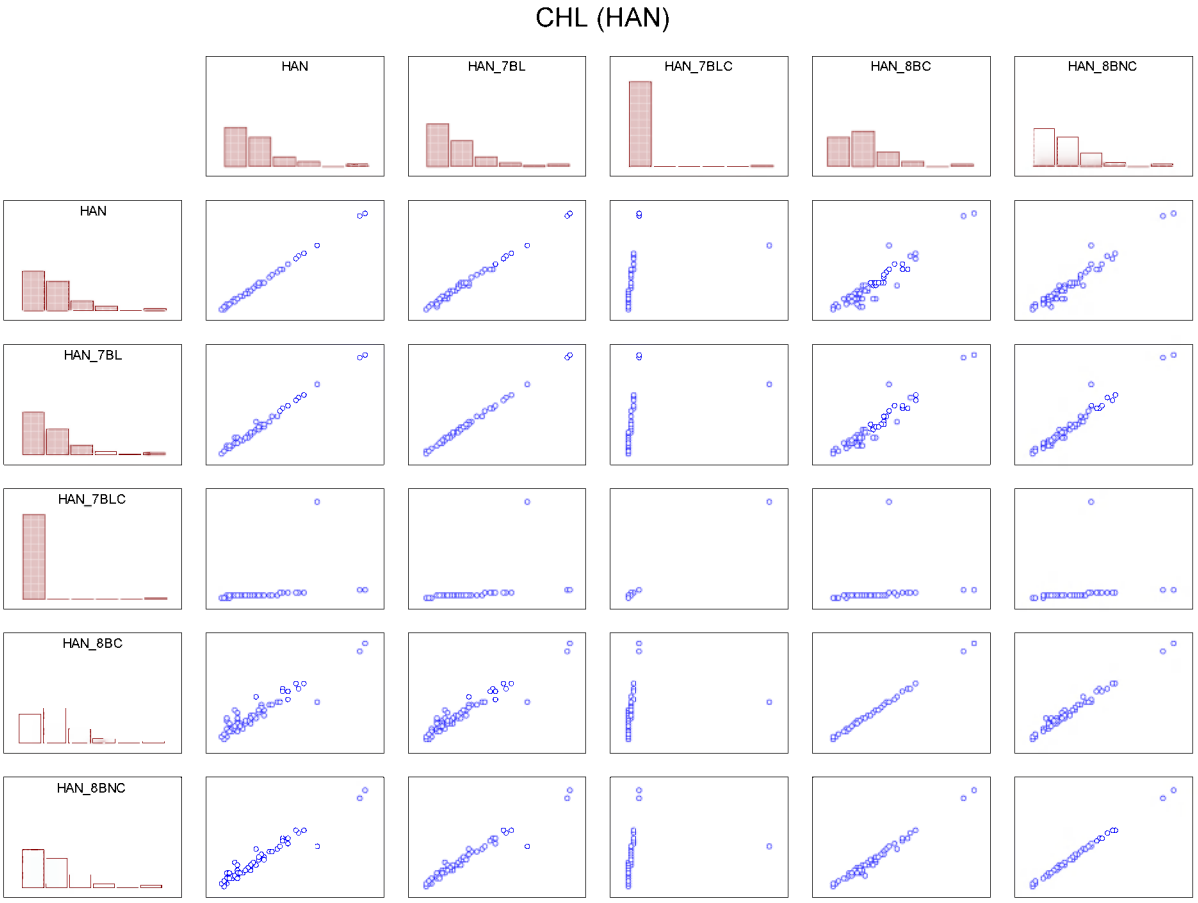

Figure 2.6 CHL concentrations from five parameterisations plotted against each other (from left to right and from top to bottom) for station Hansweert (HAN). Some scatter plots are distorted by a few outliers influencing the auto-scaling.

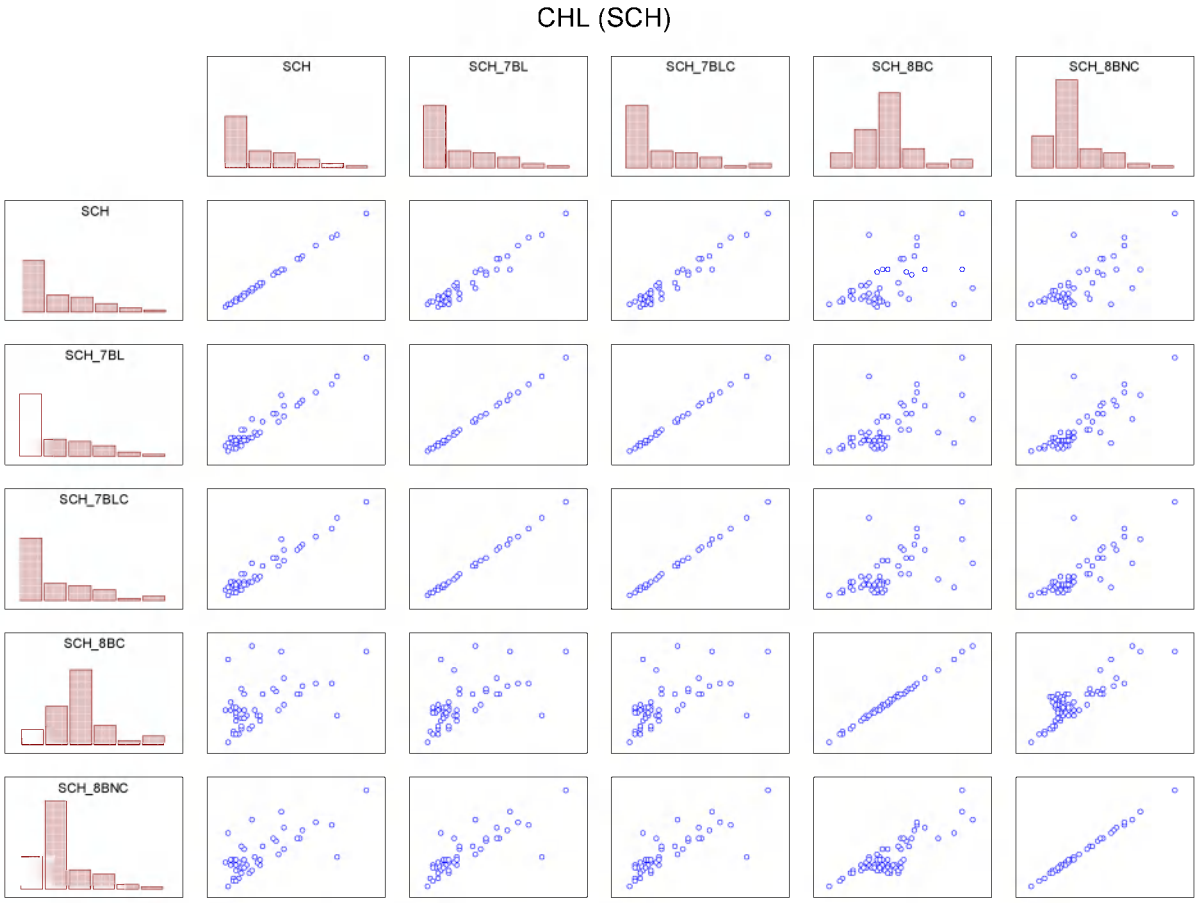

Figure 2.7 CHL concentrations from five parameterisations plotted against each other (from left to right and from top to bottom) for station Schaar van Ouden Doel.

Figure 2.8 gives an example of the Seven band SPM products for 20 Oct. 2007 and 31 Mar 2008. The top images of 20 October 2007 show SPM concentrations of ca 40 g m-3 at the top of the water column near the tidal flats in the Westerschelde, and nearby and upstream of Schaar van Ouden Doel. Channels with lower concentrations are clearly visible. At the time of image acquisition, it was ebb at Hansweert (3h after HW HAN), the fortnightly tide closer to neap than to spring, the springtide factor = 0.3 (Van der Wal et al., 2010), wind and discharge were moderate (uVlissingen = 2.6 m s-1, QSCH =75 m3 s-1).

The bottom images of 31 March 2008 show some high, up to 100 g m-3 SPM concentrations near the tidal flats and near and upstream of Schaar van Ouden Doel. At image acquisition time, it was slack neap tide at Hansweert (1 h after HW HAN, the springtide factor = 0, wind (uVlissingen)= 3.8 m s-1, and discharge(QSCH) was 450 m3 s-1 which is very high for the Zeeschelde.

A selection of additional SPM products derived from MERIS L2 data for which many pixels pass ESA's quality test (also known as PCD_1-13, see Van Kessel et al., 2008) are presented in Appendix A.3.

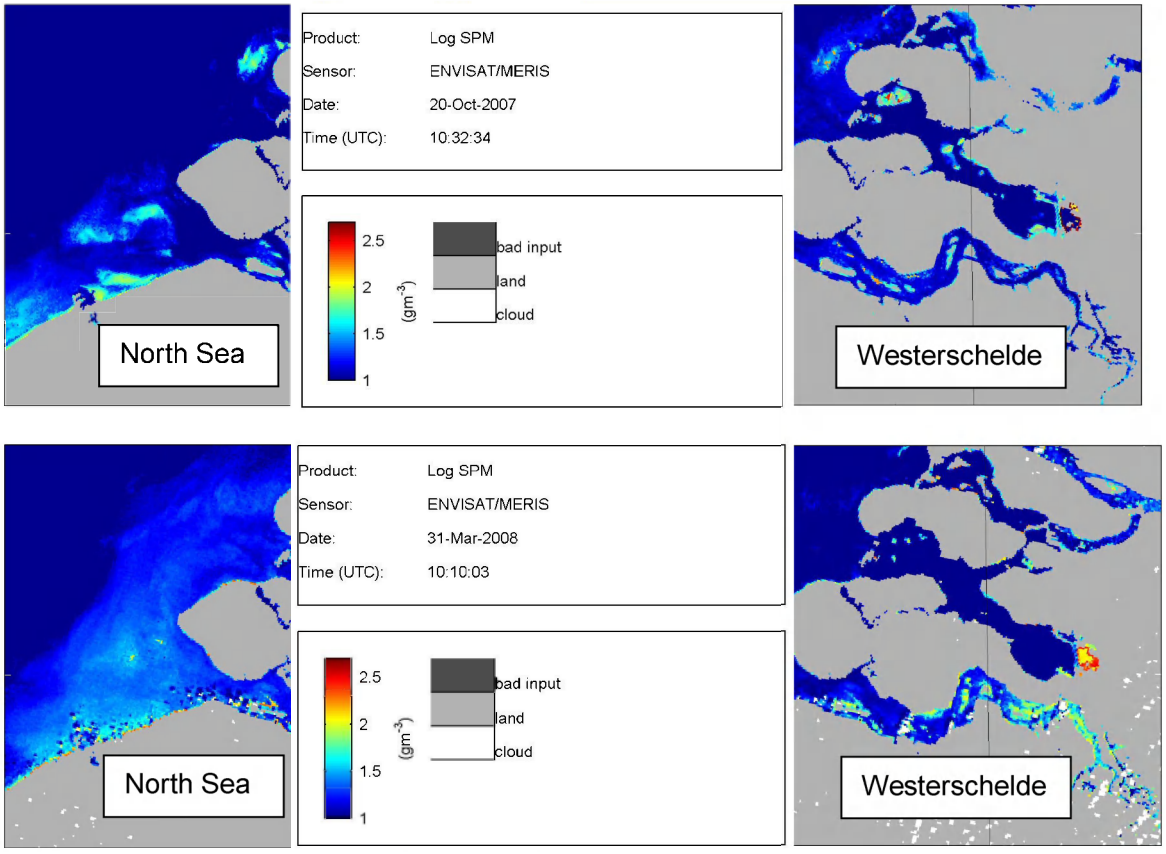

Figure 2.8 [10]logSPM products from a good image (according to ESA's quality test) of 2007 and 2008. Absorption and scattering characteristics for the North Sea (on the left hand side), and the Westerschelde (on the right hand side) had been used to process the data. Often patterns seem quite consistent, but values are lower for Westerschelde sIOPs. Be careful with values given for Oosterschelde, it needs customised processing; because sIOPs might be very different from Westerschelde. (Colour scale matched the one used in presentation of the model result, Appendix 3).

An example showing also the other parameters (CHL, CDOM, K_D) is given in Figure 2.9.

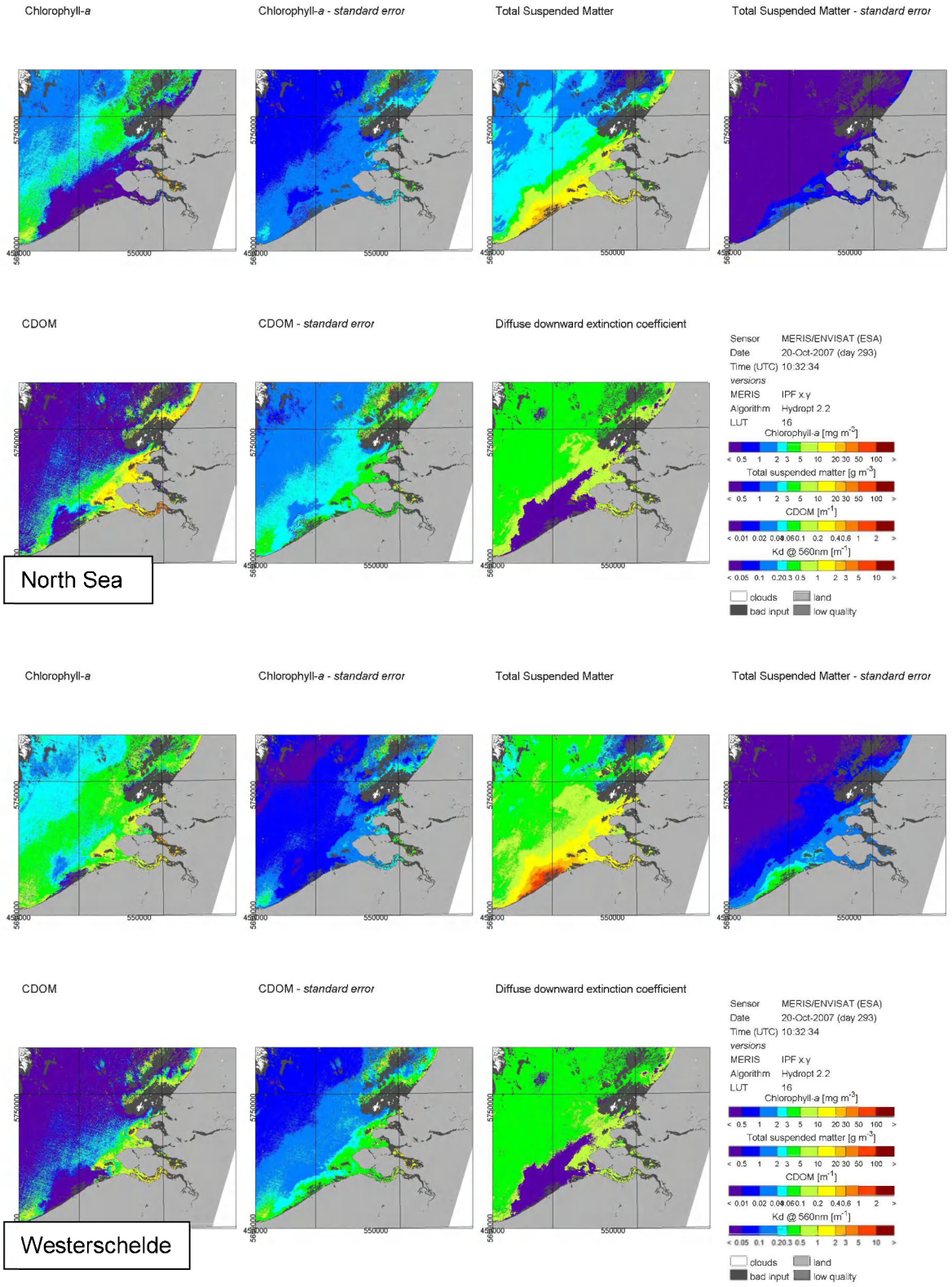

Figure 2.9 All retrieved water quality parameters and standard errors in the concentrations of the 20 Oct 2007 image. Note also the patch with low (invalid) KD560 values.

2.3.2 Time series of SPM

Figure 2.10 and Figure 2.11 show time series of SPM from remote sensing data and in situ data for the main MWTL stations. Inter-comparison of the two SPM time series shows that in situ and remote sensing SPM are often in line, although SPM at Vlissingen (VLI) seems underestimated and SPM at Schaar van Ouden Doel (SCH) seems overestimated by remote sensing. The plots also show a lack of seasonality when compared with North Sea (Eleveld et al., 2008, Figures 4-6).

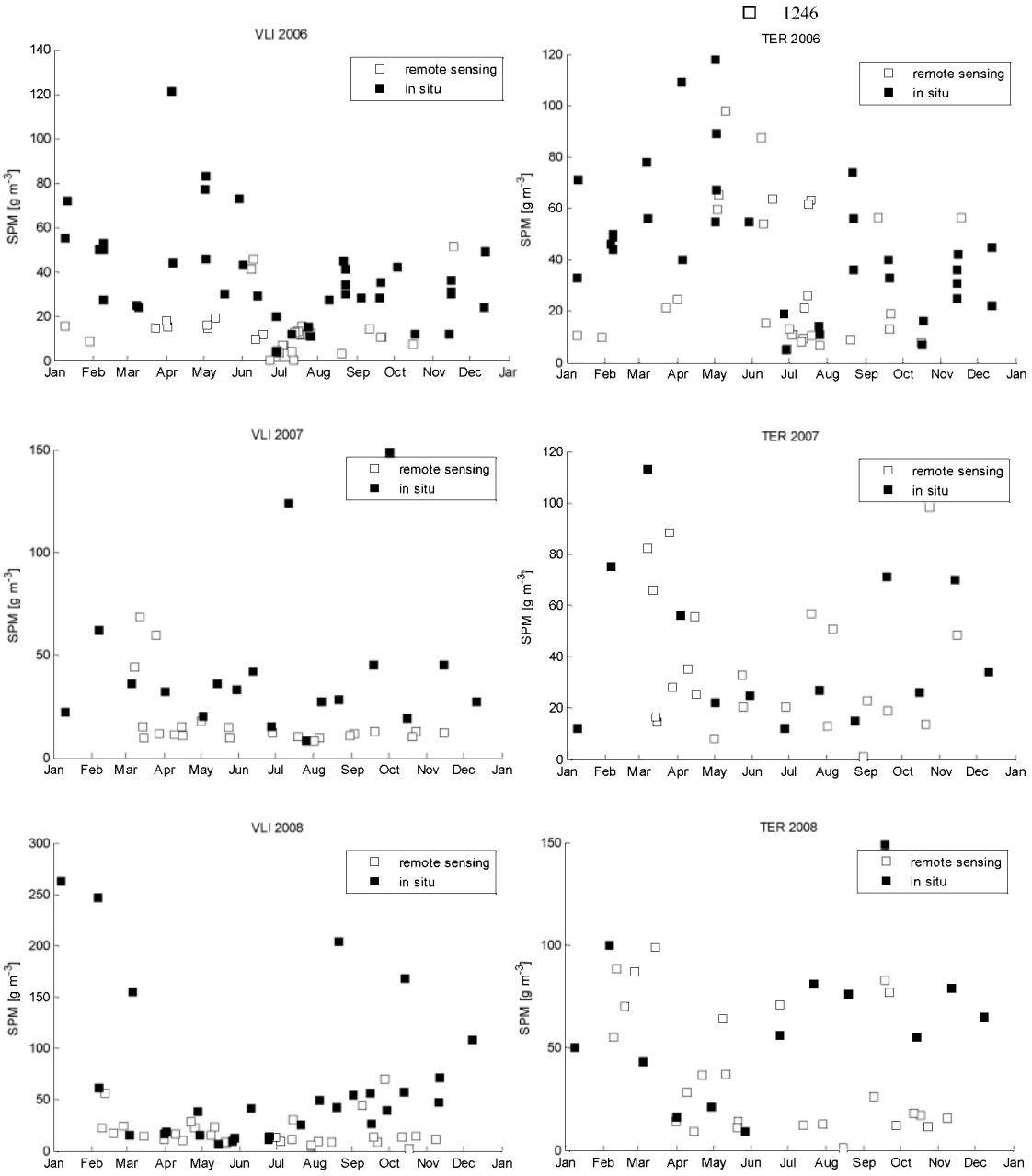

Figure 2.10 Time series of SPM from in situ measurements taken at approximately 1 m below surface (source: www.waterbase.nl) and of SPM from remote sensing (for and optical depth that can extend from a few decimetres to a few meters) confirm the large variability in SPM concentrations (All data are presented, but Y-axes scaling varies. Note the outlier in TER2006, SPM 1246 g m^{-3}).

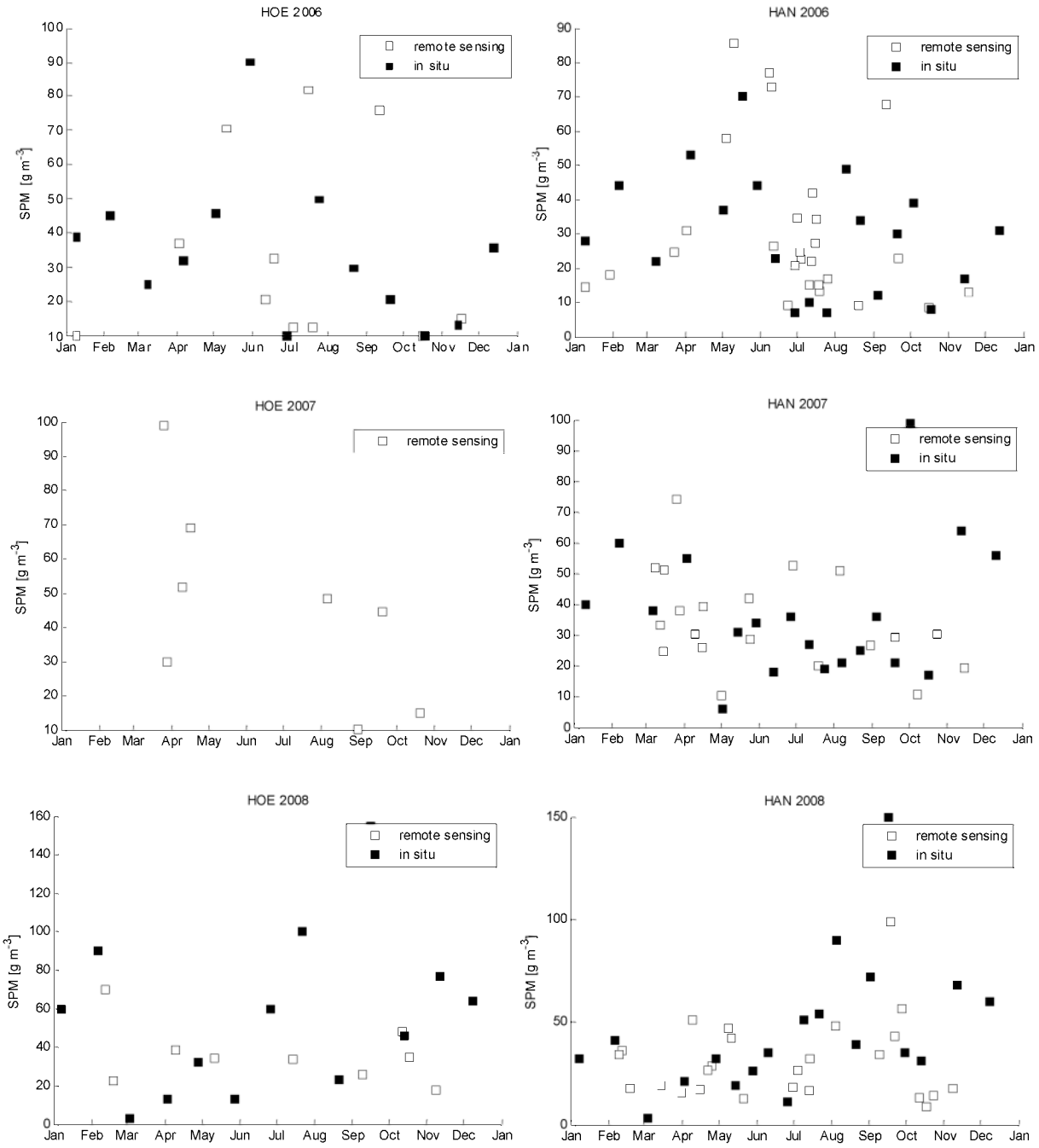

Figure 2.10 Time *series of SPM from in situ (source: [www.waterbase.nl)](http://www.waterbase.nl) and remote sensing .. (Continued)*

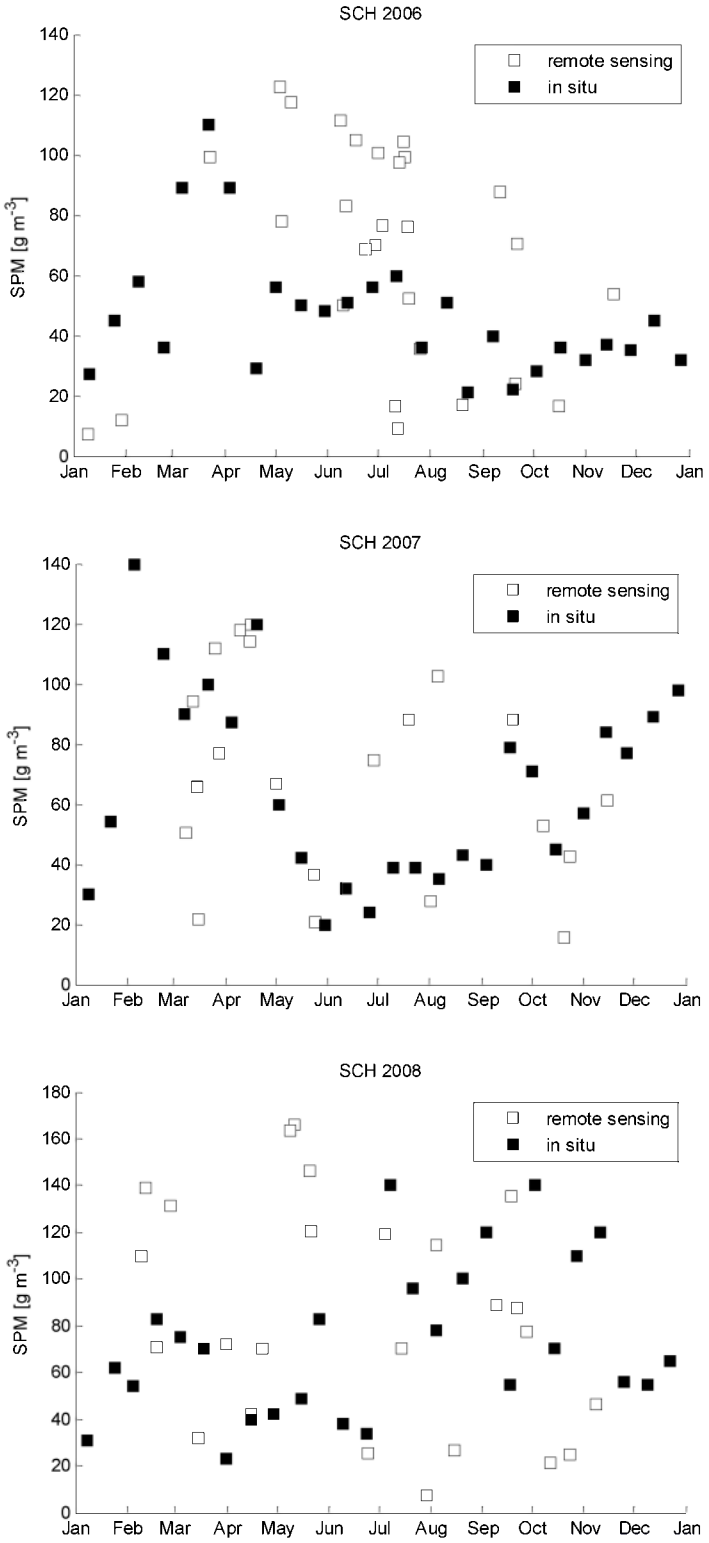

Figure 2.10 Time series of SPM from in situ (source: www.waterbase.nl) and remote sensing .. (Continued)

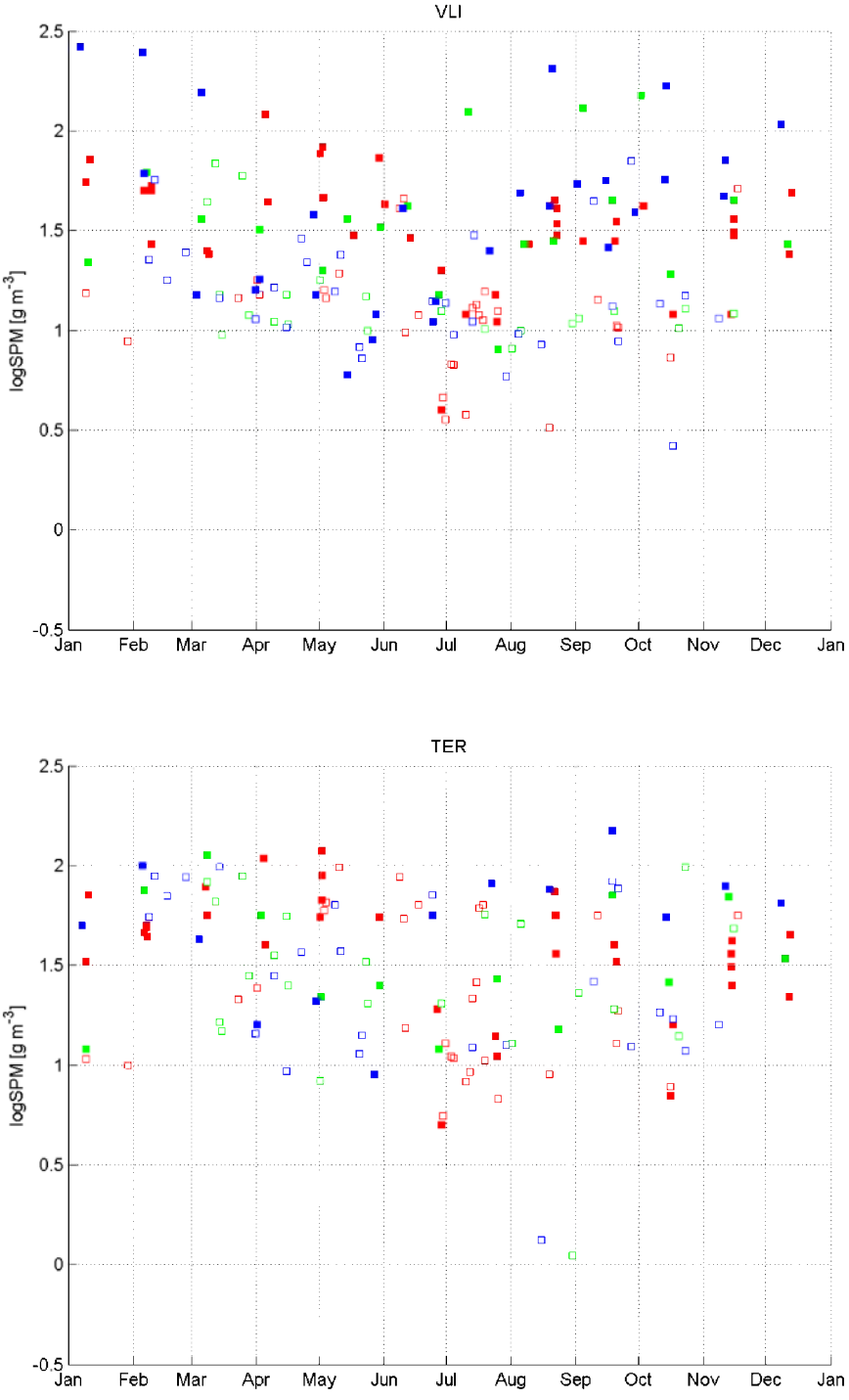

Figure 2.11 Time series (2006=red, 2007=green, and 2008 = blue) of ^{10}logSPM from in situ (filled) and from remote sensing (open). This is a different presentation of the data that were already presented Figure 10. It shows that variation in SPM from in situ and from remote sensing is large, but similar, for different years. (Y-axes scaling cut off at 0.3 and 316 g m^{-3} caused 2 outliers, one under 0.3 and one over 316, to be removed from these plots).

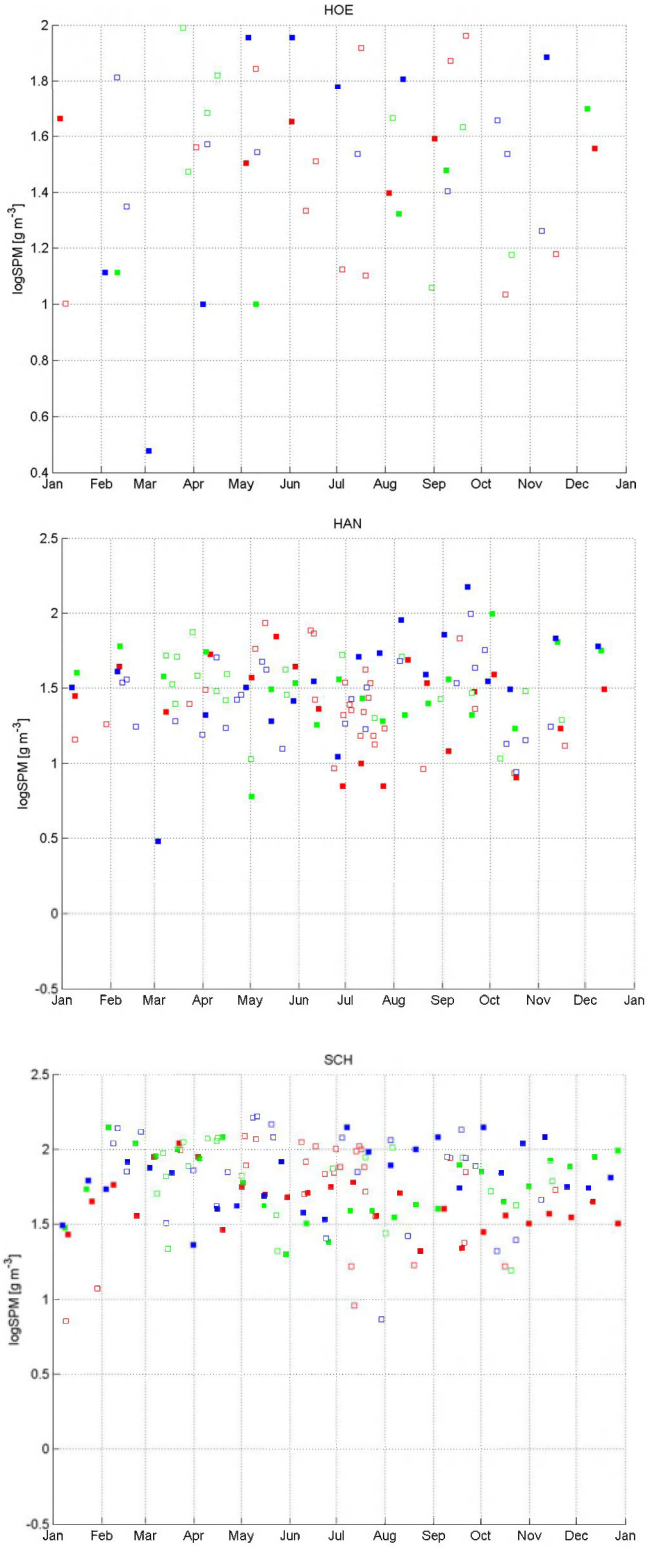

Figure 2.11 Time series (2006=red, 2007=green, and 2008 = blue) of ^{10}logSPM from in situ (filled) and from remote sensing (open) (Continued)

Figure 2.12 shows a comparison of SPM from in situ data versus SPM from remote sensing data. (Remote sensing with Original seven band settings performed similar to the other 4 parameterisations suggested in 2.1.) In this comparison averages per station are compared (Eleveld et al., 2008). There is considerable variation around the regression lines y=x. One should keep in mind that both techniques undersample the SPM variability, and might even represent a different subpopulation of the whole SPM concentration population (Blaas et al., 2007; Van der Wal et al., 2010a; Fettweis and Nechad, 2011).

Figure 2.12 also shows that usage of only absorption and scattering properties for the Westerschelde (filled black dots) caused Hansweert (and Hoedekenskerke) to be well-estimated, Vlissingen to be underestimated and Schaar van Ouden Doel to be overestimated. If absorption and scattering properties for the North Sea are used to calculate SPM concentrations from remote sensing (SPM_{rs}) for Vlissingen, then these increase (blue open circles), which results in a higher R^2 value.

In situ SPM showed no clear gradient from river to sea, which might have to do with the location of in situ points with respect to driving local sources (distance from TM Vlaamse Banken and ETM Antwerpen) and environmental factors (bathymetry). Removal of the Terneuzen 2006 in situ data outlier (see Figure 2.10) decreases SPM_{is} concentrations (blue open diamond), which results in a higher R^2 value.

MERIS imagery cannot show the full range of tidal variation in SPM concentrations, because ENVISAT is sun-synchronous and thus tides at overpass are coupled (Van der Wal et al., 2010). We can assume that SPM concentrations are influenced by tidal conditions. To match both datasets for similar tidal conditions, only the MWTL SPM measurements from 2006-2008 that occur within (9:58-10:58) the timeframe that the sensor can acquire data for this area. Together with previously mentioned improvements (North Sea optical properties for Vlissingen, and removal of one outlier for Terneuzen, this results in high R^2 values (Figure 2.12c and d).

Just for completeness, we can also look for direct match-ups between these remote sensing and in situ data sets. However, the number of in situ samples taken under favourable atmospheric conditions at overpass is usually limited. In this case, if we only look between 09:58-10:58, the min and max time bounds of an overpass, there are only two. For Hoedekenskerke at 9 Jan 2006 SPM in situ at 09:59 is 39 g m^{-3} and SPM from remote sensing at 10:30 UTC is 10 g m^{-3}; for Schaar van Ouden Doel at 4 Aug 2008 SPM in situ at 10:44 is 78 g m^{-3} and SPM from remote sensing at 10:50 UTC is 115 g m^{-3}. In such an analysis, we severely under-sample natural SPM variability and do not benefit from all available data, nor from incorporating knowledge about variance in the (geometric mean) models to relate measurements at different scales (Eleveld et al., 2008).

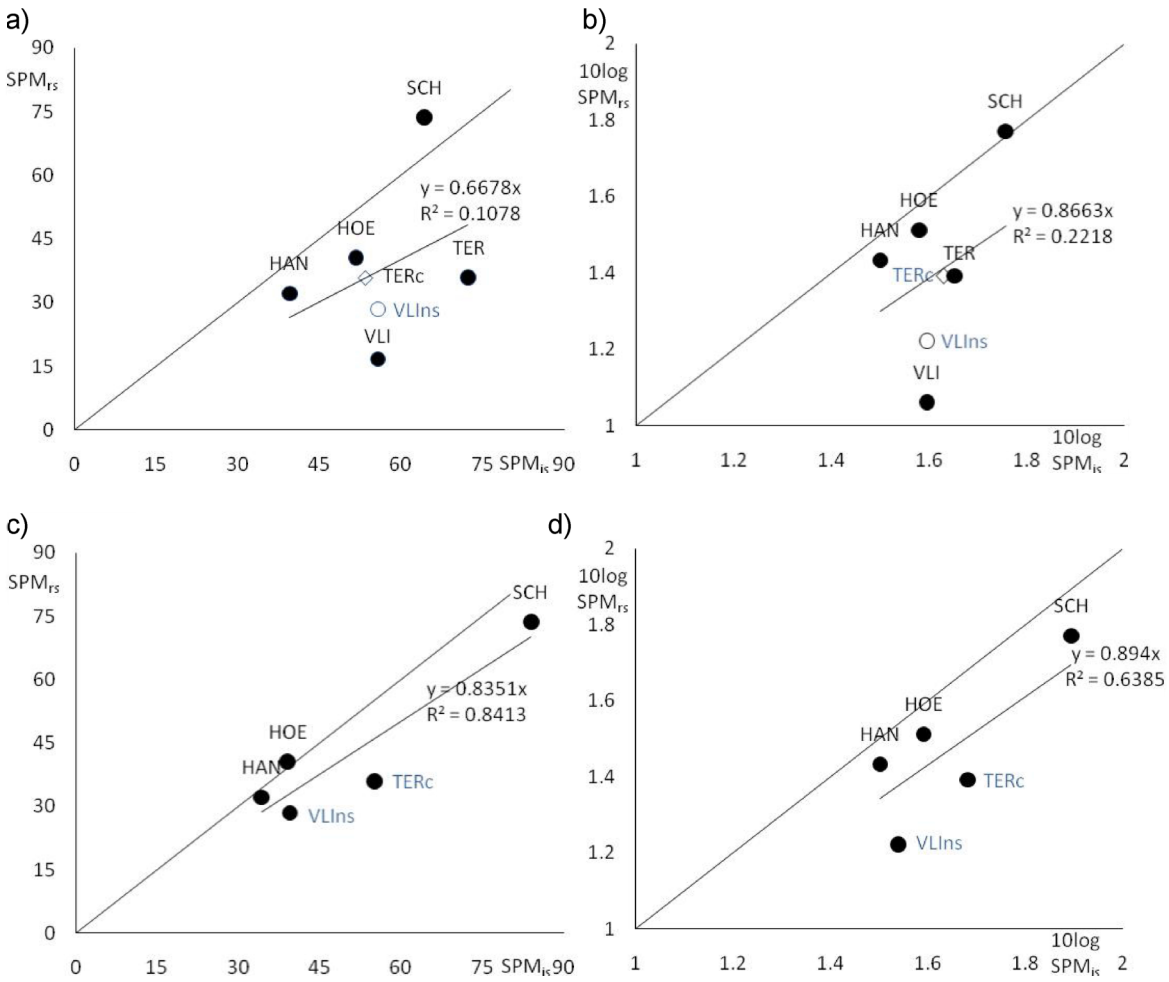

Figure 2.12 a) Mean in situ versus mean remote sensing, and b) geometric mean in situ versus geometric mean remote sensing using all in situ MWTL SPM measurements from 2006-2008, and all SPM retrieved from remote sensing from 2006-2008 (i.e that data presented in Figure 2.10 and Figure 2.11). The R-squares indicate that there is considerable variation around the regression lines y=x. The slope shows that there is an overall underestimation of SPM from remote sensing relative to in situ SPM. (The blue open circle and diamond were later added to show the effects of using Vlissingen North Sea sIOPs and removing the TER2006 in situ outlier. With these corrections in the regressions would give y=0.81x, and R^2=0.40 for the linear, and y=0.91x and R^2=0.37 for the log transformed regression respectively.)

c) Mean in situ versus mean remote sensing, and d) geometric mean in situ versus geometric mean remote sensing for MWTL SPM measurements from 2006-2008 that occur within (9:58-10:58) the timeframe that the sensor can acquire data for this area. Previously mentioned improvements for Vlissingen, and removal of the TER2006 in situ outlier are now also incorporated. R-squares increase considerably; note however that these are now based on a limited number (n) of in situ measurements (n_{VLI}= 7; n_{TER}=5; n_{HOE}=1; n_{HAN}=4; n_{SCH}=13).

Test cases Zeebrugge Harbour, and Zeeschelde near Antwerp

Figure 2.13 and Figure 2.14 show time series of SPM from remote sensing data and from in situ data for a selection of Belgian (MUMM) stations around the Harbour of Zeebrugge, and in the Zeeschelde.

2006

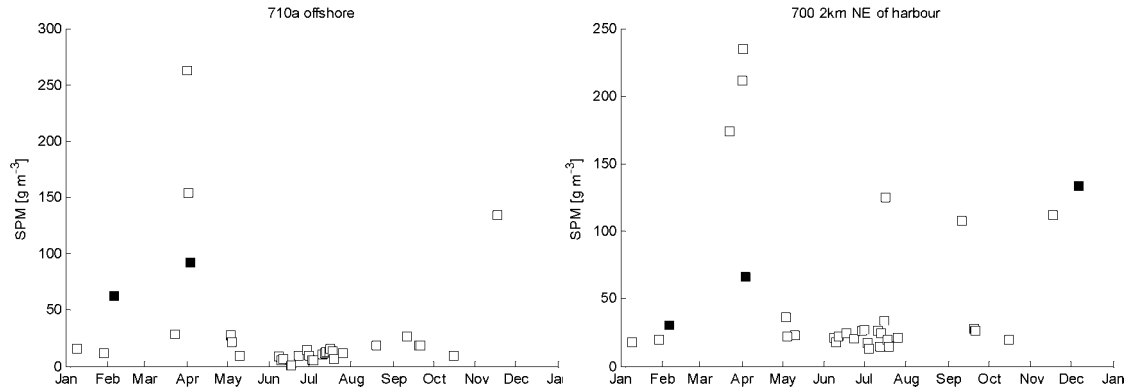

2007

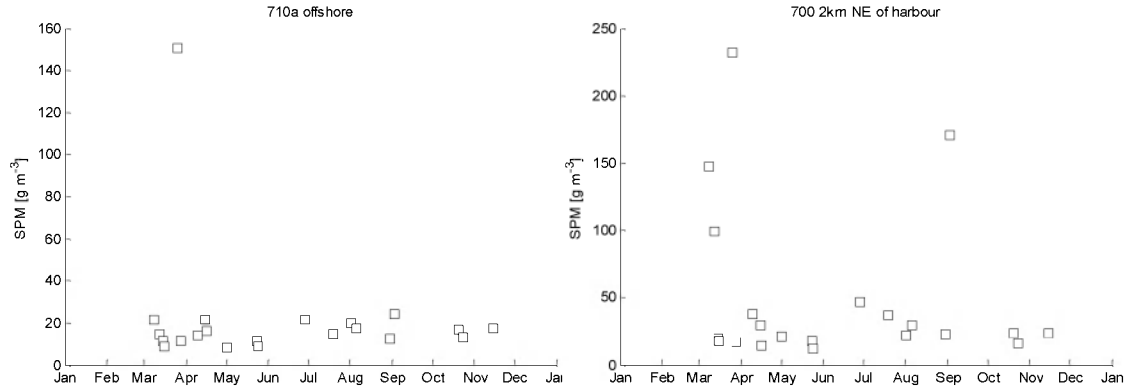

2008

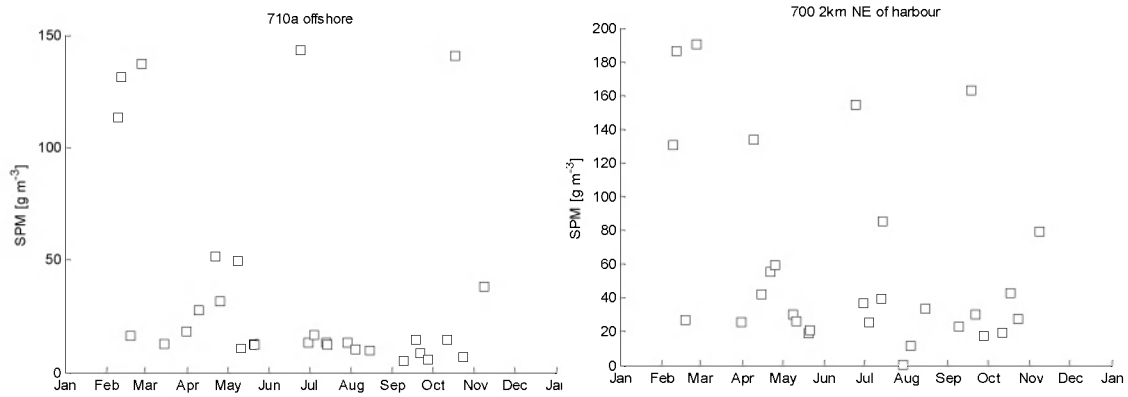

Figure 2.13 Time-series of SPM from in situ (filled squares, source: MUMM) and from remote sensing (open) for Zeebrugge, a station further offshore, and (arguably) an up- and downstream station with respect to the residual sediment flux. (The number of in situ observations was limited.)

2006

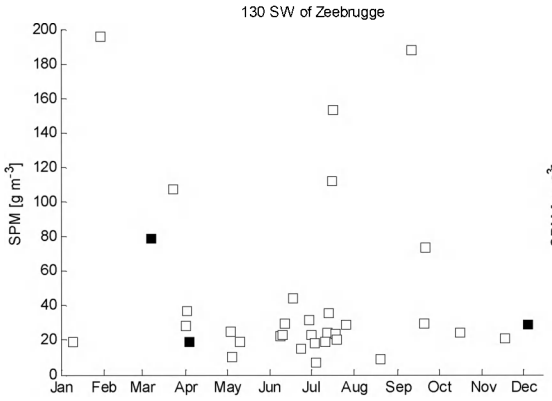

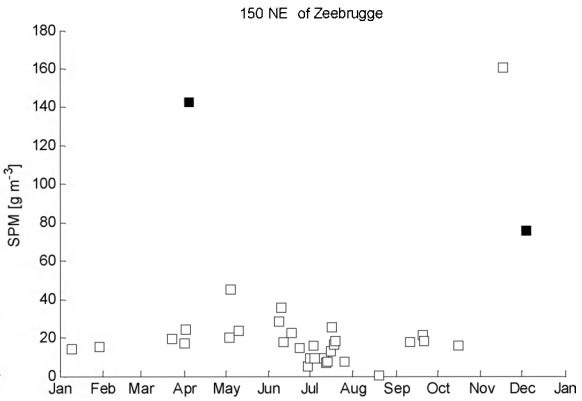

2007

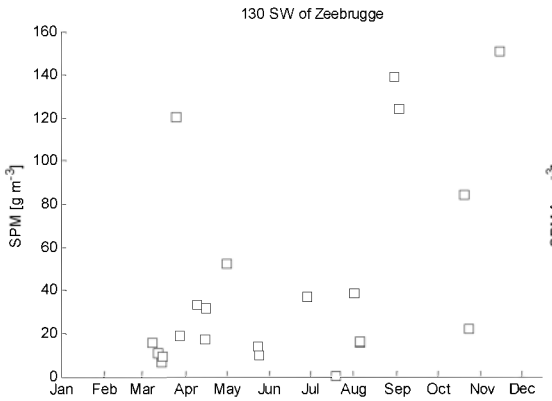

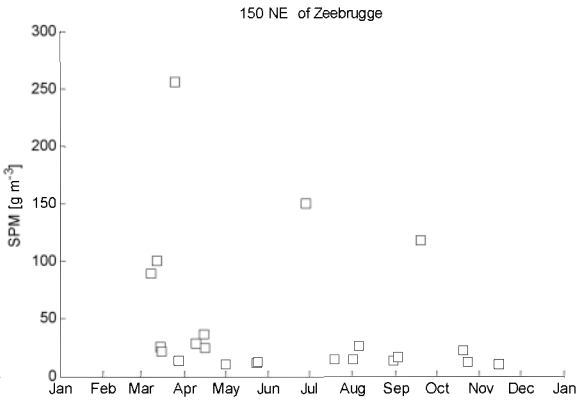

2008

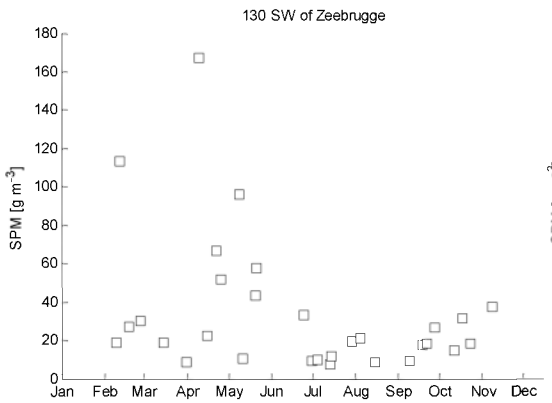

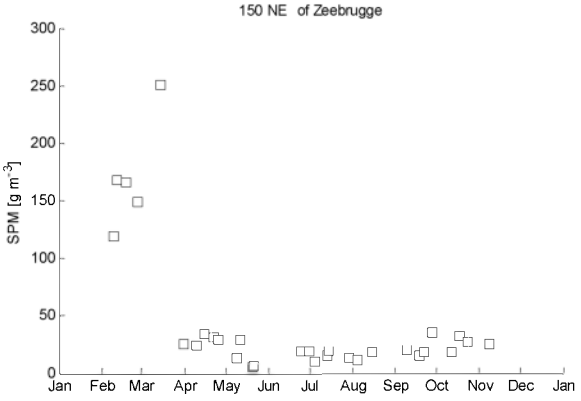

Figure 2.13 Time-series of SPM from in situ (filled) and from remote sensing (open) .(Continued)

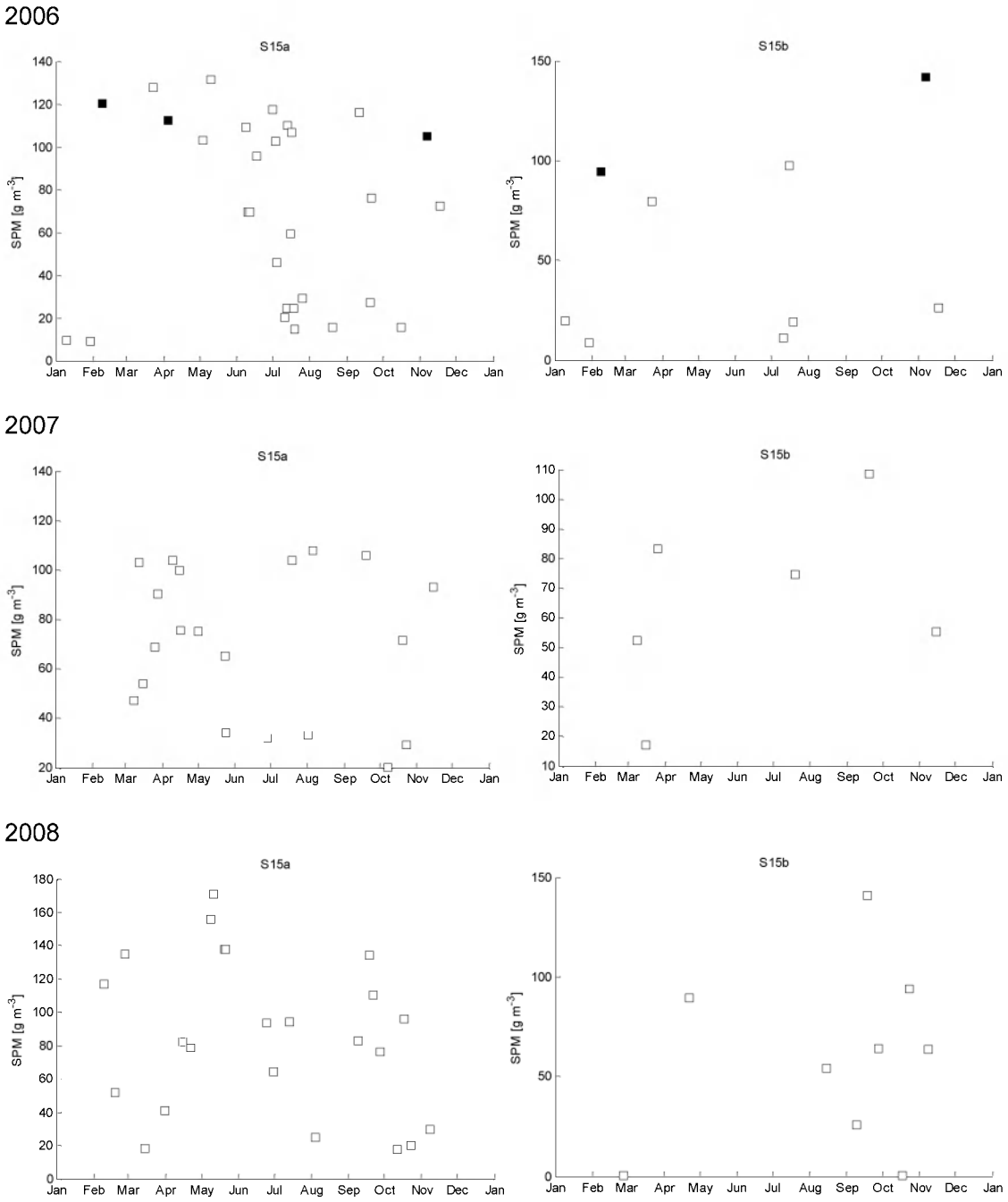

Figure 2.14 Time-series of SPM from in situ (filled squares, source: MUMM) and from remote sensing (open) going upriver on the Zeeschelde from Doel (S15) to Antwerpen –Zuidterras (S22, where the Zeeschelde becomes too narrow for accurate sampling with MERIS pixels). (The number of in situ observations was limited.)

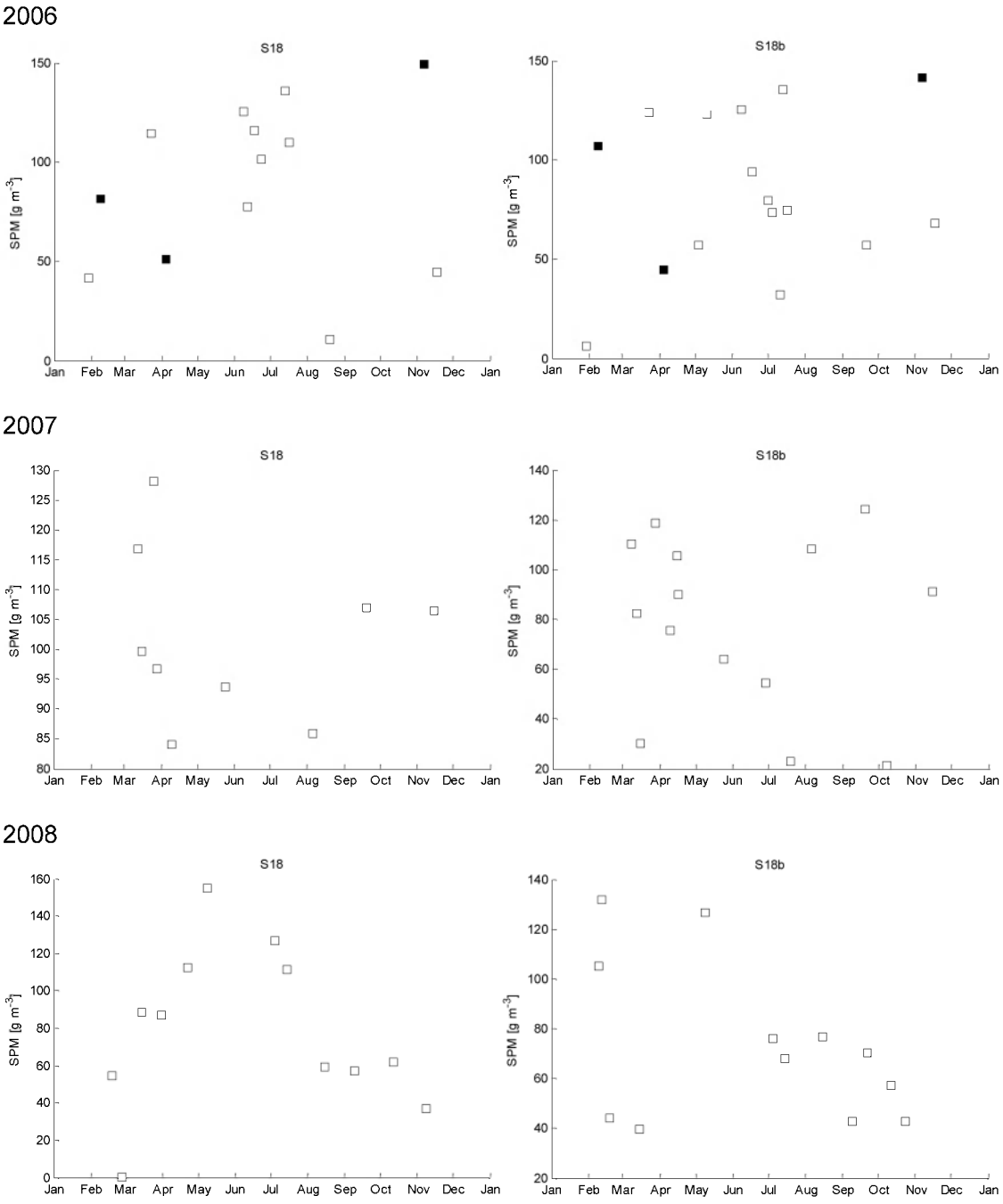

Figure 2.14 Time-series of SPM from in situ (filled) and from remote sensing (open). (Continued)

2006

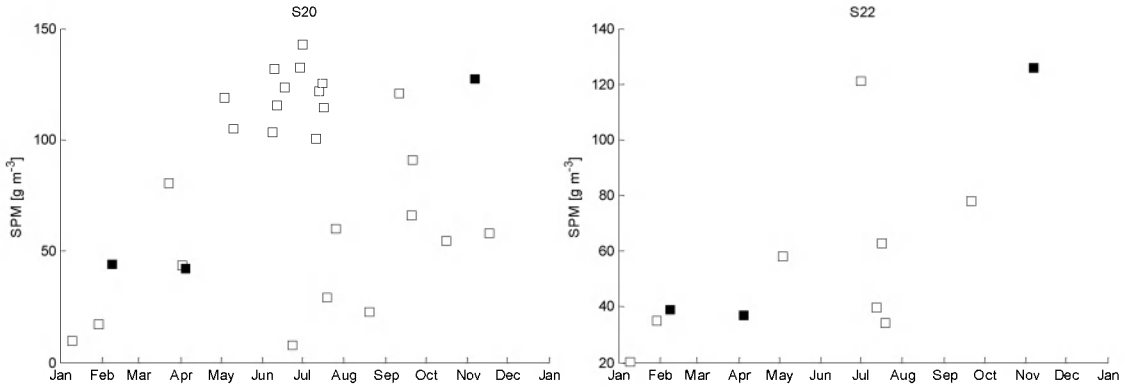

2007

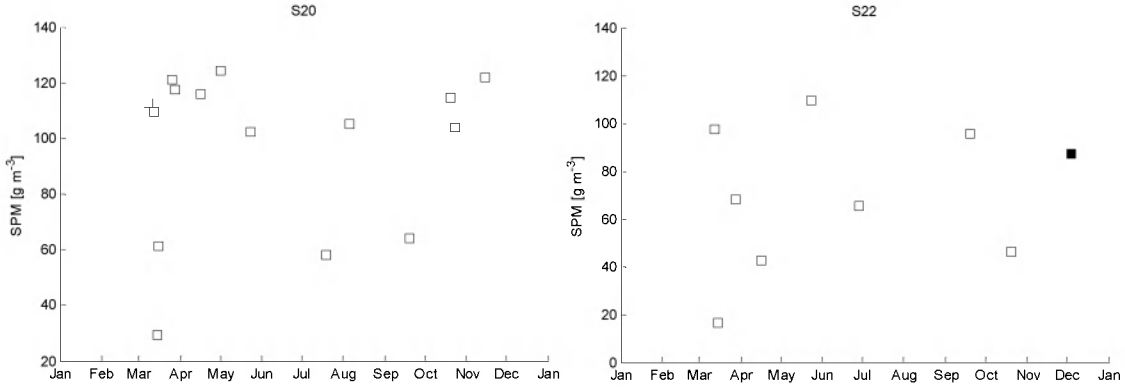

2008

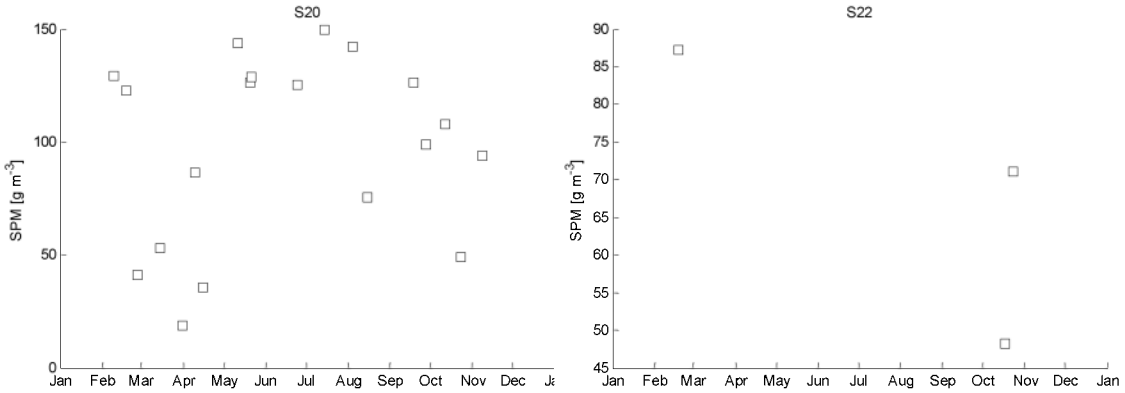

Figure 2.14 Time-series of SPM from in situ (filled) and from remote sensing (open)..(Continued)

Figure 2.13 seems to indicate that remotely sensed near-surface SPM-concentrations for the turbid Belgian coast are none-the-less frequently below 50 mg/L. Occasional higher values might indicate some seasonality in SPM concentrations, because these seem to occur less in summer. In the Zeeschelde, near the ETM (Figure 2.14) more SPM concentrations of over 50 mg/L were found. To overcome the limited number of in situ data sets for 2006-2008 we also looked at data from a longer period. Table 2.3 shows that the multi-year mean and standard deviation from in situ data, and mean and standard deviation from remote sensing data are within the same range.

Table 2.3 SPM (source MUMM)

name	in situ		SPM	SPM	SPM	SPM		remote sensing		
	date min	date max	min	max	mean	std	nr of	SPM_mean	SPM_std	nr of
			mg/l	mg/l	mg/l	mg/l	obs.	mg/l	mg/l	obs.
710_a	05-Dec-89	03-Apr-06	4.82	412.00	49.33	49.90	92	53.40	58.08	81
700	05-May-87	06-Dec-06	2.40	683.00	72.64	82.28	110	36.90	51.14	84
130	13-May-87	04-Dec-06	0.92	370.70	46.45	60.98	103	41.12	44.60	83
150	20-May-87	04-Dec-06	8.00	217.00	59.51	40.71	67	30.22	45.90	82
S15_a	01-Feb-89	06-Nov-06	16.80	274.67	93.40	54.63	89	74.20	41.22	70
S15b	20-May-87	06-Nov-06	18.90	430.00	133.31	90.38	76	53.83	39.30	22
S18	19-May-87	06-Nov-06	10.40	238.00	99.97	60.28	96	88.51	36.06	32
S18b	20-May-87	06-Nov-06	16.10	311.00	102.78	62.37	71	78.46	34.68	40
S20	13-Feb-96	06-Nov-06	15.20	363.00	84.31	68.65	42	91.94	39.03	60
S22	19-May-87	04-Dec-07	12.50	300.16	68.55	50.36	102	63.01	29.68	19

2.3.3 SPM composites

The 84 images that had been collected for the years 2006 – 2008 (Appendix A.1) were sorted into the classes Low Water (-6.1..-4.5, +4.5..+6.1 h HW HAN), INcoming (flood, -4.5..-1.5), High Water (-1.5..+1.5) and OUTgoing (ebb, +1.5..+4.5) to form semi-diurnal composites of tidal stage in hours before (-), or after (+) HW Hansweert (a mid-estuary station representative for the entire Westerschelde). Figure 2.15 shows how the 84 MERIS datasets are distributed over these classes of semi-diurnal composites. There is a slight over-representation of images that fall in the low water (LW) class, 29 datasets.

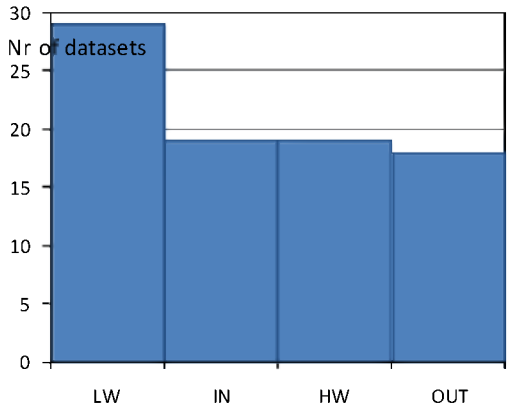

Figure 2.15 The distribution of unclouded MERIS datasets for classes of semi-diurnal composites for the entire period 2006-2008. (See Table 2.1 for classes.)

The resulting composite maps in Figure 2.18 and Figure 2.19 show that concentrations decrease gradually towards the sea. The LW composite shows high SPM (> 30 g m^{-3}) throughout the estuary except at the mouth. Flood (INcomming North Sea water) shows low concentrations in the channels, and enables a clear distinction between channels and flats. HW features low concentrations at surface (< 30 g m^{-3}) until Saeftinge. This is in accordance with in situ results (Van der Wal et al., 2010a, Fig. 7c) and seems to make sense when the length of the water column is seen as distance to bed (a source). At ebb (OUTgoing estuarine water) high concentrations (> 30 g m^{-3}) occur throughout, obscuring the distinction between channels and flat, except at the mouth of the estuary.

Figure 2.18a shows average values of about 50-60 g m^{-3} for the ETM near Antwerpen at HW at Hansweert (48 min before HW Antwerpen). Sterckx et al. (2007) also present two maps that fall in the class HW (at Hansweert) with centre channel values near Antwerpen that vary between 66-81 g m^{-3} and 36-44 g m^{-3} (of Figs 6a and b respectively). For OUTgoing tide Fig 6c (in Sterckx et al., 2007) shows a steep gradient from 36 (outer bight) to 150 g m^{-3} (in the inner bight). Because of the lower resolution, such gradients were less obvious in the current study.

Next the 84 images were sorted into the classes Neap, Neap to mean, Mean to spring, and Spring (see Table 2.2) for creation of composites of the fortnightly tidal stage. Figure 2.16 shows how the 84 MERIS datasets are distributed. Figure 2.16 shows that spring tide is overrepresented in the neap-spring composites.

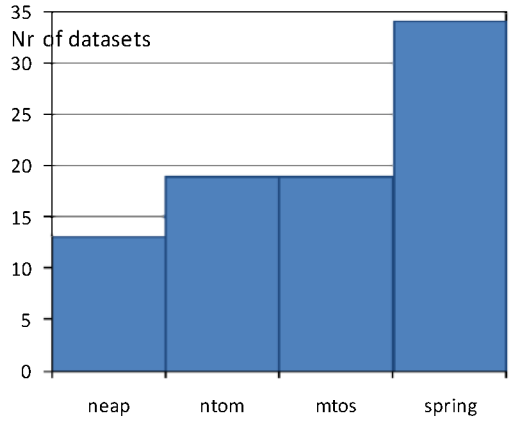

Figure 2.16 The distribution of unclouded MERIS datasets for classes of spring tide fractions (for the entire period 2006-2008). (The class ntom indicates neap to mean, mtos is mean to spring.)

Figure 2.20 and Figure 2.21 show highest concentrations at spring and mean to spring, followed by neap to mean, and lowest surface SPM concentrations were registered at neap. This was to be expected, as there is more water volume exchange, stronger currents occur at spring than at neap, which would than result in higher surface SPM concentrations. However, this is also enhanced because image acquisitions only sample co-occurrences of LW at spring and HW at neap (Van der Wal et al., 2010a p.526 and Fig. 8).

Seasonal SPM composites that were expected to represent wind-forcing (to a certain extent) were based on winter (DJF), spring (MAM), summer (JJA), and autumn (SON). Figure 2.17 shows the distribution of images for the over the entire period (2006-2008) over the months. There are more summer than winter images available, and there are no unclouded Dec. data. High winds and high SPM concentrations are perhaps under-sampled if cloud cover is

somewhat related to frontal passages that correlate with high wind. In situ SPM are also under-sampled during stormy conditions when the ships are not allowed to sail. Additional analysis showed that each year (2006, 2007 and 2008) had prolonged periods of unclouded conditions in different months. In 2006, 7 relatively unclouded MERIS images were available for June and 10 for July. In 2007, 6 images were available for March, whereas in 2008 there was a more or less equal distribution (but without images for Jan. and Dec.).

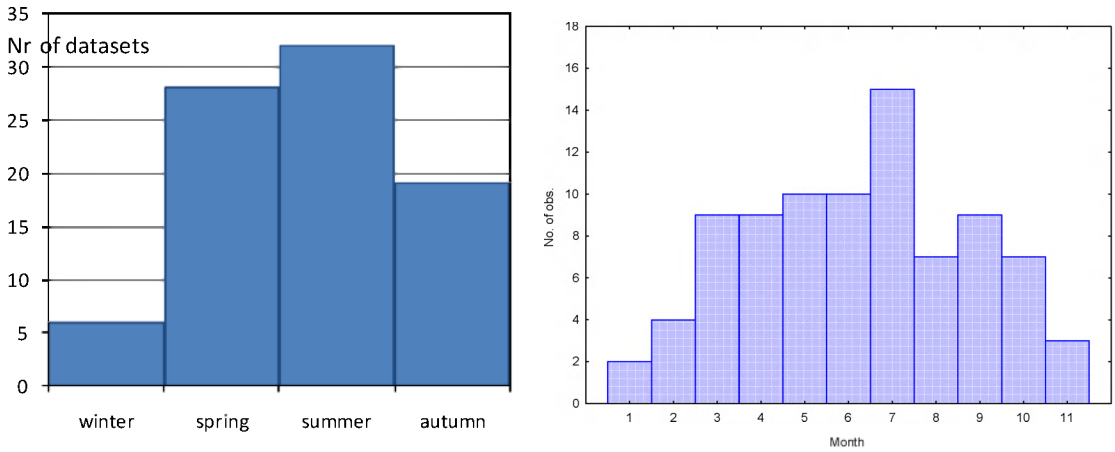

Figure 2.17 The distribution of unclouded MERIS datasets a) per season and b) month (for the entire period 2006-2008).

Figure 2.22 and Figure 2.23 show relatively high concentrations in winter, but this number is based on a limited number of samples, followed by moderate concentrations spring. Lowest concentrations occur in summer, and in autumn concentrations are increasing again. This is what can be expected, but was at first sight less evident from the SPM concentrations at the stations (see Figure 2.10 and Figure 2.11) on which SPM from remote sensing seemed to show little seasonality. This was also true for in situ SPM. Please note, however, that longer term (1995-20007) in situ SPM at stations does show seasonal variation van der Wal *et al.* (2010a, Fig 7a).

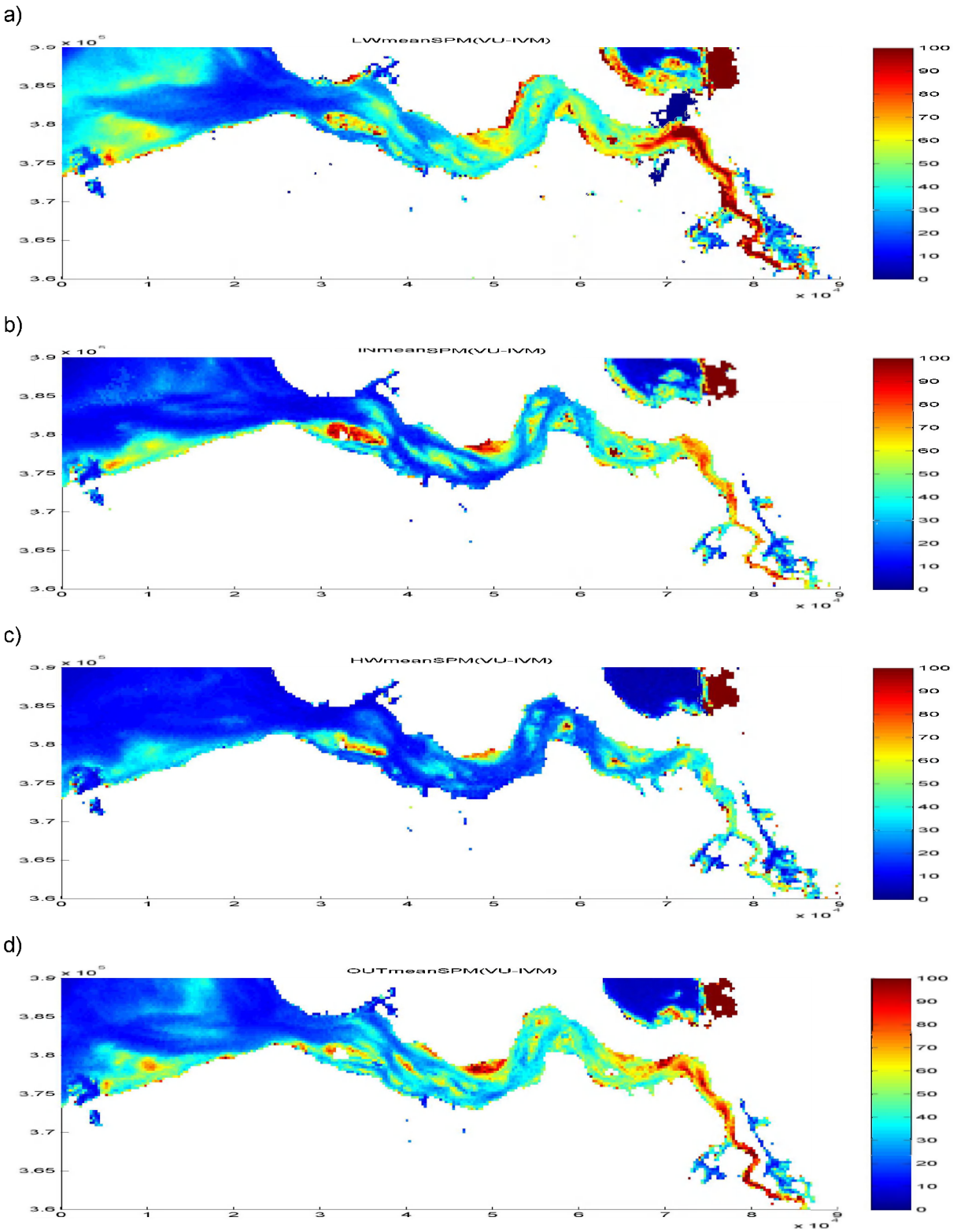

Figure 2.18 Semi-diurnal means for: a) LW (-6.1..-4.5, 4.5..+6.1), b) INcoming (-4.5..-1.5), c) HW (-1.5..+1.5), d) OUTgoing (+1.5..+4.5). A land flag should still be applied to distinguish land from sea.

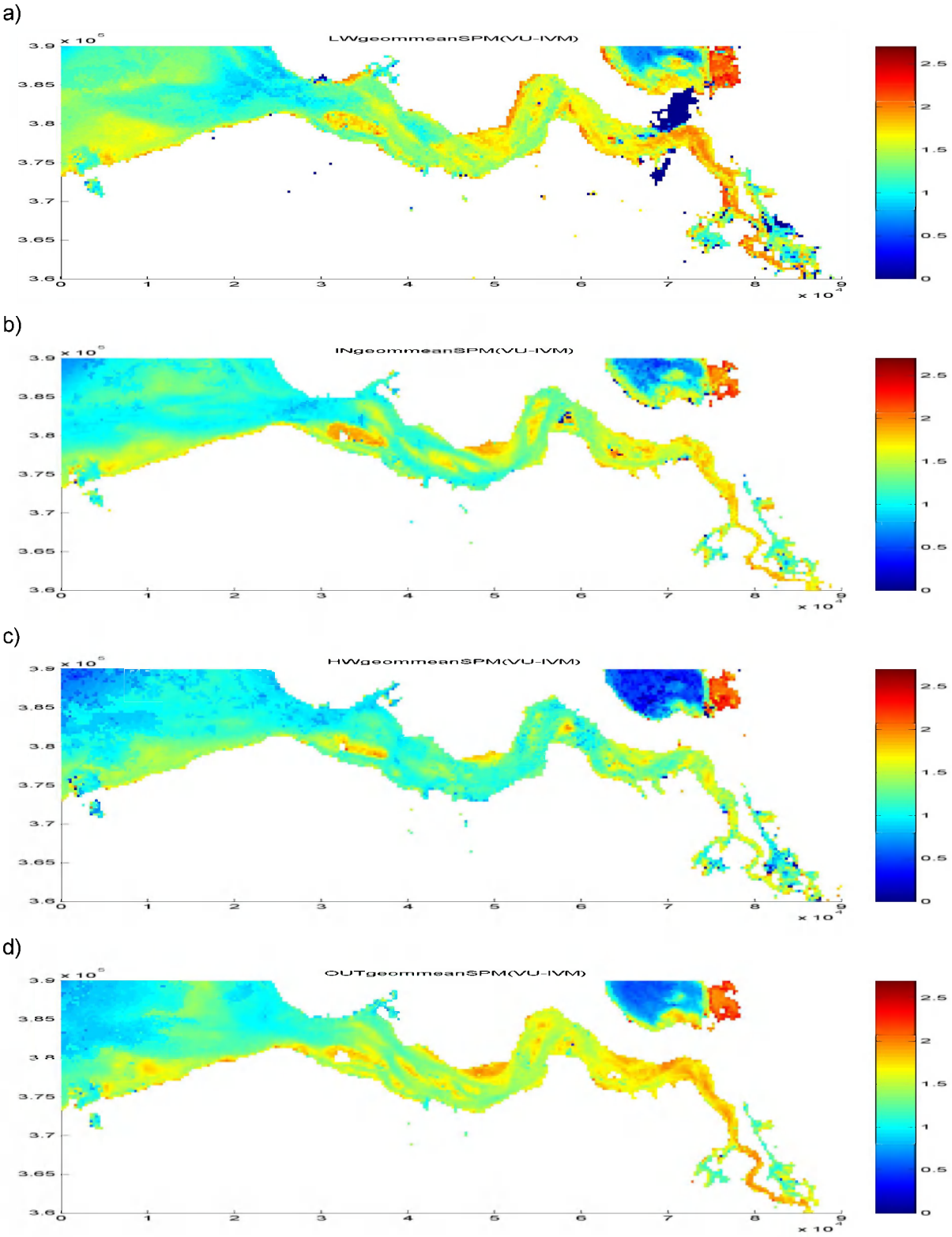

Figure 2.19 Semi-diurnal geometric means for: a) LW (-6.1..-4.5, 4.5..+6.1), b) INcoming (-4.5..-1.5), c) HW (-1.5..+1.5), d) OUTgoing (+1.5..+4.5).

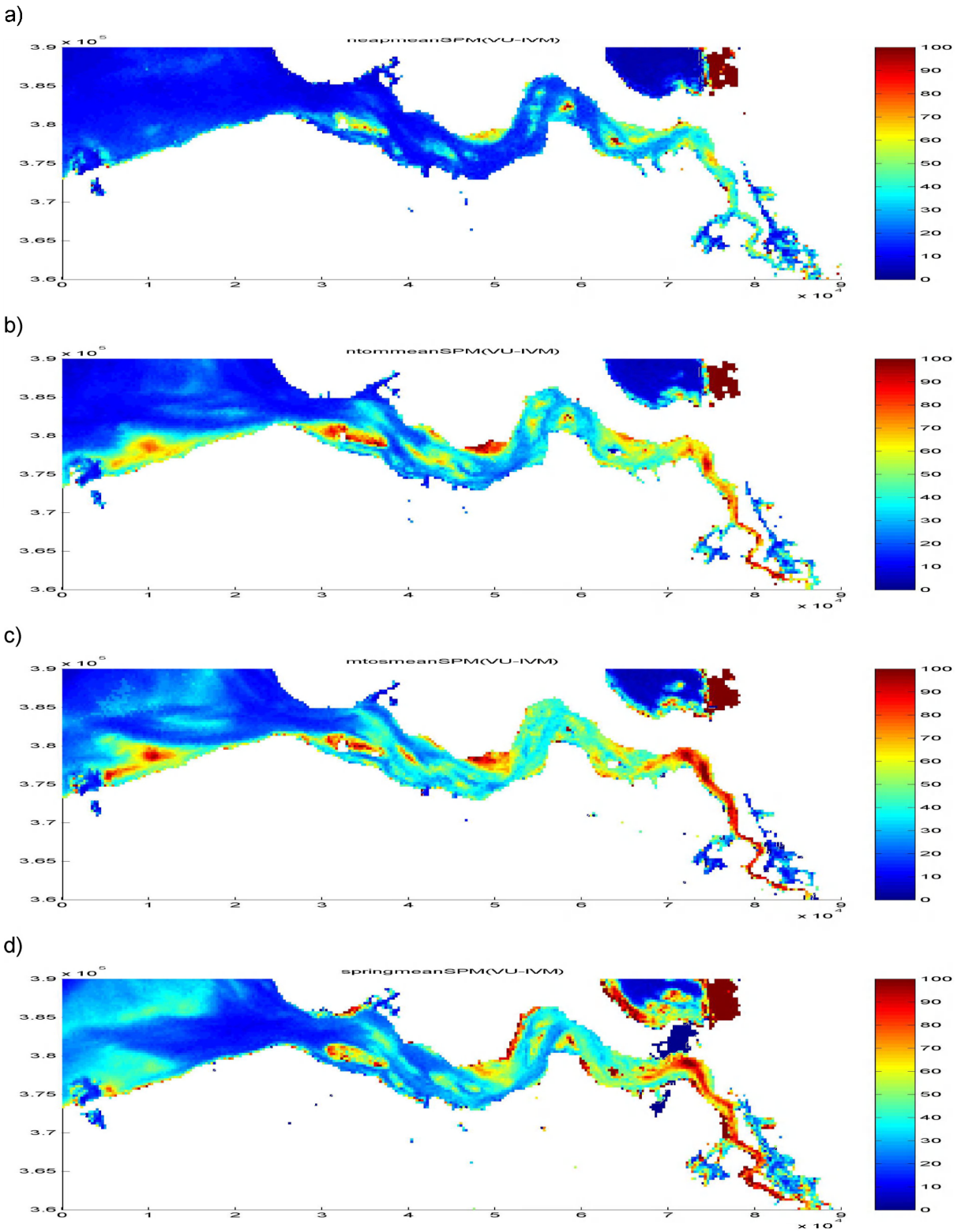

Figure 2.20 Fortnightly means for: a) Neap (0 .. 0.25), b) Neap to mean (0.25 .. 0.5), c) Mean to spring (0.5 .. 0.75), d) Spring (0.75 .. 1).

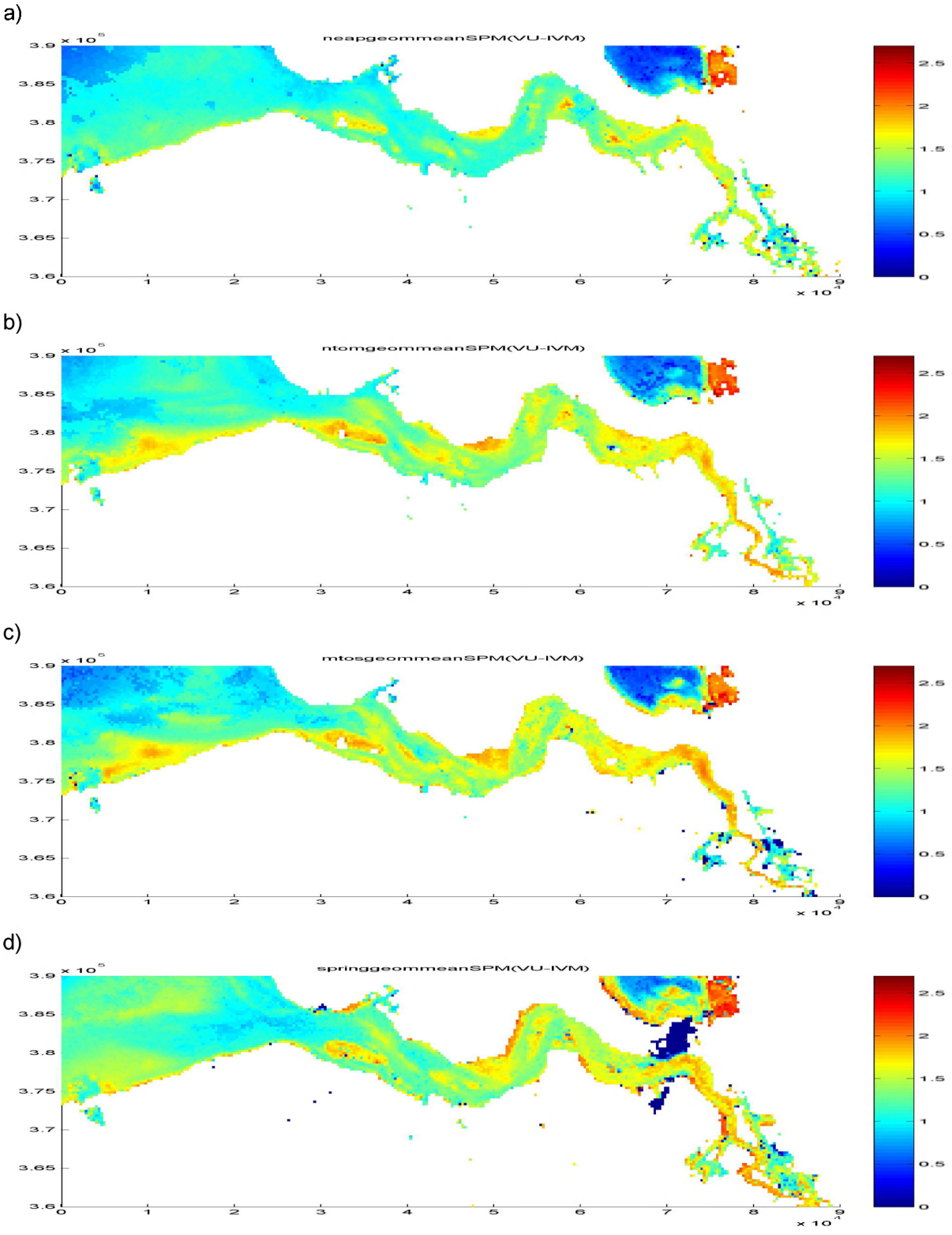

Figure 2.21 Fortnightly geometric means for: a) Neap (0 .. 0.25), b) Neap to mean (0.25 .. 0.5), c) Mean to spring (0.5 .. 0.75), d) Spring (0.75 .. 1).

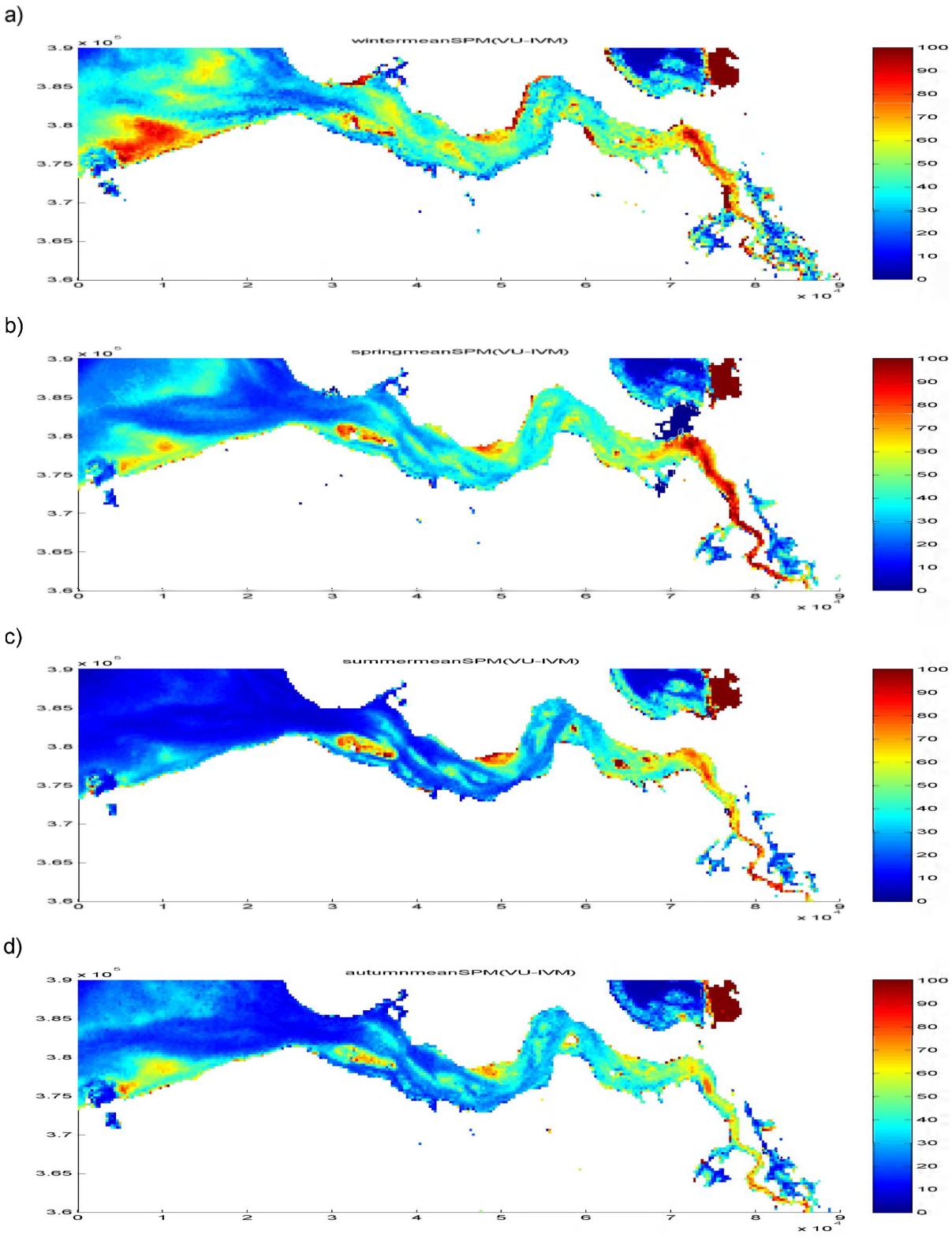

Figure 2.22 The seasonal means for: a) winter, b) spring, c) summer, d) autumn.

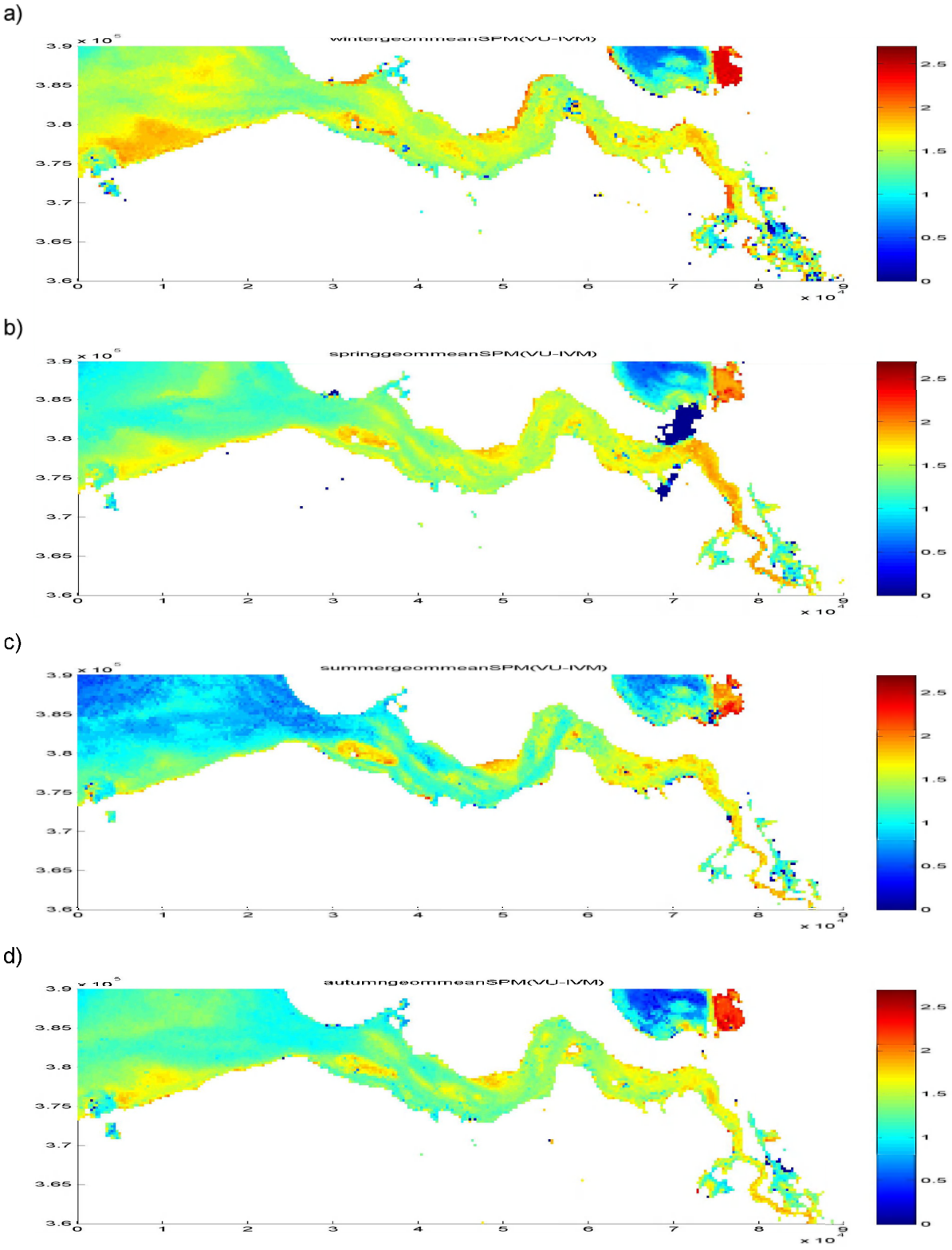

Figure 2.23 The seasonal geometric means for: a) winter, b) spring, c) summer, d) autumn.

2.4 Discussion and conclusions

The adaptations to the parameterisation of Hydropt (Section 2.2.1) were a first sensitivity test for Hydropt. The adaptations have not led to an evident improvement of the optical water quality products (Section 2.3.1). Visual comparison of the results (results from all parameterisations for three example images in Appendix A.2) shows that the differences between the images are much larger than the differences in results from processing with different settings. This seems to confirm that driving processes and environmental conditions have an important impact on surface SPM concentrations (Van der Wal et al., 2010a) and also illustrates that the algorithm is quite robust.

It was feasible to produce a larger dataset and longer time-series of products. Note, however, that the temporal remote sensing data density is low (and for the estuary similar to the in situ data density, cf. Fig 10) compared to the output that can be generated with models. Nonetheless, it enabled validation (inter-comparison) and construction of composites. Usage of one set of absorption and scattering characteristics for the Westerschelde causes SPM at Hansweert (and Hoedekenskerke) to be well-estimated, Vlissingen to be underestimated and Schaar van Ouden Doel to be overestimated. When optical properties of the North Sea are used, this somewhat increased the remotely sensed SPM concentrations for Vlissingen (Figure 2.12). SPM showed no clear gradient from river to sea, which might have to do with the location of the MWTL in situ points with respect to local sources (distance from TM Vlaamse Banken and ETM Antwerpen) and local environmental factors (bathymetry).

Both model output and SPM from remote sensing provide spatially rich data sets, but the latter have seasonal and tidal sampling biases. Due to cloud cover, not all satellite passes yield usable images: there are few good winter images available. Due to sun-synchronous satellite overpass, the sensor samples at co-occurring semi-diurnal and spring-neap tidal stages: for the Westerschelde, LW at spring, and HW at neap (Van der Wal et al., 2010a). Finally, the actual spatio-temporal variability in material properties was not fully covered in the retrieval of SPM from reflectance, if one mean sIOP set for the Westerschelde was used.

Subsequently, information on spatial patterns of estuarine dynamics has been produced by creating composites that capture characteristic timescales for driving forces (Section 2.3.3). On a semi-diurnal scale, high concentrations occur at low water and at ebb (outgoing) stage, followed by flood (incoming), and lowest concentrations occur at high water. On a fortnightly scale, highest concentrations occur at spring and mean to spring, followed by neap to mean, and neap. On a seasonal scale, highest concentrations occur in winter, followed by spring, autumn, and summer.

The method may still be improved by also creating classes based on tidal currents instead of tidal levels, and extended, e.g. by creating also classes based on discharge. Discharge is also useful to track movement of the ETM in the Zeeschelde. Further elaboration might lead to a better description of mechanisms and perhaps causal relationships (see e.g. Pietrzak et al., 2011 for the North Sea).

2.5 Recommendations

Composites can provide information about concentration distributions for every location for e.g. spring tide. These can subsequently be used when evaluating impacts from dredging or dumping on SPM (Grasmeijer and Eleveld, 2009) under certain conditions, or in other scenario studies.

Patterns in Suspended Particulate Matter (SPM) concentrations, and K_D could unveil important information about estuarine gradients and their environmental effects for LTV ecology. This would still require some research effort as for instance, regressions for CHL (not presented) indicate that the current atmospheric correction of the MERIS level-2 data seems inappropriate for determination of estuarine CHL concentrations. Perhaps this improves with the Third Reprocessing of the MERIS archives.

Acknowledgements
The European Space Agency (ESA) provided MERIS-FR data within ESA Cat-1 project 4453. Reinold Pasterkamp is acknowledged for the HYDROPT Software library. Rijkswaterstaat is acknowledged for the Waterbase data, MUMM for the Belgian in situ data.

3 Remote sensing of tidal flats in the Westerschelde

3.1 Introduction

On intertidal flats, the satellite radar (ERS SAR) backscatter signal is sensitive to surface roughness and can therefore be used to map bed roughness. As a relationship between mud content and bed roughness can be assumed (with surface ripples being more pronounced in sand than in mud), the backscatter signal from satellite radar can also be used to map mud content of the sediment. Both bed composition and mud content were derived for 2006 from ERS SAR in a previous (pilot) stage of the project (Van Kessel et al., 2008). The use of optical remote sensing (Landsat TM/ETM+) to derive information on surface characteristics of intertidal flats did not yield good results in the pilot study.
The objective of this stage of the project is to derive information from both radar and optical satellite remote sensing for the period 2006-2008. In this phase of the project, field spectra and matching samples (Section 2) were analysed to gain insight in the information that can be extracted from optical remote sensing (Section 3), which may result in a better use of optical satellite data to complement the radar data (Sections 4 and 5). In addition, mud content (Section 5) and surface roughness (Section 6) will be derived from radar remote sensing in the same way as in the pilot study.

3.2 Field spectra and sampling

Between 2003 and 2008, NIOO collected ca 1000 calibrated ground reflectance spectra of intertidal flats of the Westerschelde with a hyperspectral TRIOS Ramses radiometer (see Van der Wal & Herman, 2007 for details of spectra acquisition and processing). The data cover the visible and near-infrared range of the electromagnetic spectrum in narrow spectral bands. In the current project, the spectra have also been resampled to simulate the broader Landsat TM bands, including band 1 (blue), band 2 (green), band 3 (red) and band 4 (near-infrared). No information was available to simulate Landsat TM band 5 and 7 (shortwave infrared) or band 6 (thermal).

From photographs of the measuring sites, an estimate was made of the percentage of surface water, and the percentage cover of macrophytes, including macroalgae and vascular plants.

Simultaneously to the spectral measurements, samples were taken of the upper 3 cm of the surface for sediment grain-size and moisture content and of the upper 1 cm for chlorophyll-a. In the laboratory, sediment grain-size (including mud content, i.e., the percentage of the fraction of dry sediment < 63 μm), was determined using a Malvern laser particle sizer on freeze-dried samples. Volumetric moisture content was determined by weighing the sediment sample volume (20 cm^3) before and after freeze-drying. Chlorophyll-a was determined using HPLC (High Performance Liquid Chromotography, a technique used to identify and separate pigments). Sediment data were transformed using the procedure elaborated in Van der Wal & Herman (2007), i.e. a regression based on samples analysed both with the old and new NIOO laser particle sizer, in order to obtain a data set that is consistent and comparable with the old NIOO laser particle sizer, and by data obtained by Rijkswaterstaat using yet another laser particle sizer. In addition, mud content was log-transformed following ln (M +1), where M is mud percentage (%).

3.3 Surface characteristics from field spectra

Field spectra and sampling data were analysed to gain insight in the information which can be extracted from optical remote sensing, which may result in a better use of optical satellite data. In particular we focused on (1) chlorophyll, (2) mud and (3) moisture content, which may all affect the spectral signal.

Chlorophyll on tidal flats can be attributed to microphytobenthos (mainly diatoms), macroalgae (such as Enteromorpha) or vascular plants (such as Spartina or Aster). The spectral signature of sediment with microphytobenthos clearly differs from that of both macroalgae and vascular plants. Obviously, reflectance in the near-infrared is larger for vascular plants than for microalgae. However, the Normalized Differential Vegetation Index (NDVI), based on reflectance in the red and infrared band, and commonly used to identify vegetation, is not only significantly higher for vascular plants than for microphytobenthos, but is also significantly higher for macroalgae than for microphytobenthos. In addition, absorption in the entire visible range is larger for macroalgae and vascular plants than for sediments with microalgae. Thus, the three cover types can be easily distinguished based on spectral signature, but a more advanced technique, such as spectral unmixing, is needed to distinguish mixtures of those cover types.

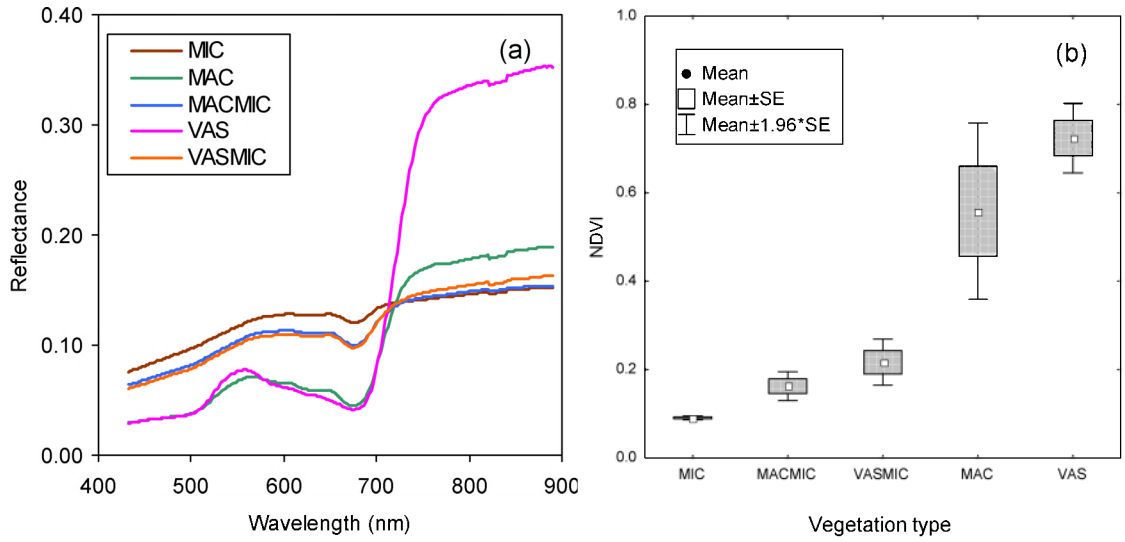

Figure 3.1 (a) Mean spectra for different vegetation types (MIC = microphytobenthos, MAC = macroalgae and VAS = vascular plants, MACMIC = mixed macroalgae and microalgae, and VASMIC is partial cover by vascular plants). (b) NDVI (Normalized Differential Vegetation Index) for microphytobenthos (MIC), macroalgae (MAC), vascular plants (VAS) and mixtures of those.

Narrow band spectra were averaged for ca 10 equally sized classes of increasing mud, chlorophyll-a and moisture content, respectively, excluding the spectra taken at stations with partial or full cover of macroalgae or vascular plants (Figure 3.2). Two spectral features are apparent in particular. An absorption feature in the red range (ca 670 nm) identifies the presence of chlorophyll-a: the higher the chlorophyll-a content, the more absorption. Interstitial moisture, on the other hand, is known to decrease the brightness of the spectra. A similar response can be expected for mud content of the sediment. Because of the strong (positive) correlation between mud, moisture and chlorophyll-a, a decrease in brightness is apparent in the spectra with increasing moisture content, mud content and chlorophyll content.

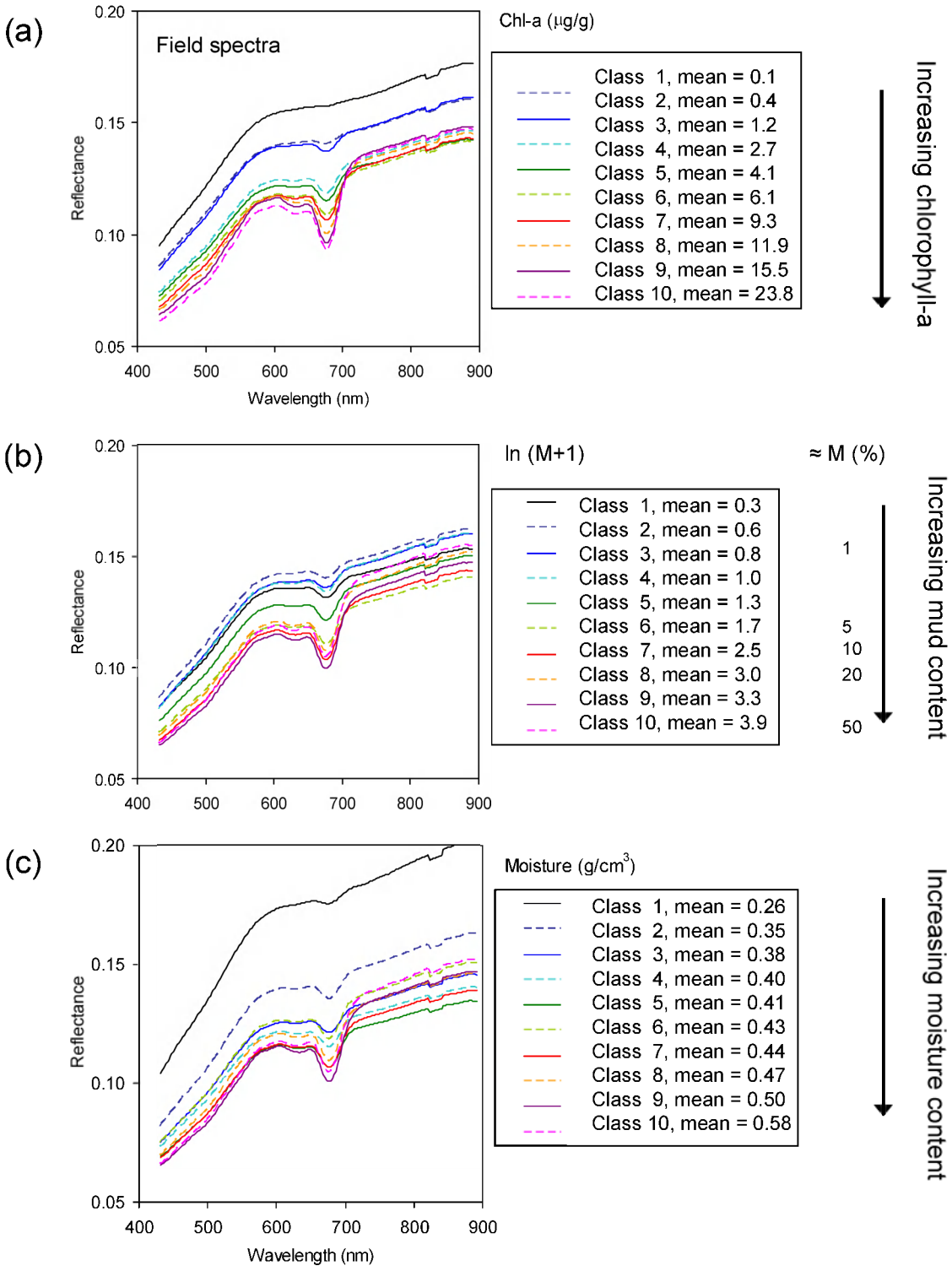

Figure 3.2 Mean reflectance spectra for 10 classes (Class 1 to 10) for sediment with increasing (a) chlorophyll-a content (Chl-a), (b) mud content (expressed as ln(M+1) in which M is mud percentage of the sediment) and (c) volumetric moisture content. Mean value of the material of interest in the sediment (i.e., chlorophyll, mud and moisture) of each class is shown in the legend.

Generalized linear models based on maximum likelihood estimation were applied to test the response of the surface characteristics to spectral indices, based on a linear predictor with a Gamma error distribution and either an *identity* or an *inverse* link function. Different models were evaluated based on Akaike's Information Criterion (AIC), optimizing the trade-off between goodness-of-fit and parsimony of the models (Van der Wal et al., 2008).

Microphytobenthic chlorophyll-a content can be identified using the NDVI (e.g., Van der Wal et al., 2010b). Figure 3.3a shows that this also holds for our field data, although the relationship is not linear, i.e. the slope slightly decreases with increasing NDVI. When focusing on the green band L2 (ca 560 nm), the impact of surface moisture can be established. The field data show a highly significant linear relationship between L2 reflectance and volumetric moisture content (Figure 3.3b). A significant negative relationship was also found between mud content and L2 reflectance, but in this case, an inverse relationship (Figure 3.3d) fitted better than a linear relationship (identity link) with ln(M+1) (Figure 3.3c). Such relationships can be used to derive estimates of mud content from optical satellite remote sensing.

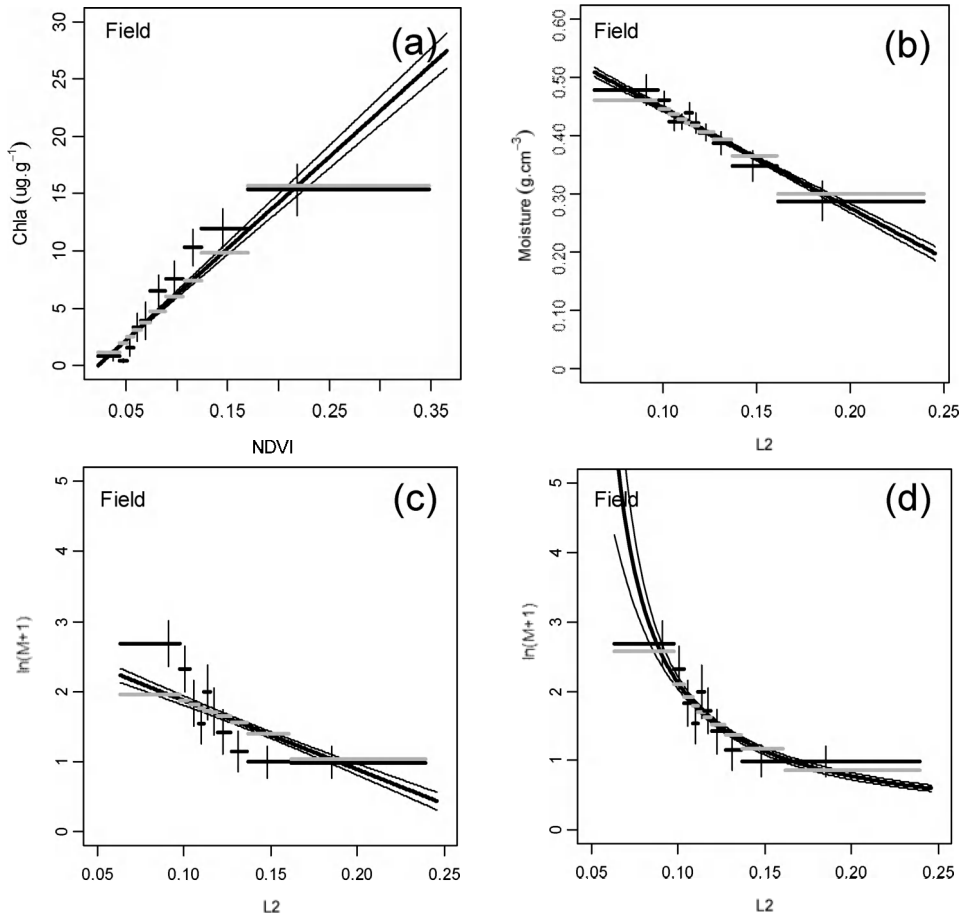

Figure 3.3 (a) Sampled chlorophyll-a versus NDVI, (b) sampled moisture content versus reflectance in the green band L2, (c) sampled mud, i.e., ln (mud percentage +1) versus reflectance in the green band L2 and (c) ln(mud percentage +1) versus reflectance in the green band L2 using an inverse relationship.

3.4 Satellite images

C-band SAR images of the ESA satellite ERS-2 were used, which have a nominal resolution of ca 30 m, and a pixel size of 12.5 m. A selection is made of all archived SAR images from 2006, 2007 and 2008 that (1) cover either the entire Westerschelde or the eastern part of the Westerschelde, (2) are acquired when water levels in the Westerschelde were below ca -1m NAP, (3) have no obvious disturbance from rain showers during overpass, and (4) are acquired in descending mode, i.e. at ca 10:40 UTC. The selected SAR data were calibrated following Van der Wal et al. (2005). However, brightness values β^0 (b0) rather than backscattering coefficients σ^0 were calculated in the present study to account for differences in incidence angles across the swath. Average β^0 values were calculated for every pixel in each image, using a moving window of 9 by 9 pixels in order to improve radiometric resolution.

In addition, Landsat TM/ETM+ images, with a 30m spatial resolution, were used in this study. Mostly unclouded, low water scenes were selected from 2006, 2007 and 2008. The images were atmospherically corrected using the method described in Van der Wal & Herman (2007). In this procedure, the Landsat image of 27 May 2005 was atmospherically corrected based on in situ calibration at semi-invariant targets during overpass using the TRIOS Ramses radiometer, and taken as reference to calibrate the other images. Clouds and cloud shadows were manually masked. The Landsat 7 ETM+ imagery also have stripes where no data is available, owing to a defect of the sensor; these areas were masked as well.

All images were rectified and transformed to the Dutch National Grid. A mask was applied to exclude (1) areas below -1 m NAP, (2) vegetation, as detected using a vegetation index from a time-series of Landsat ETM+ images acquired in summer, and (3) construction works and areas outside the Westerschelde. As some SAR images did not cover the entire western part of the Westerschelde, the analyses were made on the eastern part only (see Figure 3.11 for extent). Data were exported as Erdas Imagine (.img) raster files, which can also be directly imported in ArcGIS.

3.5 Mud content of the sediment from satellite data

As the focus of this stage of the project is on 2007 and 2008, a data set of in situ sediment samples collected by NIOO covering the eastern part of the Westerschelde from June 2007 and June 2008 were used for calibration (referred to as Cal0708). In situ mud content data from a field campaign by NIOO in May/June 2005 (referred to as Val05) were used for validation. Both data sets are part of the field data set described in section 3.2 and 3.3.
The in situ data were then related to information from matching (i.e., within two months) imagery, i.e. brightness values b0 from ERS-2 SAR images (using the mean over 9x9 pixels, corresponding to ca 112.5 m in the field) and surface reflectance from Landsat TM (using a mean value of a 3x3 pixels window, corresponding to circa 90 m in the field) in a Geographical Information System. Data from sample sites located below <-1m NAP were discarded, to exclude areas possibly covered by water. In addition, sample points in saltmarsh areas were discarded, based on NDVI.

Data were fitted using the regression analysis described above. Log-transformed mud content significantly depends on ERS-2 SAR backscatter b0 (Figure 3.4). Likewise, log-transformed mud content significantly depends on reflectance in Landsat band 2. Just like with the field data, a better relationship (i.e., lower AIC) between ln (M+1) and the inverse of band 2 was

obtained. Combining both the backscatter signal from ERS SAR and the reflectance from both Landsat bands TM2 (green) and TM5 (SWIR) in a multiple regression yielded best regression results (R^2_{adj}=0.57, n=200, p=0.00, se=0.74). The equation of this synergy method is:

ln(M+1) = -0.13 * b0db – 28.88 * tm2 + 13.92 tm5 + 2.65

in which M is the mud percentage of the dry sediment, b0db is SAR backscatter in dB, tm2 is reflectance in the green band, and tm5 is reflectance in the SWIR band from Landsat.

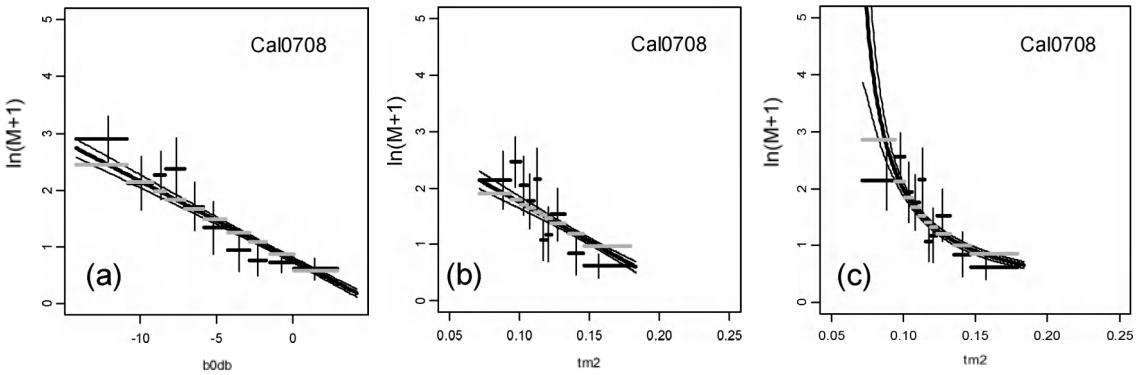

Figure 3.4 Mud content ln (M+1) as a function of (a) backscatter b0 (in dB) from ERS SAR and (b) as a linear function of reflectance in Landsat band TM2 and (c) as an inverse function of reflectance in Landsat band TM2.

Four significant models, i.e. “model SAR” based on the backscatter only, “model TM” based on a linear combination of Landsat TM2 and TM5, “model TM2inv” based on the inverse relationship with TM2 and “model Syn” combining the information from both radar and optical remote sensing, were applied to evaluate the prediction of ln (M+1) (Figure 3.5).

In all models, mud content is underestimated at higher mud contents. This effect is least pronounced for the algorithm based on synergy of ERS SAR and Landsat TM, which best approaches the 1:1 line of observed = predicted mud content (Figure 3.5a), and worst for the TM2inv model (Figure 3.5d). Although there are differences in calibration and validation, the validation of the four methods performs just as good as the calibration (cf Figure 3.5 and Figure 3.6). In both cases, there is considerable amount of scatter, as well as a consistent deviation from the 1:1 line for most methods. The TM2 method gives least scatter, but the 1:1 line is not well approximated for this method. In particular, for all methods the occurrence of cohesive sediment is rarely predicted (mud percentage >20% or ln(M+1)>3).

When making a very broad division in sediment types, i.e., “sand”, ln(M+1)<1.79 (mud percentage ca <5%) and “mixed”, ln(M+1)>1.79 (mud percentage ca > 5%), the total accuracy (defined as the total number of correctly classified samples as a percentage of total samples) is 71% for the inverse TM method, 78% for SAR, 79% for TM and 80% for the Synergy method for the *calibration* data set (Cal0708). Total accuracy for the *validation* data (Val05) is 60% for the TM method, 62% for TMinv, 63% for SAR and 73% for the Synergy method. This confirms that the Synergy method is most reliable, followed by SAR. For the validation data set, the user’s accuracy (that is 100% - error of commission) is 77% for “sand” and 65% for “mixed” for the Synergy method and 66% for “sand” and 51% for “mixed” for the SAR method.

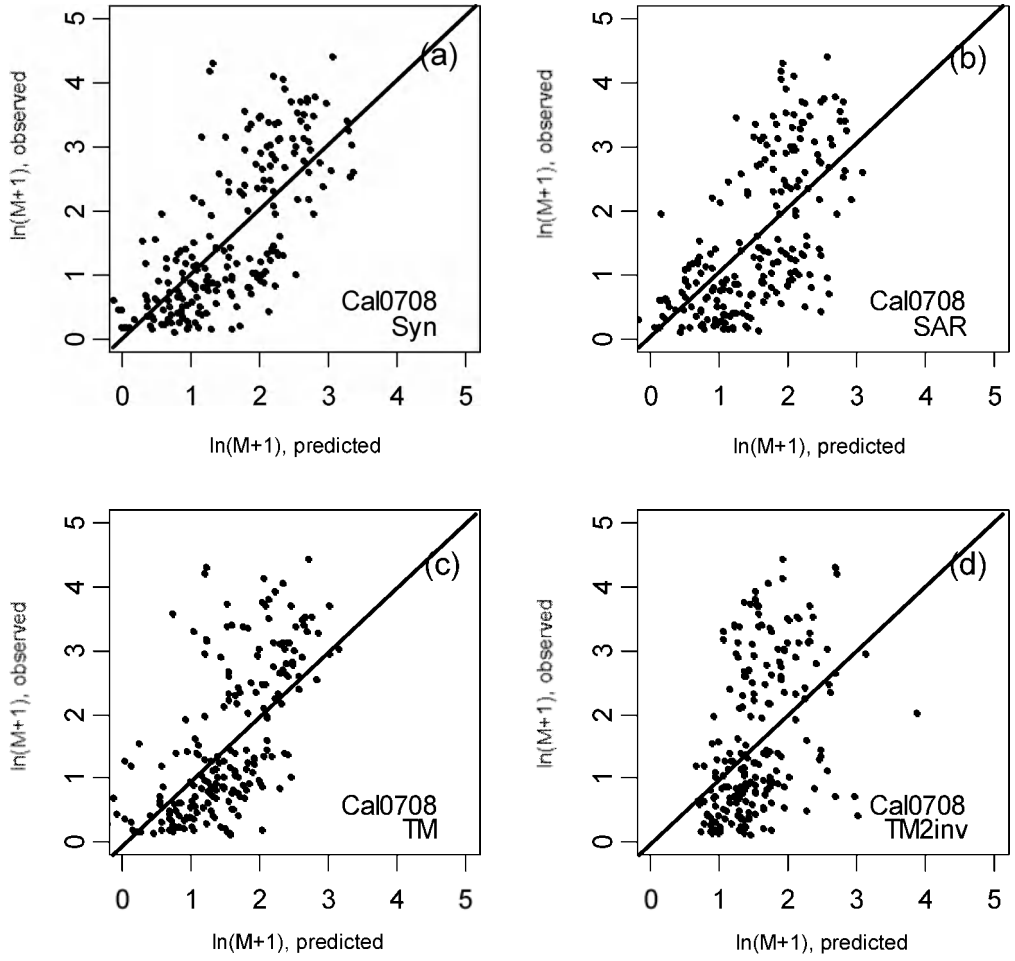

Figure 3.5 Results for calibration of the four mud content retrieval schemes. Solid line is 1:1 line.

The four mud content retrieval algorithms were applied to the satellite images to yield maps of the mud content. These are presented in Appendices B.1 to B.7. As can be expected based on the validation/calibration exercise, the TM and especially the TM2inv model underestimate high mud contents and overestimate low mud contents, while the synergy method gives best results. Although absolute values of the predicted mud content should thus be considered with care, large-scale patterns with persistent low and persistent high mud contents can be identified well in the maps and are comparable between methods.

The TM and TM2inv algorithm misclassify surface water in different ways: the TM and Syn algorithms yield very low apparent mud contents in these areas (due to the influence of the SWIR band), whereas the TM2inv algorithm yields very high apparent mud contents in these areas. This is especially visible at the edges of the tidal flats in maps derived from relatively high water levels. An improvement of the algorithms that can be easily implemented would be to set a threshold based on reflectance in the NIR or SWIR to exclude surface water areas.

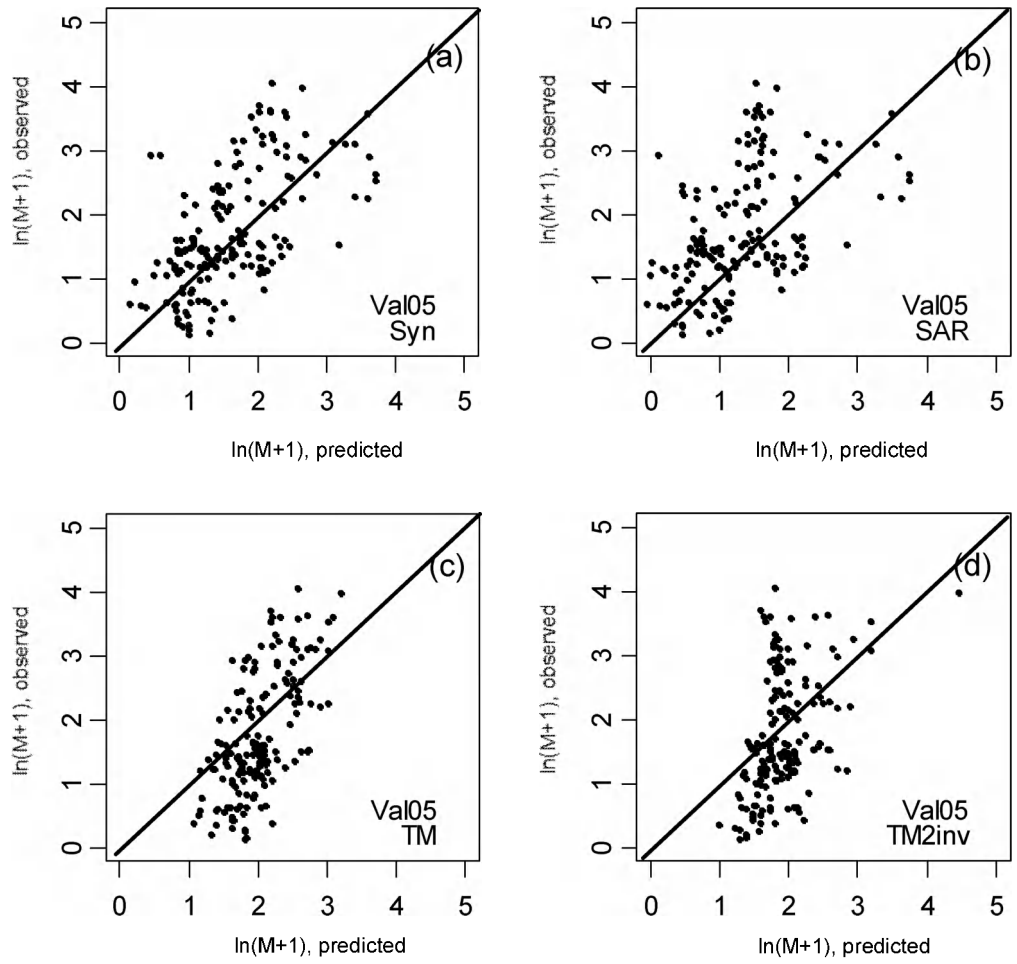

Figure 3.6. Results for validation of four mud content retrieval schemes. Solid line is 1:1 line.

The sequential maps derived from radar remote sensing show a seasonal variation, while differences between years are not directly evident (Figure 3.7). For Landsat, there aren't sufficient images to capture the intra-annual (and interannual) variation in mud content of the sediment. For example, in 2008 there is only one low water image available (albeit with some cirrus clouds).

Differences in mud content between seasons (as was also observed in in situ data of mud content, cf. Van der Wal et al., 2010a) and years may be attributed to differences in wind climate and river discharge, but also solar radiation/temperature, facilitating growth of microalgae that can trap mud particles. Figure 3.8 shows that global radiation is highest in 2006 and that wind velocities were relatively modest in winter and early spring 2006, facilitating build-up of fine sediment, but strong southwesterly winds in early April and end of May 2006 (see also paragraph 7.1), may have counteracted this process.

There is also variation on very short (within months) time-scales for all methods. For example, mean mud content varies considerably for the Landsat derived mud maps from July 2006. For Landsat imagery, this may be explained by short-term variations in actual mud content, but the variations are more likely to result from factors affecting surface and interstitial water, such as tidal stage and evaporation, organic matter, residuals of atmospheric corrections and

the specifics of the Landsat sensor that change the predicted mud content. For example, for the July 2006 series of Landsat 5 and 7 imagery, tidal stage ranges from outgoing to low tide to incoming. For SAR imagery, this short-term variation may be due to actual changes in mud content, but may also have been caused by factors affecting surface water in particular (such as rain and tidal stage), and factors that obscure a unambiguous relationship between surface roughness and mud content, such as hydrodynamic conditions (i.e., surface ripple structure may vary according to wave energy) and biological activity.

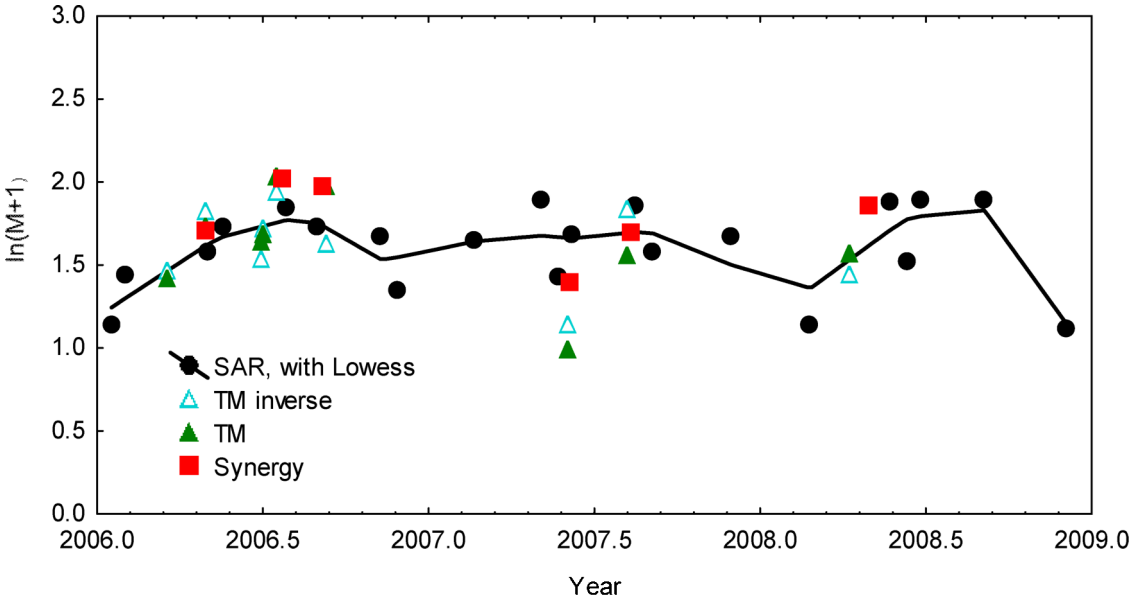

Figure 3.7 Time-series of mud content ln (M+1), with M is percentage mud in the sediment, from remote sensing, averaged for all 2007/2008 calibration stations situated above -1 m NAP, stations in vegetation excluded. Landsat images acquired at water levels above -1 m NAP at Hansweert were discarded here. A Lowess fit is plotted through the SAR derived mud contents.

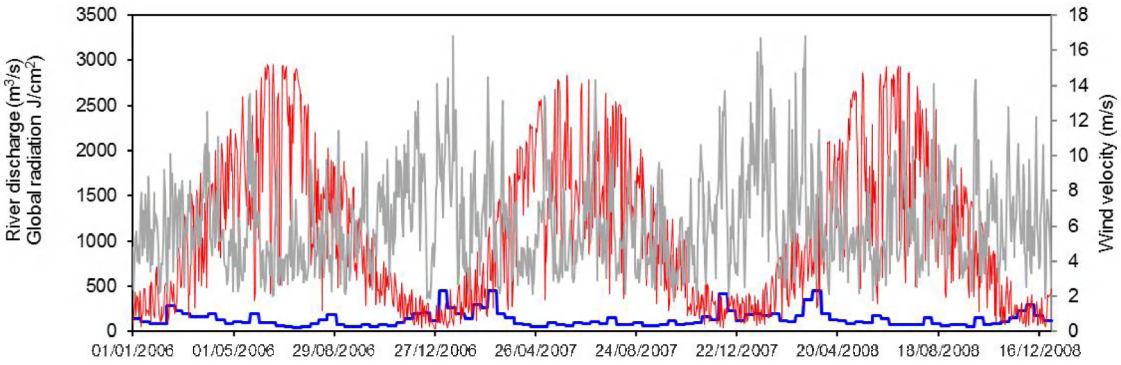

Figure 3.8 Time-series of daily mean wind speed at Vlissingen in m/s (grey line, right y-axis) and global radiation in J/cm^2 at Vlissingen (red line, left y-axis) both source http://www.knmi.nl), and time-series of Scheldt river discharge at Schaar van Ouden Doel in m^3/s (source http://www.waterbase.nl) (blue line, left y-axis).

To test the significance of the differences in retrieved mud content, we applied a main effects ANOVA on the mud contents (ln M+1) extracted from the SAR images at the calibration data stations (eastern part of the Westerschelde). As a full factorial ANOVA design was not possible due to limited number of images and the irregular distribution of images over the years, separate ANOVA tests were performed for the effect of year, season, month, season per year and image date. Sites were added as random factor in each test.

Differences in mud content between years are significant ($F_{2,4196}$=29.714, p=0.000). A posthoc HSD Tukey test shows that mud content in 2006 is not significantly different from that in 2008, but 2007 has a significantly higher average mud content. Note that this may well be due to underrepresentation of winter images in 2007 (Figure 3.7). There is also a significant effect of differences in mud content with season ($F_{3,4195}$=206.63, p=0.000) with smallest mud content in winter, followed by autumn, spring and then highest mud content in summer. A similar trend can be seen for the effect of month ($F_{8,4190}$=101.51, p=0.000) (Fig. 3.9), with a peak in July and a minimum in December/January. A test on all seasons in the period 2006-2008 also shows significant differences ($F_{12,4186}$=85.386, p=0.000). In winter (here Jan-Feb), mud contents are lowest in 2008 and highest in 2007. In Spring (March-May), mud content is highest in 2008. In Autumn (Sep-Nov), mud content is lowest in 2006, followed by 2007 and then 2008. Differences in mud content in Summer (Jun-Aug) are not significant. There is also a significant effect of image date ($F_{20,4178}$=72.664, p=0.000). For example, for 2008, mud contents on 21 May 2008, 25 June 2008 and 3 Sep 2008 are not significantly different, but predicted mud content is significantly lower on 9 June 2008.

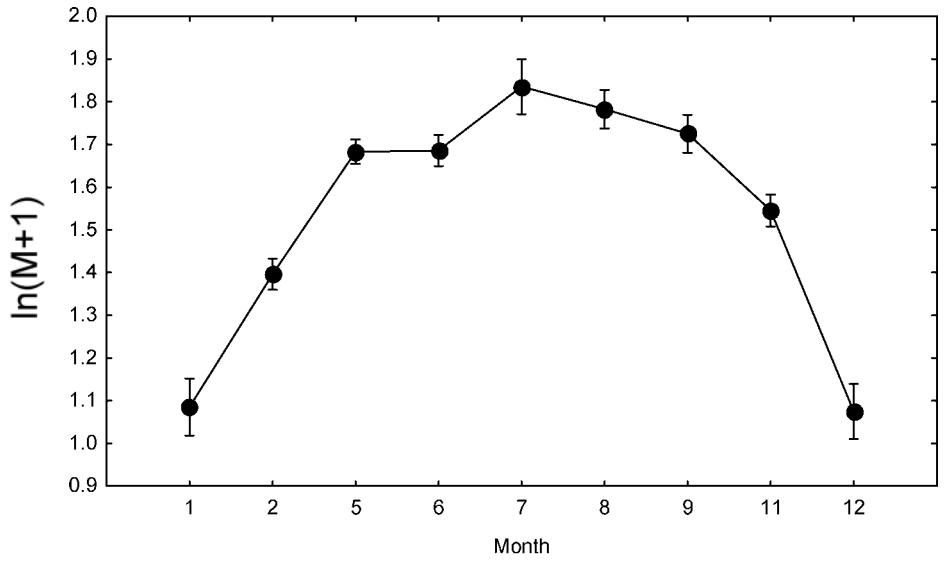

Figure 3.9 LS Means of ln(M+1) for month resulting from the ANOVA analysis of the SAR images from 2006-2008. Vertical bars denote 0.95 confidence intervals.

3.6 Bed roughness from satellite data

Information on bed roughness was derived from satellite radar. The algorithm used for retrieval of bed roughness from SAR is based on an analytical backscattering model, i.e. the Integral Equation Model (IEM) developed by Fung et al. (1992) and validated with in situ measurements of surface roughness, as described in Van der Wal et al. (2005) and Van der Wal et al. (2010a). The same procedure was also used for the LTV pilot study (Van Kessel et al., 2008).

Backscatter is assumed to depend both on the configuration of the sensor and on surface characteristics, including moisture conditions and surface roughness. An approximate solution of the model was applied using realistic assumptions on such variables, based on previous field measurements (Figure 3.9). The algorithm was validated using in situ bed roughness data of a number of tidal flats measured in the period 2003-2004 (Van der Wal et al., 2005). RMSz (root-mean-square of the heights, in cm) was taken as a measure for vertical bed roughness. This measure relates very well to both ripple length λ ($RMSz \approx \lambda/20$) and ripple height η ($RMSz \approx \eta/3$) (Van der Wal et al., 2005). The field measurements of RMSz were related to brightness values obtained from matching ERS-2 SAR images taken within the same week/month of that year, in a Geographical Information System. Results show that both the models and field data are in very good accordance for values of bed roughness under RMSz=0.6 cm (Figure 3.10). For larger values, the model indicates that surface moisture rather than bed roughness becomes dominant in determining the backscatter signal. In this domain, SAR with a larger wavelength should be used to retrieve bed roughness on intertidal flats. Since use of such sensors was outside the scope of this project, an upper limit of RMSz=0.6 cm was set to bed roughness here.

It should be noted that the method yields estimates of the surface roughness. This means that, for example, water staying on the surface, within the surface ripples, is also seen as surface, whereas it is actually masking the sediment bed. This generally leads to an underestimate of bed roughness in areas covered by a water layer. The amount of water staying on the surface will depend on tidal stage, but also on weather conditions, particularly when rain is falling during emergence of the tidal flats.

In the period 2006-2008, rainfall in the 5 hours prior and during image acquisition was very high (> 5 mm per hour on average) on 20 February 2006 and 14 August 2006 in particular, and moderate (2-5 mm per hour on average) on 1 May 2006 and 21 February 2007. Results retrieved from these images should be regarded with caution. Therefore, the images from 20 February and 14 August 2006 have been excluded from subsequent analysis.

The retrieval algorithm has been applied to the images (see Appendix B). In addition, an average bed roughness was calculated for all 2006 and all 2008 images (e.g. Figure 3.11). Such an average roughness map can be used to improve the hydrodynamic model and the mud transport model.

In general, Rug van Baarland, Plaat van Ossenisse and Plaat van Valkenisse have high values for bed roughness, whereas the eastern part of Hooge Platen and the tidal areas in the upper part of the Westerschelde (Bath, Appelzak) have low values for bed roughness (Figure 3.11). Temporal trends in surface roughness are comparable to those in mud content from SAR (roughness of the surface as detected by SAR is assumed to determine the mud content), although correlations are not linear.

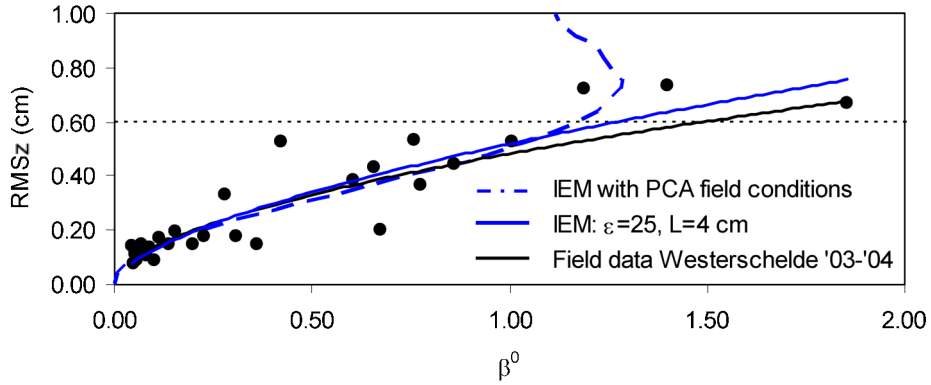

Figure 3.10 Relationship of vertical bed roughness RMSz and brightness β^0 (intensities, not dB) The solid blue line indicates model results, assuming wet sediment with a dielectric constant ε=25. The model represented by the dashed blue line incorporates correlations between bed roughness and moisture conditions as measured in the field. The black dots represent field measurements of RMSz and associated β^0 from matching ESA ERS-2 SAR images, and the black line is a regression line through these measurements.

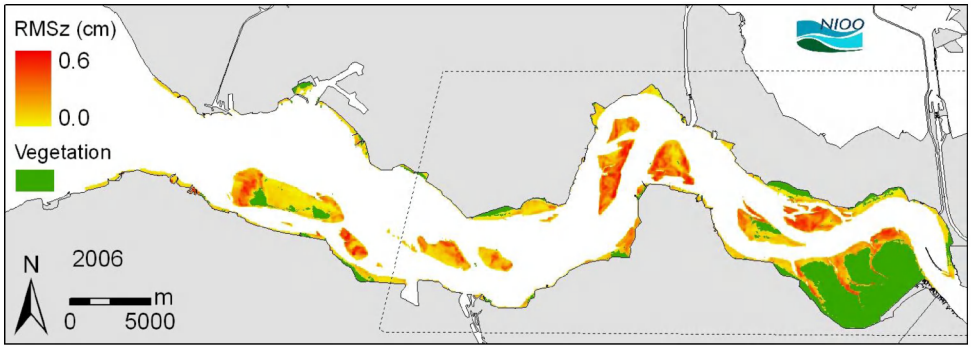

Figure 3.11 Bed roughness RMSz, averaged over dates in 2006.

3.7 Conclusions and recommendations

3.7.1 Conclusions

- Field spectra from sediment with microphytobenthos clearly differ from those of macro-algae and higher plants. The data also shows the feasibility of deriving information on chlorophyll-a of the intertidal sediments of the Westerschelde from optical remote sensing.
- Field spectra show that mud content can be derived from optical remote sensing. However, misclassifications could arise when the relationship between mud content and interstitial moisture changes, i.e., depending on tidal stage (and elevation) or evaporation.
- All models used in this study to retrieve mud content from satellite remote sensing (e.g., derived from ERS SAR, Landsat TM or a combination of those) produce significant results.
- Large-scale spatial patterns in mud content are similar for all methods to retrieve mud content from satellite remote sensing.

- However, the retrieval schemes all underestimate high mud contents. In particular the Landsat TM model also overestimates low mud contents.
- A model based on a combination of ERS SAR and Landsat TM provides the best predictions of mud content. Standard error of the regression is slightly smaller than for ERS SAR and Landsat separately, whereas the coefficient of determination is slightly higher and the 1:1 observed=prediction line is best approximated. The two independent data sources provide complementary information on the sediment. However, the synergetic use of the two sensors requires (semi-)simultaneous acquisition of images by both sensors, which is not often the case.
- ERS SAR provided the highest temporal resolution, and therefore provides the best technique for assessing intra-year variability in mud content, and, especially, surface roughness.
- Variations in mud content as derived from satellite remote sensing were significant. Seasonal variation in mud content was larger than inter-annual variation and mud contents in 2006 and 2008 were not significantly different.

3.7.2 Recommendations

- Both SAR and Landsat TM only detect the upper mm of the surface and do not provide information on the thickness of the mud layer. However, the algorithm is calibrated (and validated) with samples collected from the upper 3 cm of the surface. These limitations have to be taken into account when using the remote sensing retrieved data for validation of the mud balance.
- The models can be improved by better taking into account surface water and interstitial water. For the optical retrieval scheme, in situ data are available to validate the effects of variations in surface water and moisture content on predicted mud content.
- Further improvement of the algorithms may be achieved by using geostatistics to bring the support of the in situ data used for calibration in accordance with the support of the satellite data.
- An accuracy assessment was beyond the scope of the current project. Future research should assess the accuracy of the retrieved mud contents and quantify the sources of variation. Such a study should also include aspects like spatial autocorrelation of the data.

Acknowledgements
Annette Wielemaker-van den Dool helped with image processing and GIS and Peter Herman advised on this study. ERS SAR imagery were obtained through ESA Category I grant 5578.

4 Hydrodynamic simulation 2006

4.1 Introduction

An actualisation of the 3D hydrodynamic NEVLA-model has been performed with respect to the 3D model used in van Kessel et al. (2009). The model grid improvements made by FHR in 2009 in their 2D NEVLA model (Maximova et al, 2009a & 2009b) are integrated in the 3D NEVLA model. Furthermore, an update of the bathymetry of the BCS is performed. The model adaptations are briefly discussed below.

The hydrodynamic scenario used in last year's report (simG19) is used as reference run in the description. Run-ID's higher then simG19 represent consecutive changes. The hydrodynamic scenario used in this report is simG34. The model settings (viscosity, roughness, time step) are not changed from simG19 to simG34. A new calibration of the roughness field for the 3D model is scheduled in 2011 at FHR.

4.2 Model changes

4.2.1 Improved model grid

The model grid adaptations reported in Maximova et al (2009a & 2009b) are integrated in the 3D hydrodynamic model. All intertidal areas along the Sea Scheldt and its tributaries are included in the model grid. The numerical schematisation in the area of the DGD was refined. The total area of DGD was included in the model and a higher resolution was obtained (Figure 4.1). Also the Durme river was extended up to its tidal border (Figure 4.2).

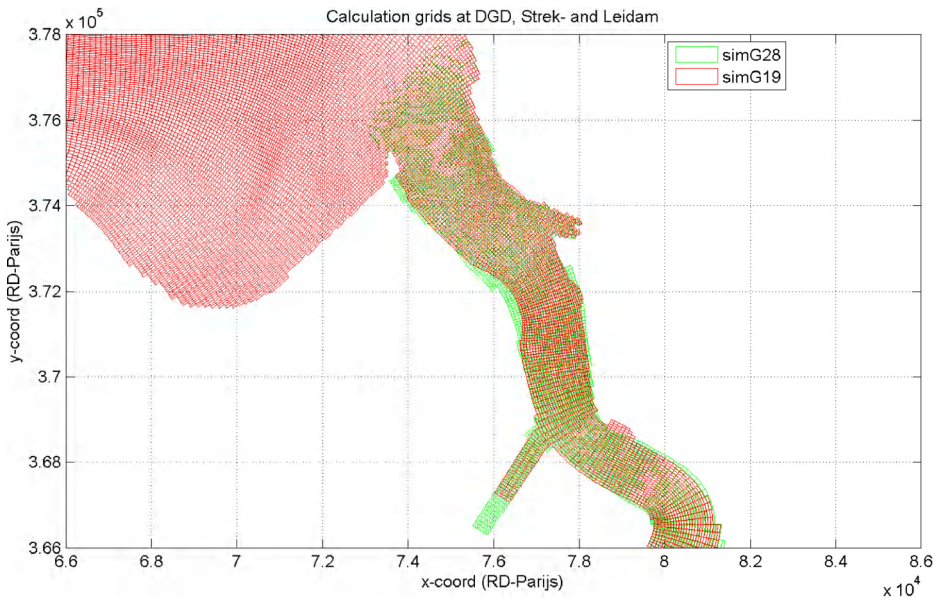

Figure 4.1 Grid adaptation around DGD for simulation G28 and higher (including G34) compared to G19.

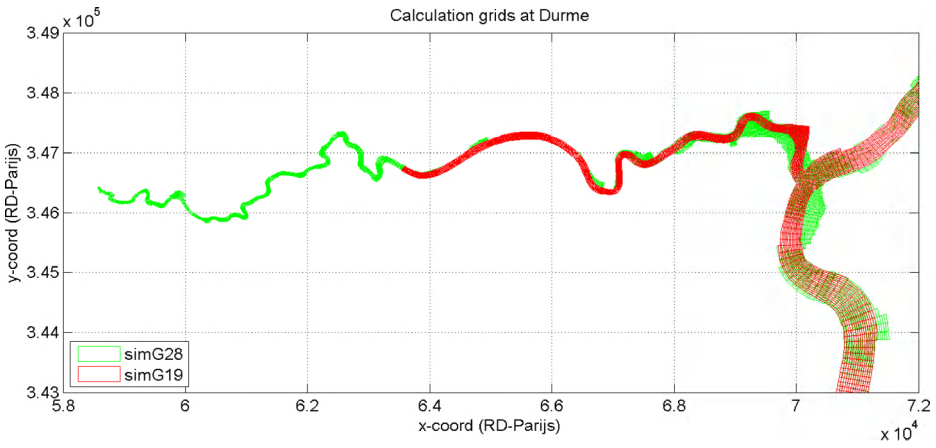

Figure 4.2 Grid adaptation at the Durme

4.2.2 Improved model bathymetry at the Belgian Continental Shelf

The bathymetry in the Western part of the Belgian Continental Shelf (BCS) was based on samples with a resolution of triple the grid resolution, which resulted in a poor interpolation of topographic features such as sandbanks. Furthermore the western part of the model was extended in a later phase without assuring a smooth transition between the existing bathymetry and the new interpolated part (Figure 4.3).

Samples of the BCS with a resolution of 25m were used to create a new bathymetry of the BCS (Figure 4.4). Attention has been paid that the transition between the existing bathymetry and the newly interpolated one is continuous.

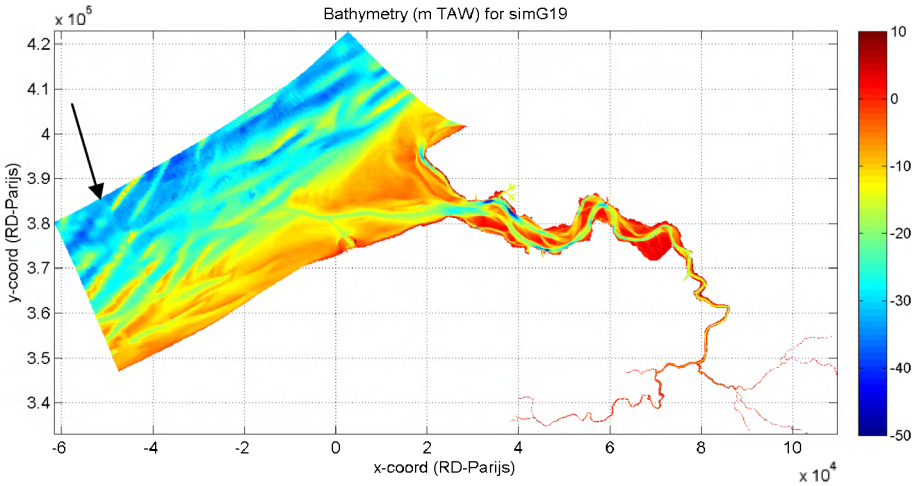

Figure 4.3 Original model bathymetry (simG19). Note the discontinuity in the western part of the BCS indicated with an arrow.

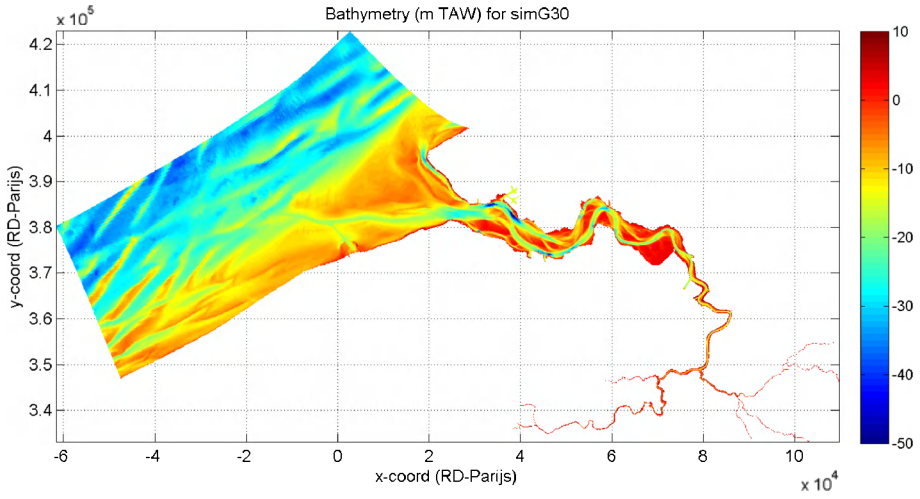

Figure 4.4 Improved model bathymetry (simG34), based on new samples on the BCS.

4.2.3 Training wall

Originally the training wall near the Zandvliet - Berendrecht sluices are represented as thin dams in the 3D model. Water cannot flow over these dams, in reality though, flow over the dams is possible beyond a certain water level between low and high water. Maximova et al (2009b) already removed the thin dams in the 2D model by adapting the bathymetry. Based on the samples used by Decrop et al. (2010), a new interpolation is made of the bathymetry of the training wall and the thin dams are removed in the 3D model.

4.3 Results for hydrodynamics

The results of the 3D hydrodynamics are presented in two parts. First, a comparison is made to the model results obtained last year (simG19). This comparison is made for the last quarter of 2006, because that was the period analysed in 2009.
Secondly, the results of simG34 are summarized for the entire year 2006.

4.3.1 Comparison with simG19

A harmonic analysis for the M2 component shows a similar behaviour for both simG19 and simG34 (Figure 4.5).

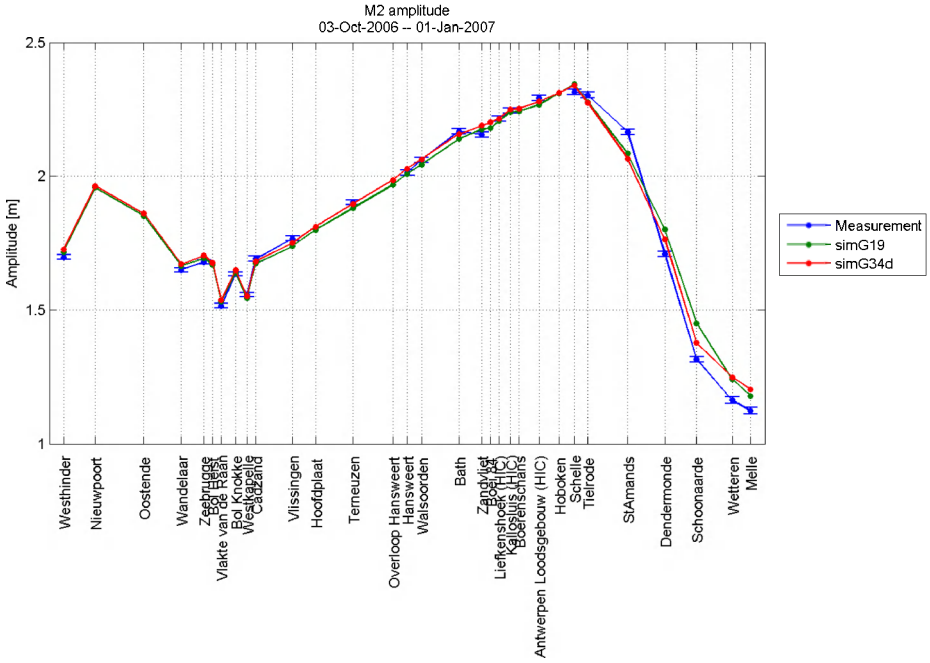

Figure 4.5 M2 water level amplitude for simG19 and simG34.

The average difference in amplitude M2 is about 1 cm. The phases of the two runs are nearly identical (difference smaller then 1°). A greater difference between the two results becomes apparent when analysing the higher harmonics (M4, M6) (Figure 4.6 and Figure 4.7). This difference is mainly due to the difference in implementation of the training wall around the Dutch-Belgian border. In simG19, these structures were implemented as impermeable “thin dams”. In simG34, these structures are implemented as obstacles in the model bathymetry that will flood above a certain water level. This results in a difference in amplitude of the higher harmonics upstream the Dutch-Belgian border, and has a possible impact on the modelled tidal asymmetry.

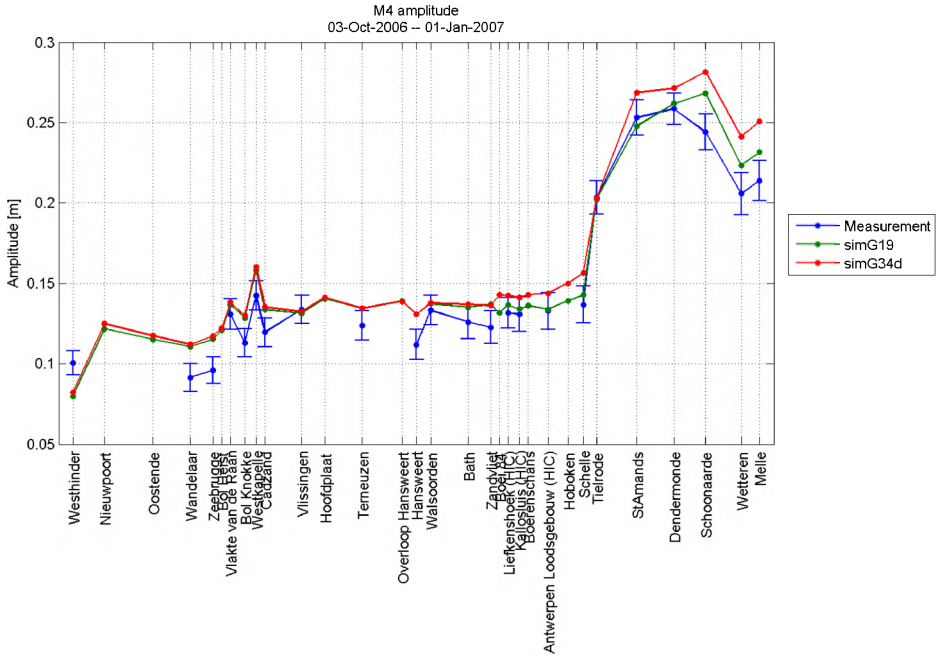

Figure 4.6 M4 water level amplitude for simG19 and simG34. M4 originates from the advection term.

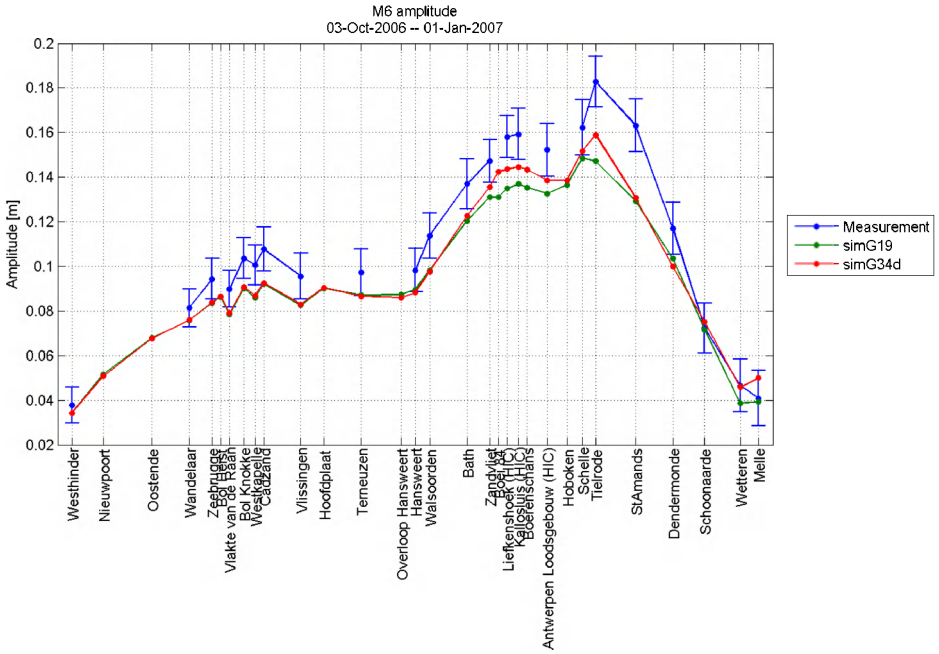

Figure 4.7 M6 water level amplitude for simG19 and simG34. M6 originates from the friction term.

The difference in M4 and M6 amplitude due to the different implementation of the training wall is around 1 cm. The difference in phase around Antwerp is 3° for M4 and 2° for M6.

4.3.2 Full year 2006 results simG34

The results of simG34 are briefly summarized for the entire year 2006.

***M2* amplitude**

Figure 4.8 shows the computed and observed M2 amplitude as analysed for the entire year 2006, for different points along the estuary. M2 is the most important tidal component and explains most of the tidal signal. The difference between the M2 amplitude for the entire year and that for the last quarter of the year (see Figure 4.5) is small, as expected.

The average difference in M2 amplitude between model and measurements is 4 cm. The model reproduces the combined effects of convergence of the estuary and friction. This is shown by the peak in amplitude around Schelle, which is visible in both measurements and model.

The Root Mean Square Error (RMSE) of computed water levels varies between 20 cm at sea to 30 cm at the upstream end of the model, at Ghent. This error is higher than the M2 amplitude difference, as other tidal components also contribute to the RMSE. In addition, the error in the non-tidal part of the water level curve plays a role, such as set-up or set-down by wind.

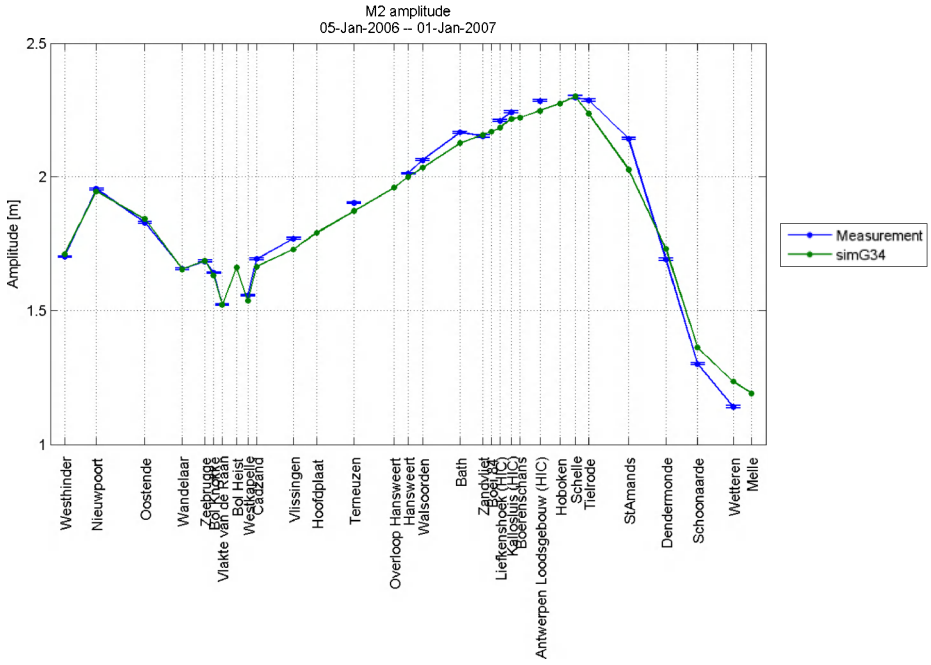

Figure 4.8 M2 water level amplitude for run simG34 (entire year 2006).

Error with low-pass filter

Figure 4.9 shows the error between modelled and measured water levels at Vlissingen, passed through a low-pass filter in order to remove the tidal signal. What remains in Figure 4.9 is the slowly varying part of the modelling error. It seems that the model overestimates the water level in the first part of the year, and under-estimates the water level in the last quarter. Such error may be expected as the model is steered at its downstream boundary by a train of different models (in this case the Continental Shelf Model and the Southern North Sea Model), and not by a timeseries of measured water levels. This modelling train induces errors; its calibration is currently performed at FHR in an attempt to reduce error in future versions of the hydrodynamics.

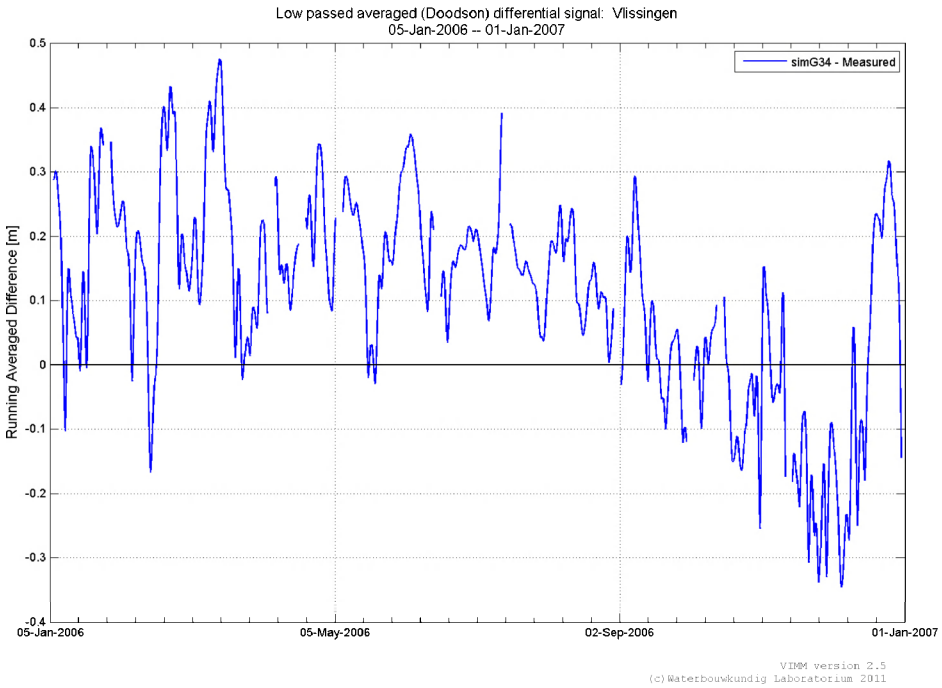

Figure 4.9 Low-passed average error at Vlissingen.

Salinity

Figure 4.10 shows the computed and measured salinity at location Boei 84 (Sea Scheldt, in the vicinity of Deurganckdok). The model performs well, bearing in mind that salinity is modelled without separate calibration. The model has a slight systematic underestimation of one half parts per thousand (ppt), which is less than the accuracy of salinity measurements. Figure 4.10 gives confidence in the model, because the processes advection and diffusion dominate the transport of both suspended sediment and salt. The salinity is strongly inversely correlated with freshwater discharge, see the bottom panel of Figure 4.10. Periods with high discharge peaks coincide with periods with low salinity.

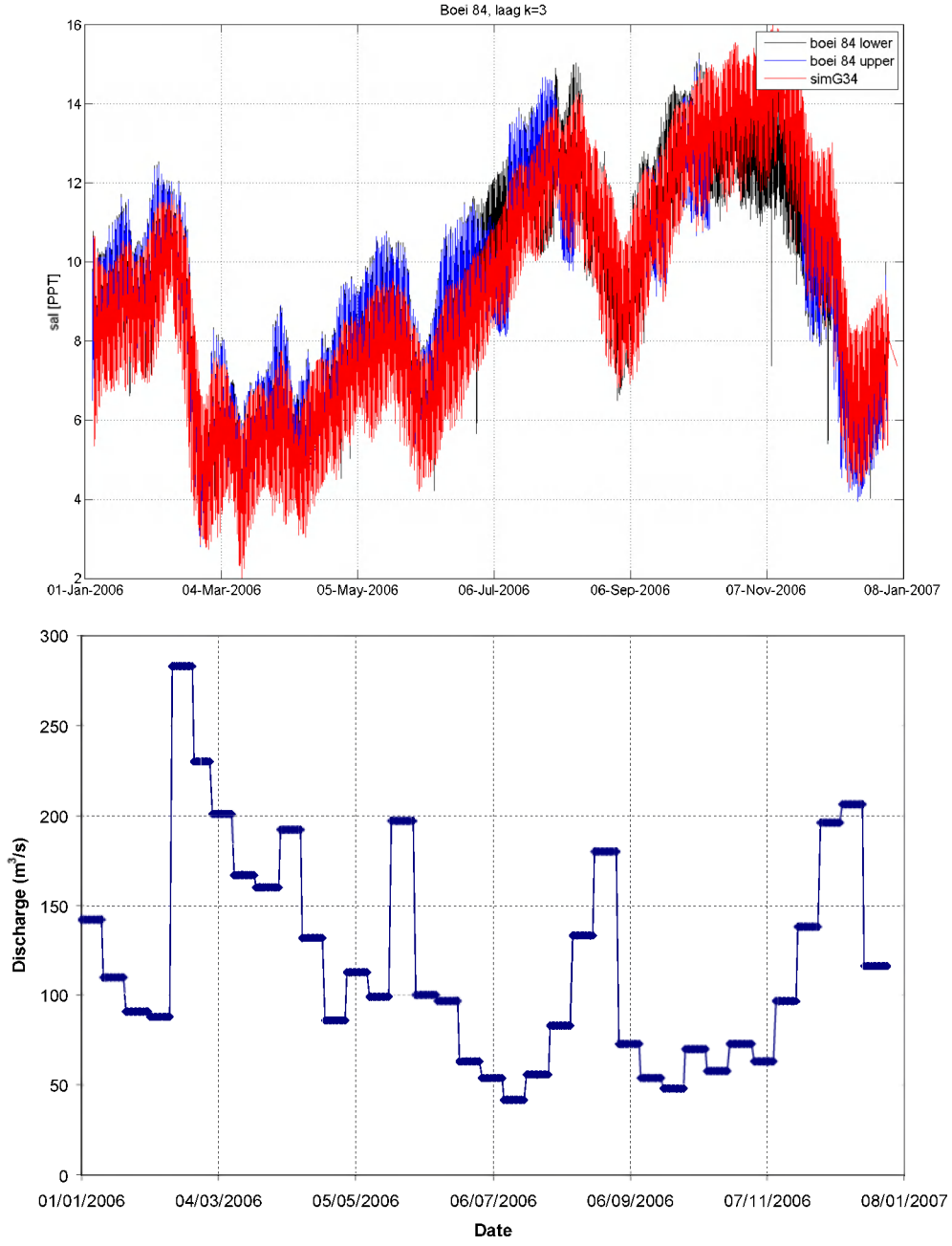

Figure 4.10 Top panel: computed and measured salinity at Boei 84. Bottom panel: 10-day average discharge at Schaar van Oude Doel (represents freshwater discharge up-estuary).

5 Mud transport

Based on the hydrodynamic simulation discussed in Chapter 4, a new mud transport simulation is carried out. Settings are equal to those applied for the 2009 simulations. (Table 5.1). However, the hydrodynamic database is further improved and extended. Results are compared with in situ and remote sensing data. The comparison between remote sensing data and model focuses on spatial sediment distribution and bed composition, including seasonal variability.

Figure 5.1 shows a comparison of computed SPM ('suspended particulate matter') levels based on the 2009 and present hydrodynamics. The present hydrodynamics covers the complete year 2006, the previous one the last quarter of 2006 only. In the months October and November the computed concentration levels are substantially different, whereas in December the levels are similar. This can be explained by the difference in salinity distribution between both simulations on 1 October 2006. For the new simulation, the salinity reflects the period of low discharge in September (see Figure 4.10). For the previous simulation, the salinity reflects the period of high discharge in December, as the hydrodynamic database of Q4 2006 is repeated multiple times for spin-up and October is preceded by December instead of September. During the simulation, the influence of the difference in salinity conditions on 1 October gradually decreases. This cyclical effect dominates over other possible differences between both simulations.

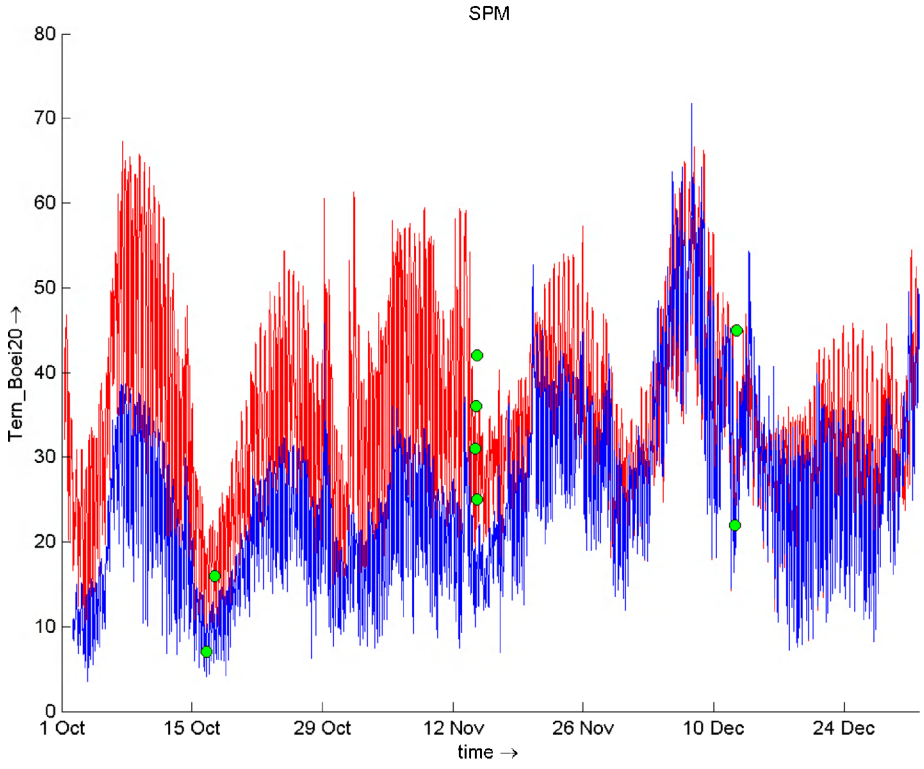

Figure 5.1 Computed and observed SPM concentration (mg/l) at Terneuzen boei 20, Q4 2006. Red: previous hydrodynamics, cyclic Q4 2006 months ; Blue: present hydrodynamics, cyclic complete 2006; Green dots: observations.

Appendix A.3 shows a comparison of remote sensing data of the near-surface suspended sediment concentration and model results at (nearly) the same time. Spatial and temporal variations are reproduced by the model to a reasonable extent. A quantitative assessment of results based on statistical techniques has not yet been carried out. Techniques developed in the framework of North Sea suspended sediment modelling (Blaas et al. 2007) may be applied.

Based on the combination of remote sensing data and model results, it is clear that in the outer estuary most of the variability in near-surface SPM levels is jointly explained by the tide (both semidiurnal and neap-spring) and wind (waves). In the inner estuary the tidal effect remains strong, but the effect of wind (waves) becomes gradually less important. However, the effect of freshwater discharge becomes important towards Antwerp and beyond. A higher freshwater discharge results in higher SPM levels. This is on the one hand caused by a higher fluvial sediment load and on the other hand by an enhanced estuarine circulation by which sediment remains trapped. Also, the turbidity maximum migrates seawards. Finally, variations in SPM levels near Antwerp are also caused by the release of dredged material from harbour maintenance for a significant part, as a substantial part of the sediment flux becomes temporarily trapped in access channels and in Deurganckdok. In the Western Scheldt this effect is much smaller, as the siltation rate in the harbours of Vlissingen and Terneuzen is limited compared with the natural gross sediment flux.

Figure 5.2 shows the computed seasonal average surface SPM concentration in Q1 – Q4 2006. A substantial seasonal variability occurs induced primarily by variations in freshwater discharge and wind. Periods with high discharge or strong wind do occur more frequently in winter than in summer. However, periods with low discharge and little wind occurring is winter show low concentrations similar to typical summer levels. An example hereof is October, 2006. A comparison between Figure 5.2 and Figure 2.22 shows that spatial concentration patterns match, with higher levels near Zeebrugge and Antwerp and lower levels in between in the Western Scheldt. However, a detailed quantitative comparison is not possible as the datasets from which the averages are computed differ. The model averages are based on a complete high-frequency dataset (interval 5 min) covering 2006, whereas the remote-sensing averages are based on 84 images scattered over the period 2006 – 2008.

Figure 5.3 shows the computed bed composition in summer and winter. Although at first sight the bed composition is similar, with low mud contents in channels and other exposed areas and high mud contents in harbour basins and at sheltered intertidal flats, still differences exist. Figure 5.4 presents the difference between the summer and winter bed composition. It is shown that in winter, due to the more severe wave climate, the mud content in exposed parts becomes lower. This mud is deposited in deeper parts, where wave effects are less. This effect occurs at a large scale in the shallow outer estuary and at a smaller scale at the edges of tidal flats in the inner estuary. Remote sensing data on bed composition confirm this seasonal trend with respect to tidal flats. Unfortunately, no validation data is available on the elevated mud fraction in deeper parts in winter.

An ongoing discussion concerns the relative importance of biological effects on the observed seasonal dynamics of mud (e.g. on stability or flocculation). The present model does not (yet) include biological effects, but is nevertheless able to explain a large part of the observed variability. This suggests that biological variability is not a dominant factor on a large scale. However, more quantification is required for firm conclusions. Also, the possible biological influence on average concentration levels and bed composition is implicitly taken into account by calibration.

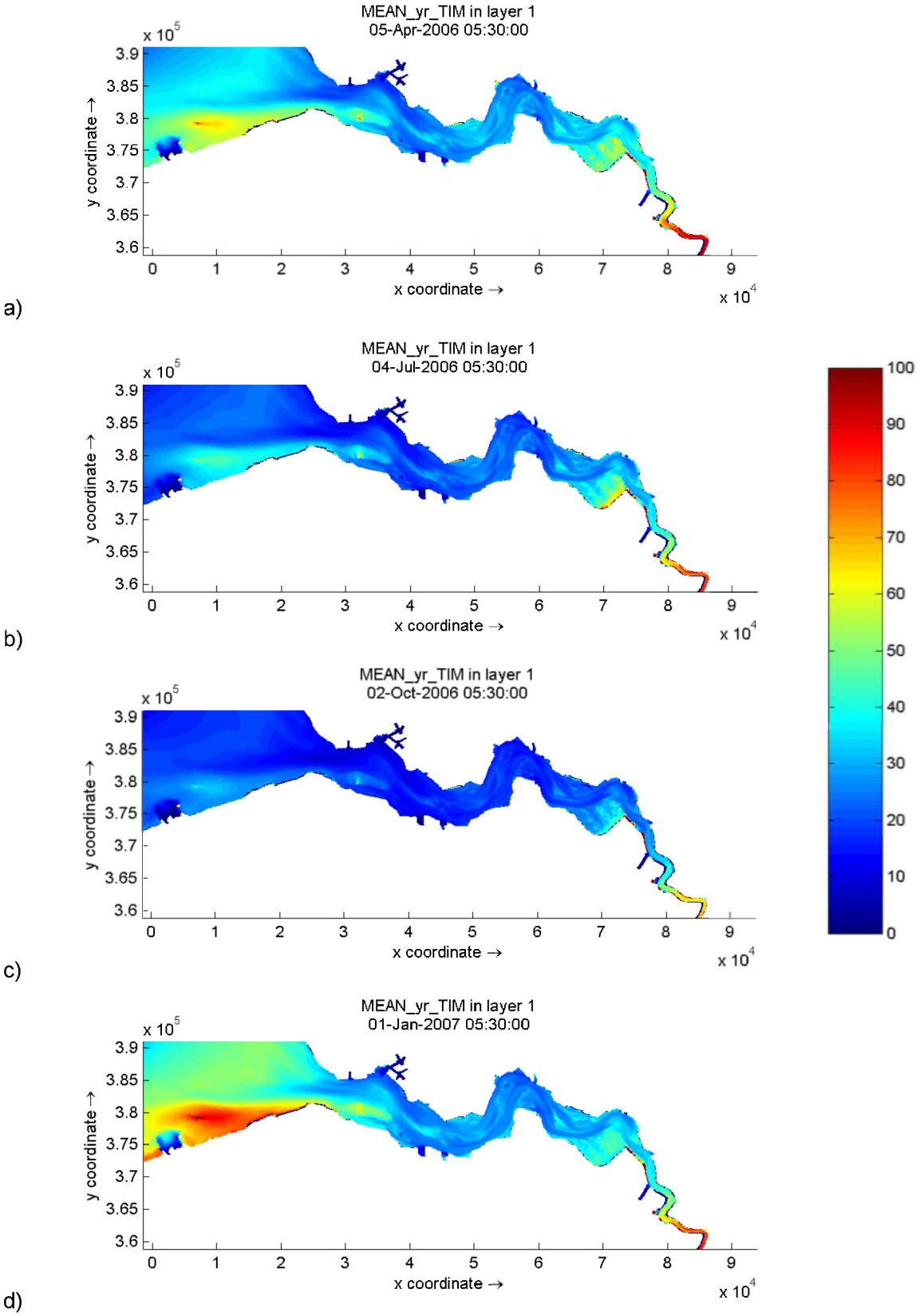

Figure 5.2 Computed seasonal-average surface SPM concentration (mg/L). a) Jan-Mar; b) Apr–Jun c) Jul–Sep d) Oct–Dec.

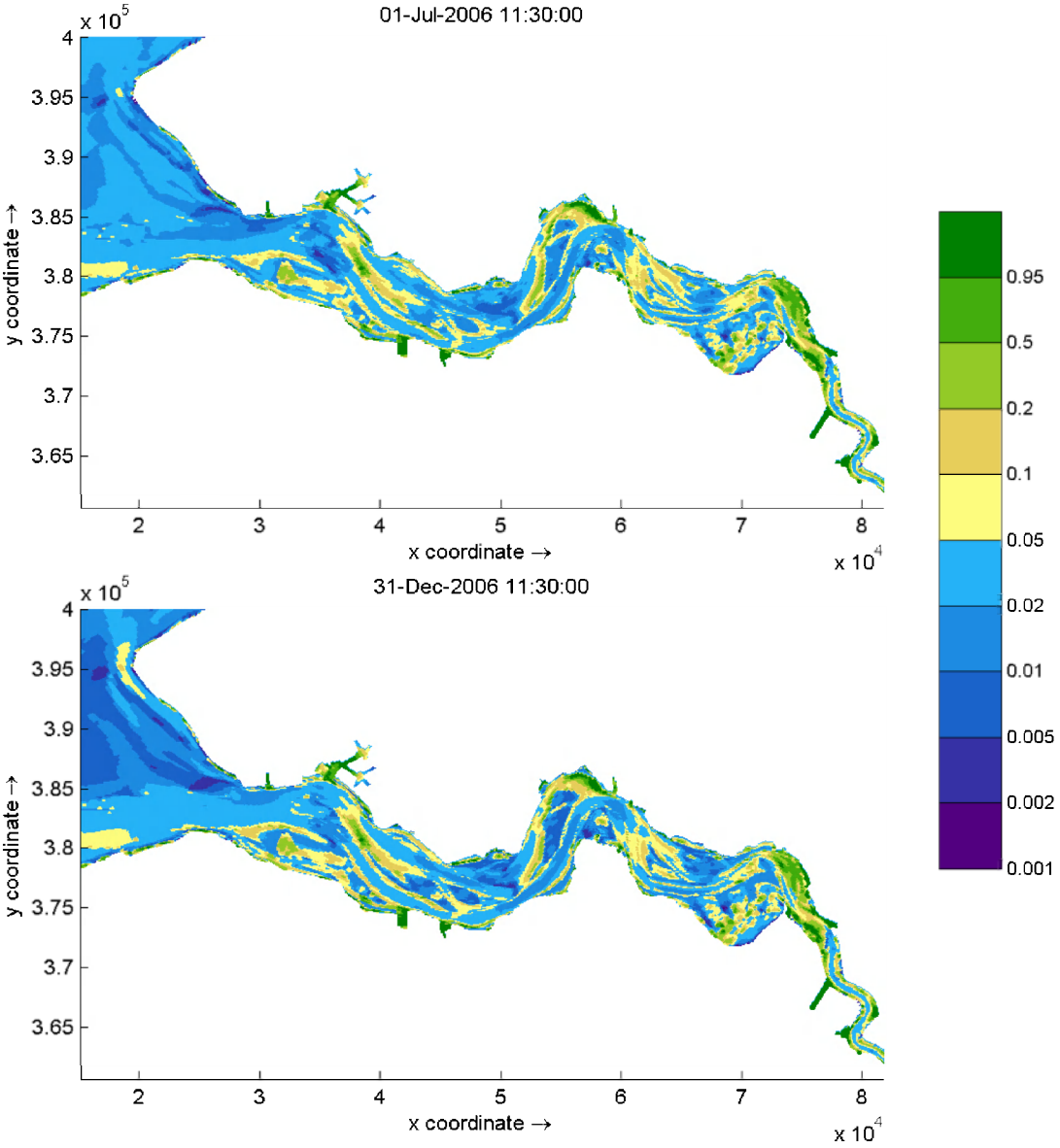

Figure 5.3 Computed mud fraction in seabed in summer (top, 1/7/2006)) and winter (bottom, 31/12/2006).

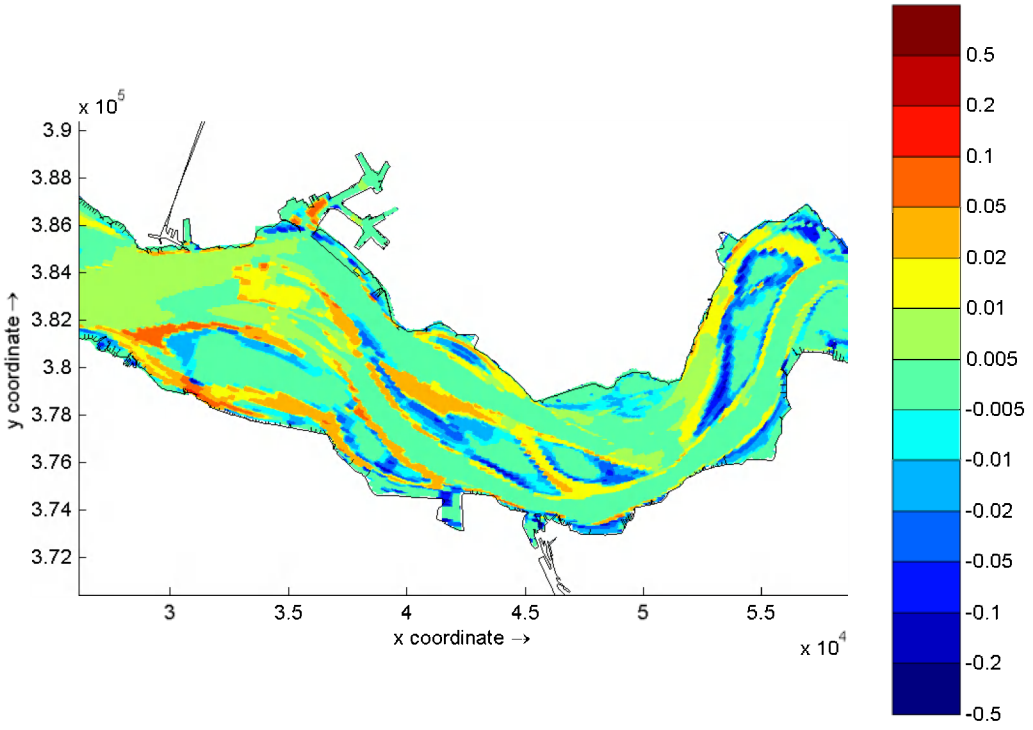

Figure 5.4 Difference between winter and summer of mud fraction in seabed.

Table 5.1 Final parameter settings used in 3D model. Note that the settings for the marine and fluvial fraction are equal. w_s = settling velocity, τ_{criti} = critical shear stress for erosion of bed layer i; M_i = erosion parameter of bed layer i; d = thickness of buffer layer; α = fraction deposition towards bed layer 2.

parameter	value	units	value	units
	fraction 1: marine		*fraction 2: fluvial*	
w_s	1.0	mm/s	1.0	mm/s
α	0.1	–	0.1	–
τ_{crit1}	0.1	Pa	0.1	Pa
M_1	1.16×10^{-5}	s^{-1}	1.16×10^{-5}	s^{-1}
d	0.05	m	0.05	m
τ_{crit2}	0.5	Pa	0.5	Pa
M_2	$1.75\ 10^{-7}$	$kg/m^2/s$	$1.75\ 10^{-7}$	$kg/m^2/s$

6 Applications

6.1 Determination of the influence zone of Deurganckdok on SPM transport

In this section we discuss the impact of DGD on sediment dynamics, elaborating further on previous work presented in van Kessel et al. (2009). As in the previous DGD simulations the initial condition for the sediment concentration in the North Sea was not equal to that of the reference simulation, the impact of DGD on the SPM dynamics in the Western Scheldt could not be assessed correctly. Therefore Run WL10 in van Kessel et al. (2009) is replaced by run WL11 in this report. Runs WL6 and WL9 are taken from van Kessel et al. (2009). A full description of this test case can be found in Belliard et al. (2010). Table 6.1 gives an overview of the scenarios.

In the simulations, dredging and dumping is implemented as follows. In a user-defined area (here DGD) all bed sediment exceeding a user-defined limit is removed at a user-defined frequency and released back at a user-defined location at a user-defined rate. This guarantees that over time, the released mass exactly matches the dredged mass. If no sedimentation occurs, no dredging and dumping takes place. In the present simulations the dredging frequency is set at once per week, the release rate is set at 10 kton/day.

Table 6.1: Overview of computations to analyse Deurganckdok effects.

Run	Description
s28_Antw_WL6	The present situation (reference)
s28_Antw_WL9	Dumping location shifted down-estuary, to “Schaar Ouden Doel”
s28_Antw_WL11	Suppressed siltation in DGD (“no harbour”)

6.1.1 Scenario WL9: down-estuary shift of dumping location

Figure 6.1 displays the time- and depth-averaged SPM concentrations for scenario runs WL9 and WL6 over a period of three months. Figure 6.2 shows the absolute and relative difference between both scenarios. A positive value in the figure implies an increase in sediment concentration in scenario WL9.

Figure 6.1 shows a difference in mud concentration between the two scenarios near Antwerp and in the eastern part of the Western Scheldt. Further seawards the difference is insignificant. The gross fluxes and the quantity of disposed sediment in the lower estuary domain are identical to those for scenario run WL6, except for an increase of about 17% in the net SPM transport flux from the Sea Scheldt to the Western Scheldt. This SPM increase also results in a higher deposition and erosion from the bed in the eastern part of the Western Scheldt (not shown in Figure 6.1).

SPM levels are affected by the downstream shift of the disposal location of DGD in a zone stretching from the eastern part of the Western Scheldt to the Upper Sea Scheldt and the Rupel tributary. This influence zone extends over 90 km with the highest differences located in the Sea Scheldt.

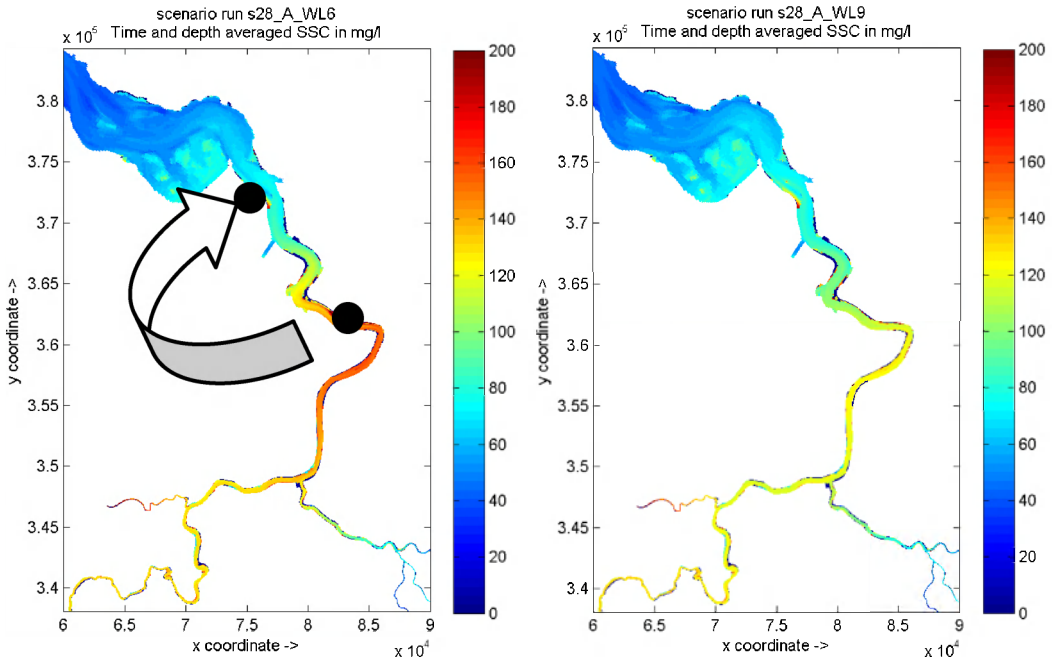

Figure 6.1: Time and depth-average SPM concentration (mg/L) (Left: reference run WL6, right: scenario run WL9). Black dots and arrow indicate position shift of dumping location.

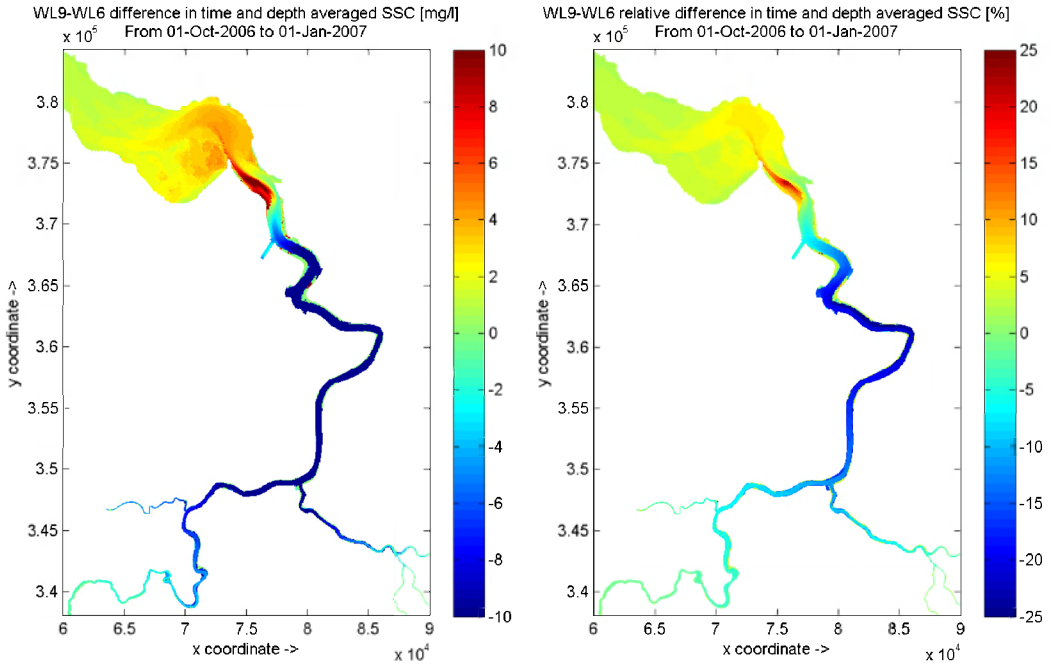

Figure 6.2: Impact of a shift in dumping location on SPM concentration. Left: absolute difference (mg/l), right: relative difference (%).

6.1.2 Scenario WL11: no harbour

Scenario WL11 was set up in order to investigate the impact of the absence of siltation in Deurganckdok on mud dynamics. DGD was not completely removed in the simulation, as it would require a new bathymetry and an additional hydrodynamic simulation. Instead, deposition of mud in DGD was disabled by setting the critical shear stress for deposition at zero inside DGD. Figure 6.3 shows the computed SPM concentration for both scenarios with (WL6) and without (WL11) deposition in DGD. Figure 6.4 shows the absolute and relative differences between both simulations. Note that in the simulation without deposition in DGD, also no sediment release because of maintenance dredging in DGD takes place.

The influence zone of scenario WL11 does not extend as far downstream as the influence zone of a shift in dumping location discussed in the previous section (6.1.1). There is no significant change in the net SPM transport flux from the Sea Scheldt to the eastern part of the Western Scheldt.

However, the suppression of siltation in DGD affects turbidity levels in a zone that extends from the limit Western Scheldt - Sea Scheldt upstream to the Upper Sea Scheldt and the Rupel tributary. This influence zone stretches over 80 km. The highest differences (>10 mg/l) occur in the Sea Scheldt around Antwerp This effect is variable in space and time. During maintenance dredging the effect is larger, notably near the release locations. However, in periods without maintenance dredging the effect is smaller (or even negative), as DGD acts as a sediment sink. On average, the strongest increase in SPM concentration because of the presence of DGD occurs near the release locations of dredged material. The strongest decrease in SPM concentration occurs down-estuary towards the Belgian-Dutch border, where the impact of DGD as sediment sink exceeds the impact of the release locations as sediment source. Averaged over a larger area, the sink effect dominates over the source effect.

6.2 Set-up of a detailed model for SPM around Zeebrugge

A detailed hydrodynamic model of Zeebrugge has been developed by Flanders Hydraulics Research using Delft3D-FLOW. For a complete description of the model inputs as well as for the calibration and validation processes, the reader is referred to Dujardin et al. (2010).

The detailed grid extends from Oostende to Nieuwvliet, just across the Dutch border and about 15 to 20 km seaward (Dujardin et al. 2010). The horizontal grid is displayed in Figure 6.5. The vertical discretisation is done with six σ-layers with an identical vertical distribution. The grid has dimensions of 212 (M-directions) × 221 (N-directions) and counts 30,029 active cells. The resolution varies from 250 m in the open sea down to approximately 30-35 m inside the harbour (Dujardin et al. 2010). Within the port, the bathymetry is generated based on the latest data of 2009 while in the far field of the computational domain especially in the open sea, the bathymetry is based on the data from 1999.

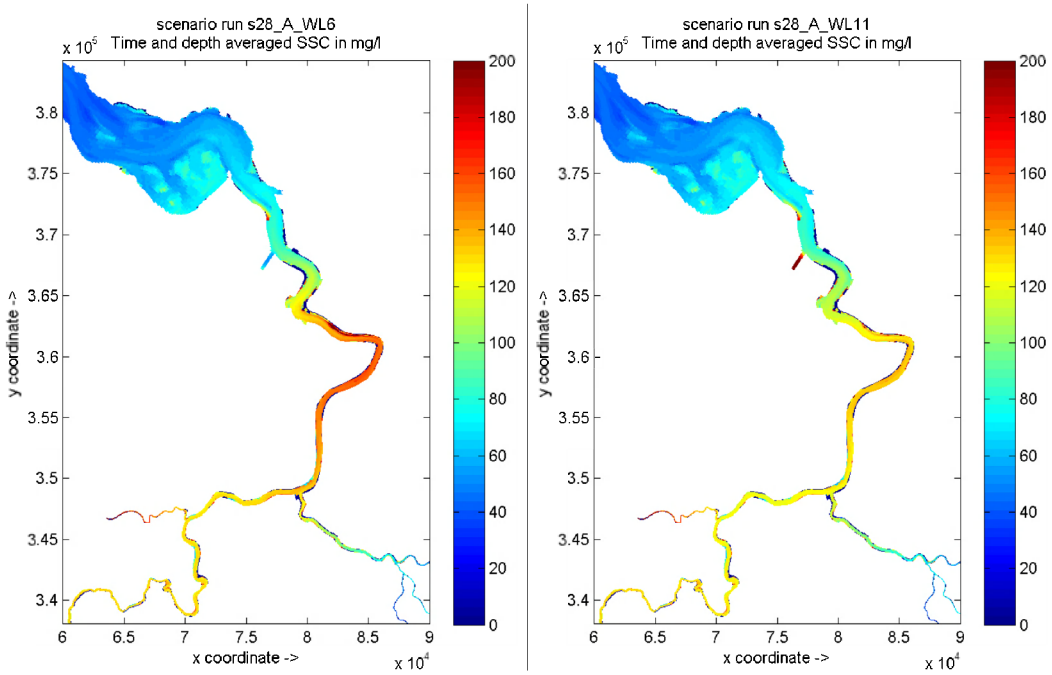

Figure 6.3 : Influence zone for suppression of siltation in DGD (Left: reference run WL6, right: scenario run WL11: the "no harbour" testcase).

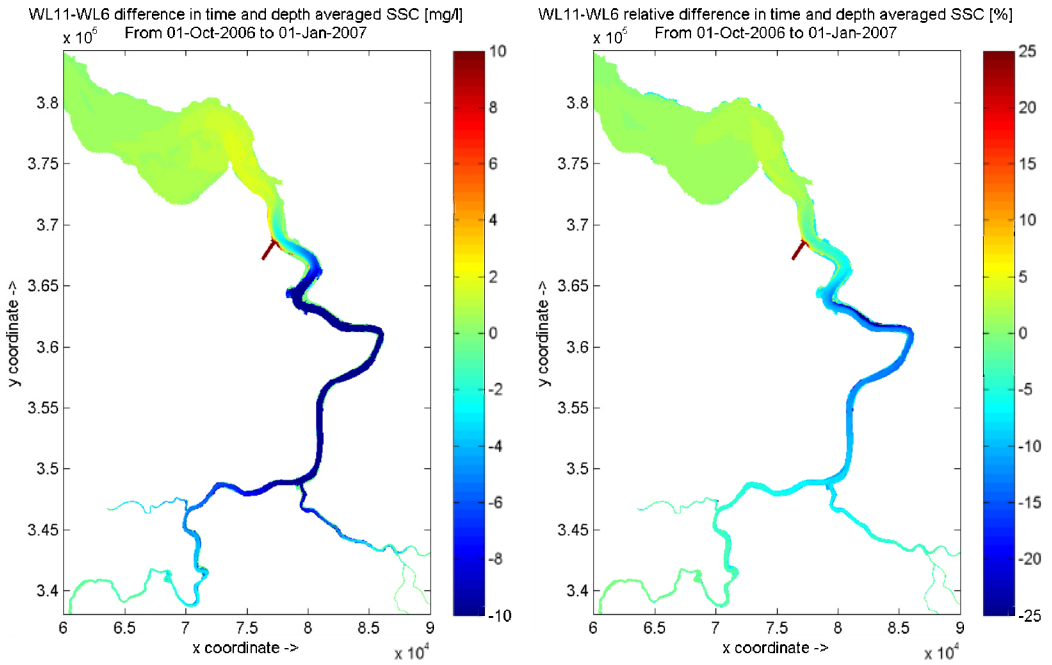

Figure 6.4: Influence zone for suppression of siltation in DGD (Left: absolute difference (mg/l), right: Right: relative difference [%]).

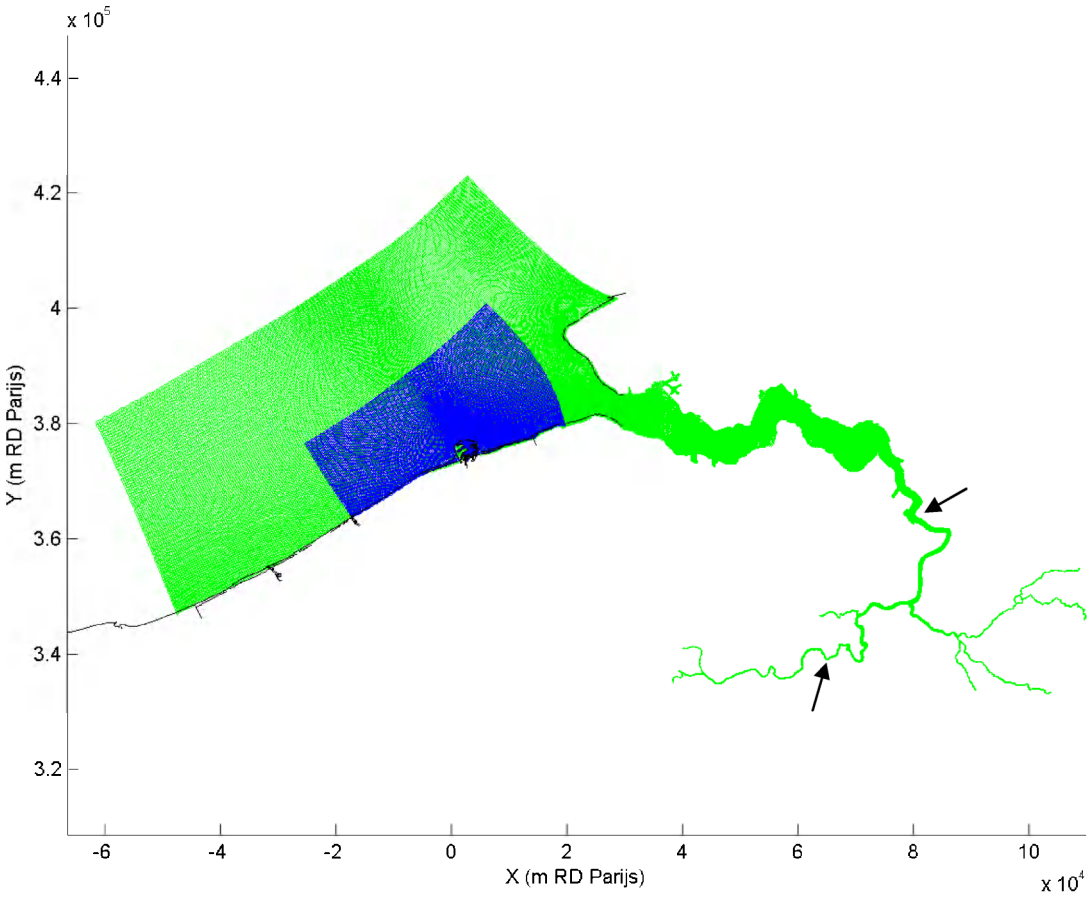

Figure 6.5: Coverage of the detailed grid of Zeebrugge (in blue) on the LTV-grid (in green). Figure from Dujardin et al. (2010). Black arrows indicated 2 ppt isohaline at high discharge (15/2/2006 00:00) and low discharge (4/7/2006 10:00), see Figure 6.10.

6.2.1 Coupling of hydrodynamics

As a first test, two tidal cycles (25h) of hydrodynamics are selected, which are representative for the entire period. Special care was taken to select two successive tidal cycles within which differences between the start and end values of both the water level and velocity are minor. Eventually, a representative period of 25 hours from 21/12/2006 at 19:50 to 22/12/2006 at 20:50 is selected and stored with a time step of 30 min in the communication file (Figure 6.6). No grid aggregation was performed.

As a next stage, a standalone software program called Flocheck is used in order to check residence times and to adapt volumes locally in critical cells which may limit the time step of further sediment transport simulation. Conceptually, the Flocheck algorithm checks the *.vol file generated from the coupling with the hydrodynamic model and correct volumes which are set to zero or even negative (which may occur at dry cells in a tidal situation) into small but positive values.

6.2.2 Set-up of the mud transport model

The Zeebrugge mud transport model works with the same substances as the overall mud transport model. It is thus set-up as a nested detailed mud transport model for the area of Zeebrugge. A two-day period is simulated, from 21/12/2006 19:50 to 23/12/2006 21:50.
In order to evaluate mass balances in the detailed model, a new set of 8 zones has been designed for this detailed mud transport model. They have been generated using the Delft3D-DIDO aggregation module. Figure 6.7 indicates their positions.

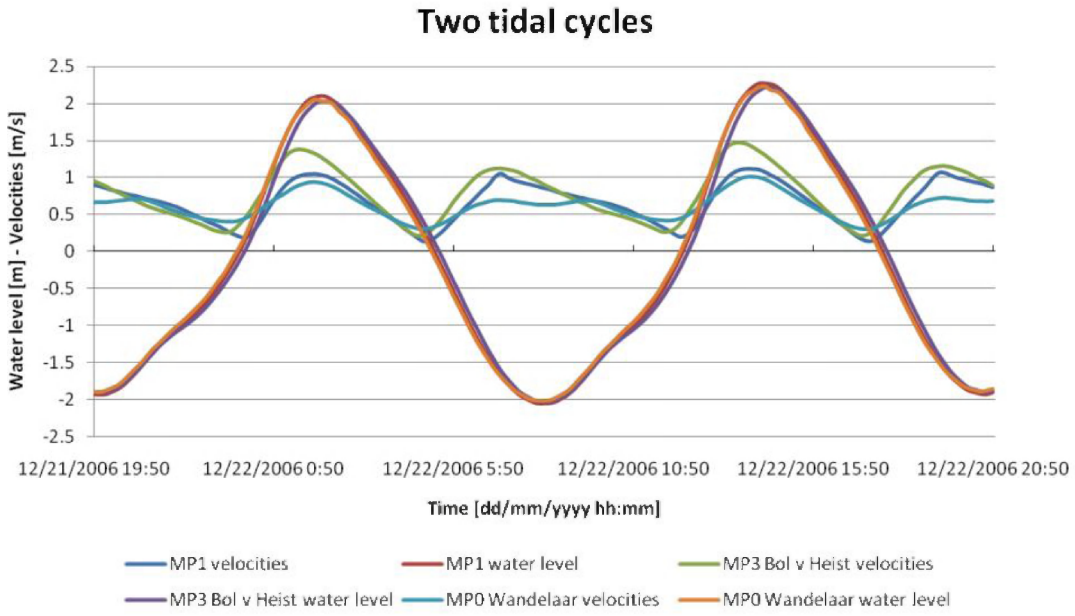

Figure 6.6: Selected period stored in the communication file. This tidal period consists of two successive tidal cycles. MP1, MP3 Bol v Heist and MP0 Wandelaar are observation points.

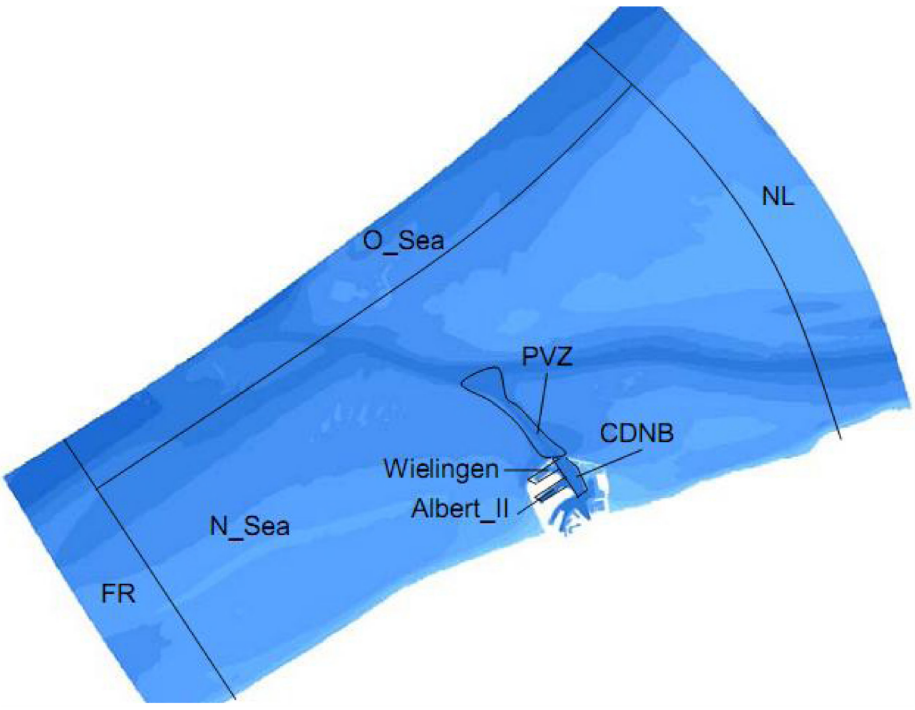

Figure 6.7: Location of the zones defined in the detailed model of Zeebrugge to make a mass balance.

The initial conditions are obtained from maps of the overall calibrated model. Three open boundaries are defined in the detailed mud transport model. Each of these open boundaries is divided in several boundary sections. The southern and northern boundaries are divided in 10 boundary sections whereas the boundary parallel to the coast is split up in 20 boundary sections.

For this first coupling, only time- and depth-averaged constant values are chosen to be prescribed in the boundary sections. Therefore, an average of the concentration values over time and over depth is computed for each observation point. Values for substance IM2 (fluvial fraction) are negligible and therefore set to zero at the boundaries of the detailed model.

Initial simulations on fine sediment transport have been made. As model calibration is still at an early stage, results are not yet presented herein. Further development of and first application of the Zeebrugge model is scheduled for 2011.

6.3 Dutch management issues

After last year's assessment of impacts of dredged sediment release on suspended sediment concentration, bed composition and the return flux towards harbour basins, long-term effects have been investigated in more detail this year.

To analyze the effect of freshwater discharge, two neap-spring periods with high and low discharge within the available 2006 hydrodynamics have been selected. These are the period of 8/2 – 24/2 for high discharge (283 m^3/s 10-day average) and 7/7 – 21/7 for low discharge (42 m^3/s 10-day average).

Figure 6.8 and Figure 6.9 show results for high and low discharge, respectively. In the upper panel the computed salinity distribution is shown along the thalweg of the Scheldt between Vlissingen and Rupelmonde and in the lower panel the SPM concentration. Figure 6.10 shows the same computed data from a top-view. It is clear that SPM levels and the location of the turbidity maximum depend strongly on the freshwater discharge. At a higher discharge SPM levels typically increase. The turbidity maximum moves in concert with the 1-2 ppt isohaline. At dynamic equilibrium it is located around 85 km for Q = 283 m^3/s and around 135 km for Q = 42 m^3/s.

The correlation between freshwater discharge and SPM level for the complete year of 2006 at Terneuzen is shown in Figure 6.11. Again a positive correlation is found. This implies that for example harbour maintenance dredging is likely to be correlated with freshwater discharge. However, it is noticed that the response time of the system with regard to changes in freshwater discharge is substantial, so no 1:1 correlation between salinity (and SPM levels) and freshwater discharge exists.

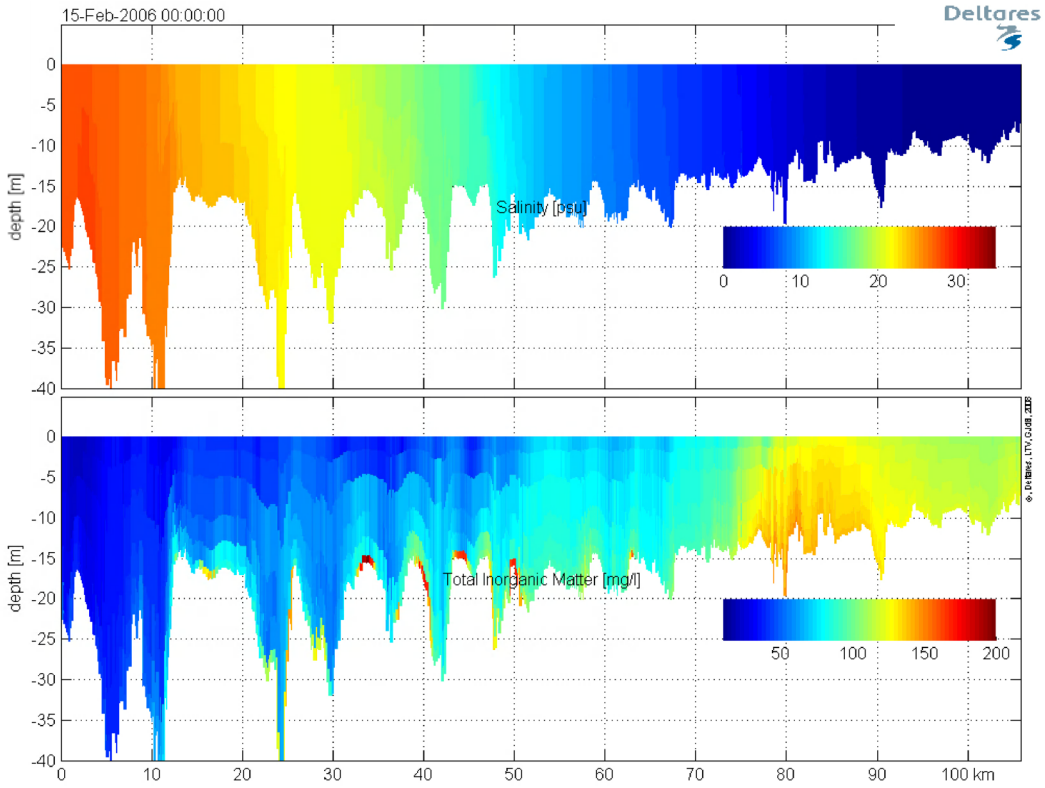

Figure 6.8 Salinity (ppt) and SPM concentration (mg/l) distribution along the Scheldt estuary for high discharge (283 m^3/s).

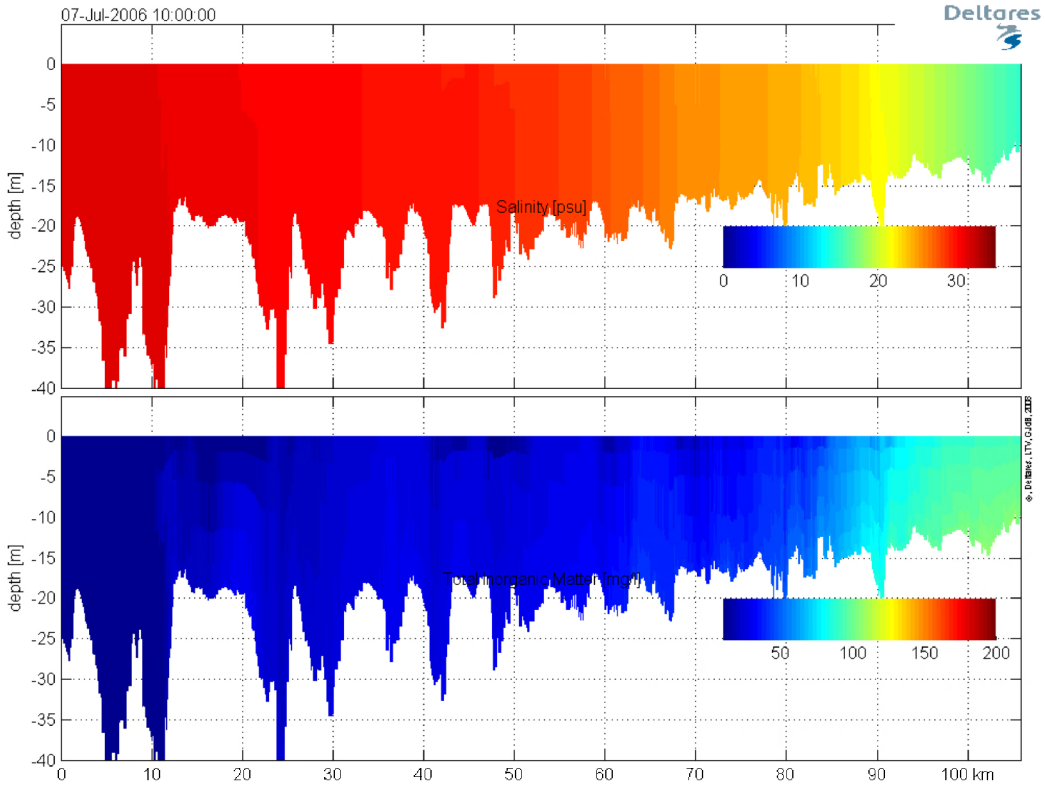

Figure 6.9 Salinity (ppt) and SPM concentration (mg/l) distribution along the Scheldt estuary for low discharge (42 m^3/s).

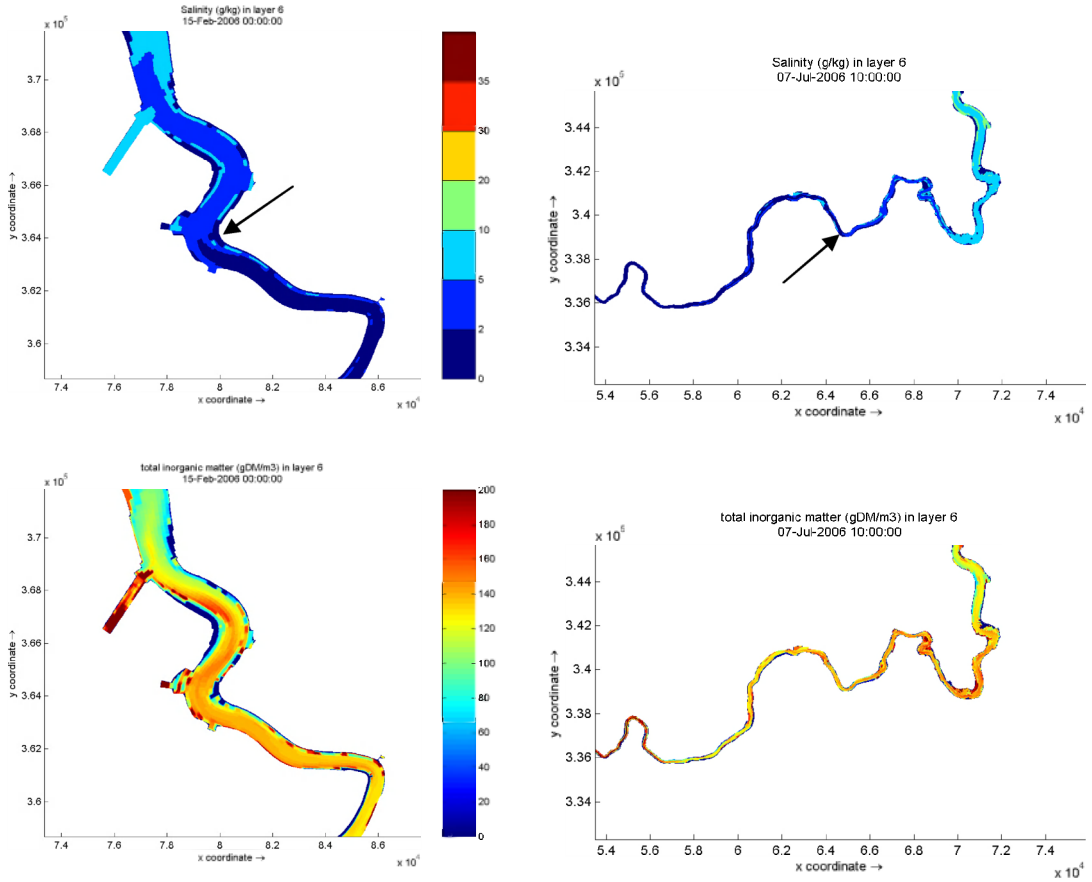

Figure 6.10 Salinity (top) and SPM (bottom) distributions at high (left) and low (right) discharge. Arrows indicate 2 ppt isohaline. For a general overview see Figure 6.5.

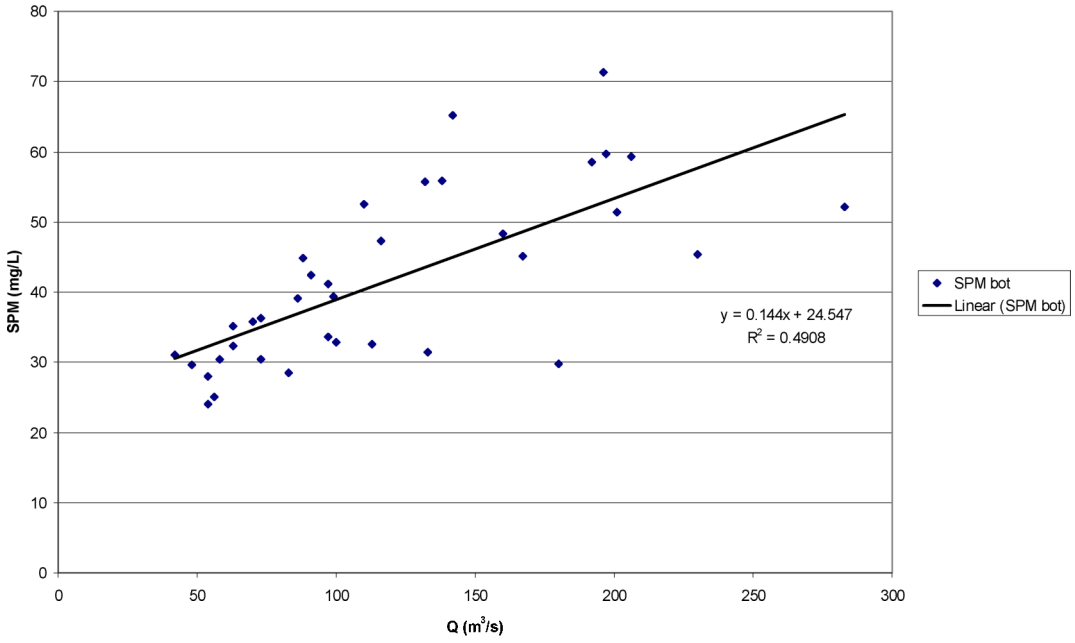

Figure 6.11 Relationship between 10-day average freshwater discharge and computed near-bed SPM concentration near Terneuzen.

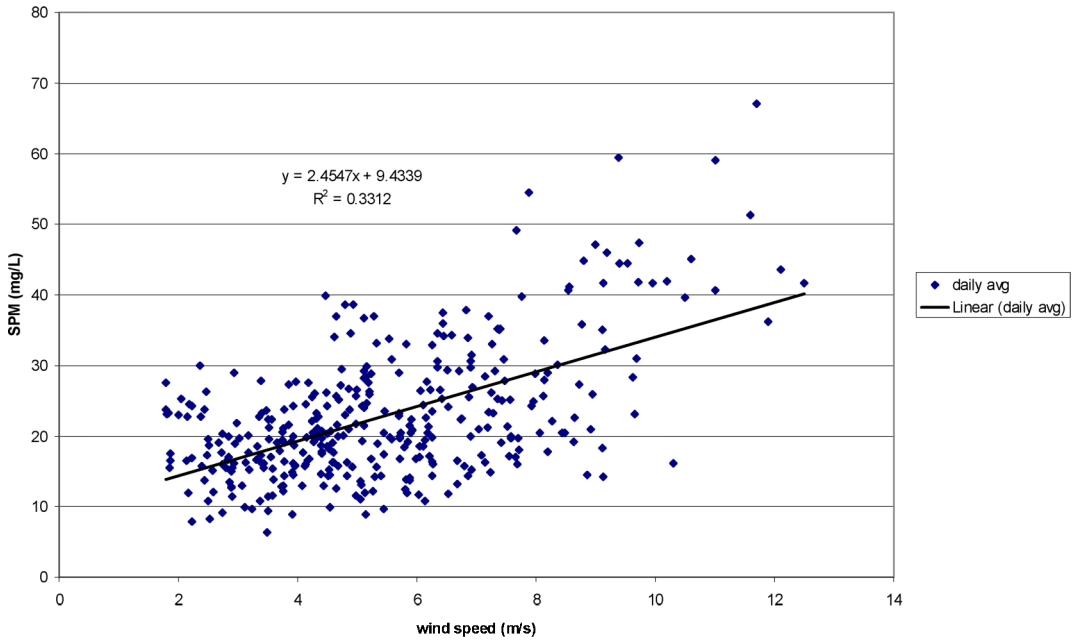

Figure 6.12 Relationship between daily average wind speed and computed near-bed SPM concentration near Terneuzen.

Harbour siltation depends on both sediment concentration in front of the harbour and exchange rate between estuary and harbour. Stormy periods will results in higher SPM levels and therefore more siltation at Terneuzen, as at this location a positive correlation exists between wind speed and SPM levels (Figure 6.12). Exchange processes may also be influenced by wind, but this is expected to be a secondary effect compared to tidal and density-driven exchange.

At Antwerp and near Deurganckdok the influence of wind is less significant. The influence of the freshwater discharge is important, but the relationship between discharge and SPM levels is more complicated than in the Western Scheldt and depends on the position of the point of interest relative to turbidity maximum. At positions seaward of the ETM, an increase of freshwater discharge will result in a strong increase in SPM, as both the ETM will migrate in seaward direction and the SPM level in the ETM will increase. However, at positions landward of the ETM, an increase of freshwater discharge will result in a limited increase or even a decrease in SPM, as the SPM level increase in the ETM will be compensated by the migration of the ETM away from the point of interest. These effects will not occur immediately, as the estuarine systems responds slowly to changes in freshwater discharge.

7 Conclusions and recommendations

7.1 Conclusions

A comparison between remote sensing data and model results shows that in many cases the SPM distribution patterns are similar. These cases include both quiet and rough weather conditions and spring and neap tides.

In 2006 seasonal dynamics are not as pronounced as the long-time average. For example, the SPM levels in autumn are very low for a prolonged period. This period (until the end of November) is characterised by the absence of storms and high freshwater discharge. This suggests an important influence of these two parameters. The model supports this hypothesis. Early April and end May, when a high freshwater discharge coincides with strong winds, very high SPM levels are both observed and computed.

With regard to the impact of a shift of the release location of dredged material from Deurganckdok, it is concluded that the location of the turbidity maximum is sensitive to such shift. A seaward shift results in a concentration increase in seaward direction and a reduction in landward direction. This offers perspectives for optimisation of the release of dredged material. Depending on the release location with respect to the location of the salinity front, a residual transport of released material in landward or seaward direction may be enforced.

The presence of Deurganckdok affects the turbidity maximum, as the net influx into this harbour basin caused by sedimentation and the net outflux from this basin by maintenance dredging is not negligible compared to the natural local sediment flux in the Lower Sea Scheldt. Depending on time and location, both higher and lower concentrations occur. During maintenance dredging the concentration tends to be higher, notably near release locations, whereas during periods without maintenance dredging the concentration tends to be lower, as Deurganckdok acts as a sediment sink. However, on average the presence of Deurganckdok results in a local increase in suspended concentration levels.

7.2 Recommendations

Future activities can include further development, application and dissemination. It is proposed not to initiate new developments within the framework of the present project, but to monitor developments in other projects. For example, a bed module for sand-mud mixtures will become available in the framework of the Building with Nature programme, which is potentially suitable for inclusion into the present Scheldt model.

Important applications are in the field of optimisation of the release of dredged material from harbour maintenance. Alternative release locations and methods (e.g. timing) may be evaluated, possibly resulting in a more favourable distribution of SPM or a reduction of harbour maintenance dredging. Also the effect of a further deepening of the estuary on the mud balance may be investigated.

8 References

Babin, M., Morel, A., Gentili, B. (1996). Remote sensing of sea surface sun-induced chlorophyll fluorescence: Consequences of natural variations in the optical characteristics of phytoplankton and the quantum yield of chlorophyll a fluorescence. International Journal of Remote Sensing 17: 2417-2448.

Belliard, J.P.; Vanlede, J.; Mostaert, F. (2010.). Modelling of mud dynamics in the Scheldt estuary within the framework of LTV: A report submitted to the University of Budapest Technology and Economics in partial fulfilment of the Degree of MSc in Hydro-Informatics and Water Management. Version 2_0. WL Rapporten, 770_53. Flanders Hydraulics research: Antwerp, Belgium.

Blaas, M., El Serafy, G.Y.H., van Kessel, T., de Boer, G.J., Eleveld, M.A., van der Woerd, H.J. (2007). Data model integration of SPM transport in the Dutch coastal zone. Proc. Joint 2007 EUMETSAT Meteorological Satellite Conference and the 15th American Meteorological Society (AMS) Satellite Meteorology & Oceanography Conference. Darmstadt: EUMETSAT. ISBN 992-9110-079-X.

Callaghan, D.P., Bouma, T.J., Klaassen, P., van der Wal, D., Stive, M.J.F., Herman, P.M.J. (2010). Hydrodynamic forcing on saltmarsh-development: distinguishing the relative importance of waves and tidal flows. Estuarine, Coastal and Shelf Science 89(1): 73-88. doi:10.1016/j.ecss.2010.05.013

Decrop, B.; Vanlede, J.; Verwilgen, J.; van Holland, G. Mostaerd, F. (2010): Permanente verbetering modelinstrumentarium. Stroming aan de toegang tot het Zandvliet-Berendrecht sluizencomplex. Rapport 2D numeriek modelonderzoek. WL Rapporten, 753_10. Waterbouwkundig Laboratorium en IMDC rapport nr. I/RA/11313/09.090/BDC, Antwerpen, België.

Dujardin A.; B. De Clercq; J. Vanlede; R. Delgado; G. van Holland; F. Mostaert (2010). Verbetering numeriek instrumentarium Zeebrugge: Bouw en afregeling detailmodel. Versie2_0. WL Rapporten, 753_08, Waterbouwkunding Laboratorium, Soresma en IMDC, Antwerpen, België.

Eleveld, M.A., Pasterkamp, R., van der Woerd, H.J., Pietrzak, J.D. (2008). Remotely sensed seasonality in the spatial distribution of sea-surface suspended particulate matter in the southern North Sea. Estuarine, Coastal and Shelf Science 80(1), 103-113. doi:10.1016/j.ecss.2008.07.015

Fettweis, M.P., Nechad, B. (2011). Evaluation of in situ and remote sensing sampling methods for SPM concentrations, Belgian continental shelf (southern North Sea). Ocean Dynamics 61(2-3), 157-171. doi 10.1007/s10236-010-0310-6 (Open Access)

Fung, A.K., Li, Z., & Chen, K.S. (1992). Backscattering from a randomly rough dielectric surface. IEEE Transactions on Geoscience and Remote Sensing, 30, 356-369.

Gilerson, A., Zhou, J., Hlaing, S., Ioannou, I., Schalles, J., Gross, B., Moshary, F., Ahmed, S. (2007). Fluorescence component in the reflectance spectra from coastal waters. Dependence on water composition. Optics Express 15: 15702-15721.

Grasmeijer, B.T, Eleveld, M.A. (2009). Evaluation of SPM measurements in the North Sea. Research in the framework of the EIA sand extraction North Sea 2008-2012. Alkyon Report I, A2273.

Hommersom, A., Peters, S., van Der Woerd, H.J., Eleveld, M.A., de Boer, J. (in press). Chi-square in an inverse bio-optical model: concentration retrieval, automatic local calibration and water type detection. Accepted by Canadian Journal of Remote Sensing.

Koninklijke Marine – Dienst der Hydrografie (2002). Waterstanden en stromen langs de Nederlandse kust en aangrenzend gebied. HP33. Koninklijke Marine – Dienst der Hydrografie, Den Haag, 336 pp.

Maximova, T.; Ides, S.; Vanlede, J.; De Mulder, T.; Mostaert, F., (2009a). Verbetering 2D randvoorwaardenmodel. Deelrapport 3: Calibratie bovenlopen. WL Rapporten, 753_09. Flanders Hydraulics Research, Antwerp, Belgium.

Maximova, T.; Ides, S.; De Mulder, T.; Mostaert, F. (2009b). Verbetering 2D randvoorwaardenmodel. Deelrapport 4: Extra aanpassingen Zeeschelde. WL Rapporten, 753_09. Flanders Hydraulics Research, Antwerp, Belgium.

Pietrzak, J.D., de Boer, G.J., Eleveld,M.A. (2011). Mechanisms controlling the intra-annual mesoscale variability of SST and SPM in the southern North Sea. Continental Shelf Research 31(6), 594-610. doi:10.1016/j.csr.2010.12.014.

Rijkeboer, M., Dekker, A.G., Gons, H.J. (1998). Subsurface irradiance reflectance spectra of inlands waters differing in morphology and hydrology. Aquatic Ecology 31: 313-323.

Sterckx, S., Knaeps,E., Bollen, M., Trouw, K.,Houthuys, R.,2007. Retrieval of suspended sediment from Advanced Hyperspectral Sensor data in the Scheldt Estuary at different stages in the tidal cycle. Marine Geodesy, 30: 1–12.

Van der Wal, D., A. Wielemaker-van den Dool, P.M.J. Herman (2010b). Spatial synchrony in intertidal benthic algal biomass in temperate coastal and estuarine ecosystems. Ecosystems 13: 338-351.

Van der Wal, D., Herman, P.M.J., 2007. Regression-based synergy of optical, shortwave infrared and microwave remote sensing for monitoring the grain-size of intertidal sediments. Remote Sensing of Environment 111 (1): 89-106.

Van der Wal, D., Herman, P.M.J., Wielemaker-van den Dool, A., 2005. Characterisation of surface roughness and sediment texture of intertidal flats using ERS SAR imagery. Remote Sensing of Environment 98 (1): 96-109.

Van der Wal, D., P.M.J. Herman, R.M. Forster, T. Ysebaert, F. Rossi, E. Knaeps, Y.M.G. Plancke, S.J. Ides (2008). Distribution and dynamics of intertidal macrobenthos predicted from remote sensing: response to microphytobenthos and environment. Marine Ecology Progress Series 367: 57-72.

Van der Wal, D., van Kessel, T., Eleveld, M.A., Vanlede, J. (2010a). Spatial heterogeneity in estuarine mud dynamics. Ocean Dynamics 60: 519–533. doi: 10.1007/s10236-010-0271-9

Van Kessel, T., J. Vanlede (2009). Impact of harbour basins on mud dynamics Scheldt estuary in the framework of LTV. Deltares & FHR report 1200253, Delft, The Netherlands.

Van Kessel, T., J. Vanlede, A. Bruens (2006). Development of a mud transport model for the Scheldt estuary in the framework of LTV. WL | Delft Hydraulics & WL Borgerhout report Z4210.

Van Kessel, T., J. Vanlede, J. de Kok (2007). Development of a mud transport model for the Scheldt estuary in the framework of LTV. Phase 1. WL | Delft Hydraulics & WL Borgerhout report Z4375.

Van Kessel, T., J. Vanlede, M.A. Eleveld, D. van der Wal (2008). Mud transport model for the Scheldt estuary in the framework of LTV. Deltares report Z4594, Delft, The Netherlands.

Vos, R.J., Hakvoort, J.H.M., Jordans, R.W.J., Ibelings, B.W (2003). Multiplatform optical monitoring of eutrophication in temporally and spatially variable lakes. Science of the Total Environment 312: 221–243.

A Remote sensing water column

A.1 Overview of the collected remote sensing data

(filenames contain acquisition date (year, month, day) and time (hours, minutes, seconds).

File	date	time
MER_FR__2PNUPA20060109_103009_000000982044_00094_20188_5070.N1	20060109	103009
MER_FR__2PNUPA20060129_100129_000000982044_00380_20474_5109.N1	20060129	100129
MER_FR__2PNUPA20060323_103539_000000982046_00137_21233_5111.N1	20060323	103539
MER_FR__2PNUPA20060401_105238_000000982046_00266_21362_5113.N1	20060401	105238
MER_FR__2PNUPA20060402_102124_000000982046_00280_21376_5107.N1	20060402	102124
MER_FR__2PNUPA20060503_104702_000000982047_00223_21820_5115.N1	20060503	104702
MER_FR__2PNUPA20060504_101552_000000982047_00237_21834_5117.N1	20060504	101552
MER_FR__2PNEPA20060510_102655_000000982047_00323_21920_3828.N1	20060510	102655
MER_FR__2PNUPA20060608_101550_000000982048_00237_22335_9560.N1	20060608	101550
MER_FR__2PNUPA20060610_105240_000000982048_00266_22364_9562.N1	20060610	105240
MER_FR__2PNUPA20060611_102132_000000982048_00280_22378_5119.N1	20060611	102132
MER_FR__2PNUPA20060617_103257_000000982048_00366_22464_5121.N1	20060617	103257
MER_FR__2PNUPA20060623_104418_000000982048_00452_22550_5095.N1	20060623	104418
MER_FR__2PNUPA20060629_105538_000000982049_00037_22636_5105.N1	20060629	105538
MER_FR__2PNUPA20060630_102426_000000982049_00051_22650_5089.N1	20060630	102426
MER_FR__2PNUPA20060703_103008_000000982049_00094_22693_5091.N1	20060703	103008
MER_FR__2PNUPA20060704_095850_000000982049_00108_22707_5093.N1	20060704	95850
MER_FR__2PNEPA20060710_100956_000000982049_00194_22793_3830.N1	20060710	100956
MER_FR__2PNUPA20060712_104708_000000982049_00223_22822_5097.N1	20060712	104708
MER_FR__2PNUPA20060713_101601_000000982049_00237_22836_5099.N1	20060713	101601
MER_FR__2PNUPA20060715_105249_000000982049_00266_22865_5101.N1	20060715	105249
MER_FR__2PNUPA20060716_102137_000000982049_00280_22879_5103.N1	20060716	102137
MER_FR__2PNUPA20060718_105831_000000982049_00309_22908_5083.N1	20060718	105831
MER_FR__2PNUPA20060719_102713_000000982049_00323_22922_9564.N1	20060719	102713
MER_FR__2PNUPA20060725_103843_000000982049_00409_23008_5073.N1	20060725	103843
MER_FR__2PNUPA20060819_105246_000000982050_00266_23366_5076.N1	20060819	105246
MER_FR__2PNUPA20060911_103002_000000982051_00094_23695_5078.N1	20060911	103002
MER_FR__2PNEPA20060920_104646_000000982051_00223_23824_3832.N1	20060920	104646
MER_FR__2PNUPA20060921_101548_000000982051_00237_23838_9566.N1	20060921	101548
MER_FR__2PNUPA20061016_102951_000000982052_00094_24196_5080.N1	20061016	102951
MER_FR__2PNEPA20061117_102407_000000982053_00051_24654_3834.N1	20061117	102407
MER_FR__2PNEPA20070308_103530_000000982056_00137_26243_1005.N1	20070308	103530
MER_FR__2PNEPA20070312_101003_000000982056_00194_26300_1006.N1	20070312	101003
MER_FR__2PNEPA20070314_104637_000000982056_00223_26329_1007.N1	20070314	104637
MER_FR__2PNEPA20070315_101538_000000982056_00237_26343_1008.N1	20070315	101538
MER_FR__2PNEPA20070325_100124_000000982056_00380_26486_1009.N1	20070325	100124
MER_FR__2PNEPA20070328_100710_000000982056_00423_26529_1010.N1	20070328	100710
MER_FR__2PNEPA20070409_102945_000000982057_00094_26701_1011.N1	20070409	102945
MER_FR__2PNEPA20070415_104109_000000982057_00180_26787_1012.N1	20070415	104109
MER_FR__2PNEPA20070416_101004_000000982057_00194_26801_1013.N1	20070416	101004
MER_FR__2PNEPA20070501_103821_000000982057_00409_27016_1015.N1	20070501	103821
MER_FR__2PNEPA20070523_104648_000000982058_00223_27331_0593.N1	20070523	104648

MER_FR__2PNEPA20070524_101539_000000982058_00237_27345_1014.N1	20070524	101539
MER_FR__2PNEPA20070628_101542_000000982059_00237_27846_1016.N1	20070628	101542
MER_FR__2PNEPA20070719_105535_000000982060_00037_28147_1017.N1	20070719	105535
MER_FR__2PNEPA20070801_104658_000000982060_00223_28333_1018.N1	20070801	104658
MER_FR__2PNEPA20070805_102115_000000982060_00280_28390_0589.N1	20070805	102115
MER_FR__2PNEPA20070805_102116_000000982060_00280_28390_0588.N1	20070805	102116
MER_FR__2PNEPA20070830_103532_000000982061_00137_28748_1019.N1	20070830	103532
MER_FR__2PNEPA20070902_104112_000000982061_00180_28791_1020.N1	20070902	104112
MER_FR__2PNEPA20070919_100658_000000982061_00423_29034_0586.N1	20070919	100658
MER_FR__2PNEPA20071007_104102_000000982062_00180_29292_0592.N1	20071007	104102
MER_FR__2PNEPA20071020_103234_000000982062_00366_29478_0591.N1	20071020	103234
MER_FR__2PNEPA20071023_103815_000000982062_00409_29521_0585.N1	20071023	103815
MER_FR__2PNEPA20071115_101535_000000982063_00237_29850_1021.N1	20071115	101535
MER_FR__2PNEPA20080209_101243_000000982065_00466_31081_1022.N1	20080209	101243
MER_FR__2PNEPA20080212_101825_000000982066_00008_31124_1023.N1	20080212	101825
MER_FR__2PNEPA20080218_102945_000000982066_00094_31210_1024.N1	20080218	102945
MER_FR__2PNEPA20080227_104648_000000982066_00223_31339_1025.N1	20080227	104648
MER_FR__2PNEPA20080314_104358_000000982066_00452_31568_1026.N1	20080314	104358
MER_FR__2PNEPA20080331_101003_000000982067_00194_31811_1027.N1	20080331	101003
MER_FR__2PNEPA20080409_102656_000000982067_00323_31940_1028.N1	20080409	102656
MER_FR__2PNEPA20080415_103818_000000982067_00409_32026_1029.N1	20080415	103818
MER_FR__2PNEPA20080422_101824_000000982068_00008_32126_1030.N1	20080422	101824
MER_FR__2PNEPA20080425_102403_000000982068_00051_32169_1031.N1	20080425	102403
MER_FR__2PNUPA20080508_101535_000000982068_00237_32355_0006.N1	20080508	101535
MER_FR__2PNUPA20080511_102115_000000982068_00280_32398_0007.N1	20080511	102115
MER_FR__2PNUPA20080520_103817_000000982068_00409_32527_0008.N1	20080520	103817
MER_FR__2PNUPA20080521_100709_000000982068_00423_32541_0009.N1	20080521	100709
MER_FR__2PNUPA20080624_103818_000000982069_00409_33028_0010.N1	20080624	103818
MER_FR__2PNUPA20080630_104943_000000982069_00495_33114_0011.N1	20080630	104943
MER_FR__2PNUPA20080704_102407_000000982070_00051_33171_0012.N1	20080704	102407
MER_FR__2PNUPA20080713_104110_000000982070_00180_33300_0013.N1	20080713	104110
MER_FR__2PNUPA20080714_100953_000000982070_00194_33314_0014.N1	20080714	100953
MER_FR__2PNUPA20080729_103818_000000982070_00409_33529_0015.N1	20080729	103818
MER_FR__2PNUPA20080804_104942_000000982070_00495_33615_0016.N1	20080804	104942
MER_FR__2PNUPA20080815_100417_000000982071_00151_33772_0017.N1	20080815	100417
MER_FR__2PNUPA20080909_101820_000000982072_00008_34130_0018.N1	20080909	101820
MER_FR__2PNUPA20080918_103526_000000982072_00137_34259_0019.N1	20080918	103526
MER_FR__2PNUPA20080921_104106_000000982072_00180_34302_0020.N1	20080921	104106
MER_FR__2PNUPA20080927_105234_000000982072_00266_34388_0021.N1	20080927	105234
MER_FR__2PNUPA20081011_101241_000000982072_00466_34588_0022.N1	20081011	101241
MER_FR__2PNUPA20081017_102404_000000982073_00051_34674_0023.N1	20081017	102404
MER_FR__2PNUPA20081023_103524_000000982073_00137_34760_0024.N1	20081023	103524
MER_FR__2PNUPA20081108_103233_000000982073_00366_34989_0025.N1	20081108	103233

A.2 Water quality parameter maps from remote sensing

Maps resulting of all derived water quality parameters from all five parameterisations:
(1) *Seven band, (2) Seven band with adapted LUT, (3) Seven band with adapted LUT and high initial concentrations, (4) Eight band corrected,(5) Eight band uncorrected.*
Three examples: 16-Oct-2006, 20-Oct-2007, and 31-Mar-2008.

Example 16-Oct-2007

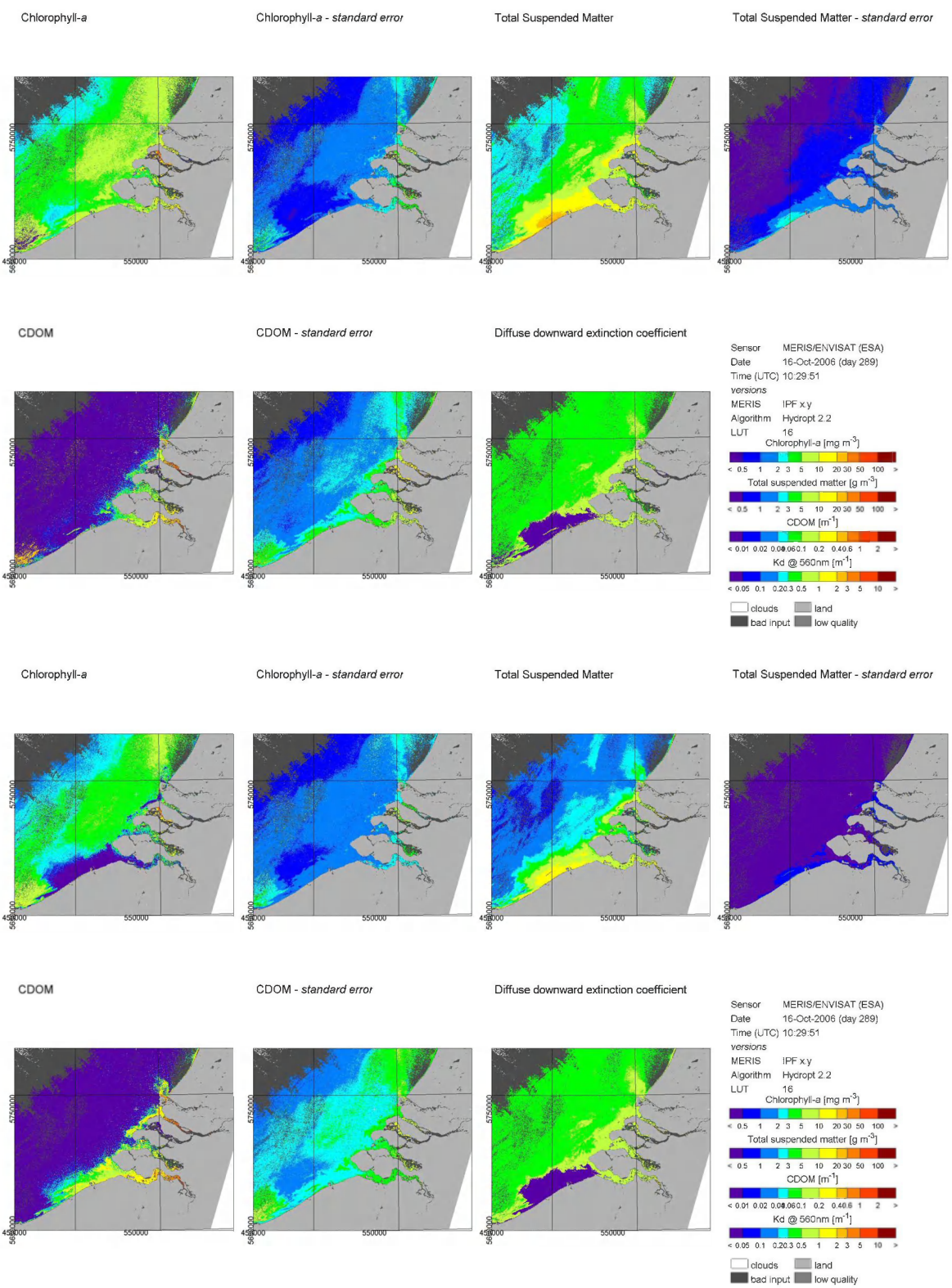

(1) Seven band. Top: North Sea sIOPs, bottom: Westerschelde sIOPs. (PCD _1_13 flags applied).

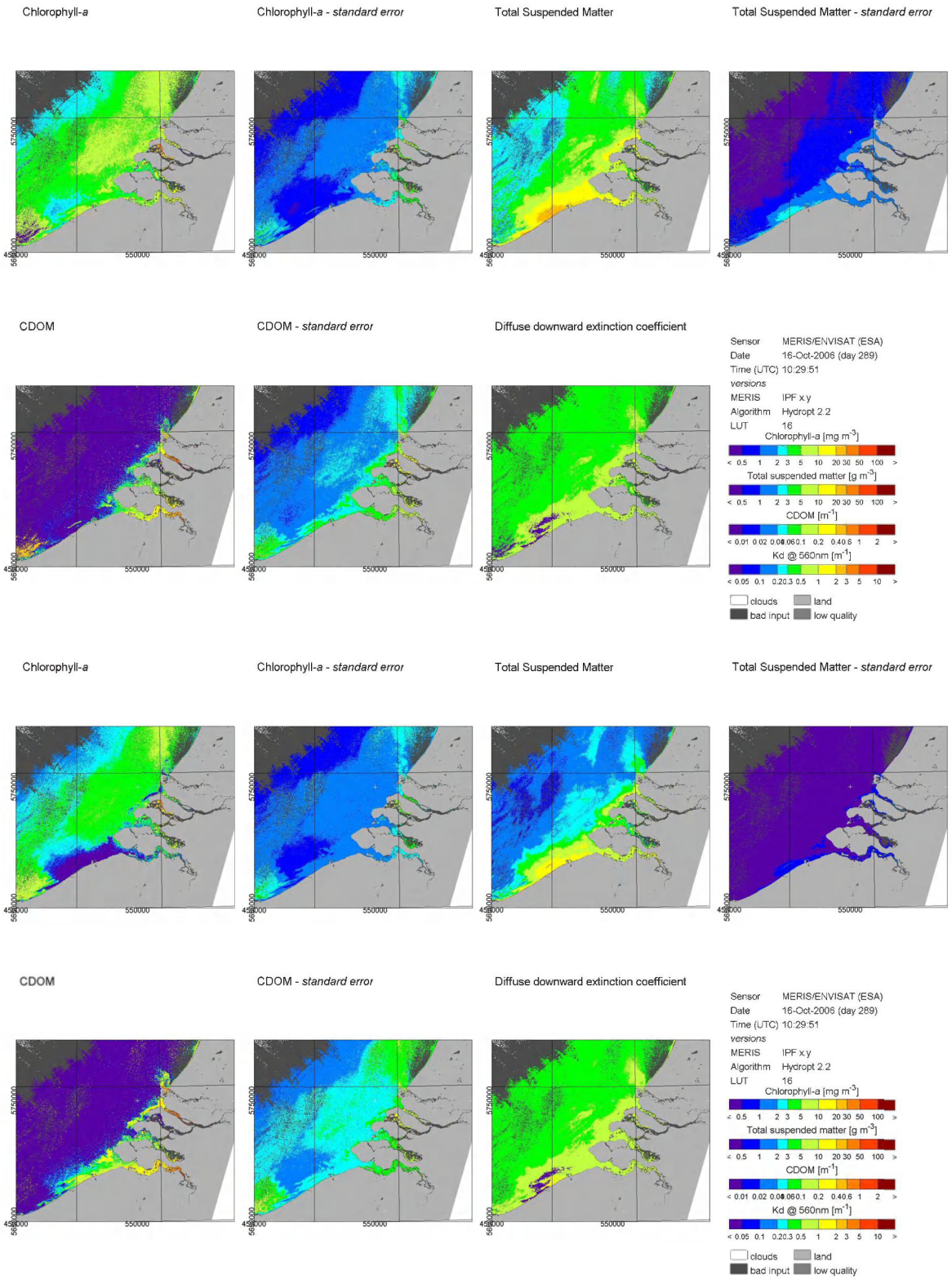

(2) Seven band with adapted LUT. Top: North Sea sIOPs, bottom: Westerschelde sIOPs.

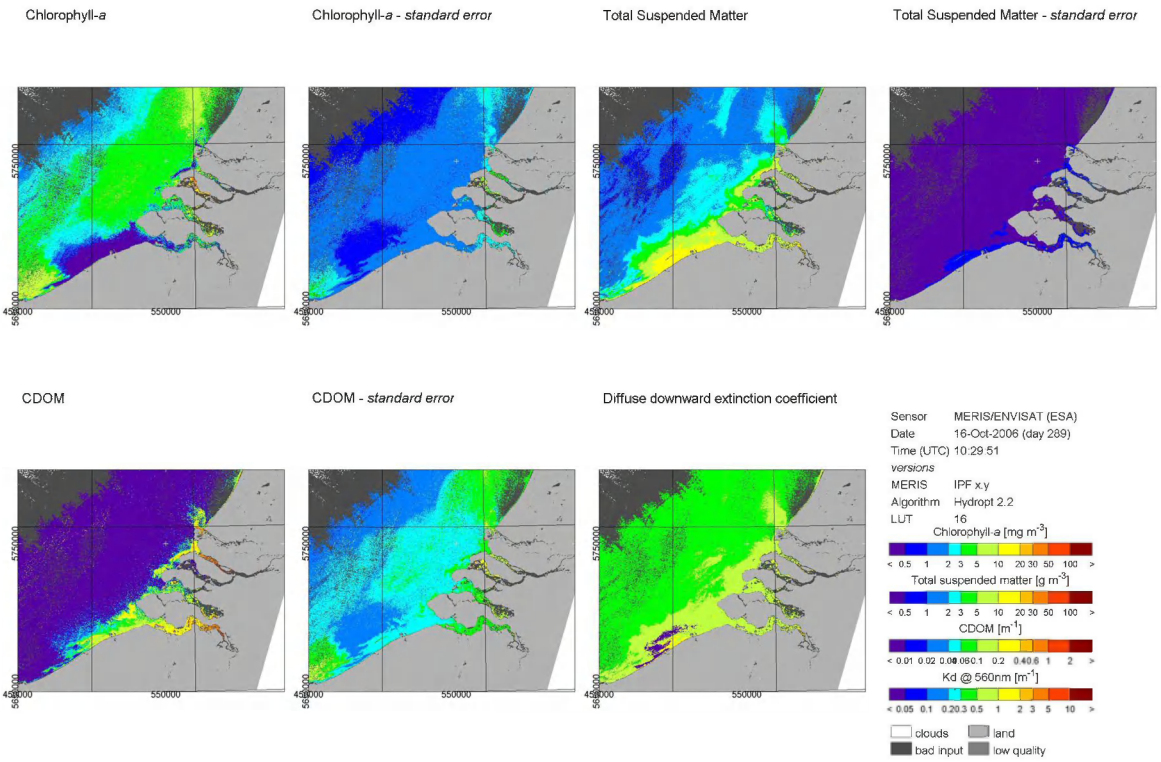

(3) Seven band with adapted LUT and higher initial concentrations and Westerschelde sIOPs.

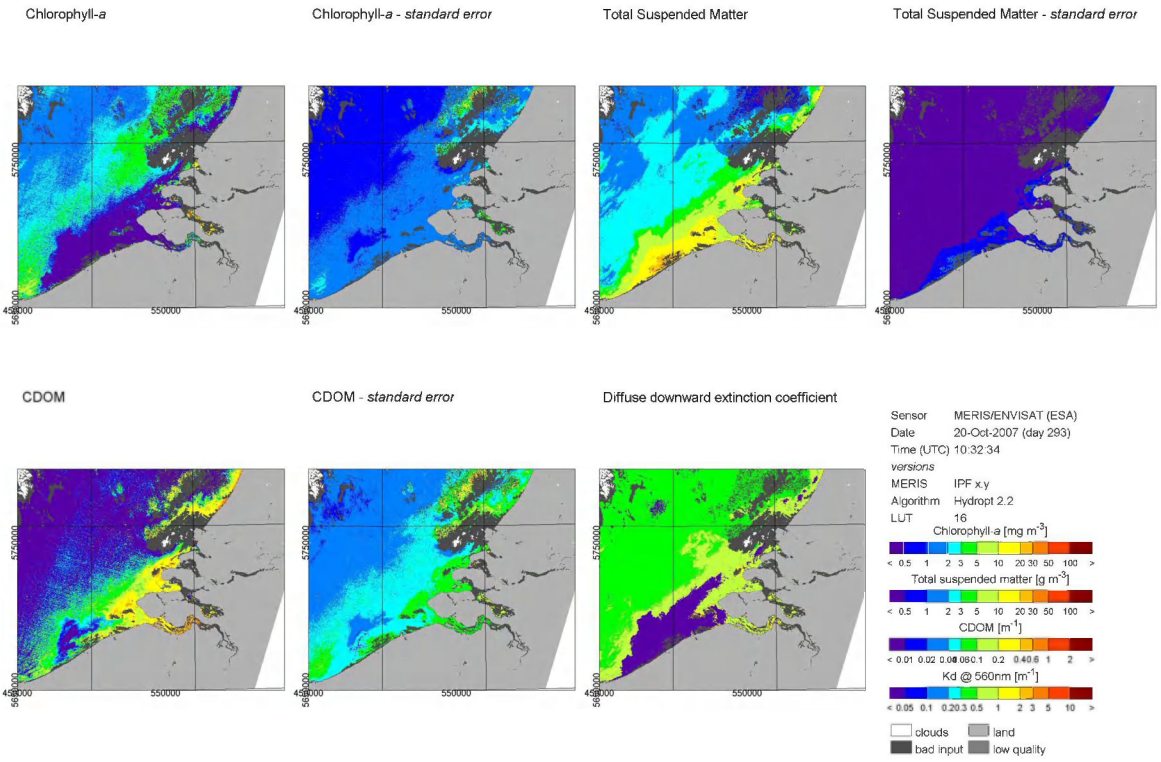

4) Eight band corrected for Westerschelde sIOPs.

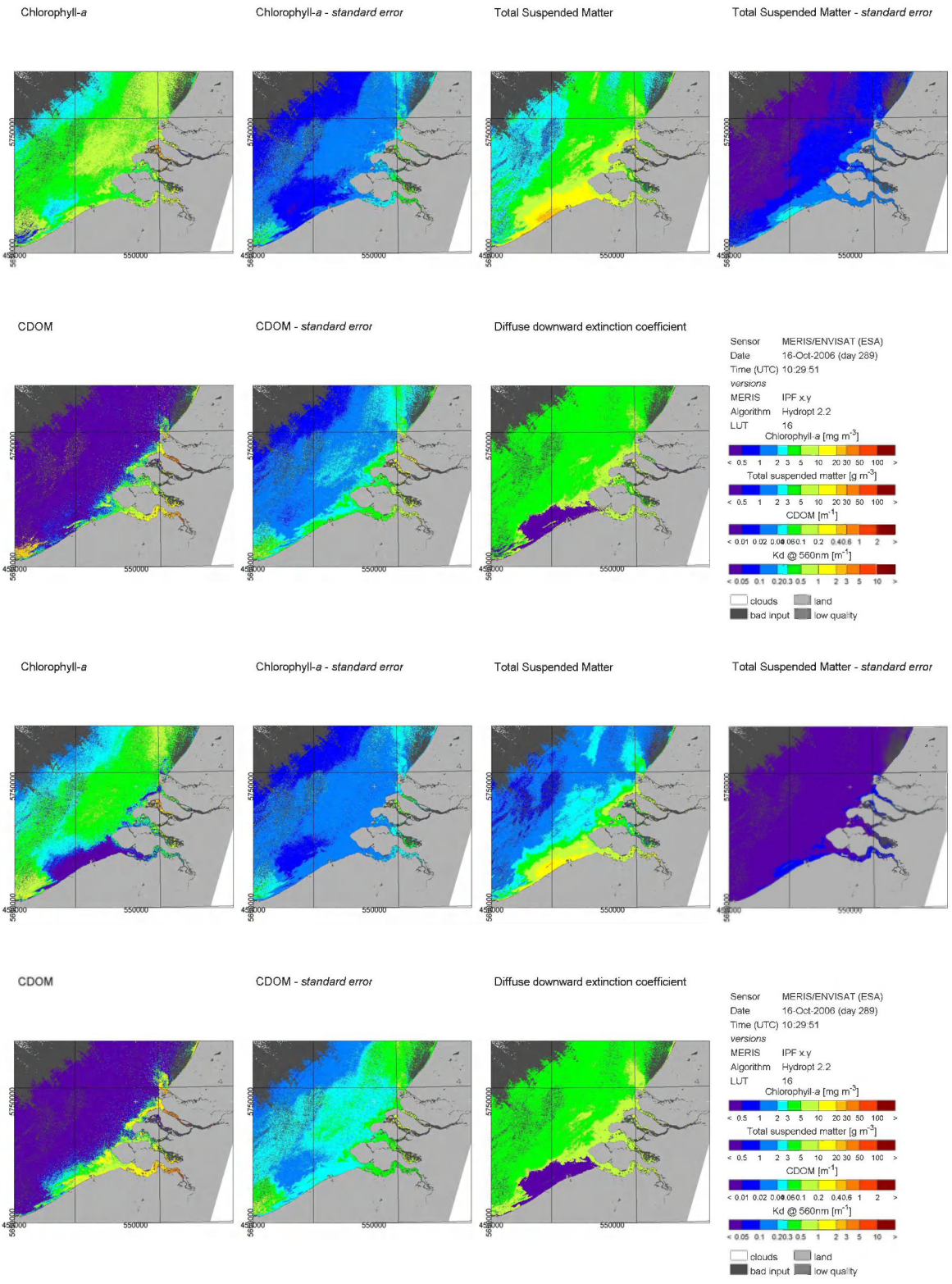

(5) Eight band uncorrected. Top: North Sea sIOPs, bottom: Westerschelde sIOPs.

Example 20-Oct-2007

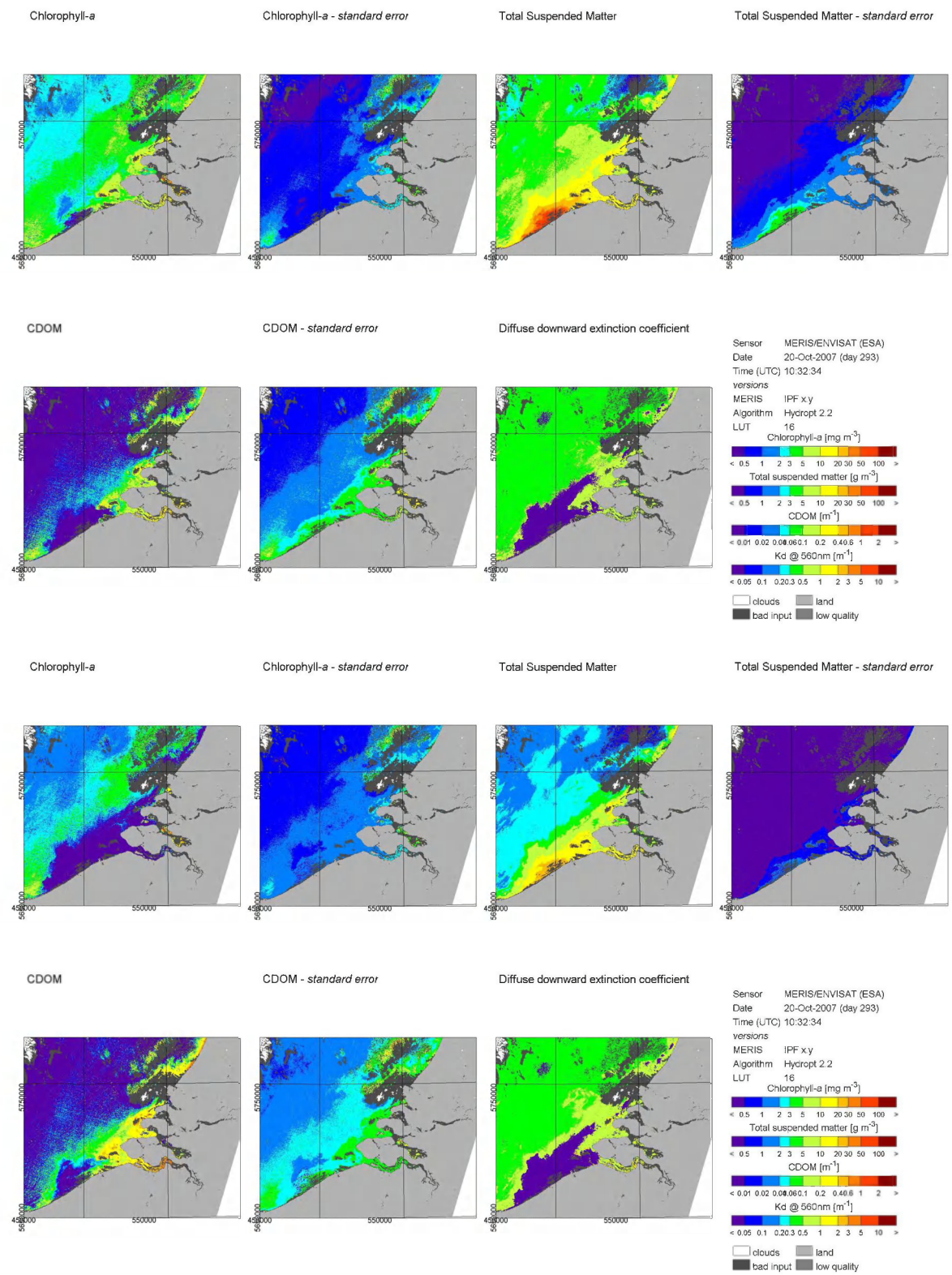

(1) Seven band. Top: North Sea sIOPs, bottom: Westerschelde sIOPs. (PCD _1_13 flags applied).

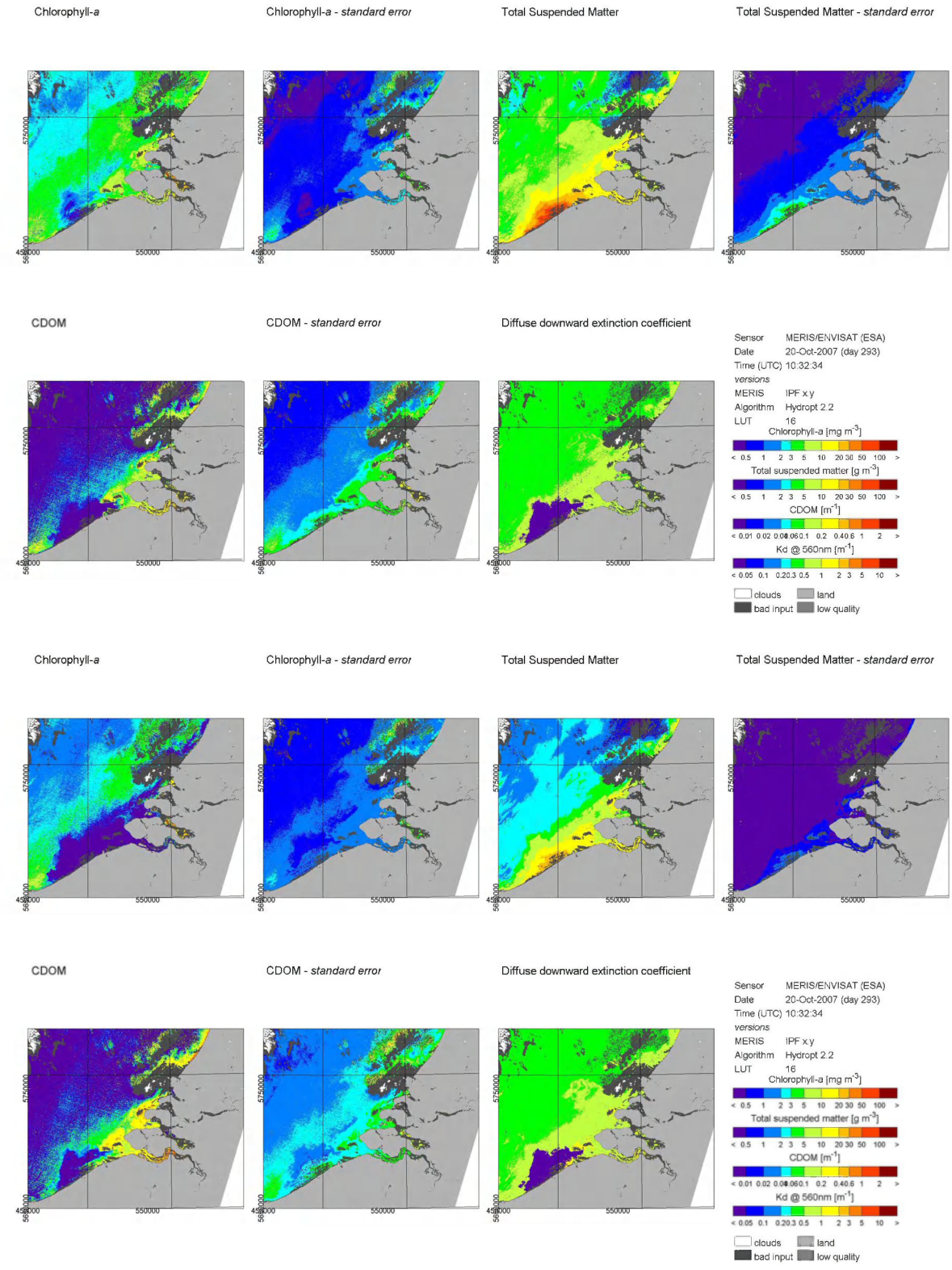

(2) Seven band with adapted LUT. Top: North Sea sIOPs, bottom: Westerschelde sIOPs.

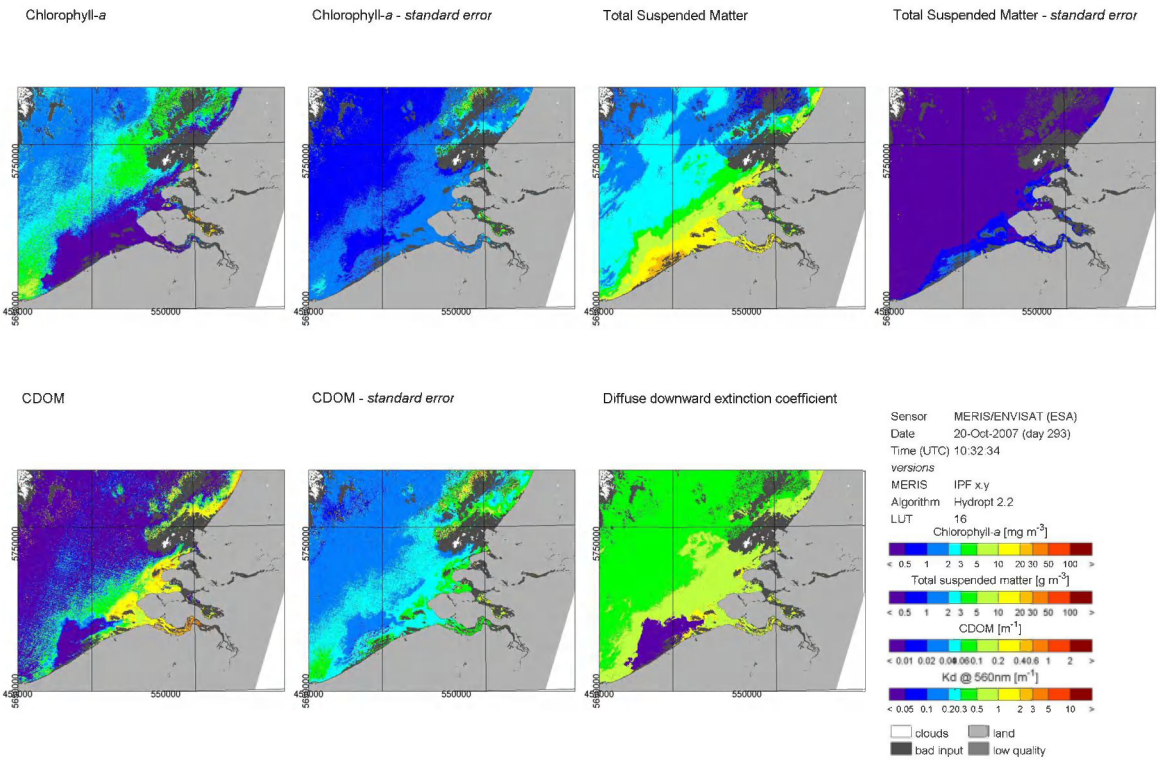

(3) Seven band with adapted LUT and higher initial concentrations and Westerschelde sIOPs.

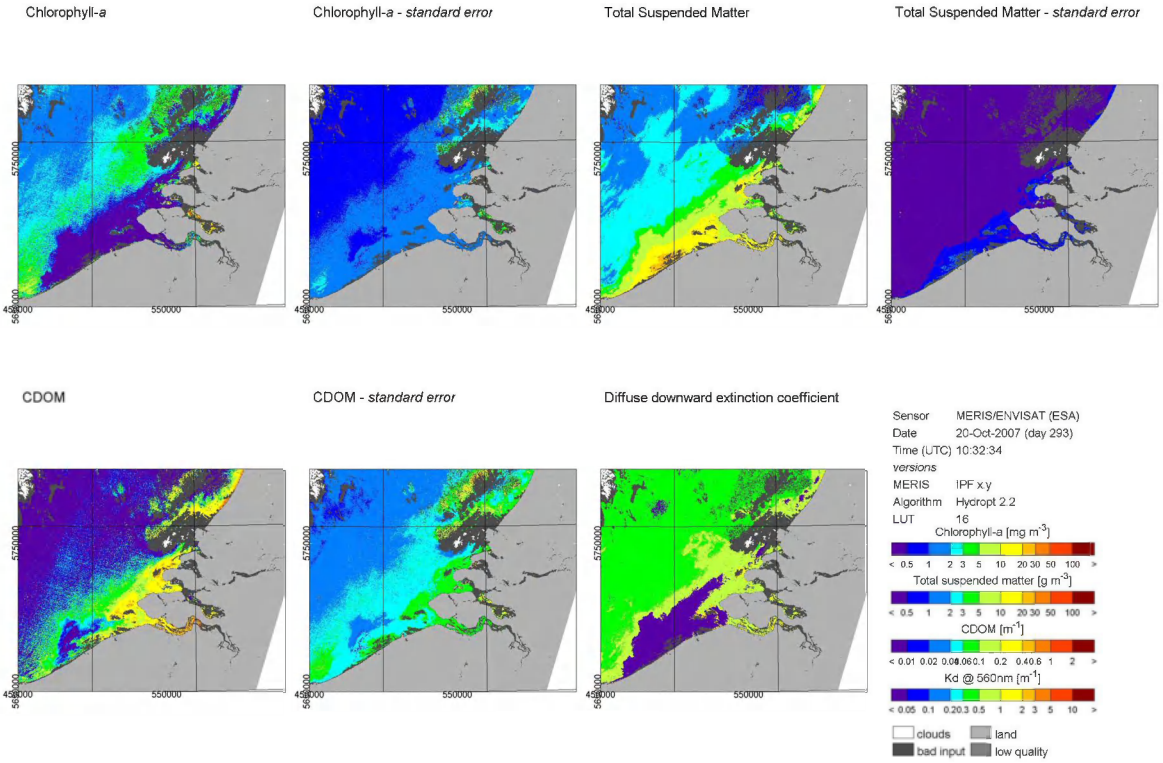

4) Eight band corrected for Westerschelde sIOPs.

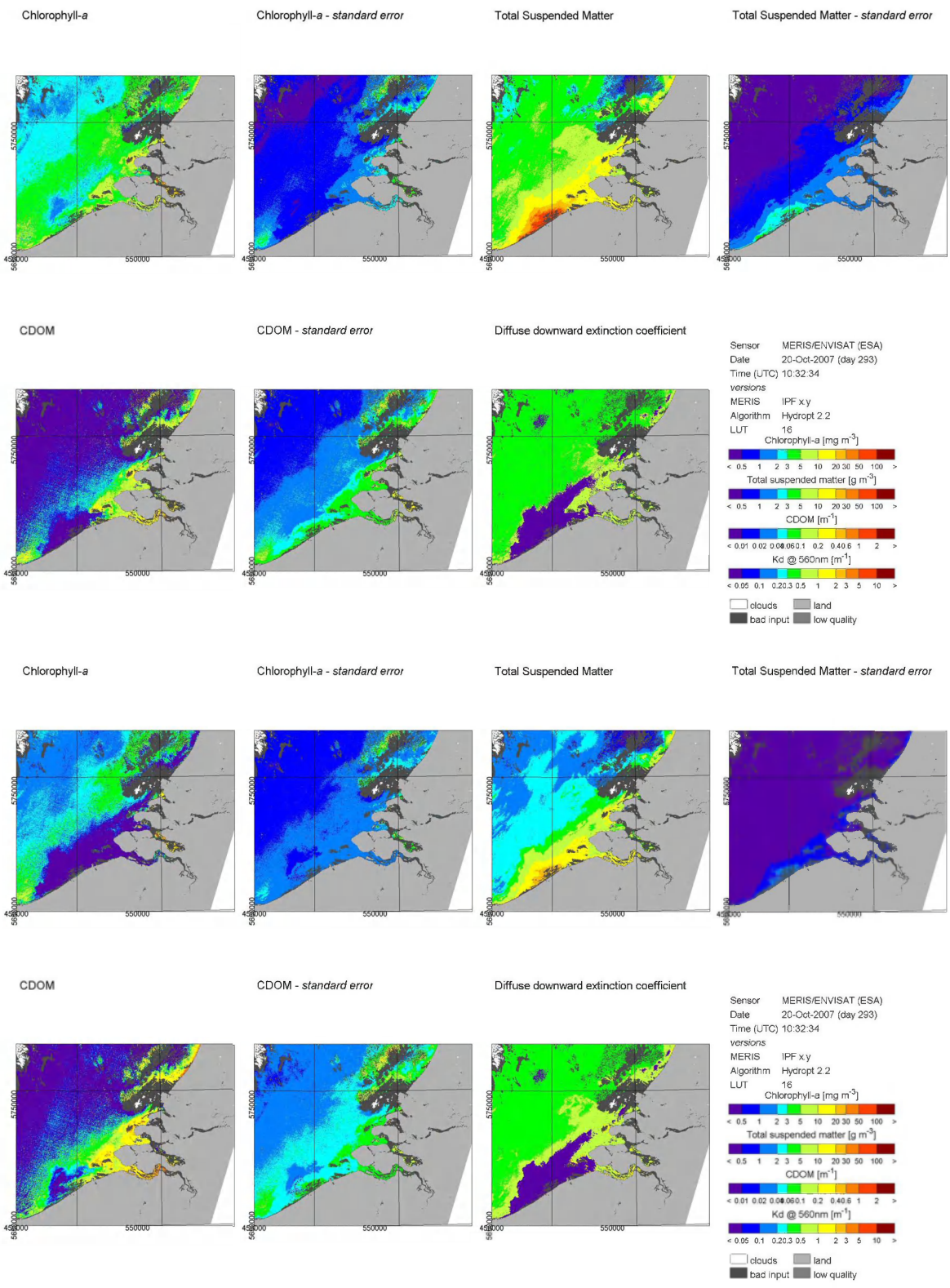

(5) Eight band uncorrected. Top: North Sea sIOPs, bottom: Westerschelde sIOPs.

Example 31-Mar-2008

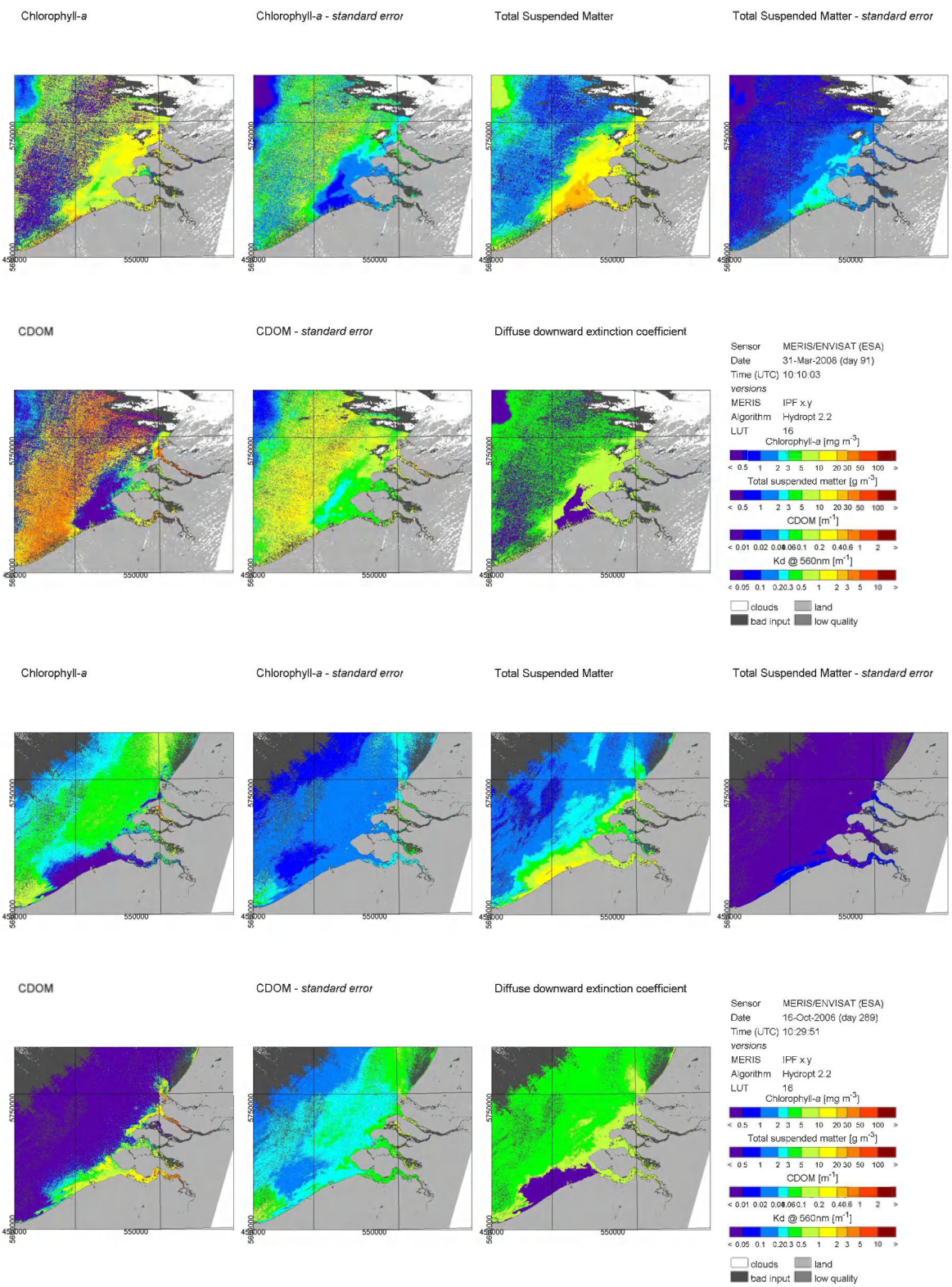

(1) Seven band. Top: North Sea sIOPs, bottom: Westerschelde sIOPs. (PCD _1_13 flags applied).

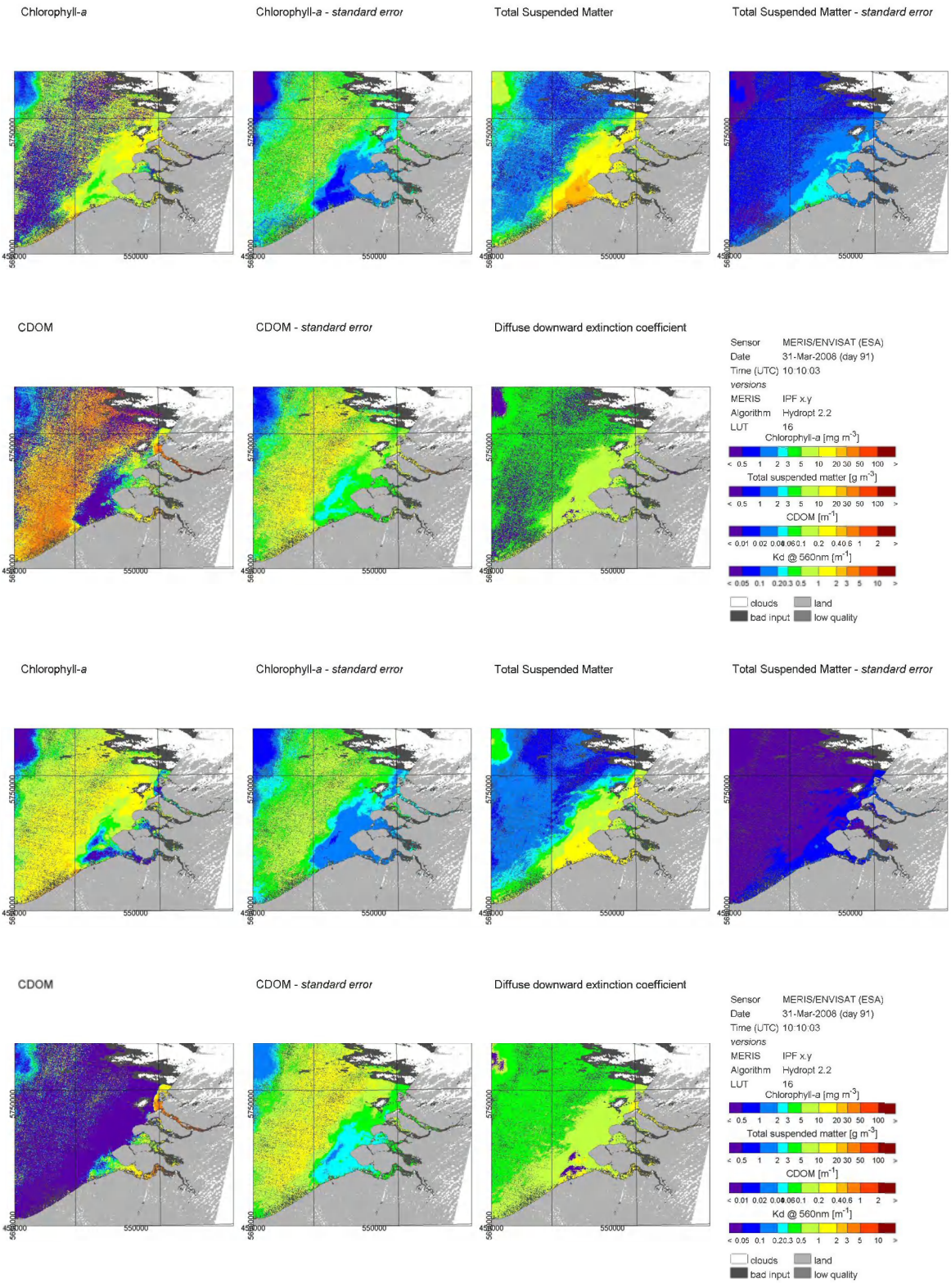

(2) Seven band with adapted LUT. Top: North Sea sIOPs, bottom: Westerschelde sIOPs.

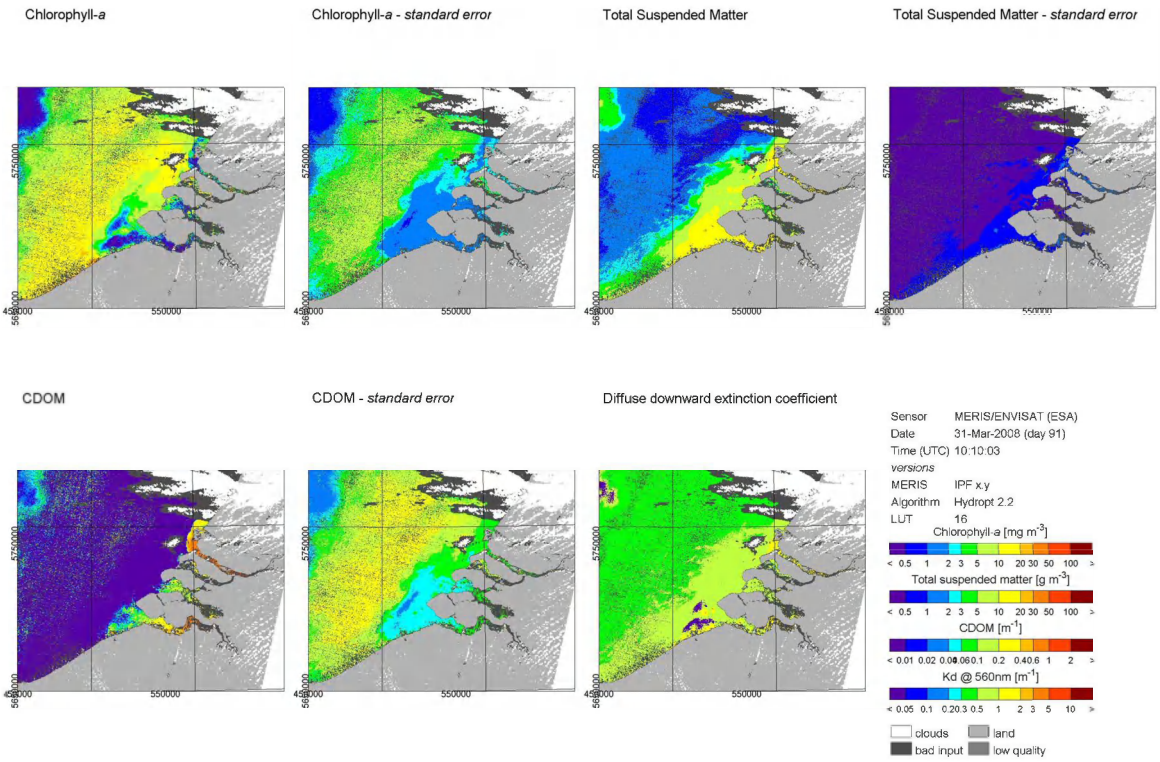

(3) Seven band with adapted LUT and higher initial concentrations and Westerschelde sIOPs.

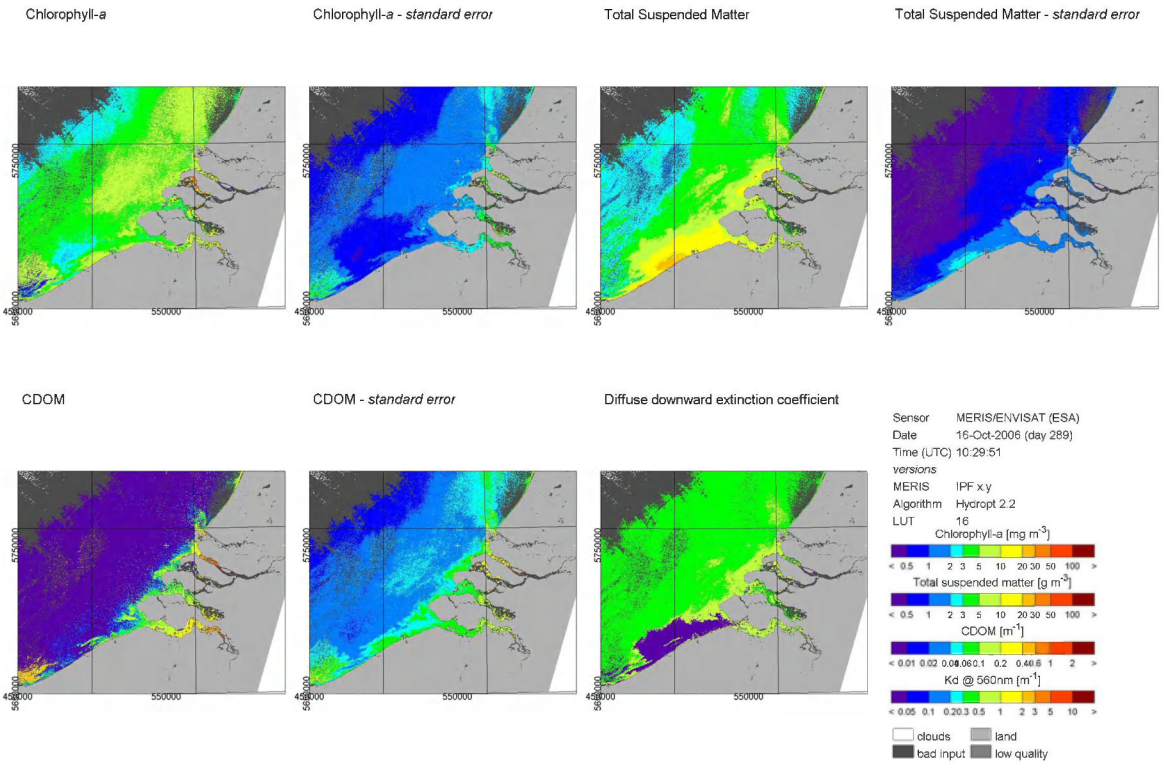

4) Eight band corrected for Westerschelde sIOPs.

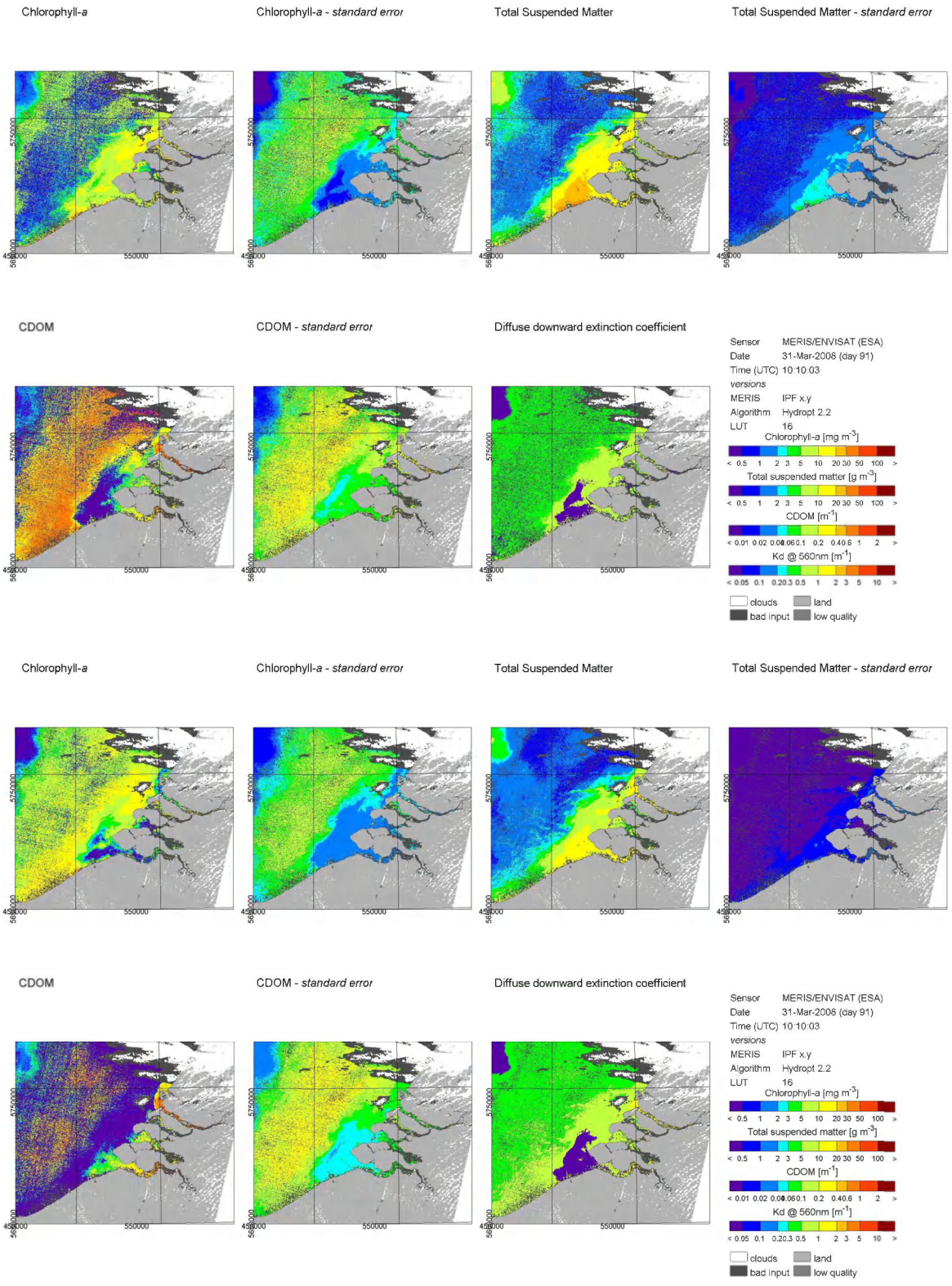

(5) Eight band uncorrected. Top: North Sea sIOPs, bottom: Westerschelde sIOPs.

A.3 Selection of SPM products

A selection of SPM products that have relatively many pixels that pass ESA's MERIS L2 data quality test (PCD_1-13, see Van Kessel et al., 2008) in the region of interest. Left North Sea sIOPs, right Westerschelde sIOPs.

11-Jun-2006
11-Sep-2006
20-Sep-2006
16-Oct-2006
17-Nov2006

14-Mar-2007
09-Apr-2007
30-Aug-2007
20-Oct-2007
23-Oct-2007

18-Feb-2008
31-Mar-2008
09-Apr-2008
04-Jul-2008
14-Jul-2008
15-Aug-2008
27-Sep-2008
11-Oct-2008
23-Oct-2008

A selection of SPM products that have relatively many pixels that pass ESA's MERIS L2 data quality test (PCD_1-13, see Van Kessel et al., 2008) in the region of interest. Left (a) North Sea sIOPs, right (b) Westerschelde sIOPs, bottom (c): computed near-surface SPM concentration at same date and time. All plots have equal concentration log-axes, ranging from 1 (10 mg/L) to 2.6 (400 mg/L). Computed plots are available for 2006 only.

11-Jun-2006

a) b)

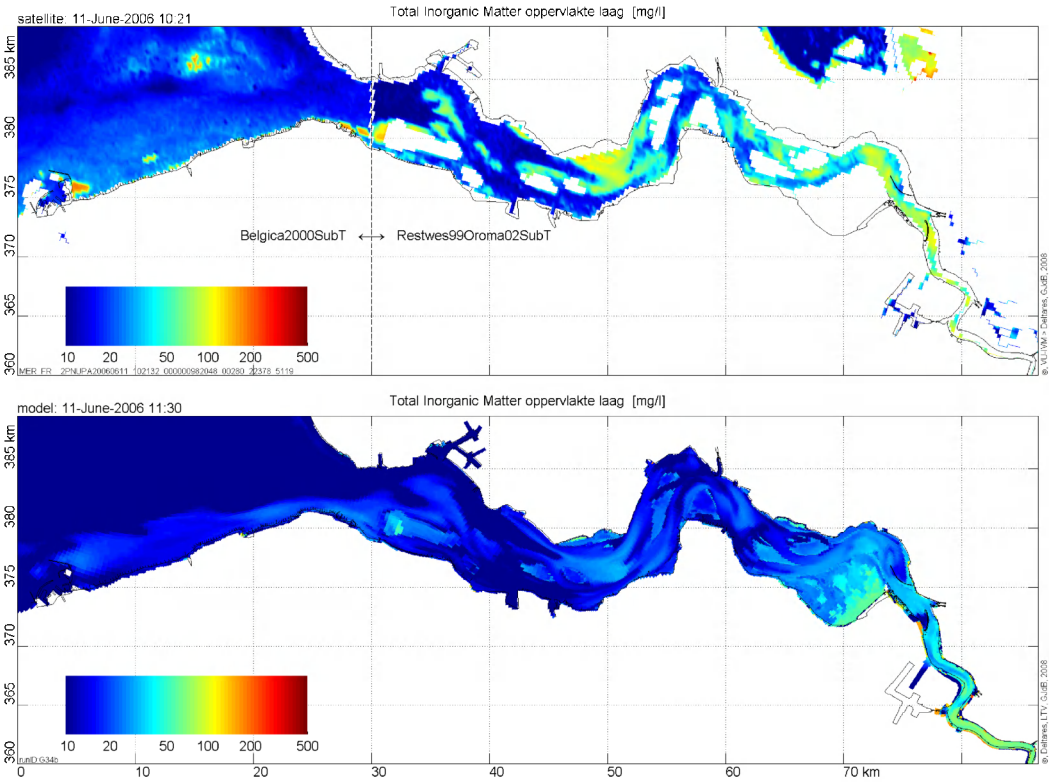

c)

11-Sep-2006

a) b)

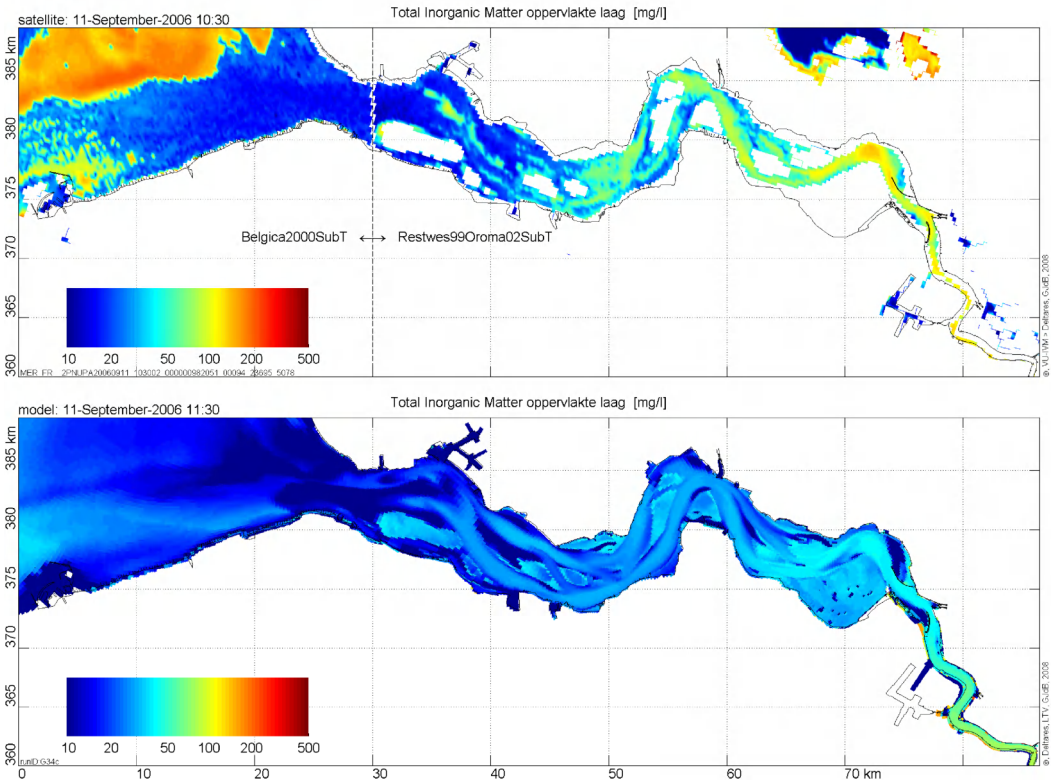

c)

20-Sep-2006

a) b)

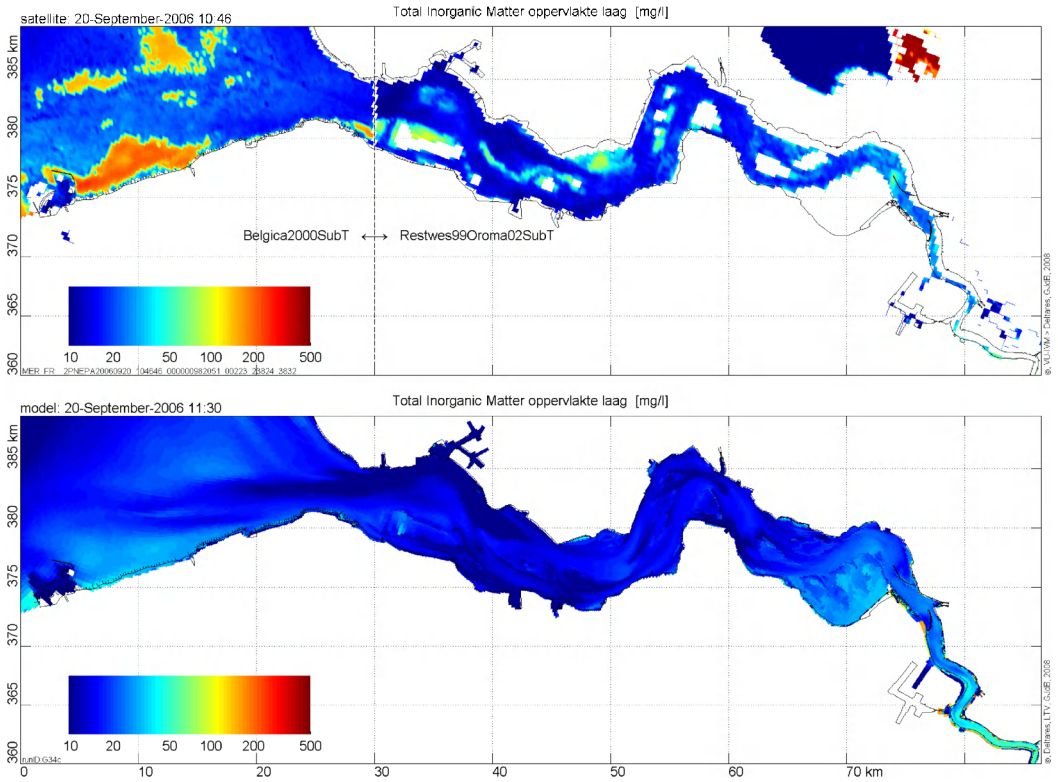

c)

16-Oct-2006

a) b)

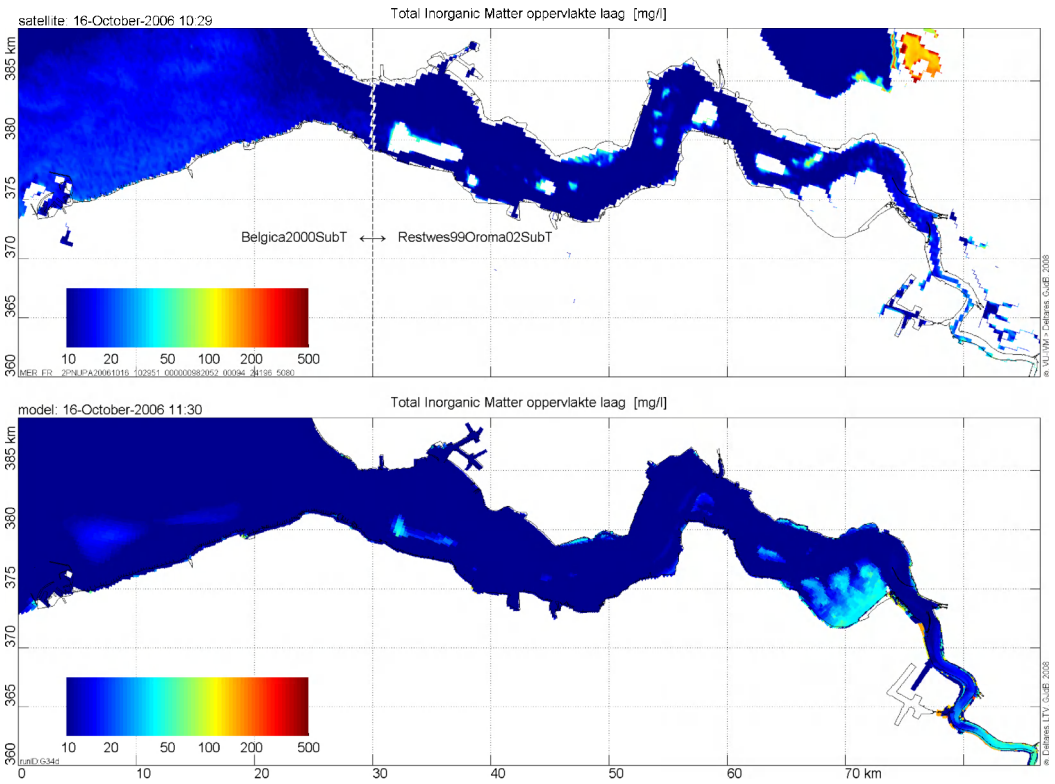

c)

17-Nov2006

a) b)

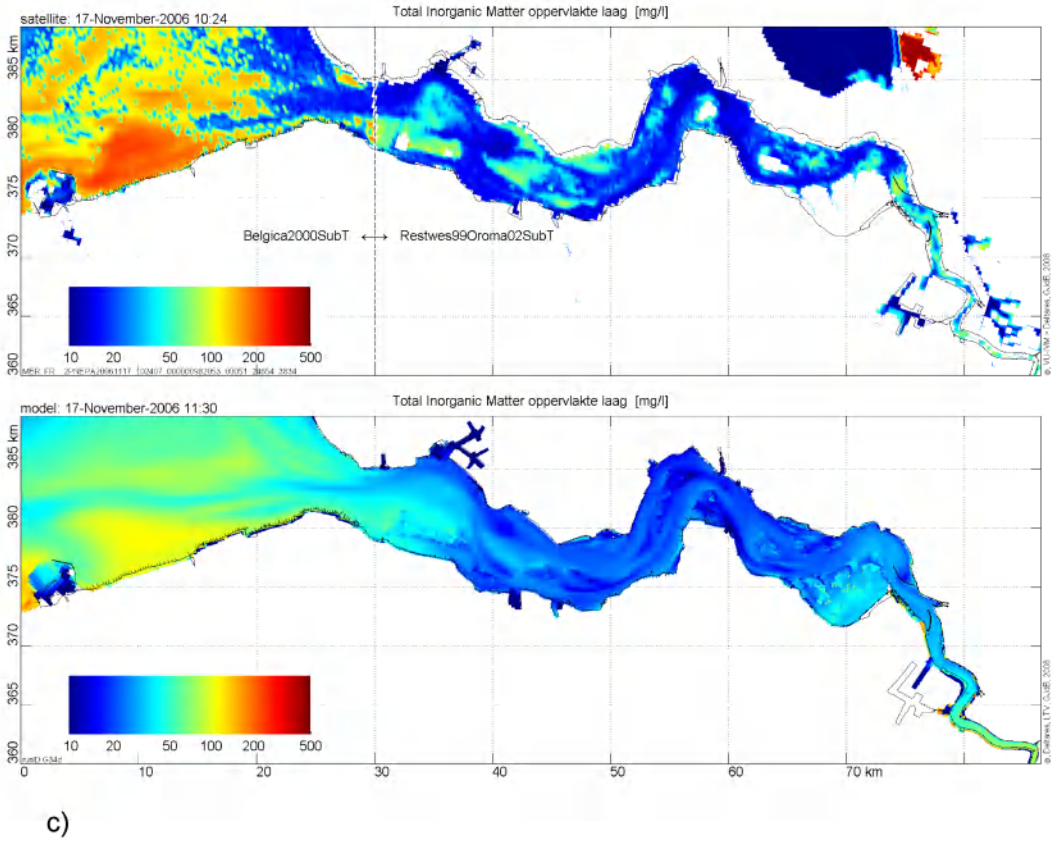

c)

14-Mar-2007

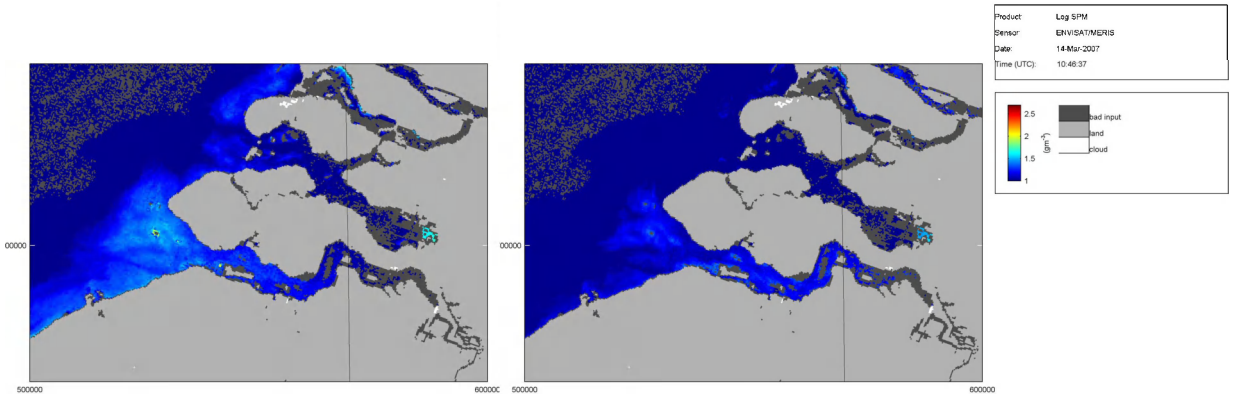

09-Apr-2007

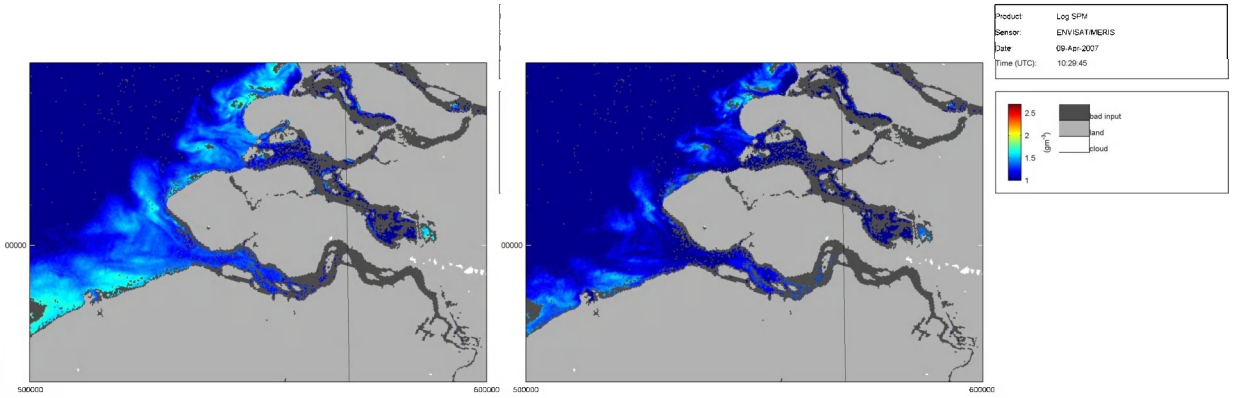

30-Aug-2007

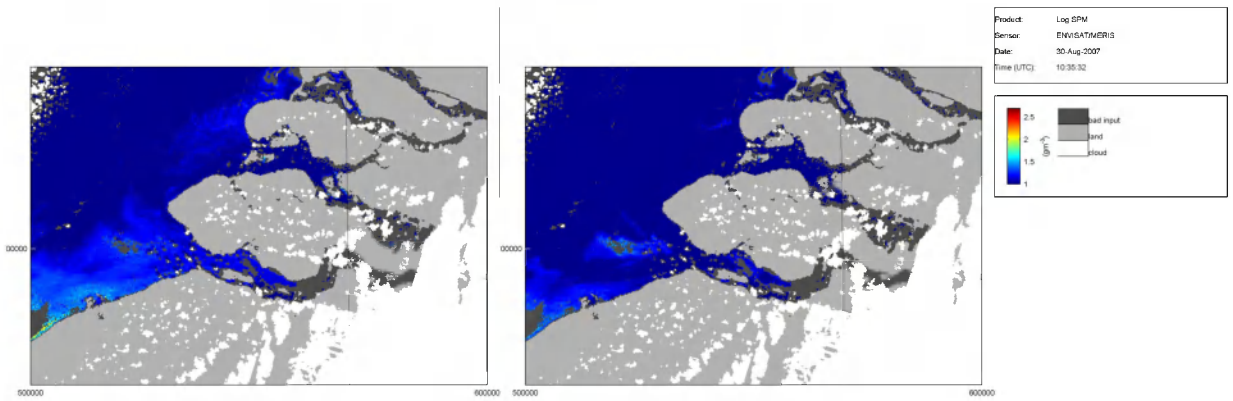

20-Oct-2007

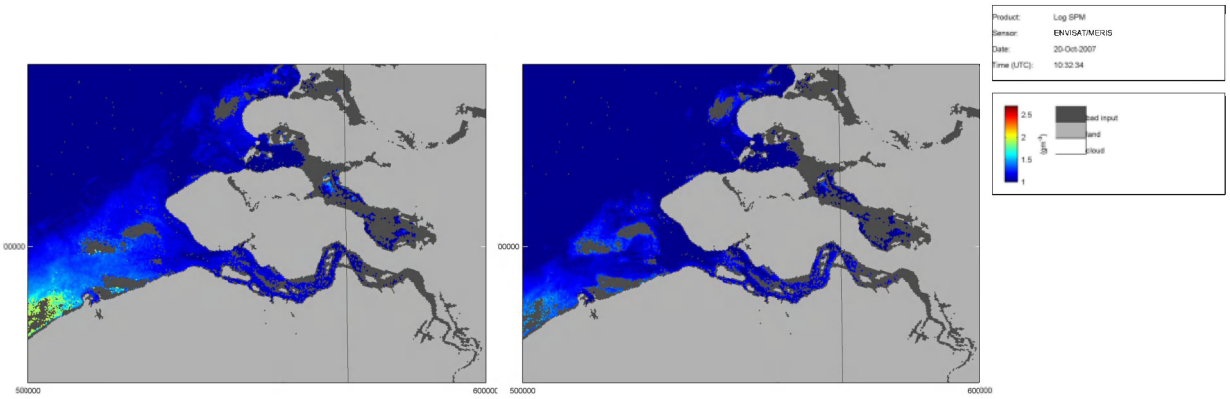

23-Oct-2007

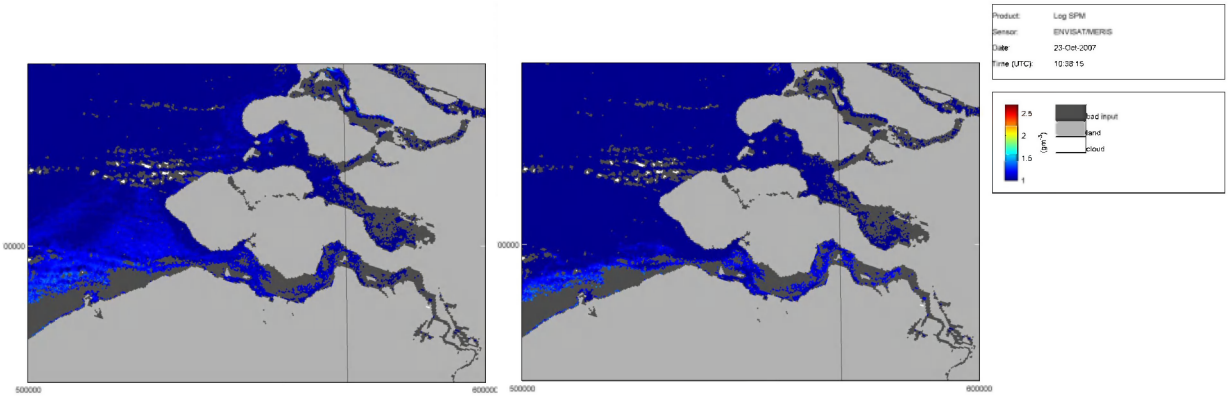

18-Feb-2008

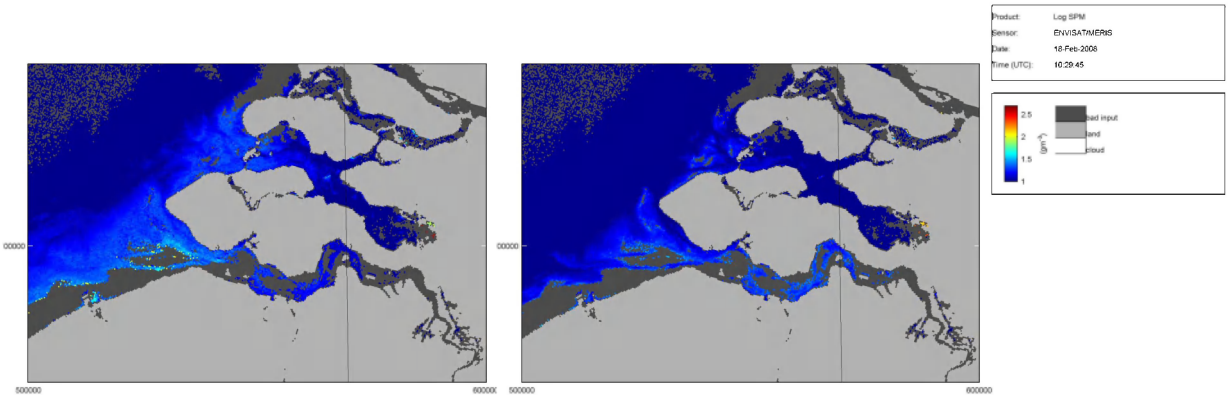

31-Mar-2008

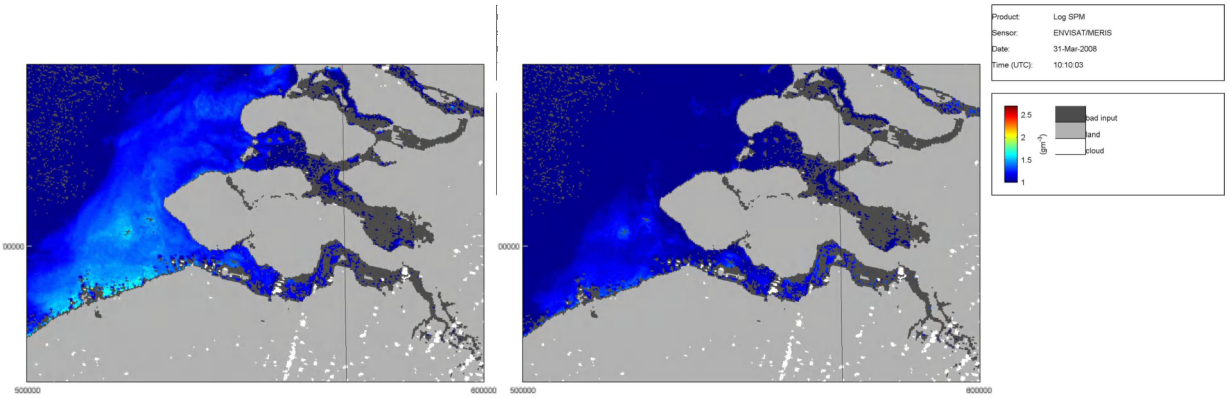

09-Apr-2008

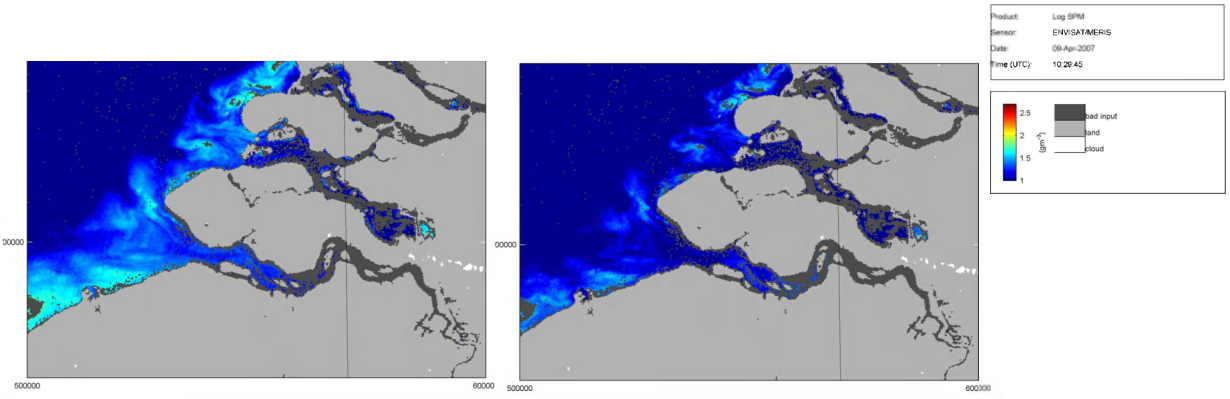

04-Jul-2008

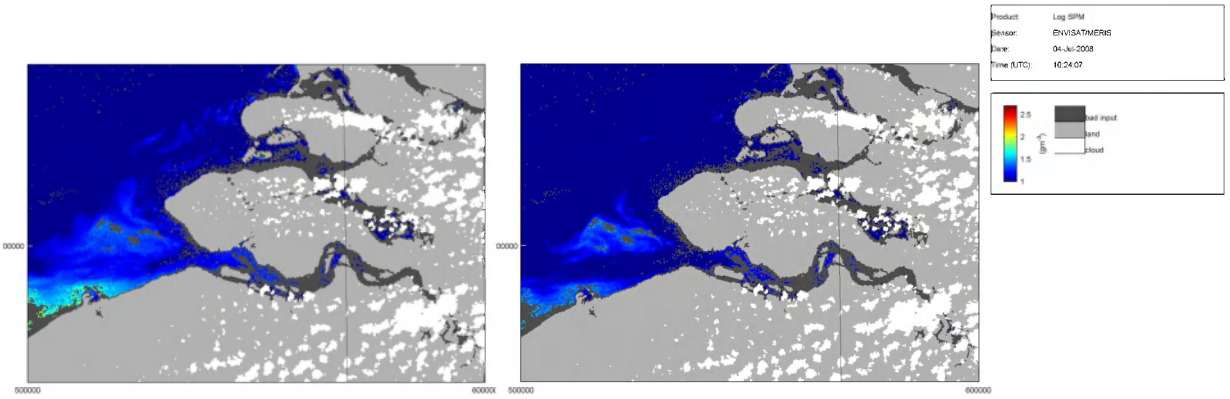

14-Jul-2008

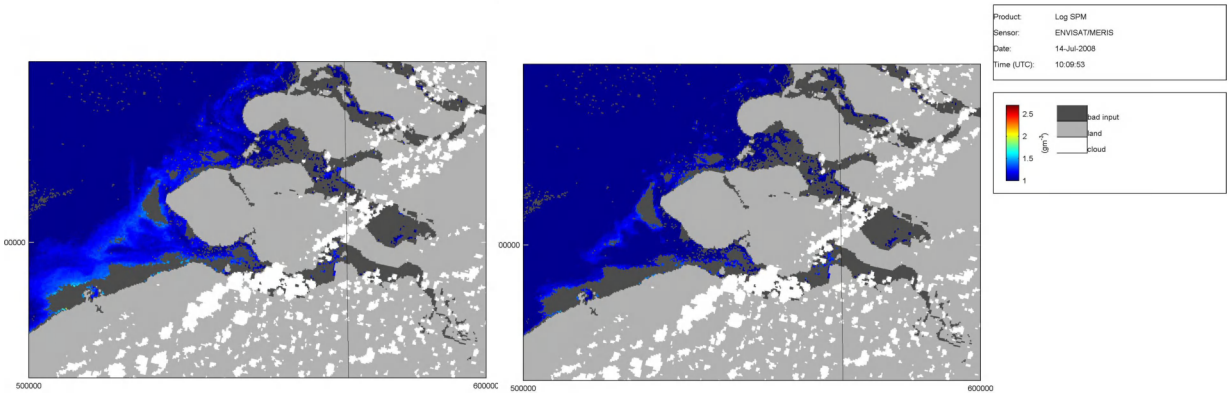

15-Aug-2008

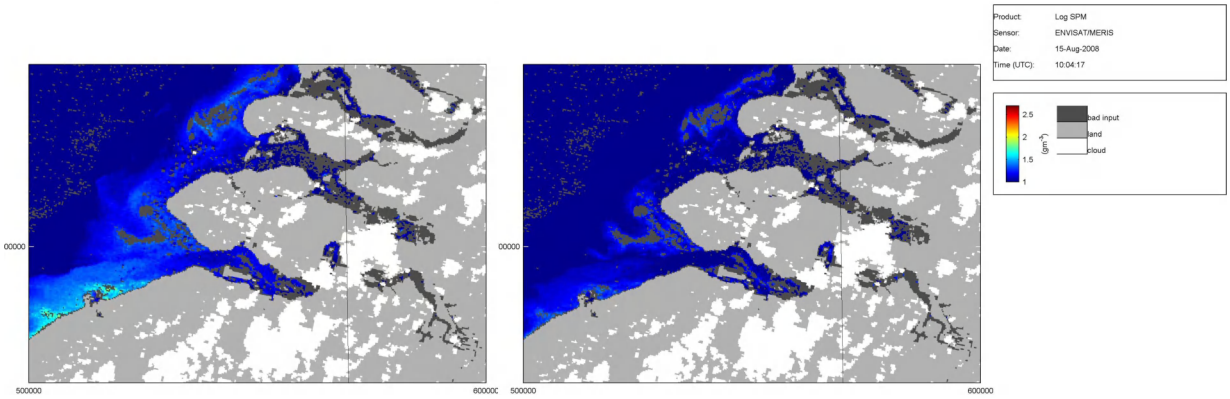

27-Sep-2008

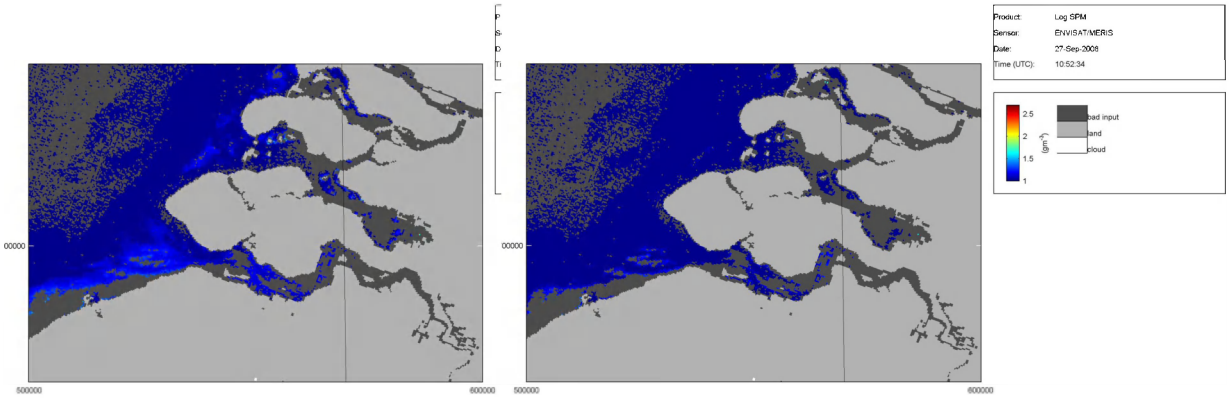

11-Oct-2008

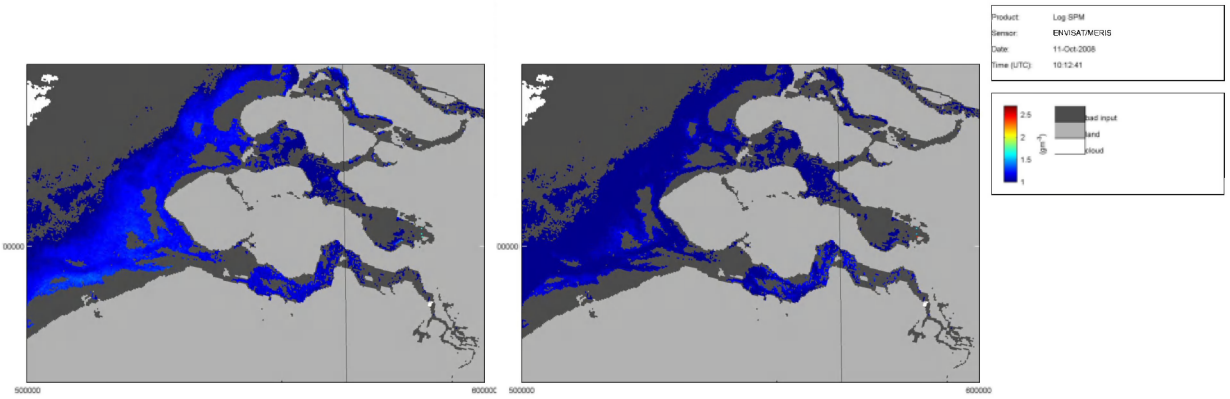

23-Oct-2008

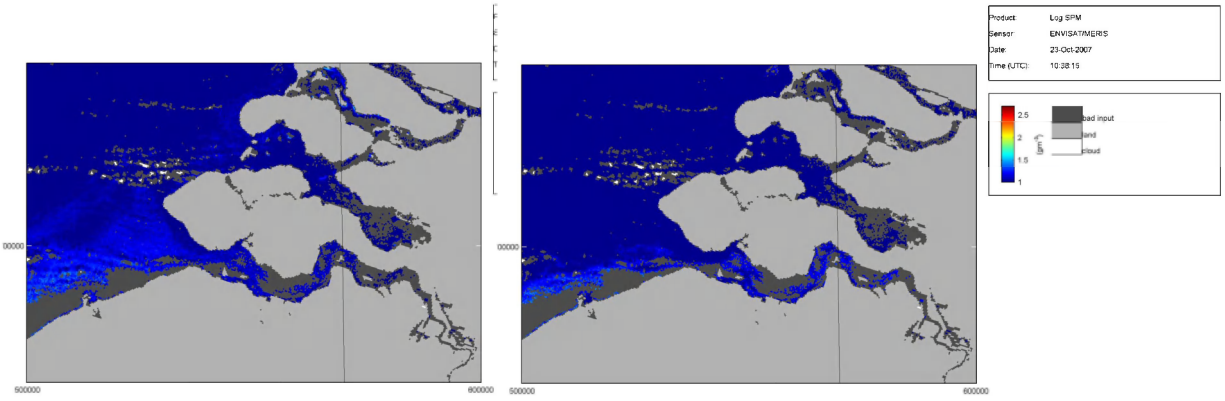

B Remote sensing tidal flats

B.1 Conditions during satellite image acquisition.

Images marked red are discarded due to high rainfall or high water level. Water conditions (hours after high water and water level in cm NAP) are given for station Hansweert (HAN). Masked clouds and cloud shadow for Landsat imagery are given as percentage of the entire intertidal Westerschelde.

Satellite	Year	Month	Day	h+HW	Level	Clouds	Remark
ERS SAR	2006	1	16	-4.8	-202		Low tide
ERS SAR	2006	2	1	-5.4	-276		Low tide
ERS SAR	2006	2	20	4.8			Rain
ERS SAR	2006	5	1	-5.7	-249		Low tide, some rain
ERS SAR	2006	5	17	-5.9	-220		Low tide
ERS SAR	2006	7	26	-4.2	-133		
ERS SAR	2006	8	14	5.5			Rain
ERS SAR	2006	8	30	5.3	-134		
ERS SAR	2006	11	8	-4.8	-147		
ERS SAR	2006	11	27	4.9	-139		
ERS SAR	2007	2	21	-6.0	-246		Low tide
ERS SAR	2007	5	2	-3.5	-92		Mid tide
ERS SAR	2007	5	21	5.8	-182		Low tide, some rain
ERS SAR	2007	6	6	5.6	-174		Low tide
ERS SAR	2007	8	15	-4.8	-124		
ERS SAR	2007	9	3	5.0	-110		
ERS SAR	2007	11	28	-5.8	-195		Low tide
ERS SAR	2008	2	25	-6.1	-220		Low tide
ERS SAR	2008	5	21	-4.2	-118		
ERS SAR	2008	6	9	4.7	-117		
ERS SAR	2008	6	25	4.7	-112		
ERS SAR	2008	9	3	-5.3	-176		
Landsat 7 ETM+	2006	3	18	-5.5	-265	1	Low tide
Landsat 7 ETM+	2006	4	28	-3.7	-111	2	
Landsat 5 TM	2006	6	30	5.6	-201	<1	Low tide
Landsat 7 ETM+	2006	7	1	4.9	-162	0	
Landsat 5 TM	2006	7	16	4.9	-155	0	
Landsat 7 ETM+	2006	7	17	4.0	-77	0	Mid tide
Landsat 5 TM	2006	7	25	-3.8	-75	3	Mid tide
Landsat 7 ETM+	2006	9	10	-5.0	-167	0	
Landsat 7 ETM+	2007	3	14	0.9	79	0	High tide
Landsat 7 ETM+	2007	4	15	-1.8	108	0	High tide
Landsat 7 ETM+	2007	5	1	-3.2	-60	0	Mid tide
Landsat 7 ETM+	2007	6	2	-4.3	-120	33	
Landsat 7 ETM+	2007	8	5	4.4	-102	0	
Landsat 7 ETM+	2008	4	8	-4.9	-216	10	Low tide
Landsat 7 ETM+	2008	8	30	-3.0	-45	0	Mid tide

B.2 Maps of mud content based on ERS SAR imagery.

Date of image acquisition is displayed as yymmdd, e.g. 081201 is 1 December 2008.
(ln M+1, with M is mud percentage)

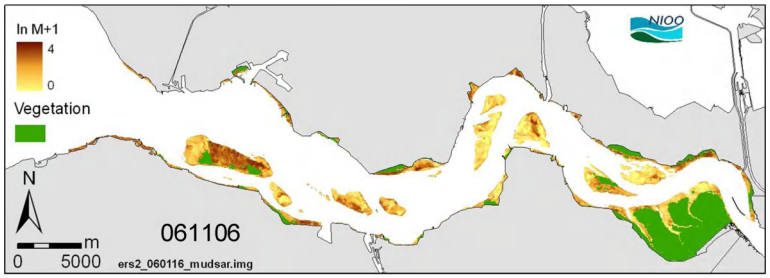

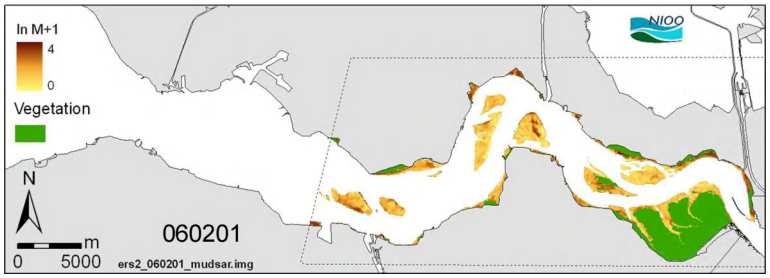

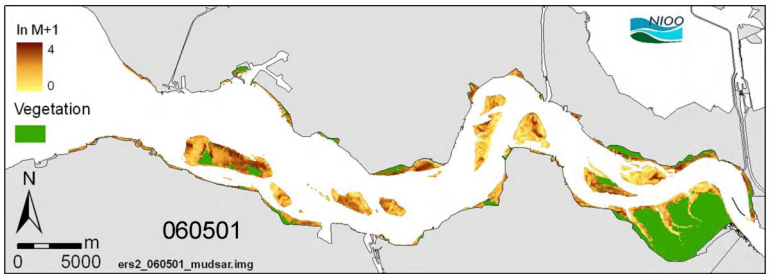

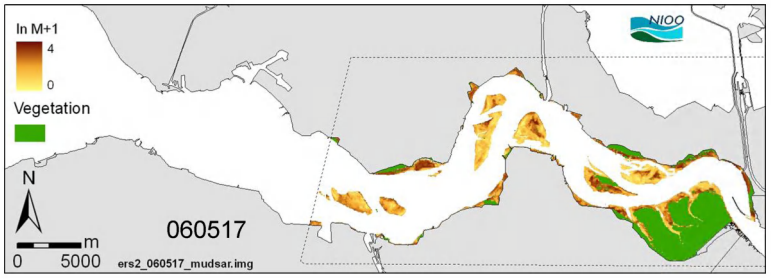

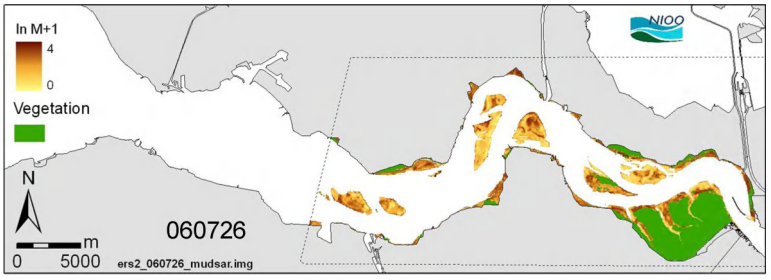

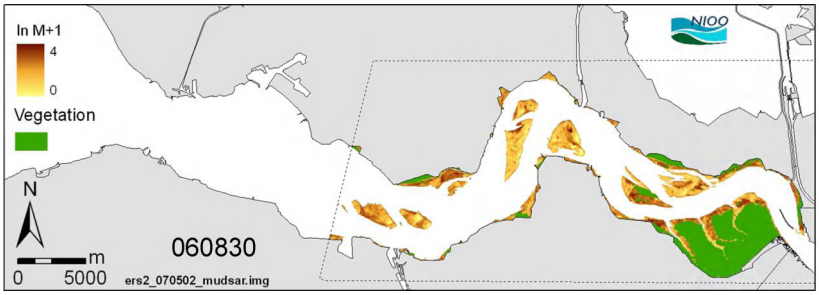
ln M+1
4
0
Vegetation
N
m
0 5000
060830
ers2_070502_mudsar.img
NIOO

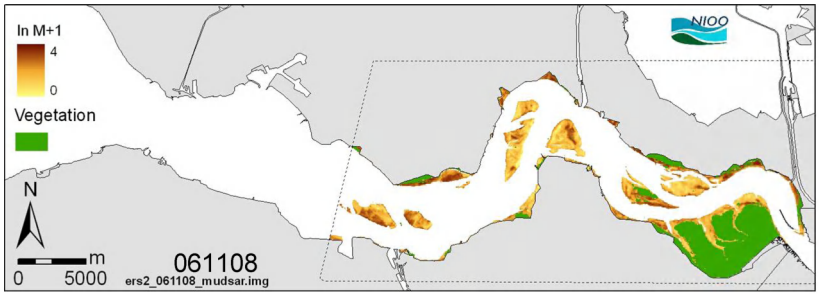
ln M+1
4
0
Vegetation
N
m
0 5000
061108
ers2_061108_mudsar.img
NIOO

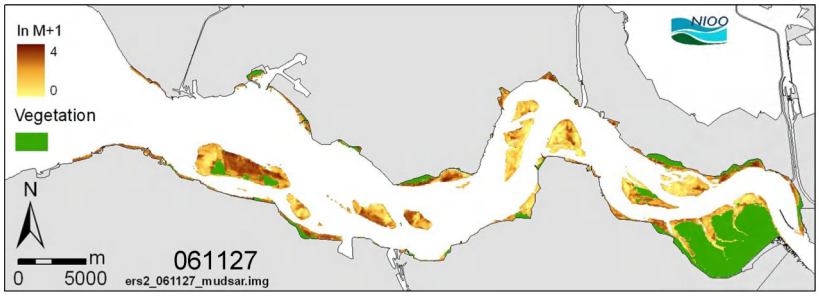
ln M+1
4
0
Vegetation
N
m
0 5000
061127
ers2_061127_mudsar.img
NIOO

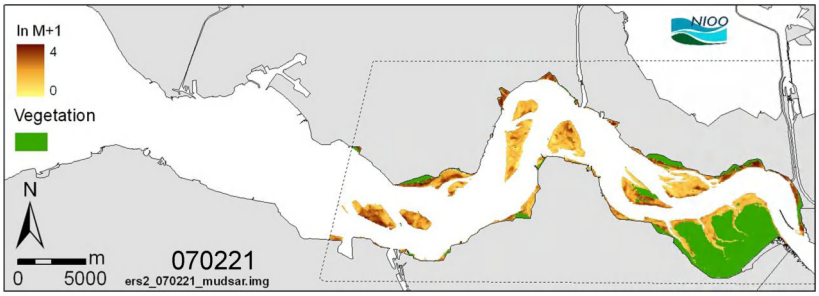
ln M+1
4
0
Vegetation
N
m
0 5000
070221
ers2_070221_mudsar.img
NIOO

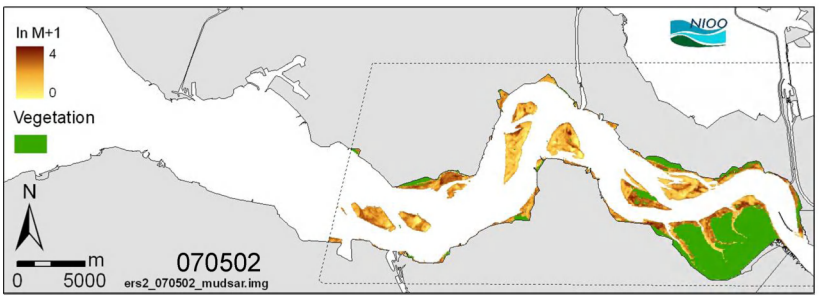
ln M+1
4
0
Vegetation
N
m
0 5000
070502
ers2_070502_mudsar.img
NIOO

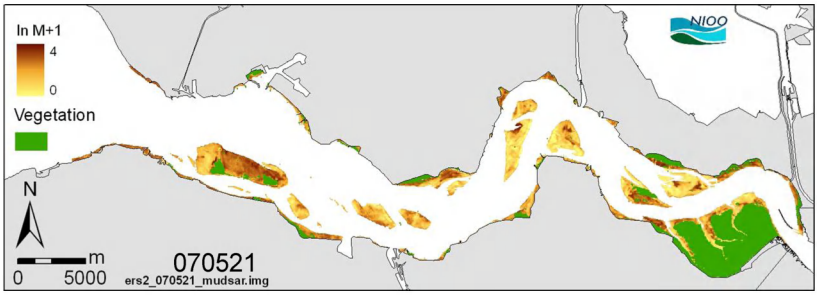
ln M+1
4
0
Vegetation
N
0
5000
m
070521
ers2_070521_mudsar.img
NIOO

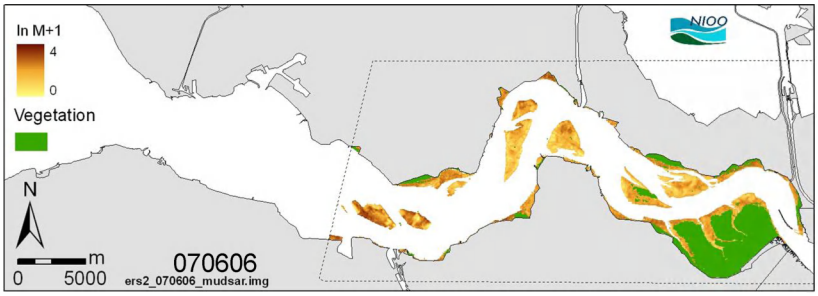
ln M+1
4
0
Vegetation
N
0
5000
m
070606
ers2_070606_mudsar.img
NIOO

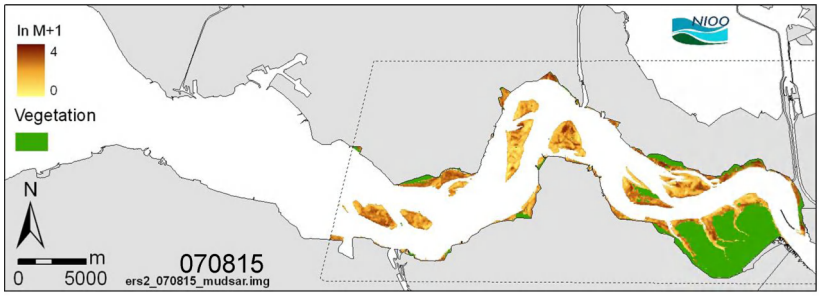
ln M+1
4
0
Vegetation
N
0
5000
m
070815
ers2_070815_mudsar.img
NIOO

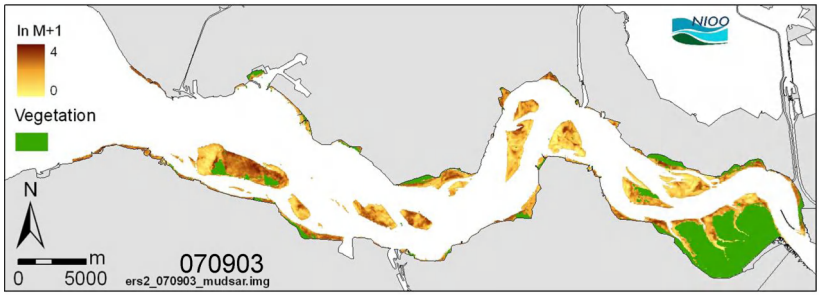
ln M+1
4
0
Vegetation
N
0
5000
m
070903
ers2_070903_mudsar.img
NIOO

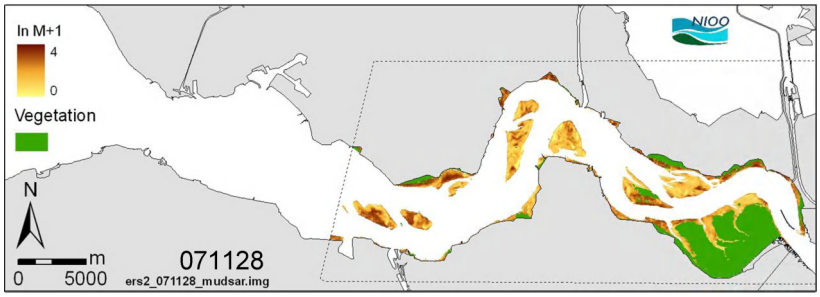
ln M+1
4
0
Vegetation
N
0
5000
m
071128
ers2_071128_mudsar.img
NIOO

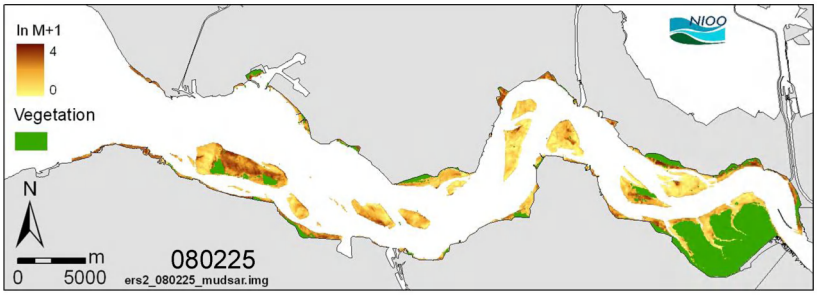
ln M+1
4
0
Vegetation
N
m
0 5000
080225
ers2_080225_mudsar.img
NIOO

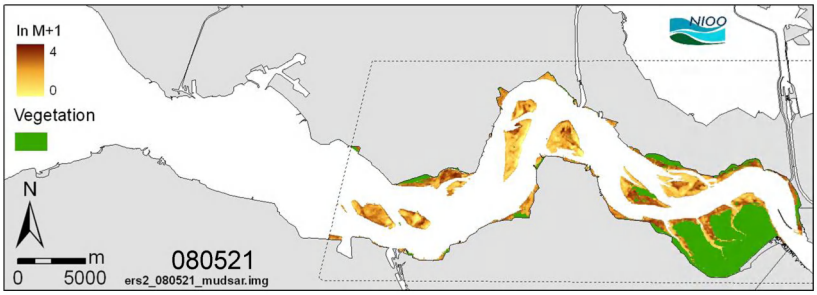
ln M+1
4
0
Vegetation
N
m
0 5000
080521
ers2_080521_mudsar.img
NIOO

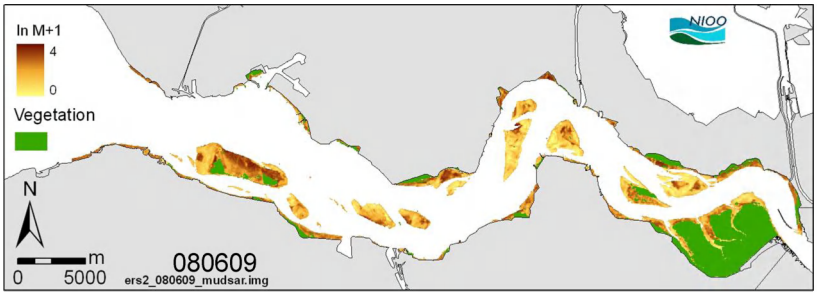
ln M+1
4
0
Vegetation
N
m
0 5000
080609
ers2_080609_mudsar.img
NIOO

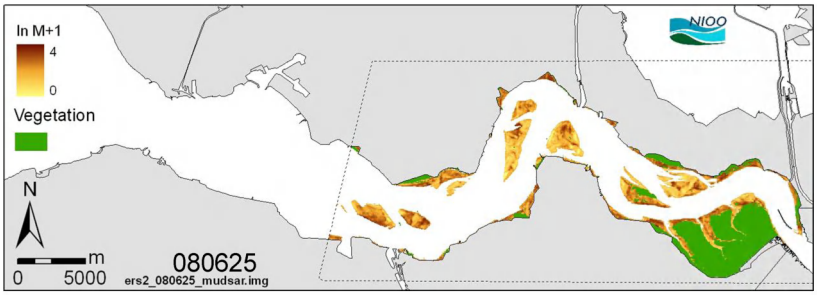
ln M+1
4
0
Vegetation
N
m
0 5000
080625
ers2_080625_mudsar.img
NIOO

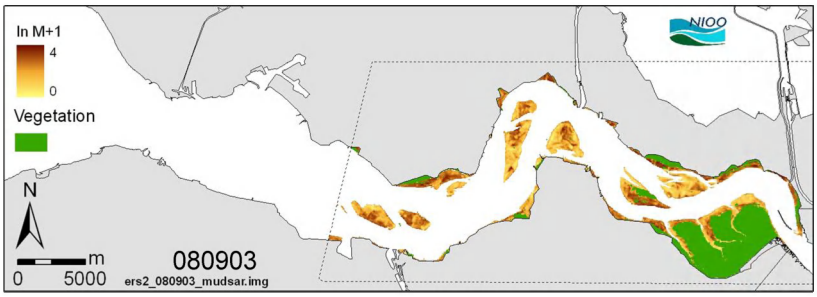
ln M+1
4
0
Vegetation
N
m
0 5000
080903
ers2_080903_mudsar.img
NIOO

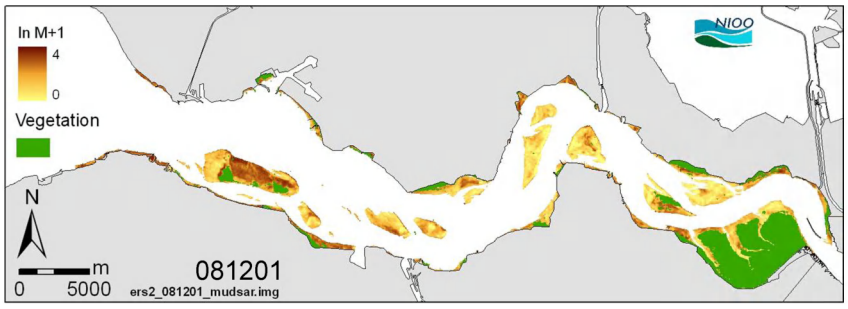
ln M+1
4
0
Vegetation
N
m
0
5000
081201
ers2_081201_mudsar.img
NIOO

B.3 Maps of mud content based on Landsat TM/ETM+ (model "TM").

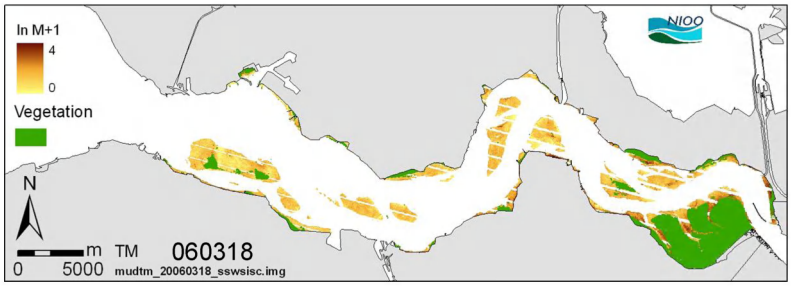

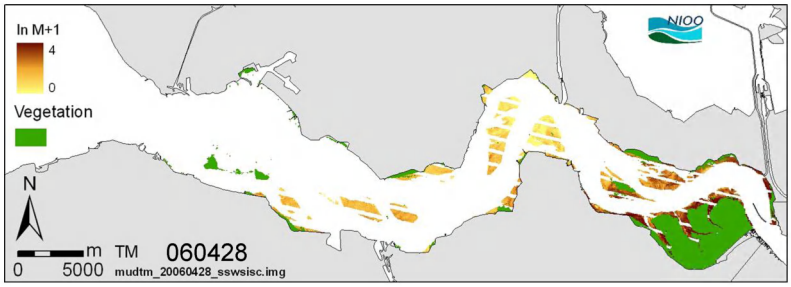

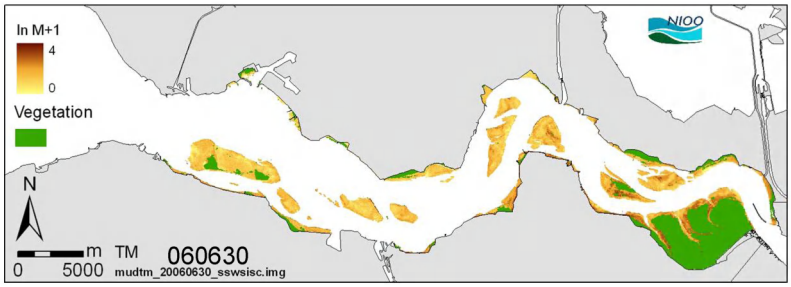

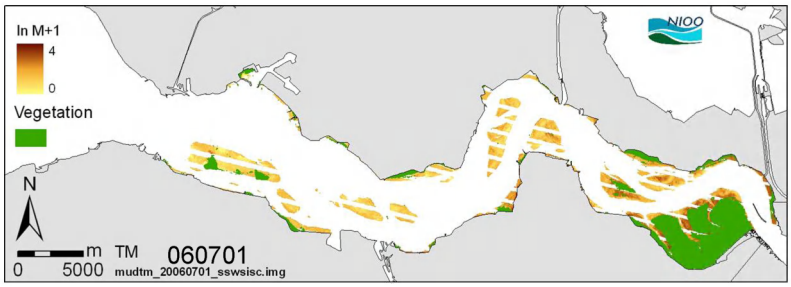

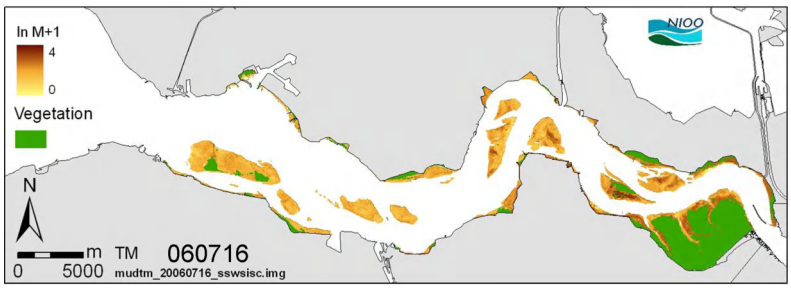

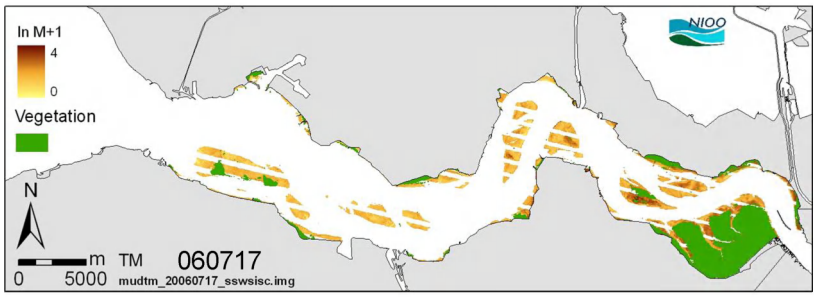
ln M+1
4
0
Vegetation
N
m
0
5000
TM
060717
mudtm_20060717_sswsisc.img
NIOO

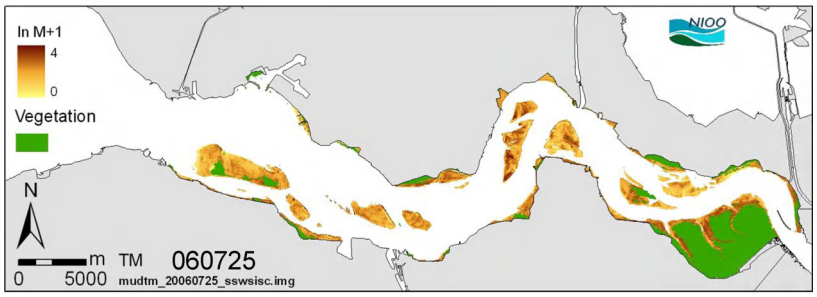
ln M+1
4
0
Vegetation
N
m
0
5000
TM
060725
mudtm_20060725_sswsisc.img
NIOO

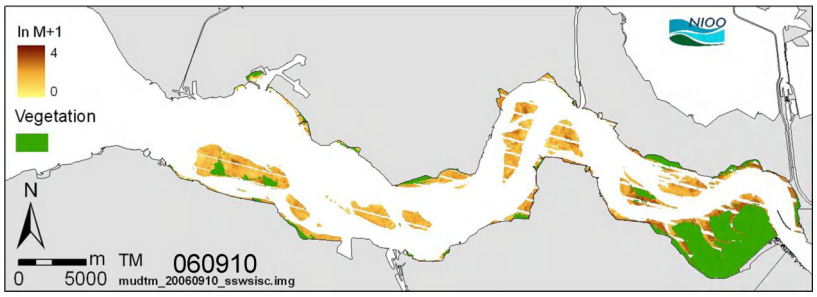
ln M+1
4
0
Vegetation
N
m
0
5000
TM
060910
mudtm_20060910_sswsisc.img
NIOO

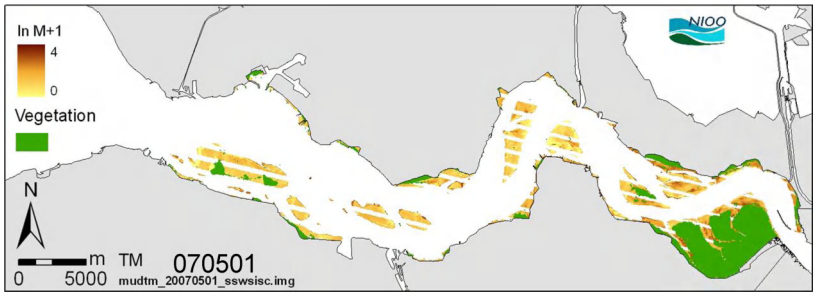
ln M+1
4
0
Vegetation
N
m
0
5000
TM
070501
mudtm_20070501_sswsisc.img
NIOO

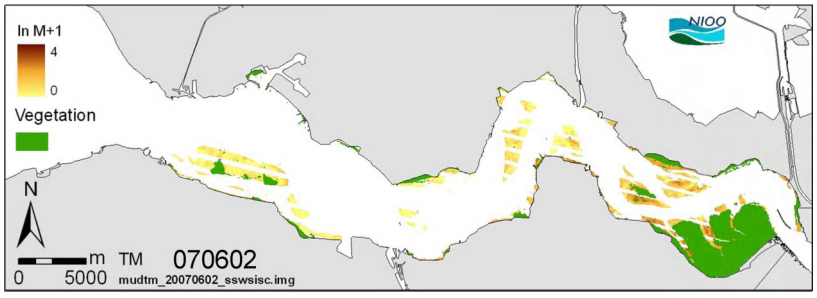
ln M+1
4
0
Vegetation
N
m
0
5000
TM
070602
mudtm_20070602_sswsisc.img
NIOO

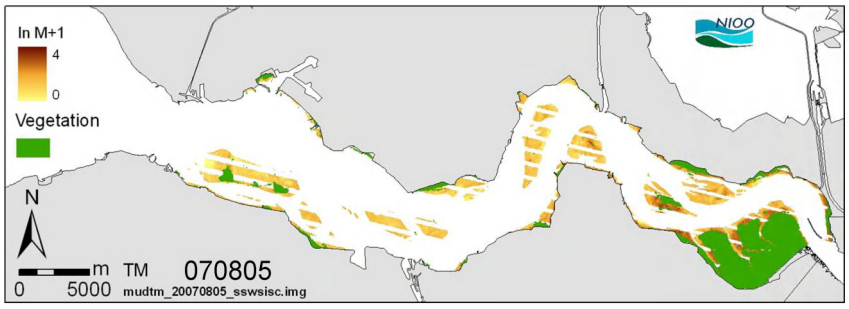
ln M+1
4
0
Vegetation
N
m
0
5000
TM
070805
mudtm_20070805_sswsisc.img
NIOO

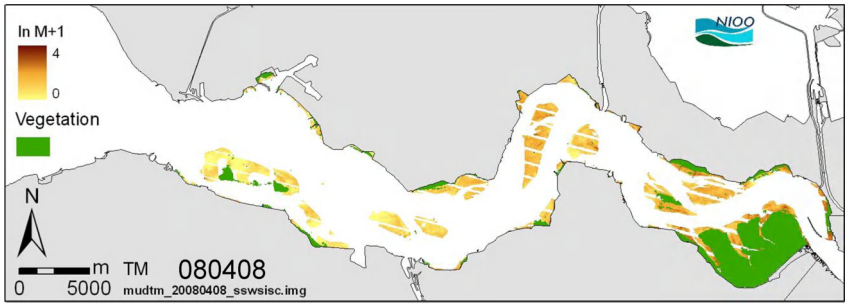
ln M+1
4
0
Vegetation
N
m
0
5000
TM
080408
mudtm_20080408_sswsisc.img
NIOO

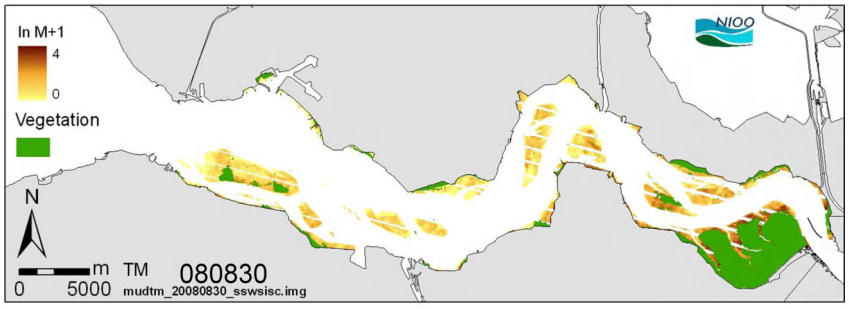
ln M+1
4
0
Vegetation
N
m
0
5000
TM
080830
mudtm_20080830_sswsisc.img
NIOO

B.4 Maps of mud content based on Landsat TM/ETM+ (model "TM2 inverse").

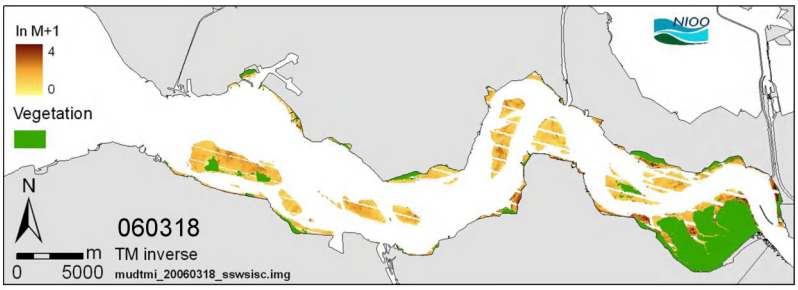

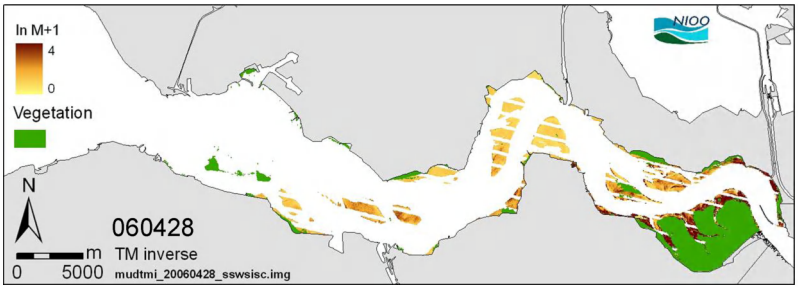

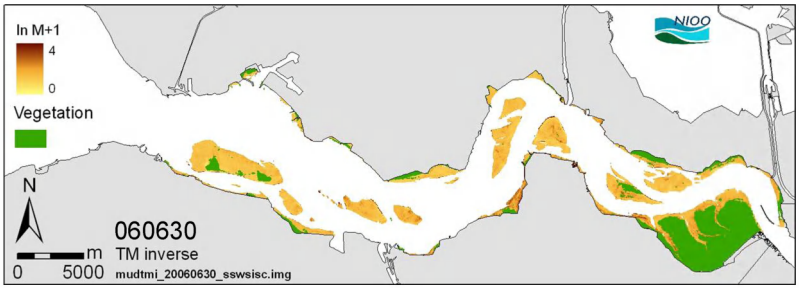

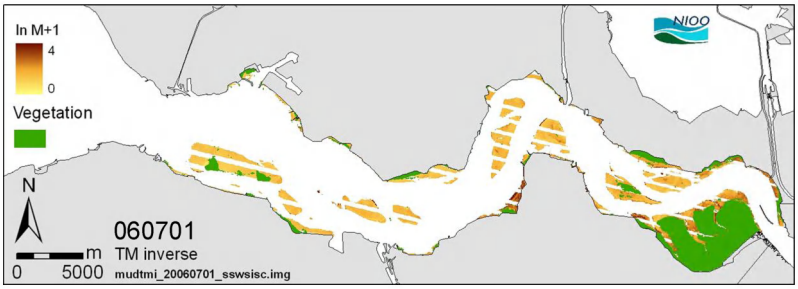

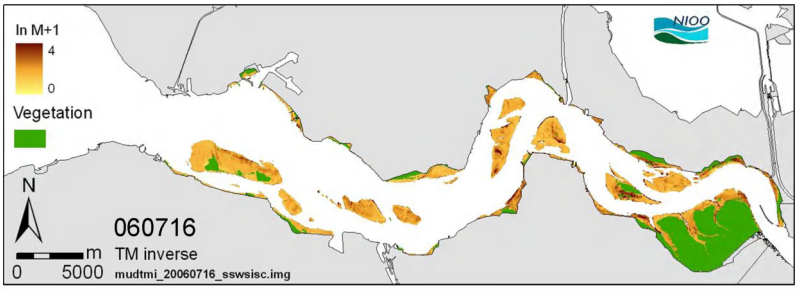

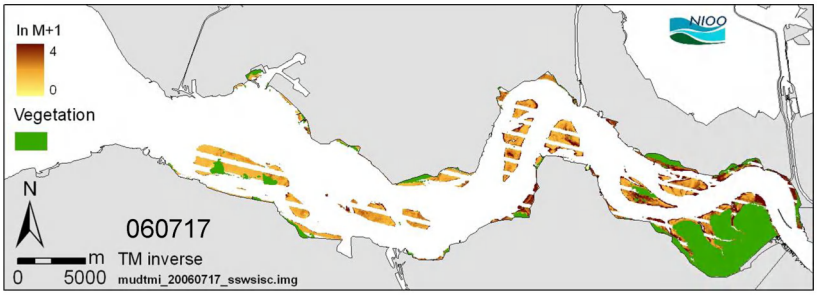
ln M+1
4
0
Vegetation
N
060717
m
0 5000
TM inverse
mudtmi_20060717_sswsisc.img
NIOO

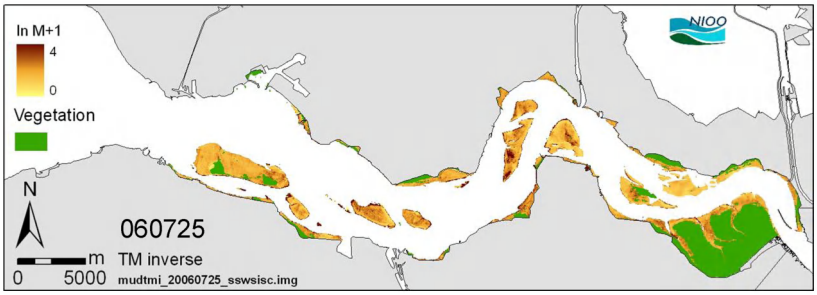
ln M+1
4
0
Vegetation
N
060725
m
0 5000
TM inverse
mudtmi_20060725_sswsisc.img
NIOO

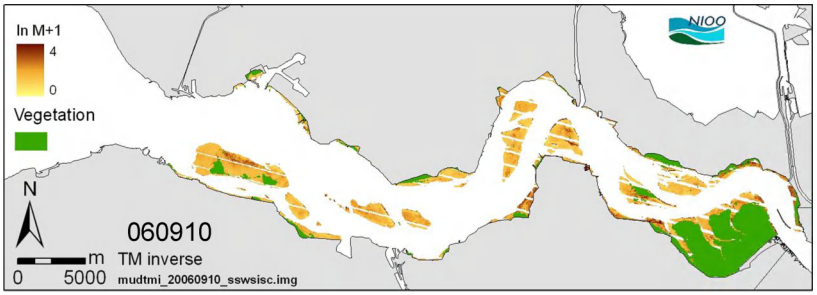
ln M+1
4
0
Vegetation
N
060910
m
0 5000
TM inverse
mudtmi_20060910_sswsisc.img
NIOO

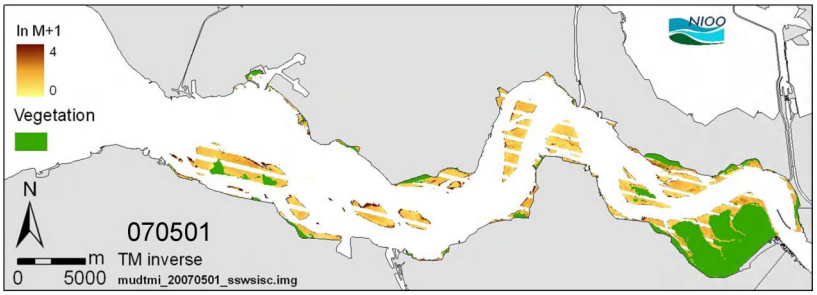
ln M+1
4
0
Vegetation
N
070501
m
0 5000
TM inverse
mudtmi_20070501_sswsisc.img
NIOO

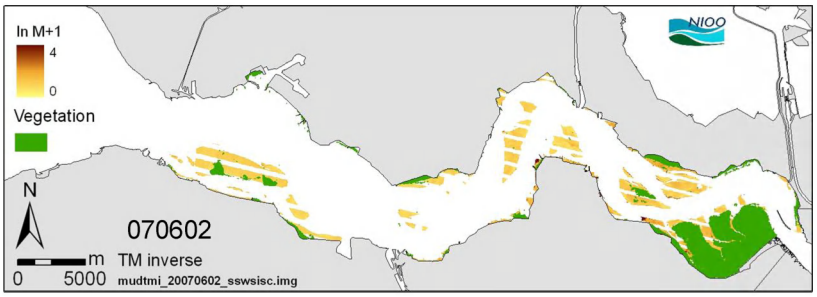
ln M+1
4
0
Vegetation
N
070602
m
0 5000
TM inverse
mudtmi_20070602_sswsisc.img
NIOO

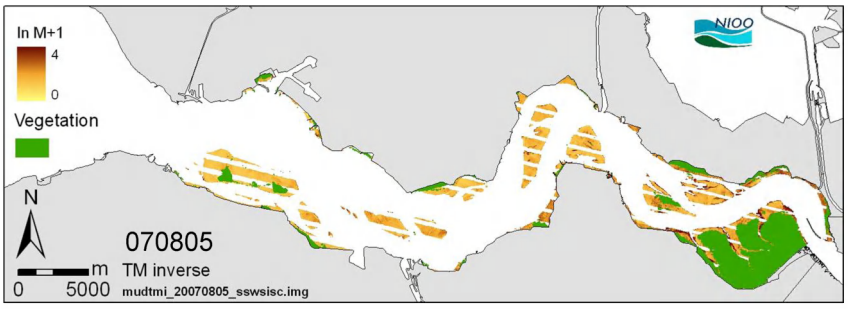
ln M+1
4
0
Vegetation
N
070805
m
0 5000
TM inverse
mudtmi_20070805_sswsisc.img
NIOO

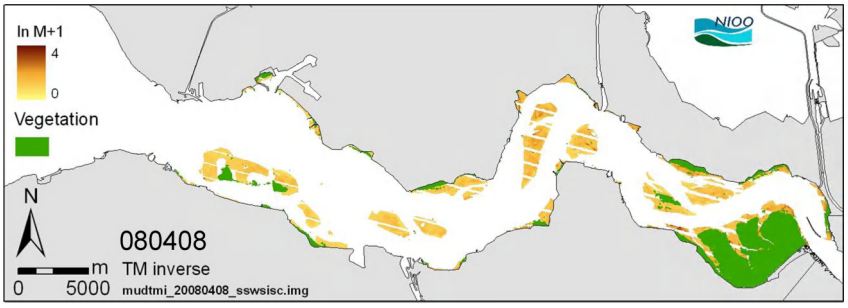
ln M+1
4
0
Vegetation
N
080408
m
0 5000
TM inverse
mudtmi_20080408_sswsisc.img
NIOO

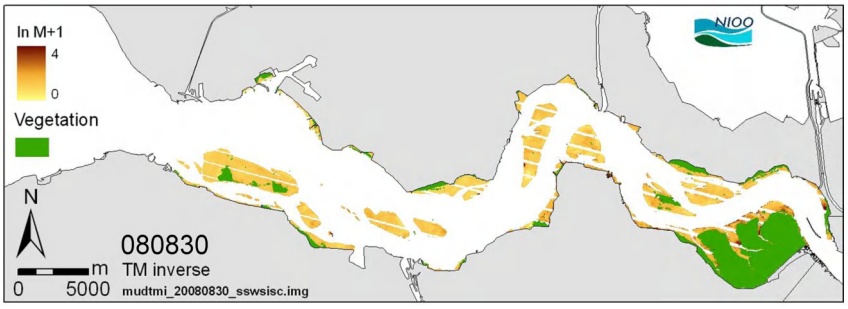
ln M+1
4
0
Vegetation
N
080830
m
0 5000
TM inverse
mudtmi_20080830_sswsisc.img
NIOO

B.5 Maps of mud content based on synergy of ERS SAR and Landsat TM/ETM+ (model "Synergy").

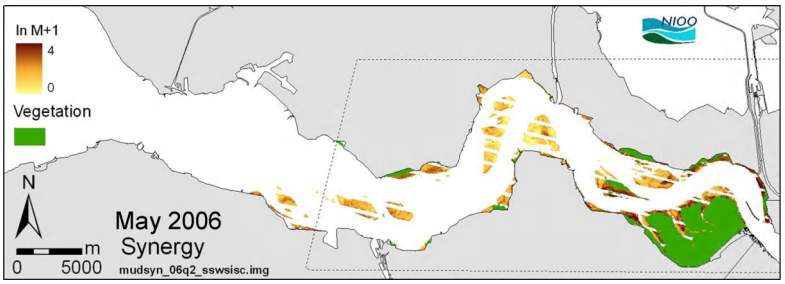

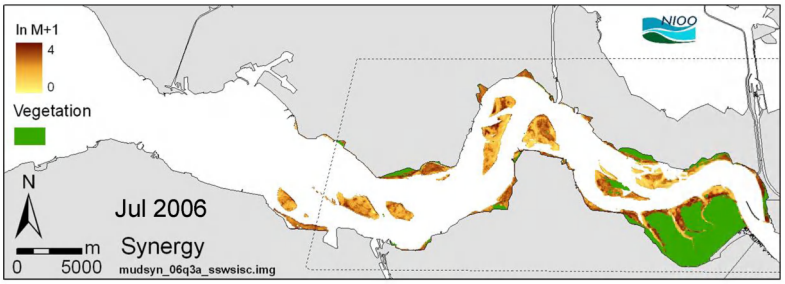

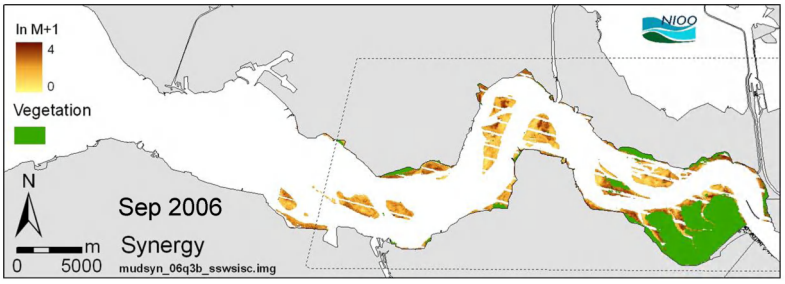

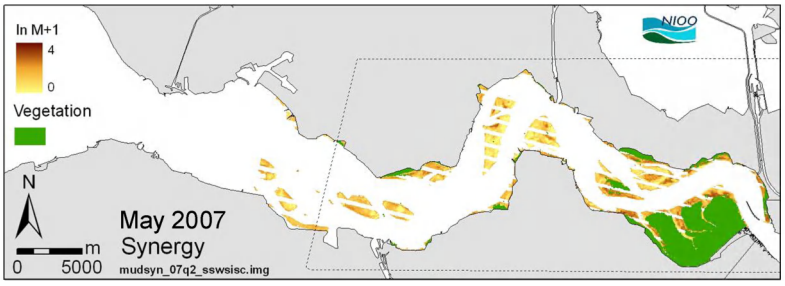

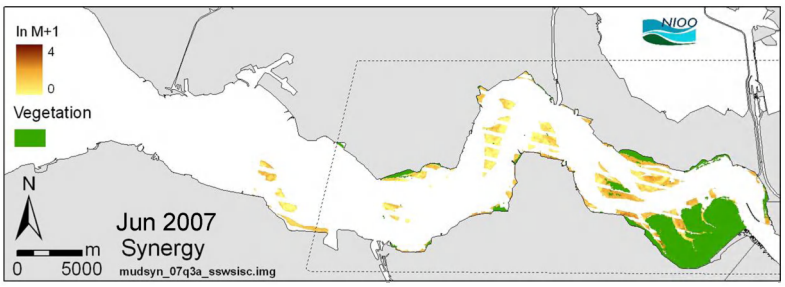

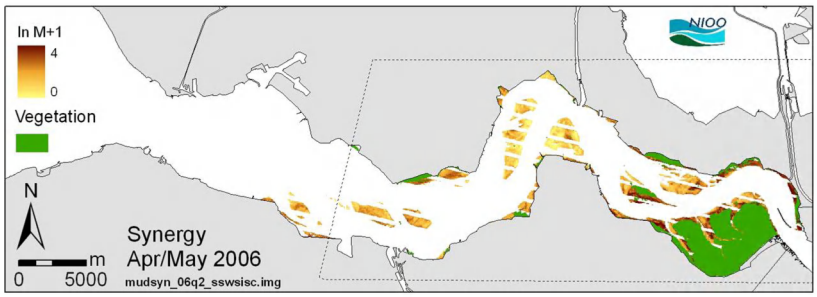
ln M+1
4
0
Vegetation
N
Synergy
Apr/May 2006
m
0 5000
mudsyn_06q2_sswsisc.img
NIOO

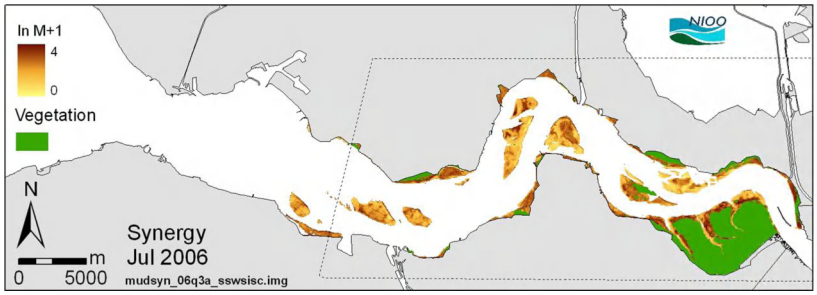
ln M+1
4
0
Vegetation
N
Synergy
Jul 2006
m
0 5000
mudsyn_06q3a_sswsisc.img
NIOO

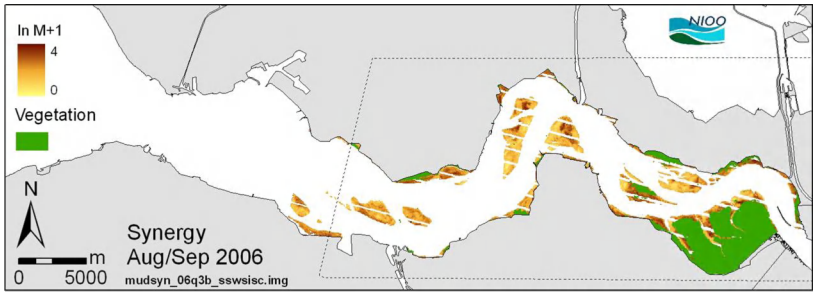
ln M+1
4
0
Vegetation
N
Synergy
Aug/Sep 2006
m
0 5000
mudsyn_06q3b_sswsisc.img
NIOO

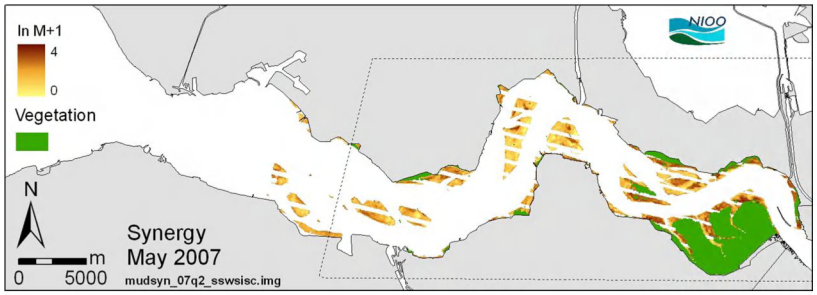
ln M+1
4
0
Vegetation
N
Synergy
May 2007
m
0 5000
mudsyn_07q2_sswsisc.img
NIOO

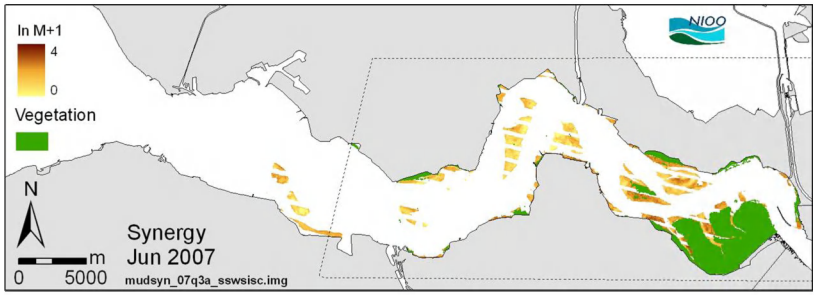
ln M+1
4
0
Vegetation
N
Synergy
Jun 2007
m
0 5000
mudsyn_07q3a_sswsisc.img
NIOO

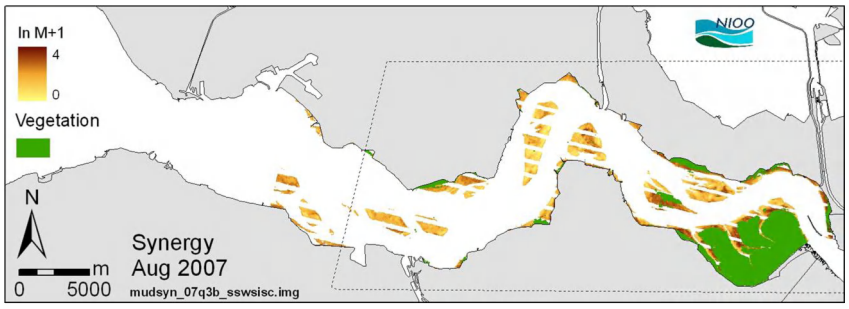
ln M+1
4
0
Vegetation
N
m
0 5000
Synergy
Aug 2007
mudsyn_07q3b_sswsisc.img
NIOO

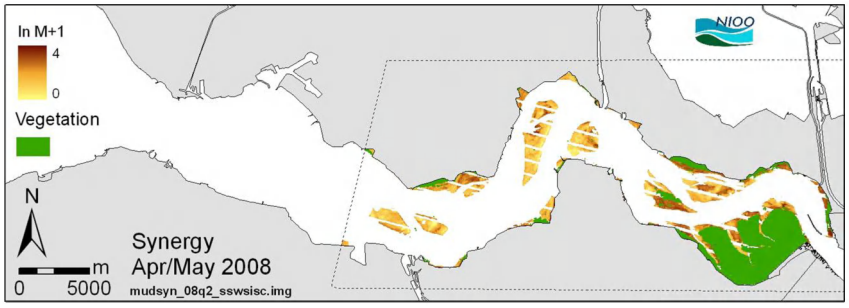
ln M+1
4
0
Vegetation
N
m
0 5000
Synergy
Apr/May 2008
mudsyn_08q2_sswsisc.img
NIOO

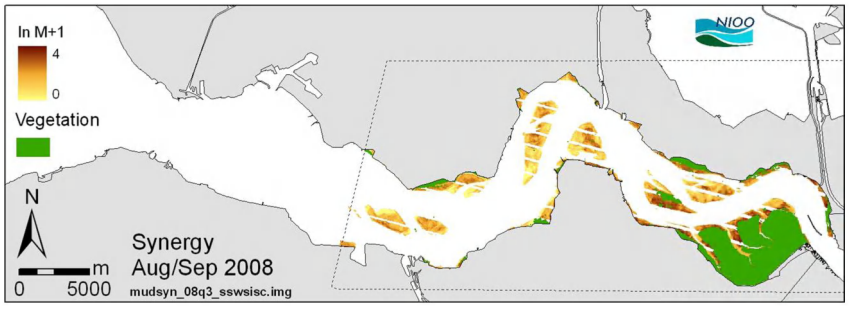
ln M+1
4
0
Vegetation
N
m
0 5000
Synergy
Aug/Sep 2008
mudsyn_08q3_sswsisc.img
NIOO

B.6 Combination of ERS SAR (June) and Landsat (August) image used for calibration with in situ data of June 2007 and June 2008 (model "Synergy").

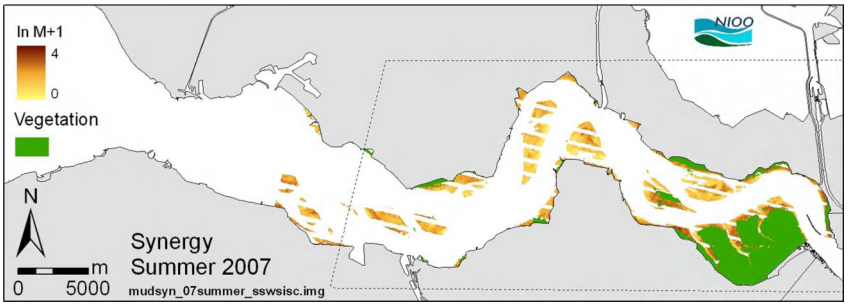

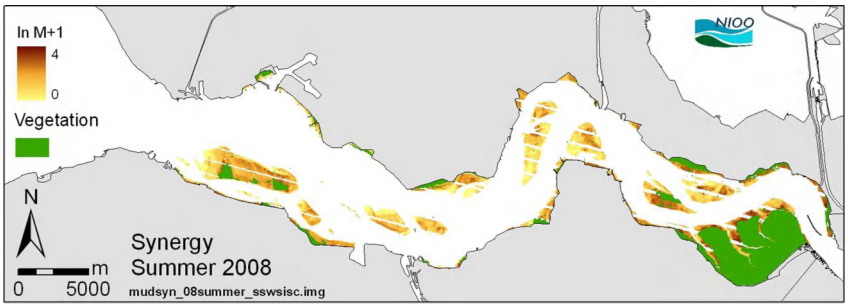

B.7 Maps of roughness RMSz based on ERS SAR imagery.

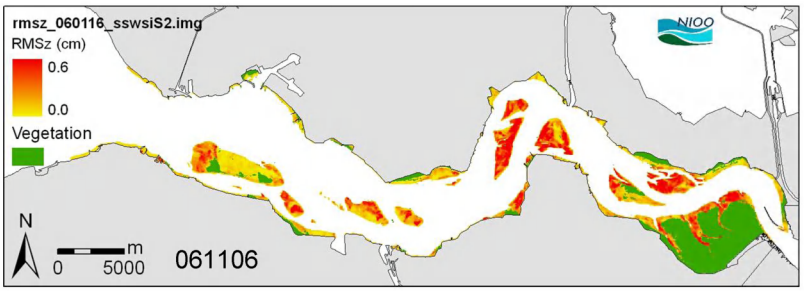

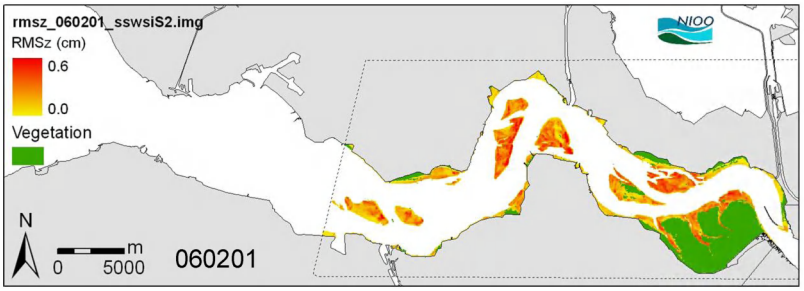

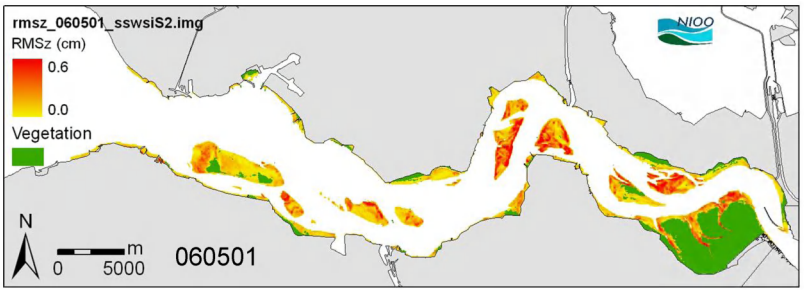

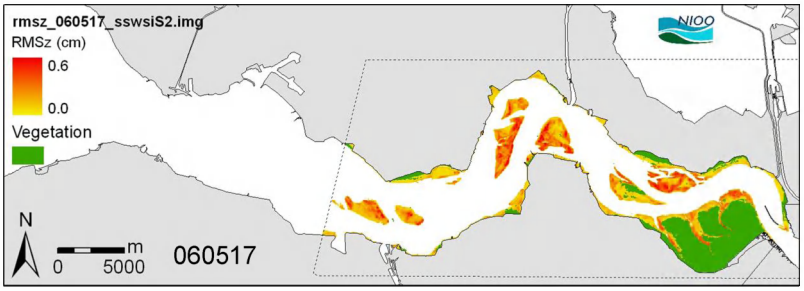

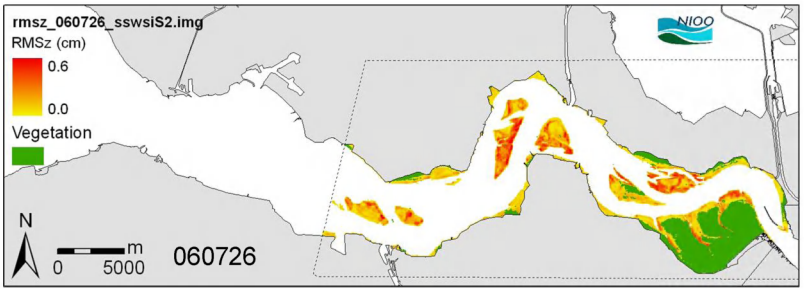

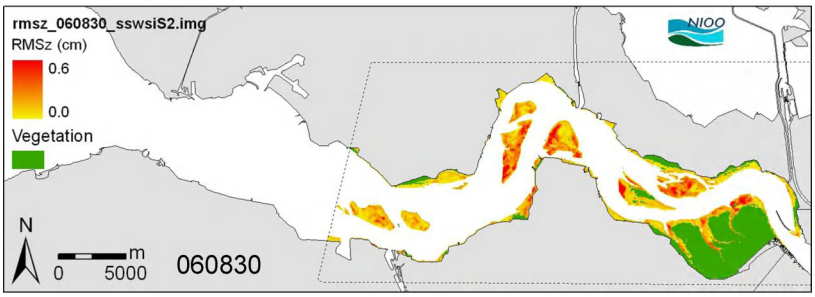
rmsz_060830_sswsiS2.img
RMSz (cm)
0.6
0.0
Vegetation
N
0
5000
m
060830

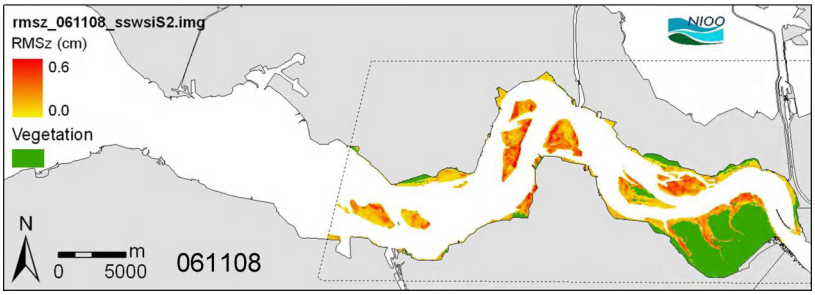
rmsz_061108_sswsiS2.img
RMSz (cm)
0.6
0.0
Vegetation
N
0
5000
m
061108

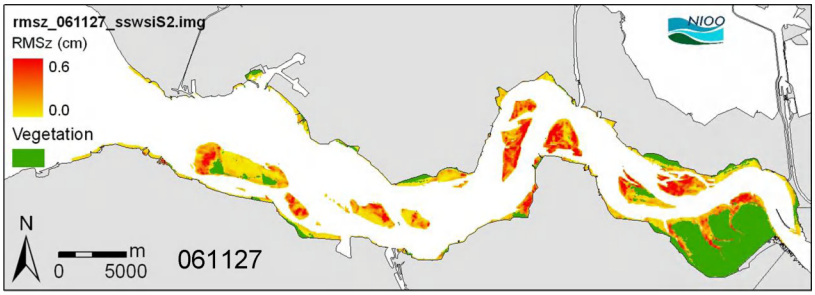
rmsz_061127_sswsiS2.img
RMSz (cm)
0.6
0.0
Vegetation
N
0
5000
m
061127

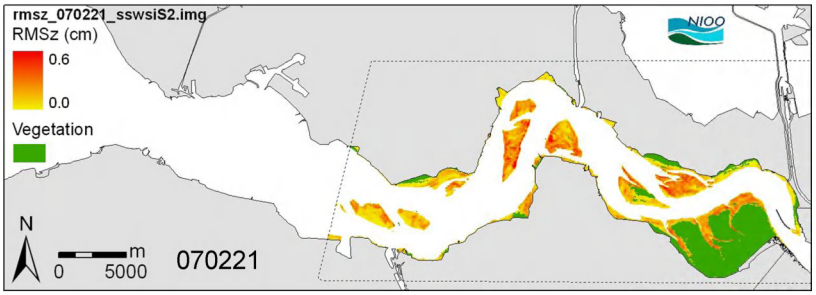
rmsz_070221_sswsiS2.img
RMSz (cm)
0.6
0.0
Vegetation
N
0
5000
m
070221

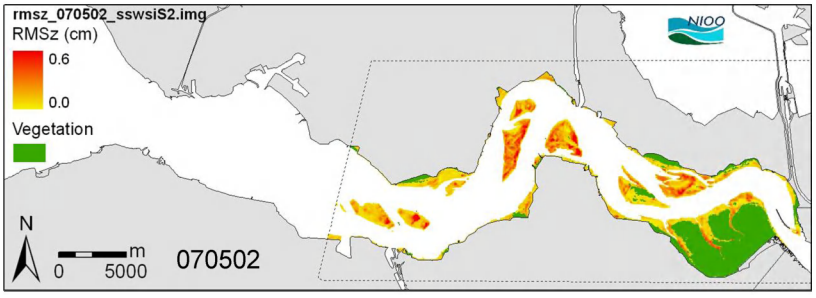
rmsz_070502_sswsiS2.img
RMSz (cm)
0.6
0.0
Vegetation
N
0
5000
m
070502

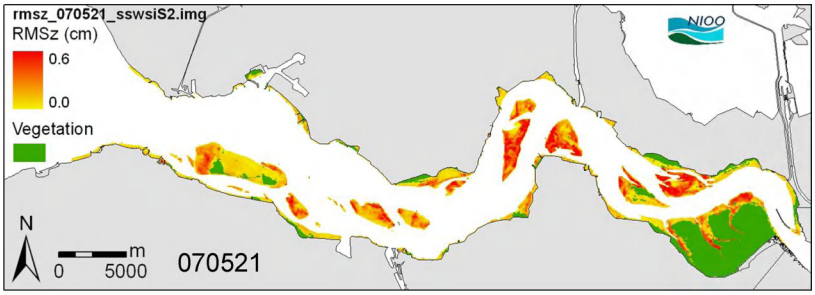
rmsz_070521_sswsiS2.img
RMSz (cm)
0.6
0.0
Vegetation
N
0
5000
m
070521
NIOO

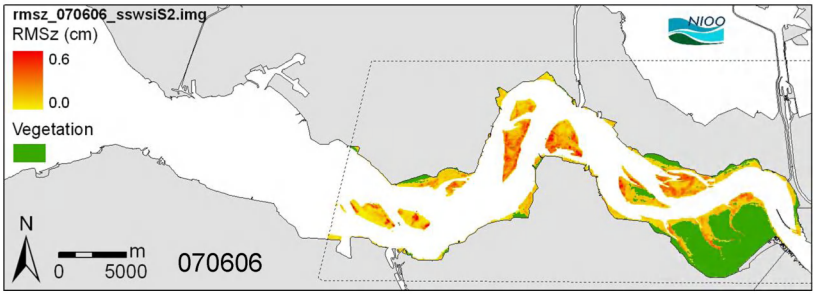
rmsz_070606_sswsiS2.img
RMSz (cm)
0.6
0.0
Vegetation
N
0
5000
m
070606
NIOO

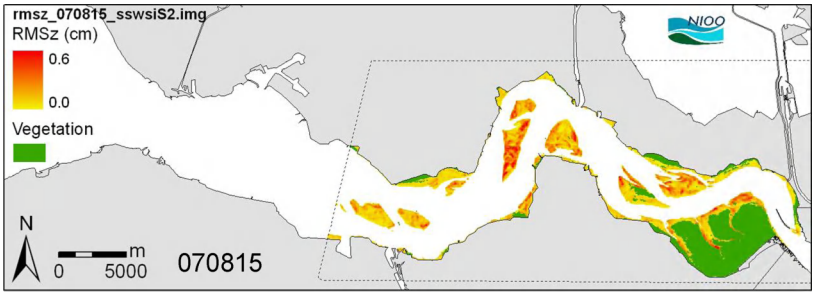
rmsz_070815_sswsiS2.img
RMSz (cm)
0.6
0.0
Vegetation
N
0
5000
m
070815
NIOO

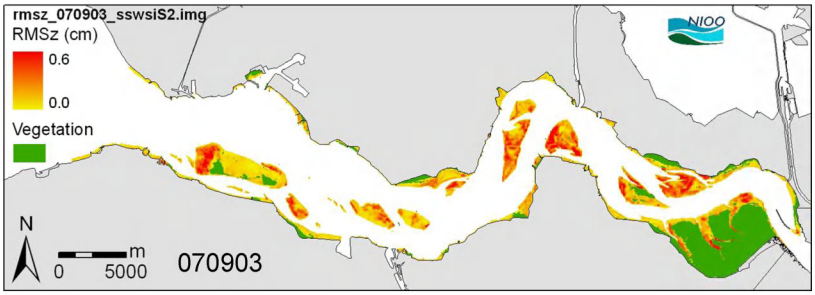
rmsz_070903_sswsiS2.img
RMSz (cm)
0.6
0.0
Vegetation
N
0
5000
m
070903
NIOO

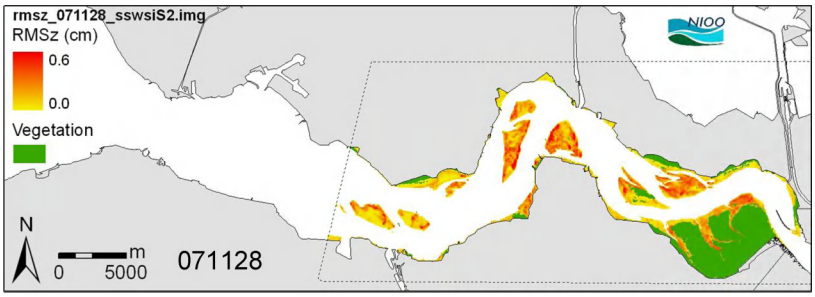
rmsz_071128_sswsiS2.img
RMSz (cm)
0.6
0.0
Vegetation
N
0
5000
m
071128
NIOO

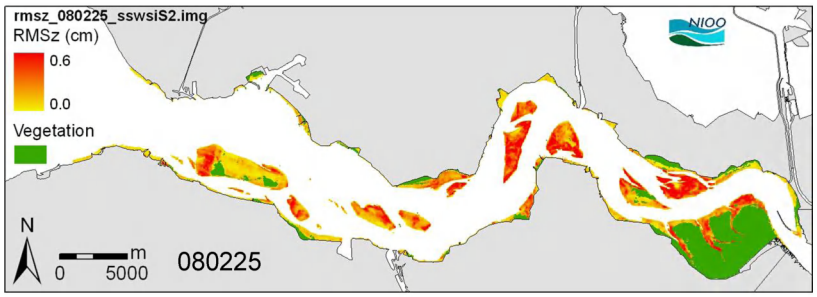
rmsz_080225_sswsiS2.img
RMSz (cm)
0.6
0.0
Vegetation
N
0
5000
m
080225
NIOO

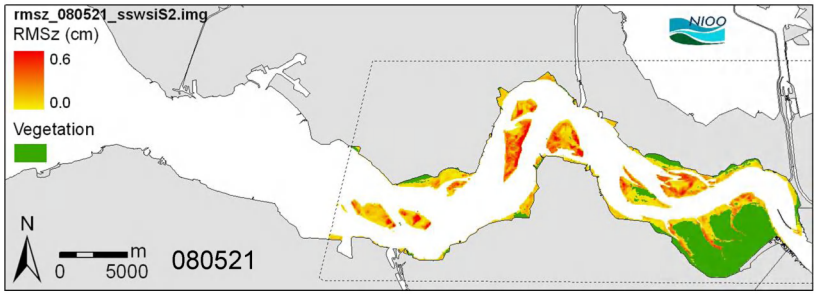
rmsz_080521_sswsiS2.img
RMSz (cm)
0.6
0.0
Vegetation
N
0
5000
m
080521
NIOO

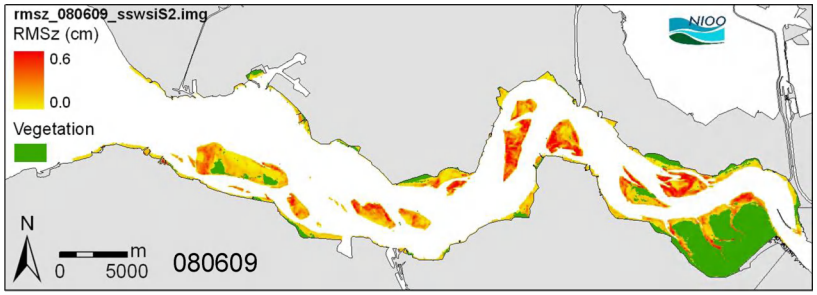
rmsz_080609_sswsiS2.img
RMSz (cm)
0.6
0.0
Vegetation
N
0
5000
m
080609
NIOO

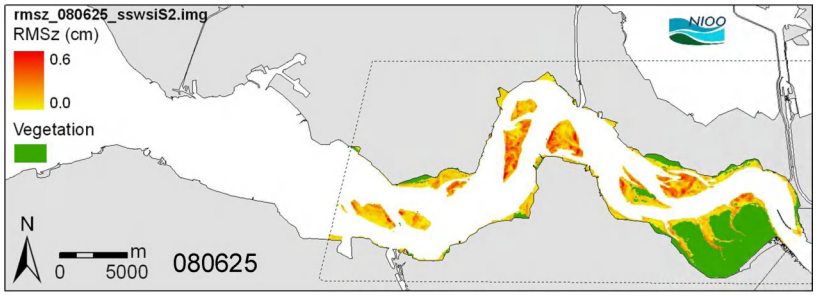
rmsz_080625_sswsiS2.img
RMSz (cm)
0.6
0.0
Vegetation
N
0
5000
m
080625
NIOO

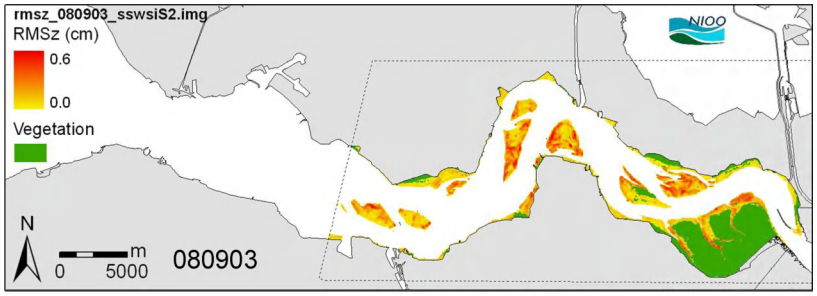
rmsz_080903_sswsiS2.img
RMSz (cm)
0.6
0.0
Vegetation
N
0
5000
m
080903
NIOO

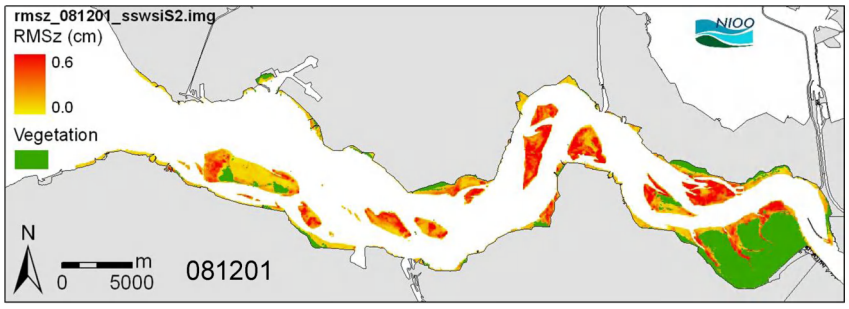
rmsz_081201_sswsiS2.img
RMSz (cm)
0.6
0.0
Vegetation
N
0
5000
m
081201
NIOO

C Mass balance from mud model

Schematised mass balance map of the Scheldt estuary for scenario WL6